NASA CR-165,498

NASA Contractor Report 165498

NASA-CR-165498
19820018830

MECHANISMS OF DEFORMATION AND FRACTURE IN HIGH-TEMPERATURE LOW-CYCLE FATIGUE OF RENÉ 80 AND IN 100

Glenn Roy Romanoski, Jr.

University of Cincinnati
Cincinnati, Ohio

March 1982

Prepared for

NATIONAL AERONAUTICS AND SPACE ADMINISTRATION
Lewis Research Center
Under Contract NSG-3-263

were observed. Testing at 900 C, 700 C, and 600 C caused precipitation of grain boundary carbides. At 700 C, carbides precipitated on slip bands. The fine grained structures exhibited planar slip on (111) planes. Dislocations looped the large gamma precipitates. This structure led to stress saturation and propagation was observed. Increasing temperatures

ENTER:

46 1 1 RN/NASA-CR-165498

DISPLAY 46/2/1

82N26706*# ISSUE 17 PAGE 2415 CATEGORY 39 RPT#: NASA-CR-165498 NAS 1.26:165498 CNT#: NSG-3263 82/03/00 227 PAGES UNCLASSIFIED DOCUMENT

UTTL: Mechanisms of deformation and fracture in high temperature low cycle fatigue of Rene 80 and IN 100 TLSP: Final Report

AUTH: A/ROMANOSKI, G. R., JR.

CORP: Cincinnati Univ., Ohio. CSS: (Dept. of Materials Science and Metallurgical Engineering.) AVAIL.NTIS SAP: HC A11/MF A01

MAJS: /*CRACK INITIATION/*FATIGUE TESTS/*HEAT RESISTANT ALLOYS/*HIGH TEMPERATURE TESTS/*METAL FATIGUE/*NICKEL ALLOYS

MINS: / COFFIN-MANSON LAW/ GAS TURBINES/ HEAT TREATMENT/ INELASTIC STRESS/ INTERGRANULAR CORROSION/ MICROSTRUCTURE/ TRANSGRANULAR CORROSION

ABA: Author

ABS: Specimens tested for the AGARD strain range partitioning program were investigated. Rene 80 and IN 100 were tested in air and in vacuum; at 871 C, 925 C, and 1000 C; and in the coated and uncoated condition. The specimens exhibited a multiplicity of high-temperature low-cycle fatigue damage. Observations of the various forms of damage were consistent with material and testing conditions and were generally in agreement with

TABLE OF CONTENTS

N82-26706#

I. INTRODUCTION

Economic and reliable operation of gas turbines for industrial, commercial and military applications depends on long and predictable lifetimes for all components. The demands placed on materials in gas turbines include cyclic and sustained stresses and strains at high temperatures where corrosion processes are often a life-determining factor. The design and operation of light weight high performance jet engines represents a tremendous challenge to both designers and materials specialists. A recently published summary analysis[1] made to determine the various causes of accidents and mishaps in the Air Force identified engine failures as the single most important cause of aircraft accidents/incidents. A breakdown of the causes for failure of engine components is shown in Figure 1. As can be seen, a significant number of failures are attributed to failure modes generally associated with the hot section (turbine) of the engine.

It is possible to address each failure mode separately, but experience reveals that materials used for turbine components accrue damage having multiple character. Fatigue results from variations in the power requirements for flight profiles as well as from thermal fatigue caused by start-up and shut-down. On examining the temperature distribution for steady state operation of a turbine blade (Figure 2), it can be seen that temperatures on the order of 1000C are encountered. At these temperatures creep and corrosion are persistant modes of damage.

Although a particular mode may be the major contributor to total

damage, it is usually a combination of modes interacting in a complex fashion that is ultimately responsible for failure[3]. Hereafter, "High-Temperature Low Cycle Fatigue," HTLCF, will imply all damage mechanisms contributing to failure, not just pure fatigue.

It is generally accepted that localized inelastic strain controls the life of components in a fatigue environment. Such strains usually occur in a fillet or a notch (Figure 3), and the failure mode is referred to as high-strain or low-cycle fatigue. A considerable amount of effort has been expended on relating fatigue life to inelastic strain and other appropriate parameters. The Coffin-Manson relationship was the first such attempt. Many of the fatigue-life laws formulated thereafter represent some modification of the Coffin-Manson equation. Most are emperical equations based on satisfying a best correlation with laboratory test data. Some are based on a mathematical description of assumed damage mechanics. Design of critical gas turbine components requires confidence in predicting HTLCF behavior of materials beyond laboratory testing experience. Confidence in any fatigue-life predictive methodology must be founded on a knowledge of actual damage mechanisms. Beginning with an observed damage mechanism, a model is constructed and a fatigue-life law is formulated incorporating all parameters in the same manner that they relate to the damage process.

It is the objective of this research to investigate damage mechanisms in HTLCF of René 80 and IN 100 and to relate such observations and analysis to fatigue life.

II. LITERATURE REVIEW

A. Physical and Mechanical Metallurgy of Nickel-Base Superalloys

It is appropriate to review some salient features of nickel-base superalloys in general to provide a background for the discussions which will follow. Several good reviews[4-8] which will serve as a basic reference are available in the literature.

The aircraft jet engine industry has progessed through improvements in the high temperature capability of nickel-base superalloys. The mainstay of the nickel-base superalloys are those with at least 40 percent Ni and are of the Al-Ti age-hardening type. In these alloys, Cr is present to provide oxidation resistance along with some auxiliary strengthening of the matrix. Other elements are also present to provide solid solution strengthing of the matrix. The major part of the strengthening at high temperatures, however, is due to the precipitation of the ordered gamma prime phase, γ', generally as $Ni_3(Al,Ti)$.

In many alloys there are elemental additions such as B and Zr to improve high temperature creep properties and/or fabricability.

Physical properties of interest include: melting range, density, dynamic modulus, thermal conductivity, and thermal expansivity. Mechanical properties of interest include: high temperature tensile, creep rupture properties and mechanical and thermal fatigue resistance. Other parameters such as weldability, machineability, formability, hardness, oxidation resistance and resistance to various corrosive media play an important role in the selection of an alloy for a given application. Unfortunately no single alloy embodies the optimum of all

properties; therefore, a compromise is usually required.

1. Physical Properties

One very useful property of nickel-base superalloys is the retention of very high strength levels at large values of the ratio - operating temperature/alloy melting point - known also as the homologus temperature. Homologus temperature is often used to specify regimes of material behavior.

Density is a design consideration. In conjunction with the pressure from hot expanding gases in a jet turbine, rotating components must support the centrifugal forces caused by their own mass.

Dynamic modulus relates stress to time independent strain. It is an important parameter in calculations of clearance and stress.

Thermal conductivity and thermal expansivity are familiar parameters which take on special significance in jet turbine design. Adequate clearance must be allowed to permit unobstructed expansion of all components. Thermal conductivity and thermal expansivity are the principal determiners of thermal stresses and thermal fatigue behavior. A material with a high thermal conductivity and low thermal expansivity is most desirable.

2. Chemical Properties

Phase stability is an important consideration for nickel-base superalloys since basic property data (short term) is used to predict their in service behavior (long term). Many such considerations are thermodynamic in nature, but not only so. Most observed degradation

processes, although thermodynamically favorable, proceed only (or at a much accelerated rate) under stress and/or attending deformation.

During operation, gas turbine components are subjected to oxidation and hot corrosion. Hot corrosion is a form of accelerated oxidation in atmospheres containing sulphates, sodium salts, halides, vanadium and lead oxides, all of which can be found in fuel burning systems. Nickel forms a low melting point eutectic with nickel sulphide and hence, in sulphur-bearing gases, attack of a nickel-base alloy surface is rapid and drastic. Nickel-base superalloys rely on the formation of surface films of Al_2O_3 and Cr_2O_3 for high temperature surface protection. Mechanical and thermal cycling, however, can crack and spall these protective oxide films and expose clean unprotected metal for further attack. Superalloys are sometimes used in a coated condition, but such coatings possess poor mechanical strength and crack under high strains.

3. Mechanical Properties

Components in a jet turbine are designed to operate below yield stresses. However, tensile properties of nickel-base superalloys may degrade after long hours of service. This reduction in properties must be anticipated in design.

When an alloy undergoes permanent plastic deformation under stress, the amount of deformation being a function of time, it is said to creep. Such permanent deformation is important for two reasons. When calculations for clearances are made, account must be made for dimensional changes of creeping components. Creep is a failure mode

which may limit the safe life of a component.

Thermal and mechanical fatigue may be the most important properties in view of the consequences but are also the most difficult to predict from test data. The basic property to be understood is high-temperature low-cycle fatigue behavior.

4. Strengthening Mechanisms in Nickel-Base Superalloys

If the fullest capabilities of nickel-base superalloys are to be realized, it is important that the basic factors controlling the mechanical properties be understood. R. F. Decker of International Nickel Company has assembled an excellent review of this subject[6]. Some important aspects of this review will be summarized here.

The nickel matrix, γ, alone is not inherently endowed with a high temperature capability in agressive environments, but when combined with other elements, alloys can be utilized to 0.8 T_m (melting point) and for times up to 100,000 hours at somewhat lower temperatures. This endurance must be attributable to the high tolerance of Ni for alloying without phase instability and, with Cr additions, the tendency to form Cr_2O_3 - rich protective scales.

Solid-solution elements in γ are Co, Fe, Cb, Cr, Mo, Ta, W, V, Ti, and Al[9-11]. These elements differ from Ni by 1 to 13% in atomic diameter and 1 to 7 in N_v, the electron vacancy number. Hardening has been related to this atomic diameter oversize as measured by lattice expansion[12,13]. An additional effect can be attributed to the lowering of stacking fault energy by these high N_v elements[14,15]. The lowering of stacking fault energy by alloying elements would make

cross-slip more difficult in γ. Above 0.6 Tm, the range of high temperature creep, γ strengthening is diffusion dependent. The slow-diffusing elements, Mo and W, would be expected to be potent hardeners[16].

Nickel-base superalloys owe much of their high temperature capability to the presence of the γ' precipitate. The compatibility of crystal structure and lattice constant ($\sim$0-1% mismatch) with γ allows homogeneous nucleation of γ' with low surface energy and long time stability. γ' contributes strength to the γ- γ' alloy by anti-phase boundary (APB) as well as in the conventional precipitate-matrix fashion. For small sizes, dislocations cut the γ' precipitates. Beyond a certain γ' particle size, by-passing will occur by either looping or dislocation climb. Several basic factors contribute to the magnitude of hardening: anti-phase boundary (APB) and fault energy of γ', γ strength, γ' strength, coherency strains, volume percent γ', particle size of γ', diffusivity in γ and γ' and, possibly, γ - γ' modulus mismatch. All of these factors are not additive[17,18].

Above about 815°C, γ' ripens making dislocation by-passing easier and consequently reducing the flow stress of the material[19]. Despite the tolerance of the nickel base for heavy solid-solution and γ' strengthening, a limit exists beyond which undesirable phases precipitate. γ' can degenerate to η or Ni_3Cb with an attending degradation of strength. Sigma, an electronic compound, can precipitate in the temperature range of 650C to 925C, especially under stress. Sigma is inherently brittle and often precipitates in a platelike form.

Both of these factors contribute to a reduction in mechanical properties. The occurrence of sigma phase can be predicted through electron vacancy number calculations, of the residual matrix[20].

A common form of creep damage is grain boundry sliding. In nickel-base superalloys, advantage is taken of discontinuous carbides which enhance grain boundary irregularity and impede sliding. The common classes of carbides in nickel-base superalloys are MC, $M_{23}C_6$, Cr_7C_3 and M_6C.[6] MC usually takes a coarse random cubic or script morphology. $M_{23}C_6$ shows a marked tendency for grain boundary forms. At 760C to 870C, nearly continuous platelet forms predominate while at 980C more blocky and less continuous types are found. M_6C can precipitate in blocky form in grain boundaries and in Widmanstatten intragranular form. It is apparent that continuous grain boundary $M_{23}C_6$ and Widmanstatten M_6C are to be avoided for best ductility and rupture life.

Control of grain size and shape are a primary consideration in the treatment of nickel-base superalloys for high temperature service. Since creep damage generally accrues at grain boundaries, improved properties can be realized in large grained structures. Cast superalloys have also exhibited increased rupture life and creep resistance with increased component-thickness to grain-size ratio[23]. It is special control of grain structure, that is, directionally solidified and single crystal forms, which promises further progress in the high temperature capabilities of nickel-base superalloys.

B. Damage Mechanisms in High-Temperature Low-Cycle Fatigue

Many nickel-base superalloys were developed for critical components of gas turbines. Experience has shown that these components are LCF - life limited ($<10^4$ cycles). The inelastic strains which give rise to this failure mode result from stress concentrations in component geometry and thermal cycling caused by start-up and shut-down. A report compiled by Oak Ridge National Laboratory (ORNL) entitled "Time Dependent Fatigue of Structural Alloys"[24] is a comprehensive reference of this general subject. Review papers which address damage mechanisms in nickel-base superalloys more specifically are also available in the literature[25-30].

The multiplicity of HTLCF damage has been recognized by investigators[31]. The expression "creep-fatigue-environment interactions"[30] is broadly accepted in recognition of the complex, interdependent nature of damage which occurs in nickel-base superalloys in service and in laboratory tests. Each of these modes of damage can be quite serious when considered separately, but when all are operative in HTLCF, their interaction generally effects an increased rate of net damage accumulation.

In the high strain regime of HTLCF, it is commonly observed that cracks nucleate very early in cyclic life, often during the first cycle.[24] Regardless of the strain level, propagation is at first (competitive) among the many heterogeneously nucleated cracks until one or more dominate or coalesce, leading to final failure. Damage mechanisms in HTLCF, therefore, are those processes which contribute to the

initiation and subsequent propagation of these cracks.

Several topics of importance to damage mechanisms in HTLCF will be explored. Each topic will be introduced and discussed in a general way followed by specific references to investigations presented in the literature which demonstrate some pertinence to the present work.

1. Deformation Behavior

Nickel-base superalloys accommodate the inelastic strains of cyclic deformation in two ways; by heterogeneous motion of dislocations on very few slip planes, planar slip, or in a more homogeneous fashion on a greater number of slip planes, wavy slip. Understanding the prevailing slip character is essential to understanding the various fatigue cracking modes and their dependence on variables such as temperature and strain rate[28].

Planar slip is favored by a low stacking fault energy, ordering, the presence of coherent precipitates, low temperatures ($< 0.4\ T_m$), small strains, and high strain rates. Cyclic strain reversals are repeatedly accommodated in planar arrays called persistent slip bands, PSB. These planes accumulate damage (dislocation debris) until decohesion between planes results. Such PSB cracking occurs between planes of greatest resolved shear stress (that is at approximately 45° to the principal stress axis) and appear as intrusions and extrusions on the material surface. This initial stage of fatigue cracking is called Stage I cracking. After these Stage I cracks develop, their propagation is often redirected normal to the principal stress axis.

Wavy slip is favored by high stacking fault energy, inco-

herent precipitates or particles, high temperatures (> 0.4 T_m), large strains and low strain rates. The principal requirement for wavy slip is the ability for dislocations to change glide planes. This can be accomplished by cross-slip or dislocation climb. Both require thermal activation and therefore wavy slip is more prevalent at high temperatures. Climb and cross-slip are time-dependent processes, so the nature of deformation will be strain rate or frequency dependent. Fatigue cracking under wavy slip conditions can occur in two modes; transgranular cracking perpendicular to the principal stress axis which is called Stage II fracture, or intergranular cracking.

Gell and Leverant[32] observed Stage I fatigue cracking in the nickel-base superalloy, Mar-M200. They proposed a model to explain results based on weakening of the cohesive energy of the active slip planes by reversed shear deformation and the fracture of bonds across the weakened planes by the local normal stress.

Gell and Leverant[33] also studied the influence of temperature and cyclic frequency on the fatigue fracture of single crystals of Mar-M200. Except for the lowest frequency at the higher temperature where creep damage was extensive, crack initiation occurred at subsurface microporosity. Cracks initiated and propagated in the Stage I mode at the lower temperatures and higher frequencies, whereas Stage II crack initiation and propagation was found at the higher temperatures and lower frequencies.

Fournier and Pineau[34] investigated the low-cycle fatigue behavior of Inconel 718 at 25C and 550C. Electron microscopy showed

that precipitates were sheared in the course of cyclic straining and that plastic deformation proceeded by the propagation of planar bands. These bands were identified as twins. Cracking was generally initiated along the interfaces between these twin bands and the matrix, but at elevated temperatures and low stain rates, intercrystalline cracking took place as well.

Merrick[35] found the low-cycle fatigue crack initiation in three wrought nickel-base alloys at 538C to be of classical Stage I type and also at favorably oriented twin boundaries.

Menon and Reimann[36] studied low-cycle fatigue crack initiation in René 95 at temperatures up to 650C. Very high resistance to LCF cracking was attributed to the homogeneous deformation characteristics of necklace René 95. The dislocation substructure in the warm-worked grains seemed to be very effective in dispersing slip thoughout a grain, thus forcing the material to deform homogeneously.

Wells and Sullivan[37] found deformation of Udimet 700 at 927C to be more homogeneous than at 760C, consequently the lifetime was greater at the same value of plastic strain range.

Antolovich et. al.[38] studied the LCF behavior of René 80 at 871C as affected by prior exposure at 982C, either stress free or at 1/3 the yield. The prior exposure caused significant microstructural changes and life reductions which were most pronounced for stress exposed specimens tested at high strain rates. Dislocation substructures were extensively studied. A similarity of slip mode was found for all conditions indicating that a difference in life could not be attri-

buted to basic differences in the plastic deformation process.

Additional references[39-41] pertaining to the role of deformation mode on high temperature fatigue behavior are available.

2. Transgranular Crack Initiation

One predominant mode of transgranular crack initiation has already been discussed, that is cracking of persistent slip bands, Stage I cracking. It is generally observed up to about 0.4 T_m at ordinary strain rates but to higher temperatures at very high strain rates. Initiation frequently occurs at microstructural defects. In cast nickel-base superalloys, these defects can be found intragranularly. They include casting pores and nonmetallic inclusions. MC carbides are often present in platelet form and contain pre-existing cracks. Any carbides present at the material surface provided a site for localized oxidation with subsequent crack initiation. Transgranular cracks may also initiate at stress concentrations resulting from cracks in a surface oxide layer or coating.

The tendency for Stage I - type transgranular cracking is well documented by the cases previously cited.

Gell and Leverant[32,42] have observed matrix slip and crack initiation to occur at precracked MC carbides and to a lesser extent at micropores in Mar-M200. Fatigue lives were greatly affected by the size of preexisting cracks in MC-type carbides contained in the microstructure.

Menon and Reimann[36], in their study of crack initiation in René 95, found the number of cycles to produce crack initiation to be

strongly affected by brittle constituents of the microstructure such as MC carbides. It was found that the specimens that had shorter lives were characterized by MC carbide cracking at the site of crack initiation, whereas those which had longer lives under the same conditions of loading and temperature were characterized by only slip band cracking with no evidence of MC carbide cracking or decohesion in influencing the initiation.

Coffin[43] has noted crack initiation at oxidized carbides at the surface of Inconel 718 tested in air at 850C.

3. Intergranular Crack Initiation

Intergranular cracking is a mode of damage generally associated with creep. For a given alloy, the creep component during HTLCF increases with increased temperature, maximum stress, mean stress, hold time, and with reduced frequency. Cracking may initiate below the material surface. Triple point or wedge cracks are favored by high stresses and relatively low temperatures. Cavitation is a common grain boundary damage mechanism. It is favored by low stresses and high temperatures. Cavities, if present, can be found on grain boundaries with high resolved shear stresses. They are also generally associated with grain boundary particles or carbides because of the high shear stresses developed at those locations. Intergranular cracks can initiate at the interface between second phase particles residing at the grain boundaries and the adjacent grains.

Most intergranular crack initiation can be related to environmental degradation of the grain boundaries. These cases will be

discussed in the next section. However, Wells and Sullivan[44] studied the effect of temperature on the LCF behavior of Udiment 700 and concluded that observations of interior sections support a contention that the transition to intergranular crack initiation with increasing temperature originates from mechanical rather than chemical processes. This appeared to result from the lack of mechancial constraint normal to the surface in conjunction with reduced grain boundary strength[45].

Gell and Leverant[42] found intergranular crack initiation and propagation in conventionally - cast Mar-M200. In columnar - grained Mar-M200 crack initiation occurred on short transverse segments of grain boundaries but crack propagation was transgranular.

Wells and Sullivan[46] proposed interactions between creep and low-cycle fatigue in Udimet 700 at 760C to take the form of cavitation at grain boundaries. It was surmised that the high internal stresses associated with both creep and plastic deformation are attributed to the pileup of dislocations at grain boundaries. It was postulated that the pileup of dislocations is relaxed by cavitation and that the rate of deformation is governed by the growth of these cavities as they annihilate dislocations. These cavities were observed to be a source of intergranular cracking in creep and low-cycle fatigue.

More recently Min and Raj[47] have proposed that grain boundary cavitation can account for hold-time effects. The nucleation of cavities is stress and time dependent. It can be aided by grain boundary sliding provided a certain type of cycle is applied to the specimen. The cycle should be unsymetrical in such a way that the tension

hold period is longer than the compression hold period.

4. Environmental Damage

The deleterious effect of a gaseous environment on nickel-base superalloys has already been discussed. Damage is a result of oxidation which may have a variety of influences on the mode and rate of fatigue cracking. As mentioned previously, stress concentrations resulting from cracks in a surface oxide layer will serve crack initiation. Cyclic deformation accelerates environmental attack by repeatedly rupturing potentially protective oxide films. It is therefore obvious that the mechanical properties of the oxide layer will affect fatigue life. Nonmetallic inclusions present in the alloy may intersect the surface. These phases may be easily oxidized and hence provide sites for crack initiation. Grain boundaries are particularly susceptable to environmental attack because of the presence of easily oxidized carbides as well as providing an easy diffusion path. Once initiated, the rate of crack advance is also affected if not controlled by the oxidation process. Oxidation may preceed the crack tip even depleting the alloy of easily oxidizing elements in a localized region around the crack tip. One possible beneficial effect can result from the oxidation process blunting the crack tip and slowing crack advance.

Coffin[48] recognized cyclic-strain induced oxidation of high temperature alloys in his early investigations. An explanation of the observed effects was based on localized and reversed grain boundary deformation, leading to repeated rupture of the protective oxide film, and accelerated oxidation in the region of deformation.

In cast Udimet 500 subjected to high-temperature low-cycle fatigue (McMahon and Coffin[49]), localized oxidation at grain boundaries played an important role in crack nucleation and propagation. Evidence was presented of a surface ridging and pronounced grain boundary penetration due to oxidation, a denuded γ' zone adjacent to the oxide, and cracking of the oxide. The ridging was selective and presumed to occur on those boundaries where high stress exists. The phenomenon was veiwed as analogous to stress-corrosion cracking.

Most alloys when tested at elevated temperatures under cyclic loading conditions which include hold times usually exhibit a lesser fatigue resistance in terms of cyclic life if the hold is in tension rather than in compression. However, Teranishi and McEvily[50] found that a compression hold can be more damaging than a tension hold for 2 1/4 Cr-1Mo steel. The reason for the effect of hold time on cyclic life can be related to the behavior of the oxide immediately after the hold period. After a tension hold the oxide spalls to produce a new surface which, at least in the early stages of the test, does not contain macroscopic cracks. On the other hand, after a compression hold the oxide cracks rather than spalls, thereby creating localized stress and strain concentrations which facilitate the early nucleation of fatigue cracks.

Low-cycle fatigue tests on A286 by Coffin et. al.[51,52], which covered a frequency range of 5 to 0.1 cpm, have shown a pronounced frequency dependence when the tests were run in air. In contrast, tests run in a vacuum did not show such a frequency effect. It was concluded

that, in the prescribed frequency range, environmental effects were responsible for the frequency dependence.

In studying the effect of frequency on HTLCF of cast René 80 at 871C Coffin[53] found, in all cases, crack nucleation to be intergranular with oxide ridging to be the responsible mechanism. Propagation, on the other hand, was transgranular for all frequencies considered. This transgranular crack propagation is believed to account for the frequency insensitivity found at high strain and short lives, through crack tip blunting due to oxidation with decreasing frequency. This transgranular characteristic acts to enhance the high strain, low frequency, and hold time fatigue resistance of René 80.

Antolovich et. al.[3,38,54] concluded from work on René 80 and René 77 that LCF damage at elevated temperature is primarily in the form of oxidation or oxide penetration along surface connected boundaries. A crack is said to initiate at a critical degree of boundary penetration.

Menon[55] found that the inherent creep strength of René 95 can be realized only in vacuum and that the presence of an oxidizing environment caused premature fracture of creep specimens due to oxidation and accompanying surface cracking. Fracture in the air environment resembled stress corrosion with one single crack being responsible for the final failure. His observations indicate that oxidation enhances crack nucleation and propagation at grain boundaries.

Dennison et. al.[56] found a similar behavior for cast IN 100. Fracture occurred by propagation of surface nucleated cracks.

Udimet 700 was tested in static tension at 927C by Chaku and McMahon.[57] An air environment decreased rupture life and ductility, except in very coarse-grained cast specimens, because of premature failure by stress-assisted grain boundary oxidation and cracking. In very coarse-grained cast specimens greater life and ductility were found in air than in vacuum, presumably due to the paucity of transverse grain boundaries and to some type of surface hardening effect.

5. Coatings

In view of the foregoing discussion, it is apparent that the environment plays an important role in initiation of fatigue cracks at high temperatures. Improved resistance to HTLCF can be expected if oxidation resistant coatings are applied to nickel-base superalloys.[28] The use of nickel-aluminide coatings on gas turbine engine blades and vanes that operate above 815C is one example. The application of a coating to the surface of a material can have a number of effects relevant to the fatigue properties of the coating-substrate composite: (1) the deformation behavior of the substrate may be changed because of the presence of a surface layer having a different elastic modulus and yield strength from that of the substrate; (2) as long as the coating is sound, oxygen is kept away from the substrate and the effects of oxygen absorption and gross oxidation are eliminated; and (3) since the coating is at the surface, the fatigue properties of the coating in a gaseous environment become important. If the fatigue properties of the coating are better than that of the substrate, increased life may be expected. On the other hand, if the fatigue properties are

poorer than the substrate, cracks in the coating will serve as surface notches and as paths for oxygen to reach the substrate. Reduced fatigue life of the composite would then be expected. Coatings frequently are more brittle than the substrate, so it is important that the maximum strain in the fatigue cycle does not exceed the fracture strain in the coating or else cracking of the coating will occur in the first tensile cycle.

Wells and Sullivan[32] studied the HTLCF behavior of coated Udimet 700 at 927C. They found an aluminide coating eliminated intergranular crack initiation in the adjacent substrate and tended to crack at pit-like defects at the free surface. A significant increase in life was obtained by coating. Smoothing the coating improved life further. The importance of understanding the unique compositional/microstructural/mechanical nature of a coating in achieving optimum thermal fatigue resistance for high-temperature materials has been recognized.[58]

C. Crack Growth Under Creep and Fatigue Conditions

Damage mechanisms in HTLCF, have been defined as those processes which contribute to the initiation and subsequent propagation of cracks. Propagation of cracks may constitute a significant portion of cycles or time to failure in a laboratory test. There has been considerable research into the propagation of cracks in elastic bodies. In this case the familiar Paris equation generally applies. It relates the crack advance in a cycle to the stress intensity range at the crack tip.

$$\frac{da}{dN} = C(\Delta K)^m \qquad [1]$$

where ΔK = Stress intensity range
C,m = constants

In the case of the HTLCF, cracks must propagate through a body experiencing both elastic and inelastic strains. There have been a few investigations in this general area. Also, studies of "creep crack growth" behavior using FCP type specimens loaded statically are relevant to HTLCF crack propagation, particularly if hold times are involved. Crack growth per cycle or per unit time has been related to; stress intensity, energy integral (J-integral), energy rate integral (C*-integral), inelastic strain range, crack opening displacement (COD), crack tip opening displacement (CTOD) and net section stress. There has been noted in all cases a threshold value of the driving force parameter required to effect crack advance.

Several attempts[59-64] have been made to measure the LCF crack propagation rates of different alloys in the fully plastic regime under controlled plastic strain amplitudes. Some of these test results show that fully plastic fatigue cracks usually grow by a Stage II mode and that growth can be represented by the following equation:

$$\frac{da}{dN} = A(\Delta \varepsilon_p)^{\alpha} a \qquad [2]$$

where $\Delta\varepsilon_p$ = plastic strain range
a = crack length
A,α = constants

The same equation was used in a theoretical model of fatigue crack growth derived by Tomkins.[65]

Huang and Pelloux[66] studied fatigue crack propagation in Hastelloy-X in air, at 25C and at 760C under controlled plastic strain amplitudes in the fully plastic LCF regime. It was found that $da/dN = A(\Delta\varepsilon_p)^{\alpha} a$ is only an approximation of the more general equation $da/dN = B(\Delta J)^{\alpha}$. It was shown that the theoretical models predicting LCF lives by integrating the fully plastic crack growth rates will be in error if the $(da/dN, \Delta J)$ relationship is not used.

Although quantitative studies of crack growth rates in plastic fields are few, much HTLCF behavior is related to crack propagation in qualitative terms.

The work of Gell and Leverant[42] on the HTLCF of Mar-M200 at 760C and 927C has already been referred to. The LCF lives of the columnar grained and single crystal materials were similar at both temperatures and were one to two orders of magnitude greater than those of conventionally-cast material. The variations in the fatigue lives among the three forms of Mar-M200 were related to the more rapid rate of intergranular crack propagation compared to that of transgranular propagation. In conventionally-cast Mar-M200, cracks were initiated in grain boundaries and crack propagation occurred rapidly along an almost continuous grain boundary path. In the columnar grained material, crack initiation occurred on short transverse segments of grain boundaries, but crack propagation was transgranular.

Woodford and Mowbray[29] studied the effect of material characteristics and test variables on the thermal fatigue behavior of several cast superalloys. Coarser grain size specimens had reduced

crack propagation rates. Taken in conjunction with the results from a directionally solidified specimen, it was concluded that in the range of test conditions studied, slower solidification leads to reduced thermal fatigue crack propagation rates. In all cases it was shown that cracking was principally interdendritic.

Solomon[67] investigated the frequency dependence of LCF crack propagation in A286 at 593C. He found that dividing the frequency range studied into two regimes provided a better correlation with crack growth rates. It was surmised that the existence of more than one frequency regime reflects the influence of more than one time dependent phenomenon. Non-environmentally controlled time dependent processes are believed to control the lowest frequency regime, while environmental factors become dominant at higher frequencies.

Waring[68] has extended some of the crack propagation models to account for strain hold periods. Data obtained on three austenitic stainless steels show good agreement with predictions and confirm that the reduction in fatigue endurance for cycles containing hold periods at the maximum tensile strain can be explained in terms of the interaction between the creep damage formed during periods of stress relaxation, and the steadily advancing fatigue crack. Under these conditions a saturation in fatigue life occurs with increasing hold period.

Sandananda and Shahinian[69] investigated crack growth behavior under creep-fatigue conditions in Udimet 700 using compact tension specimens. The crack growth data were analyzed in terms of the stress intensity factor as well as the J-integral parameter. Crack growth

behavior was shown to depend on the initial stress intensity level and the duration of hold-time at the peak load. For stress intensities that are lower than the threshold stress intensity for creep crack growth, the crack growth rate decreases with increase in hold time even on a cycle basis to the extent that complete crack arrest could occur at prolonged hold times. This beneficial creep-fatigue interaction is attributed to the stress relaxation due to creep. For stress intensities greater than the threshold stress intensity for creep crack growth, the growth rate on a cycle basis increases with increase in hold time. For conditions where there is no crack arrest, the crack growth appears to be essentially cycle-dependent in the low stress intensity range and time dependent in the high stress intensity range. Both the stress intensity factor and the J-integral were shown to be valid only in a limited range of loads and hold times where crack growth rate increases continuously.

Sadananda and Shahinian[70] also compared creep crack growth behavior in Udimet 700 to that in Alloy 718 determined earlier.[71] The results showed that the crack growth rates in Udimet 700 were significantly lower, the threshold stress intensity for crack growth was larger, the temperature sensitivity of the growth rate was smaller, and the creep life was much longer than those in Alloy 718. These differences were attributed to the difference in the mechanisms of the crack growth in the two alloys. In Alloy 718, the crack growth was presumed to be due to two competing processes ; a grain boundary diffusion process which contributes to the crack growth, and a creep deformation pro-

cess which retards the growth. In Udimet 700 it was presumed that the crack growth occurs as a result of deformation which nucleates voids or cracks at the grain boundary junctions ahead of the main crack and of the joining of these cracks to the main crack. As a result, the crack growth rates were significantly lower than those due to the grain boundary diffusion controlled process.

Ellison and Sullivan[72] evaluated Udimet 700 under combined creep and fatigue conditions. They found early initiation of intergranular surface cracks, formed by a static creep process, and their subsequent transgranular propagation in fatigue due to the alternating load.

Jones and Tetelman[73] have characterized the elevated temperature static load crack extension behavior of type 304 stainless steel. Crack extension rates obtained as a function of temperature over the range 650C to 800C and as a function of specimen geometry at 750C were correlated with both net section stress and the apparent stress intensity factor. The results indicated that the stress intensity correlation is strongly dependent on specimen geometry, whereas the net section stress correlation appears to be generally valid. A direct correspondence between crack extension and local (crack tip) displacement was noted when creep crack extension rates at 750C were compared with COD obtained from actual castings of the crack tip.

Van Leeuwen[74] was successful in applying fracture mechanics to creep crack growth. He found that: (1) Creep crack growth rates correlate with stress intensity only for creep brittle materials. They

correlate better with net section stress for creep ductile materials. (2) Creep crack growth rates correlate with CTOD rate, but the application of this relationship to design is difficult because accurate calculation of CTOD rate is in itself a formidable problem. (3) Creep crack growth rates correlate with the energy rate integral, C*, which is an adaptation of the J-integral involving substitution of strain rates and displacement rates for strains and displacements. This method holds great promise for design calculations, because C* can be calculated using finite element analysis, as well as measured in constant displacement rate test.

The role the environment plays in crack propagation is not easily quantified. Air is usually an agressive environment and may cause large increases in crack growth rates. At this time it is not clear whether environmental effects are rate controlling, or whether plastic deformation processes near the crack tip are rate controlling with some modification due to the environment.[75]

D. Role of Cyclic Stress-Strain Response in HTLCF

Fatigue damage results from cyclic stresses and strains whether they be mechanically or thermally induced. A laboratory test is performed under prescribed conditions of stress and/or strain. In some tests a fixed stress program is imposed and the resulting strain response is monitored. The stress response is identical for every cycle of the test and the strain response changes as it may to reflect metallurgical changes and damage processes. In the case of HTLCF testing, a fixed strain program is usually imposed and the resulting

stress response reflects metallurgical changes and damage processes. It is sometimes useful to impose both stress and strain control as is the case with cyclic creep rupture testing. (Both stress and strain should be monitored continuously during any test).

Cyclic stress and strain are the causes of fatigue damage but are quite often used as a measure of damage. Stress and strain parameters often show good correlation with cyclic life as is the case with the Coffin-Manson equation. This should be qualified. HTLCF damage has been used as a general term for those physical processes which degrade the mechanical integrity of a material subjected to cyclic stresses and strains at high temperatures in a gaseous invironment. It is because cyclic stress and strain are the necessary driving force for fatigue damage processes and an accelerator for those attributed to environmental effects that stress and strain can be related to damage and, therefore, cycles to failure of a test specimen or component. Any change in the damage driving parameters (i.e. stress, strain, temperature) will change the nature, quantity and/or rate of damage accumulation. Procedures for calculating fatigue life should be based on a knowledge of damage mechanisms accounting for the driving parameters in the same way that they are known to affect damage mechanisms. It should be pointed out that, the greater is the maximum tensile stress, the smaller will be the damage (crack, "oxide spike", etc.) required to cause separation of a specimen or component.

Specific references to appropriate literature have already been made in previous sections.

E. Methods for Life Prediction

A case for mechanistically based life prediction methodologies for HTLCF has already been made. However, most recognized "fatigue laws" are empirical equations based on satisfying a best correlation with laboratory test data and incorporate damage driving parameters in an appropriate manner. A few of these fatigue laws will be reviewed.

1. Coffin-Manson Equation

The first fatigue law proposed to relate fatigue failure to imposed inelastic strain was the Coffin-Manson equation[76,77]:

$$\Delta\varepsilon_p N_f^{\beta} = C_1 \qquad [3]$$

where $\Delta\varepsilon_p$ = inelastic strain range
N_f = cycles to failure
β, C_1 = constants

Several theories have been proposed to confirm the Coffin-Manson equation[24]. It is generally observed that in the high-strain regime, microcracks nucleate and start to grow very early in life and thus the physical process characterized is that of high strain crack growth. A proposed high-strain crack growth law, Eq. [2], already discussed, can be integrated to yield the Coffin-Manson equation if the cycles required for initiation are ignored.

2. Frequency-Modified Coffin-Manson Equation

Another phenomenological approach incorporates the frequency of a characteristic cycle of strain into the Coffin-Manson equation to account for time-dependent damage processes.[78] It has been found convenient to use the quantity $(N_f \nu^{K-1})$ as a parameter for combining frequency and life. The Coffin-Manson equation becomes

$$\Delta\varepsilon_p (N_f \nu^{K-1})^{\beta} = C_2 \qquad [4]$$

where $\Delta\varepsilon_p$ = inelastic strain range
N_f = cycles to failure
ν = effective frequency
K, β, C_2 = constants

Note that K serves as a measure of time dependency; when K = 1, Eq. [4] is independent of frequency.

3. Coffin's Frequency Separation Model

This model postulates that the basic parameters necessary to predict the creep-fatigue life are the inelastic strain range, the tension going frequency, and the loop-time unbalance.(79) Each of these parameters measure a different aspect of life.

$$N_f = C(\Delta\varepsilon_{in})^{\beta} \quad \nu_t^{m} \left(\frac{\nu_c}{\nu_t}\right)^{K} \qquad [5]$$

where $\Delta\varepsilon_{in}$ = inelastic strain range
N_f = cycles to failure
ν_t = tension frequency
ν_c = compression frequency
C, β, m, K = constants

4. Ostergren Model

Ostergren's model(80,81) is based upon the premise that low-cycle fatigue is primarily a problem of crack propagation. Accordingly, cracks nucleate very early, and the majority of the life is spent growing these cracks to a critical size. The model's measure of fatigue damage is the tensile hysteretic energy aborbed by the specimen. The life is predicted by postulating a power-law relationship between the measure of fatigue damage and the life.

$$N_f = C(\Delta\varepsilon_{in} \times \sigma_t)^{\beta} \qquad [6]$$

where $\Delta\varepsilon_{in}$ = inelastic strain range
N_f = cycles to failure
σ_t = peak tensile stress
C, β = constants

It should be noted that Eq. [6], like the Coffin-Manson law, is valid only for time-independent fatigue. When time-dependent mechanisms are present, as in the creep-fatigue interaction, Eq. [6] is modified by a frequency factor which takes into account the time dependency.

$$N_f = C(\Delta\varepsilon_{in} \times \sigma_t)^{\beta} \quad \nu^m \qquad [7]$$

5. Damage Rate Model

The damage rate approach[82] is a phenomenological approach based upon the premise that low-cycle fatigue is primarily a process of crack propagation and cavity growth. Microcracks and cavities are assumed to be originally present in the virgin material, and the majority of the low-cycle-fatigue life is spent growing these microcracks and cavities to a critical size at which time they link up and form a macrocrack. The basic equation below describes the assumed relationship between the "damage" rate and the controlling mechanical factors. For tensile loading:

$$\frac{d(\ln a)}{dt} = T \left|\varepsilon_p\right|^m \left|\dot{\varepsilon}_p\right|^k \qquad [8]$$

For compressive loading:

$$\frac{d(\ln a)}{dt} = C \left|\varepsilon_p\right|^m \left|\dot{\varepsilon}_p\right|^k \qquad [9]$$

where a = crack length
ε_p = plastic strain
$\dot{\varepsilon}_p$ = plastic strain rate
T, C, m, K = constants

Integrating this equation for the simplest case, where the cyclic loading is both symetrical and applied at high frequency (no hold-times), results in the following estimate of the failure cycles:

$$N_f = \left[\frac{m+1}{4A}\right] \left[\frac{\Delta \varepsilon_p}{2}\right]^{-(m+1)} \left[\dot{\varepsilon}_p\right]^{1-k} \qquad [10]$$

where N_f = cycles to failure
$\Delta \varepsilon_p$ = plastic strain range
$\dot{\varepsilon}_p$ = plastic strain rate
A, m, K = constants

6. <u>Strain Range Partitioning</u>

Strain Range Partitioning is an approach for creep-fatigue life prediction. The inception and early development are attributed to Manson, Halford and Hirschberg of NASA. The literature abounds with related articles(83-96) including the proceedings of a recent AGARD conference.(97) The method incorporates grain boundary sliding (creep) and slip plane sliding (plasticity) as assumed mechanisms of damage accumulation. An analysis or prediction of life, therefore, requires partitioning of the total inelastic strain range into its four generic components and attributing to each component a proportionate amount of damage. The four basic types of inelastic-strain cycle include: $\Delta \varepsilon_{pp}$ type (plasticity reversed by plasticity); $\Delta \varepsilon_{cc}$ type (creep reversed by creep), $\Delta \varepsilon_{pc}$ type (plasticity reversed by creep) and

$\Delta\varepsilon_{cp}$ type (creep reversed by plasticity). The idealized hysteresis loops are shown in Figure 4. The $\Delta\varepsilon_{pp}$ type of strain is time independent and does not require thermal activation. The remaining three cycle types have at least one time dependent component. In practice, even simple strain cycles imposed on test specimens have some amount of the $\Delta\varepsilon_{pp}$ type of cycle.

When several types of strain ranges are involved, the first step is to compute a life from the basic life relationship of each strain range as if the strain range were the entire sum of strain ranges involved in the analysis. Once these lives have been calculated, the expected life is obtained by weighting each of the lives calculated according to that fraction of the total inelastic strain range that is truly associated with that strain range component. The basic equation is:

$$\frac{1}{N_f} = \frac{F_{pp}}{N_{pp}} + \frac{F_{cc}}{N_{cc}} + \frac{F_{pc}}{N_{pc}} + \frac{F_{cp}}{N_{cp}} \qquad [11]$$

where N_f = cycles to failure
N_{ij} = number of cycles to failure if the entire inelastic strain range was comprised of $\Delta\varepsilon_{ij}$ type deformation
F_{ij} = the fraction of the inelastic strain range which is comprised of $\Delta\varepsilon_{ij}$ type deformation

Note that since the PC and CP type cycles are mutually exclusive, Eq. [11] would be applied with only three terms on the right-hand side.

7. Antolovich's Oxidation Model

Antolovich et. al.[3,38,54] have proposed a model based on oxidation related crack initiation. The model is based on the obser-

vation that damage in René 80 and René 77 takes the form of oxygen or oxide penetration along surface connected boundaries. A crack is said to initiate at a critical degree of boundary penetration. The equation expressing this failure criterion in simplified form (assuming no significant metallurgial changes) is:

$$\sigma_i \max (l_i)^p = C_o \qquad [12]$$

where σ_i max = maximum tensile stress at initiation
l_i = relative oxide depth
p = constant, usually about -0.25
C_o = material constant

Calculation of l_i is based on the assumption that oxidation follows parabolic kinetics. Excellent correlation has been found with Nimonic 90. However, some alloys such as Waspaloy show good correlation only for tests of a given cycle character. This may be expected since the behavior of the oxides of these alloys are cycle dependent.

III. EXPERIMENTAL

A. Material

This investigation was performed on specimens tested for the AGARD Strain Range Partitioning (SRP) Program.[97] The author selected two materials, René 80 (NASA and TRW) and IN 100 (NASA and ONERA). The material and testing conditions of these specimens appeared to provide a good basis for sorting out many factors and attending mechanisms controlling fatigue life. Specimens examined cover a matrix of material conditions, temperature, inelastic strain characters and cyclic lives. Several tests were performed on René 80 at the University of Cincinnati to elucidate perplexing observations. The chemical compositions are given in Table 1.

B. Specimens and Heat Treatments

Rene 80 (NASA & TRW)

Tubular, hourglass-shaped specimens with threaded ends were individually cast as solid round bars and machined to the configuration shown in Figure 6. The uncoated specimens were heat treated as follows:

1218C/2 hours vacuum/argon quench to room temperature

1093C/4 hours vacuum/argon quench to room temperature

1052C/4 hours vacuum, furnace cool in vacuum to 649C within 1 hour, air cool to room temperature (this simulates the coating cycle)

843C/16 hours vacuum/furnace cool to room temperature.

The coated specimens were prepared with a CODEP B-1 alu-

minide coating. The alumina precoat was deposited on both the internal and external surfaces of the specimens by the electrophorsis technique. All other aspects of the coating application process conformed to General Electric Company Specification No. F50T58-S1. The resulting coating thickness was approximately 0.05mm. The coated specimens were given the following heat treatment:

1218C/2 hours vacuum/argon quench to room temperature

1093C/4 hours vacuum/argon quench to room temperature

Coating cycle as per G.E. Specification No. F50T58-S1

843C/16 hours vacuum/furnace cool to room temperature.

René 80 (U of C)

Solid, longitudinal specimens were cast as solid round bars and Hot Isostatically Pressed (a procedure believed to heal casting porosity). The specimens were subsequently machined to the configuration shown in Figure 7. The heat treatment, which should have been similar to that described above, was accidentally omitted. The resulting microstructure contains only coarse γ' rather than a duplex micostructure containing coarse and fine γ'. This mistake in heat treatment is of little consequence to the analysis of these tests, since no direct comparisons will be made to other tests.

IN 100 (NASA)

Tubular, hour-glass shaped specimens were individually cast to near final demensions. Approximately 0.2mm thickness of material was machined from the inside and outside diameters to produce the finished test section dimensions as shown in Figure 6. No heat

treatment was applied to the cast specimens.

IN 100 (ONERA)

Solid longitudinal test specimens were cast and machined to dimensions shown in Figure 8. All specimens were given the following vapor phase aluminization heat treatment:

cleaning-wet sandblasting with quartz "module 23"

trichlorethylene vapor scouring

aluminization at 1150C, 3 hours, argon cooling.

C. Mechanical Testing

René 80 and IN 100 (NASA)

NASA - Lewis Research Center performed high-temperature, low-cycle fatigue tests on coated and uncoated René 80 at 1000C and uncoated IN 100 at 925C. The tests were performed using closed-loop, servo-hydraulic testing machines and axially loaded specimens with diametral extensometry. The temperatures were achieved by direct resistance heating of the test specimens. The environment was still, laboratory air. Stress versus time and strain versus time signals were recorded continuously for only a few tests. Stress-strain hysteresis loops were recorded continuously throughout each test. Hirschberg has described the facility in detail in Reference 98.

The fatigue test program involved isothermal strain cycling to establish the four basic types of creep-fatigue life relationships defined by the strain range partitioning method. The four basic types of reversed inelastic strain, $\Delta\varepsilon_{pp}$, $\Delta\varepsilon_{pc}$, $\Delta\varepsilon_{cp}$ and $\Delta\varepsilon_{cc}$, are referred to as PP, PC, CP and CC, respectively. The

idealized stress-strain hysteresis loops for these four basic types of deformation are illustrated in Figure 4. The PP, PC, CP and CC types of strain range-fatigue life relationships were obtained by conducting High Rate Strain Cycle (HRSC), Compressive Cyclic Creep Rupture (CCCR), Tensile Cyclic Creep Rupture (TCCR), and Unbalanced Cyclic Creep Rupture (UCCR) or Balanced Cyclic Creep Rupture (BCCR) types of tests, respectively. Complex stress-strain cycle tests were also performed. These tests were designated Verf.

The strain-controlled PP type tests cycles were applied using either a triangular or sinusoidal strain versus time waveform at a frequency of 0.5 to 1.0 Hz. In analyzing the results of the PP type tests, it was assumed that the imposed strain rates were high enough to preclude the occurrence of creep strain, thus producing inelastic strains that could be classified as plasticity. For the PC, CP and CC type cycles, the creep strain was imposed by controlling the load on the specimen at a constant value until the desired creep strain limit was reached, whereupon, the loading direction was reversed and the other half of the cycle was imposed. If it was desired to impose creep strain in this portion of the cycle, the load was again held at a constant value until the desired opposite creep strain limit was attained, or if plasticity was desired, the specimen was rapidly loaded until the opposite strain limit was reached. The time required for the plasticity poriton of the cycle was on the order of 0.5 to 2.0 seconds. It should be noted that the strain rate for strain reversal in the cyclic creep rupture tests was controlled mechanically. This was done by permitting

only a very low flow rate of hydraulic oil to the servo value.

The high-temperature tensile and creep-rupture properties were also determined for these two materials at the appropriate temperatures.

René 80 (TRW)

TRW Inc. performed high-temperature, low-cycle fatigue tests on coated and uncoated René 80 at 871C and 1000C in an ultrahigh vacuum. The test procedure was very similar to that described for the NASA tests. However, the tests were conducted at 1000C in an ultrahigh vacuum environment below 10^{-7} torr and at 871C in a poorer vacuum environment of approximately 10^{-6} torr. Stress versus time and strain versus time signals were recorded continuously for all tests. Stress-strain hysteresis loops were recorded periodically throughout each test.

René 80 (U of C)

The author performed high-temperature, low-cycle fatigue tests on uncoated René 80 at 1000C. The tests were performed using a closed-loop, servo-hydraulic testing machine (MTS Model) and axially loaded specimens with longitudinal extensometry. The temperature was achieved using an RF induction heating unit (Cycle-Dyne). The water-cooled induction coil was a five-turn coil with a 0.85 inch inside diameter. The environment was still, laboratory air. Stress versus time and strain versus time signals were recorded continuously for all tests. Stress-strain hysteresis loops were recorded periodically throughout each test.

The tests performed include three tensile cyclic creep

rupture, TCCR, tests, one strain hold test, one continuous cycling test and one creep-rupture test in which the load was increased after specific increments of time. Several interrupted tests were performed by freezing the specimen (turning off the induction heater) while the specimen was under load at the point of maximum strain.

The TCCR tests were performed using a relay device borrowed from NASA-Lewis. This device was modified to employ an RC circuit to control the rate of load reversals electronically rather than mechanically. This modification resulted in a significant improvement in control of the system command signal. The details of the modification and an explanation of the test procedure can be found in Appendix A.

Because the author had more control over the tests done at U of C than those done at other laboratories these tests played a very important role in this study. Details of the test control exerted by the author are noted in Appendix B.

IN 100 (ONERA)

ONERA (Office National d'Etudes et de Recherches Aerospatiales) performed high-temperature, low-cycle fatigue tests on coated IN 100 at 800C, 900C, 1000C and 1100C. The tests were performed using a closed-loop, servo-hydraulic testing machine (Schenck system) and axially loaded specimens with longitudinal extensometry. The tem-

peratures were achieved using an RF induction heating unit (CELES GHF). The induction coils were of the nonclassical transverse type. The environment was still laboratory air. Stress versus time, strain versus time, and stress-strain hysteresis loops were recorded continuously throughout each test. The test program included high-rate continuous cycling tests, strain-hold tests, stress hold tests, and creep-rupture tests. Some tests were performed by alternating periods of pure fatigue with pure creep.

D. Specimen Selection

Specimens were systematically selected to cover a matrix of material conditions, temperatures, inelastic strain characters and cyclic lives. An outline of this matrix can be found in Figure 9. An attempt was made to choose specimens such that all "high strain" or all "low strain" specimens were subjected to nearly equivalent inelastic strains. This was done to make comparisons between temperatures, cycle types, and coated and uncoated conditions more meaningful.

E. Scanning Electron Microscopy (SEM) and Energy Dispersive Analysis of X-Rays (EDAX)

The guage section was cut from selected specimens normal to the longitudinal axis (usually about 7.5 mm below the fracture) using a Bronwill, thin-sectioning machine. The specimens were cooled with a continuous stream of water during this operation. These gauge sections were subsequently cleaned in an ultrasonic-acetone bath. After a brief examination under a low magnification, stereoscopic microscope, they were mounted upright on aluminum pedestals with a high-conductive,

silver paste.

Detailed observation and photographic documentation of the fracture surface and the guage section surfaces of each selected specimen was performed on a Cambridge 600 SEM. Micrographs were usually taken of the fracture surface with a stage tilt of about 30 to 35 degrees and of the guage section surfaces with a stage tilt of about 60 to 65 degrees. Simi-quantitative chemical analysis of microstructural constituents was occasionally performed using the EDAX unit attached to the SEM.

Chronologically the next procedure in the investigation involved optical microscopy of longitudinal sections of the selected specimens. However, optical microscopy of mechanically polished specimens yielded some erroneous observations and failed to resolve particular damage features. A procedure was developed for electropolishing these specimens for SEM observation. It should be pointed out that optical microscopy did yield many valid observations.

After SEM investigation of the fracture and gauge section surfaces, these same specimens were glued upright on plexiglass blocks and sectioned longitudinally along several specimen diameters. Steel wires were spot welded opposite to the cut surface. These pieces were mounted on the cut surface in a two-part, epoxy, cold mount in such a way that the steel wires were exposed. The surfaces were ground smooth on wet, 600 grit, silicon carbide paper. The exposed surfaces were electropolished in an electrolyte of 45% Butyl Cellosolve ($C_6H_{14}O_2$), 45% Acetic acid (CH_3COOH) and 10% Perchloric acid ($HClO_4$) by volume. The electro-

lyte temperature was between 5C and 10C. The voltage was increased until a plateau in the amperage versus voltage curve was achieved. Polishing times were about 15 seconds. Specimens were broken out of the epoxy and prepared for SEM in the manner already described.

SEM observations made of specimens prepared in this manner are regarded with the highest confidence.

F. Optical Microscopy

After SEM examination of the fracture surface and guage section surfaces, each selected specimen was cut longitudinally through the specimen axis along several different diameters as described in the previous section. These pieces were mounted on the cut surface in degassed epoxy mounts. Black, alumina particles were mixed in with the epoxy to give good edge protection. The specimens were mechanically polished and chemically etched with an electrolyte consisting of 2 gms $CuCl_2$, 40 ml HCl and 80 mls methanol. Detailed observation and photographic documentation was performed using a Reichert "Me F" microscope.

G. Transmission Electron Microscopy (TEM)

The specimens tested at U of C were studied with TEM. After testing, the guage sections were turned down to 3 mm diameter rods with a lathe. Transverse slices, approximately 0.5 mm thick, were sectioned from these rods using a Bronwill thin sectioning machine. The blanks were then ground down to approximately 0.13 mm with 600 grit, silicon carbide paper. Cooling water was used during both sectioning and grinding.

The blanks were electro-thinned using a Fischione

electropolishing unit. The hole in the specimen holder was 1.5 mm in diameter. A solution of 45% Butyl Cellosolve ($C_6H_{14}O_2$), 45% Acetic acid (CH_3COOH) and 10% Perchloric acid ($HClO_4$) by volume was used as an electrolyte. The polishing conditions were: 45 volts, 16 to 17 milliamperes, pump speed at 80 and electrolyte temperature at 5C to 10C. The thinning normally took 7 to 9 minutes. After thinning, the foils were immediately rinsed with high purity ethanol.

The foils were examined on a JEOL, 200 kV electron microscope. The scope is equipped with a 30° tilt and 360° azimuthal rotation stage. After examination, the foils were stored in air in small vials for further examination.

IV. RESULTS AND DISCUSSION

A. High-Temperature, Low-Cycle Fatigue Tests

Results given in this section are those presented by the originating laboratories (TRW, NASA and ONERA) in the AGARD conference proceedings.[97]

1. René 80 Tested in Vacuum at 1000C and 871C (TRW)

The fatigue test results are presented in Table II. Note that eight CCCR tests were conducted on uncoated material at 1000C instead of the usual five. Three extra tests (89U-PC-1, 94U-PC-14 and 97U-PC-15) were conducted here because analysis of the data for the first five tests indicate that drift may have occurred in the zero point for the load and strain control settings, resulting in erroneous readings. Thus, the values of total, inelastic, and partitioned inelastic strain range for these five tests may be in error.

The fatigue test results from Table II are plotted against longitudinal strain range in Figures 10 through 13. Each figure contains three different graphs including a plot and least squares fit of total strain range versus observed cycles to failure, inelastic strain range versus observed cycles to failure and partitioned inelastic strain range versus life relationships computed using the interaction damage rule. Figures 10 and 11 contain the results of tests conducted at 1000C on uncoated and coated material, respectively, while Figure 12 and 13 contain the results of tests conducted at 871C on uncoated and coated material, respectively.

For the tests conducted at 1000C, Figures 10 and 11, the

results indicate that the relative positions of the failure lives for the four basic types of strain range components (PP, PC, CP and CC) change little as a result of the presence of the aluminide coating. In all instances, PP deformation resulted in the longest cyclic lives, while PC deformation resulted in the shortest cyclic lives by approximately one order of magnitude below the PP line. The CP and CC lives were quite close together and fell between the PC and PP lives, ranging from 2/3 to 1/2 order of magnitude below the PP lives.

The results of the tests conducted at 871C, Figures 12 and 13, were consistent with those conducted at 1000C in that the aluminide coating had little effect on the relative positions of the failure lives for the four basic types of strain range components. In all cases, PP deformation resulted in the longest cyclic lives. Unlike the 1000C results, however, the PC and CP lives were both comparable, ranging from 1/2 to 1 order of magnitude below the PP lives. In terms of total inelastic strain range the CC results were somewhat comparable to those for the PC and CP, but partitioned inelastic strain range results indicated that CC had greater cyclic lives than PC and CP by approximately 1/2 order of magnitude at the higher stain range values.

The results for each of the basic types of deformation have been plotted separately in Figures 14 through 17 in terms of total strain range versus observed cycles to failure and partitioned inelastic strain range versus life relationship computed using the interaction damage rule. For each of these plots a least squares fit was made of all of the data. In the original reporting of this data by TRW

Inc.[97], the authors stated that; "These least squares lines suggest that, for all four types of deformation, there was little difference between coated and uncoated material at 1000C and 871C and further, there was little effect of temperature on the fatigue results." A more critical analysis of the data reveals that significant differences can be discerned. For example, PP type deformation resulted in greater fatigue life for coated than uncoated specimens at low values of inelastic strain range. At high values of inelastic strain, the data tends to merge. This trend is represented by the broken lines in Figure 14. There was no consistent difference between the 871C and 1000C data.

The PC data, Figure 15, is indistinguishable in terms of temperature or the presence or absence of a coating by any conventional means of analysis.

The CP data, Figure 16, also appears indistinguishable when plotted as partitioned inelastic strain range versus cycles to failure. This observation is contingent on the validity of the SRP method. If the data is plotted in the conventional manner, that is total inelastic strain range versus cycles to failure, Figure 18, it can be seen that the uncoated material exhibits greater lives than the coated material by a factor of 2 or 3 for the specimens tested at 1000C. The data for 871C tests are indistinguishable in terms of the presence or absense of a coating and are comparable to the coated, 1000C data.

The CC data, Figure 17, is indistinguishable in terms of temperature or the presence or absence of a coating by any conventional means of analysis.

To summarize these fatigue results more clearly, the least squares lives shown in Figures 14 through 17 are included in the composite plot of Figure 19. These results indicate that PP deformation resulted in the longest cyclic lives. When a time-dependent creep component was introduced into the cycle, however, an effect was observed which was dependent upon which portion of the cycle contained the creep component. The PC type of deformation, in which creep was introduced in the compression portion of the cycle, resulted in the shortest cyclic lives, one order of magnitude below those for PP deformation. The CP type deformation, in which creep was introduced in the tensile portion of the cycle, resulted in failure lives slightly higher than those for PC, i.e. slightly less than an order of magnitude below those for PP. The CC type deformation resulted in failure lives approximately 1/2 an order of magnitude below those for PP deformation.

The results for the HRSC tests conducted at a number of different temperatures on uncoated material in a poorer vacuum (approximately 10^{-6} torr) are shown in Figure 20. This figure contains a plot of total strain range versus observed cycles to failure and a plot of inelastic strain range versus observed cycles to failure. No tests were conducted under these conditions at 871C, but the least squares lines from Figure 12 for the ultrahigh vacuum tests have been included for comparative purposes. The results for inelastic strain range indicate a decrease in fatigue life as temperature is reduced. It has been generally acknowledged that, in the absence of time-dependent deformation (creep), a material's ductility will be an indication of its

relative fatigue resistance, with a decrease in ductility usually resulting in a decrease in fatigue life. Ductility results for cast Rene 80 indicate a decrease with decreasing temperature from 1000C. Thus, the inelastic strain range results for Rene 80 do reflect the decrease in fatigue life with decreasing ductility.

2. René 80 Tested in Air at 1000C (NASA)

The fatigue test results are presented in Table II. Examination of the data did not reveal significant differences between uncoated and coated results. Hence, the PP, PC, CP and CC life relationships were established for the combined data set. The data and least squares curve fit are plotted in Figures 21(a) through 21(e). The assumption that the uncoated and coated data could be considered of the same population is borne out in Figure 20(f) where it can be seen that uncoated and coated results are evenly distributed above and below the central 45 degree perfect agreement line.

To summarize the fatigue results more clearly, the least squares lines shown in Figures 21(a) through 21(d) are included in the composite plot of Figure 21(e). These results indicate PP and PC deformation resulted in comparable cyclic lives at intermediate values of partitioned inelastic strain range but the PP deformation exhibited greater lives at lower strain range values. The CP deformation resulted in cyclic lives approximately 1/2 an order of magnitude below the PP and the PC lives. The CC lives fell between the CP and the PP lives.

It would seem appropriate to compare the 1000C-Vacuum test results (TRW) with the 1000C-Air test results (NASA) for the

uncoated and coated specimens. This comparison is probably the most valid inter-laboratory comparison that can be made for the AGARD, SRP data, because identical specimens and similar test procedures were reportedly employed.

The results for the HRSC tests are plotted in Figure 22. The specimens tested in air resulted in cyclic lives which range from 1/2 to 1 order of magnitude below the vacuum tested specimens. This might be expected since oxidation has been found to enhance crack initiation and propagation.[24,30] (A more likely explanation will be presented in a subsequent section).

3. IN 100 Tested in Air at 925C (NASA)

The fatigue test results are presented in Table II. The data and least squares curve fit are plotted in Figures 23(a) through 23(e). The few data exhibit little scatter for PC, CP and CC type deformation. The CC deformation resulted in the longest cyclic lives, while the PC deformation resulted in the shortest cyclic lives, approximately an order of magnitude below the CC lives. The PP deformation resulted in lives just short of the CC lives, while the CP lives were just short of the PP lives.

4. IN 100 Tested in Air (ONERA)

The fatigue test results are presented in Table II. The results are plotted in Figures 24(a) through 24(d). It can be seen that the cyclic lives are comparable for 900C and 1000C.

To summarize the fatigue results more clearly, the least square lines shown in Figures 24(a) through 24(c) are included in the

composite plot of Figure 24(d). The PP deformation resulted in the longest cyclic lives for all values of inelastic strain, while CP deformation resulted in the shortest lives by approximately 1/2 order of magnitude below the PP lives. The PC and CC lives were between the two.

B. Material Response to Cyclic Stress and Strain

The tests performed at U of C will be frequently referred to in the following discussion. Although few in number, they represent well documented data (see Appendix B). Only a few simultaneous stress-time and strain-time records were available for the NASA tests.

1. Stress-Strain Hysteresis Loops

In a HTLCF test, the hysteresis loop represents the stress and strain coordinates of the test volume with an origin of zero stress and zero strain representing the undeformed, untested state of the material. The hysteresis loop represents two categories of information simultaneously; the imposed stress or strain command of the testing system and the resulting strain or stress response of the test volume. HTLCF tests are generally performed in strain control which means that the test system imposes a value of strain on the test volume which corresponds to an electronic command. The command is repeated identically, cycle after cycle, including preprogrammed values at which strain reversals and possibly strain holds will occur. In such a test, the strain coordinates of the hysteresis loop, although representing instantaneous values of strain in the test volume are invariant, cycle after cycle. It is the stress coordinate that is variable in every cycle and therefore represents true material response which often

reflects metallurgical changes and damage processes. If the test were performed in stress control, the stress coordinate of the hysteresis loop would be invariant, cycle after cycle, and the strain coordinate would represent the true material response.

The test system command signal generally follows a time basis. Although the hysteresis loop has no time coordinate, it does reflect the rate of stress or strain imposed by the system. Such behavior is related to the thermal component of plastic deformation.

It is important to know the nature of the test control to make a meaningful interpretation of stress-strain hysteresis loops. Since a considerable analysis of stress and strain response will follow, the control for a typical, SRP test will be reviewed. The stress-strain hysteresis loop for a TCCR test performed on René 80 in air at 1000C (U of C) can be seen in Figure 25. The system command was essentially load control with reversals occuring at strain limits which were preset symetrically about the origin. Note the hold at a constant load. During this period, the command signal was free from any time basis such that the hold was as long or as short as required to achieve the positive strain limit.

The effect of strain rate is also apparent in Figure 25. Loops 1 through 4 were performed consecutively by increasing the stress rate (system command) after each cycle to effect a higher strain rate (material response). Strain-time and stress-time records for this experiment can be seen in Figure 26. The rate of stress reversal in loop 4 was 2.44 times as great as in loop 1 and resulted in a maximum

negative stress 17% greater in absolute value at the negative strain limit. This is indicative of a significant strain-rate sensitivity for René 80 at 1000C. The tests performed at NASA and TRW were controlled in a manner similar to that discussed above, except, the rate of strain reversals were not as well controlled.

The idealized hysteresis loops for the four basic types of inelastic strain range were presented in Figure 4. These loops are considered idealized because they consist of only one SRP component. In the idealized loops, creep is initiated from an elastically loaded specimen. This is not practical in a laboratory test because the resulting creep rate would be too low to achieve a significant strain in a reasonable period of time. Therefore, creep is initiated at a stress greater than the elastic limit (in tension or compression) such that any creep component is preceded by a plastic PP component. This behavior is illustrated in Figure 27 by the hysteresis loops recorded during testing of René 80 at U of C.

2. Stress-Strain Relationships

There is considerable evidence that HTLCF failure can be initiated in a variety of ways; by coating cracks, by oxide cracks, by oxidized carbides at the specimen surface, by cracked grain boundaries and numerous others. It has been demonstrated that a significant portion of cyclic life is spent in the propagation of a crack-like entity from this initiation site.[24,80,81] Whether the crack be transgranular or intergranular, the driving force for crack advance is the stress and strain imposed on the bulk specimen. It is the bulk deformation

response of the material which governs the nature of the stress and strain field at the crack tip. Therefore, it is clear that the bulk material response under cyclic conditions and holding must be understood.

Stress can be related to inelastic strain in a hysteresis loop (from the onset of yielding to the maximum stress) by the familiar Holloman equation:

$$\sigma = A \varepsilon_p^{\,n} \qquad [13]$$

Where σ = true stress

ε_p = true plastic strain

n = strain hardening exponent of the cyclically stable material

A = material constant

The cyclic plastic strain range can also be related to the maximum stress (positive or negative) for a number of different tests performed under similar conditions:

$$\sigma_m = A \, \Delta \varepsilon_p^{\,n'} \qquad [14]$$

where σ_m = true stress at the positive or negative peak of the hysteresis loop

$\Delta \varepsilon_p$ = true plastic strainrange

n' = cyclic strain hardening exponent of the cyclically stable material

Hysteresis, stress-strain values such as maximum stress, minimum stress, holding stress and various components of the strain range for the specimens studied in this investigation can be found in

Table II.

The maximum stress is plotted against plastic strain range for HRSC (PP) tests on René 80 (TRW and NASA) in Figures 28 through 30. (Note: These tests were performed in strain control). The data follows the expected pattern and can be represented by the Holloman equation. There is no indication that the coating affected the cyclic stress response for these tests. Recall that the HRSC tests on René 80 in vacuum exhibited longer lives for coated than uncoated specimens for 1000C and 871C (Figure 14). This observation cannot be explained in terms of the stress response.

In comparing the vacuum tests (TRW) for 1000C and 871C in Figures 28 and 29 respectively, the expected behavior is observed. That is, the maximum stress for any equivalent inelastic strainrange is less for tests at 1000C as seen in Figure 29. This behavior was observed for the minimum stress as well.

It should be noted that there was no significant difference between cyclic lives at 871C or 1000C for PP tests and PC tests as can be seen in Figures 14 and 15 respectively. This may be a result of two offsetting factors. Since the PP and PC tests at 1000C have a smaller maximum tensile stress compared to 871C tests of equivalent inelastic strain range, the 1000C test specimens would require a larger crack to cause failure. Perhaps offsetting this advantage is the fact that many forms of damage, particularly grain boundary damage, occur more readily at the higher temperature.

As was mentioned in the previous section, it is

appropriate to compare the 1000C - vacuum tests (TRW) with the 1000C -Air test (NASA). A comparison of maximum stress versus inelastic strainrange for PP type tests can be seen in Figure 30. The maximum stress curve for the vacuum tests falls significantly below that for the air tests. There should be little difference between deformation behavior in air versus vacuum, particularly for coated specimens. This observation may explain why the specimens tested in air resulted in cyclic lives from 1/2 to 1 order of magnitude below the vacuum tested specimens (Figure 22). Experiencing a much lower maximum stress, the vacuum tested specimens required a much larger crack to cause failure and therefore more cycles.

Based on correspondence with the originating laboratories and the evidence presented in Appendix B, it was concluded that the NASA tests represent the true cyclic stress-strain response for René 80 at 1000C. The cyclic stress-strain response for René 80 tested in vacuum at 1000C and 871C is too low as reported by TRW Inc. However, the data within each temperature is self consistent and hence comparisons within the set of tests performed by TRW Inc. are believed to be valid. No further quantitative comparisons will be made of these tests with those performed at NASA.

There are several likely explainations for this lower-than-expected stress response. It may represent an error in scale factor which would mean that the tests were performed correctly, but the stresses were misrepresented, i.e. lower by a constant factor. This could have happened if the wrong excitation voltage was applied to the

load transducer. Although less likely, it may also mean that the actual test temperatures were much higher than the reported values of 1000C and 871C.

The cyclic stress-strain response for continuous cycling (PP) tests is generally symmetrical about the stress equals zero line if they were performed in strain contol with strain reversals occurring symetrically about the strain equals zero line. The maximum and mimimum stress in the hysteresis response for René 80 tested in air at 1000C (NASA) and IN 100 tested in air at 925C (NASA) are plotted against inelastic strain range in Figures 31 and 32 respectively. The curves represent the continuous cycling tests. Also plotted in the figures is the maximum stress response for the PC tests and the minimum stress response for the CP tests. Unlike the PP tests in which time-independent, plastic deformation is reversed by time-indepent, plastic deformation, the time-independent component of the PC and CP hysteresis loop is reversing a time-dependent, creep component. As seen in Figure 31, most of the "time-independent" strain reversals for PC and CP tests fall short of the PP response for equivalent inelastic strain range, particularly at higher strain ranges. This is not unexpected considering the strain rate for strain reversals in these tests were considerably lower than the PP tests. Recall the strain-rate sensitivity of Rene 80 at 1000C as was demonstrated in Figures 25 and 26.

The stress response for strain reversals in the PC and CP tests on IN 100 at 925C is similar to the PP stress response as seen in Figure 32.

3. Strain Rates in Hold-Time Tests

Most of the hold-time tests studied in this investigation were cyclic creep rupture tests in which a large portion of the inelatic strain was achieved during a hold at constant load. It is noteworthy that most life-time prediction methods (i.e. SRP) correlate inelastic strain with cycles to failure. Since inelastic strain is used as the measure of damage in each cycle, it seems reasonable to surmize that the rate at which this inelastic strain is achieved is related to the rate of damage accumulation in each cycle. Also, the amount of time-dependent damage, such as oxidation or creep related damage, which may occur in each cycle depends on the amount of inelastic strain in the cycle and the rate by which it is achieved.

Consider the TCCR (CP) test, GR-1, performed on uncoated René 80 at 1000C (U of C). The imposed conditions of this test performed in load control were as follows: $\Delta \varepsilon_{total}$ = 0.928% and holding load = 4670 Newtons (initial stress = 172 MPa). The resulting inelastic strain at half life was 0.597%. The hysteresis loop for this test can be seen in Figure 33. The specimen failed after 130 cycles and 16.56 hrs. Load reversals were achieved at the rate illustrated in Figure 26(1). Segments of the strain-time record for this test can be seen in Figure 34. Note that the first cycle is essentially equivalent to a monotonic creep rupture test in which a strain reversal occurs in the secondary creep regime. Also note that the creep rate increases in successive cycles with a smaller secondary creep regime accounting for less and less of the inelastic strain.

There are several factors which may contribute to this increasing creep rate: The first is a microstructural softening which is due to γ' agglomeration or ripening.[3,38,54] This phenomenon generally occurs after the first few cycles at 1000C. Also, a cursory examination of dislocation substructures (see Figure 90) revealed little differences between a test specimen which was interrupted early in cyclic life compared to one interrupted late in cyclic life. It is concluded that coarsening contributes little to the increase in strain rates observed during cyclic creep rupture tests.

A second possiblity is "cyclic creep acceleration". Considerable study of this phenomena has been done for aluminum at intermediate homologous temperatures.[99-101] It has been observed that the application of a cyclic stress results in a greater creep rate than would be observed for a monotonic application of the same maximum stress. No specific reference could be found to document a similar study on a nickel-base superalloy at high temperature.

As will be discussed in the next section, the principal mode of damage in HTLCF is the initiation and subsequent propagation of cracks with a considerable portion of the cycles or time to failure spent in propagation. A number of cracks may intiate and grow during a HTLCF test. These cracks may link-up during the course of propagation and form the crack which is ultimately responsible for failure. Another possibility is that the most critical crack may have initiated first or propagated along the most favorably oriented grain boundary. Failure of a test specimen occurs at a particular combination of crack size and

maximum stress. If the maximum tensile stress in a test is low, the crack size required to cause specimen failure will be relatively large. As seen in Figure 27, the tensile cyclic creep rupture test, Case II, presently being considered achieves an inelastic strain equivalent to the strain hold test and continuous cycling test with a much lower maximum stress. As will be demonstrated in the next section, this TCCR test tolerated cracks of considerable depth before failure occurred. It is concluded that the presence of these cracks is the principal cause of the increasing strain rate observed in Figure 34. This conclusion is supported by the evolution of a more compliant, hysteresis stress-strain response. The hysteresis loops for four different cycles are superimposed in Figure 33. The increasing compliance of the specimen is obvious in the stress reversals. It is the author's opinion that the increase in specimen compliance also accommodates creep strain during the hold at constant load. Relating the changing specimen compliance to the growth of the principal crack is a nontrivial exercise due to the presence of numerous cracks in the gauge section accomodating longitudinal strain. Also, as cracks penetrate the specimen, a decreasing cross section must bear the load. Therefore, the true stress is increasing and contributes to the increasing strain rate.

The observation of an accelerating creep rate in the hold of a tensile cyclic creep rupture test was also made for René 80 tested by NASA and TRW. The strain-time records for two such tests performed on René 80 at 1000C (NASA) can be seen in Figures 35 and 36.

The TCCR (CP) test, Ree 305 was performed on coated René

80 at 1000C (Figure 35). The imposed conditions of this test performed in load control were as follows: $\Delta\varepsilon_{total}$ = 1.022% and stress hold = + 152.9 MPa. The resulting inelastic strain components at half life were: PP = 0.134% and CP = 0.496%. The specimen reportedly failed after 48.

The TCCR (CP) test, Ree 208 was performed on uncoated René 80 at 1000C (Figure 36). The imposed conditions of this test performed in load control were as follows: $\Delta\varepsilon_{total}$ = 1.098% and stress hold = 172.6 MPa. The resulting inelastic strain components at half life were: PP = 0.218% and CP = 0.480%. The specimen reportedly failed after 35 cycles and 17.97 hrs.

Note the similarity between Figures 35 and 36 and Figure 34. Recall that the NASA tests were performed in load control with diametral strain extensometry. It is not clear how cracks normal to the longitudinal axis accommodate diametral strain, but they apparently do.

Increasing strain rates were also observed in successive cycles of compression hold tests; i.e. CCCR tests.

Since strain rate increases steadily as cracks advance through the guage section of a specimen, it would seem reasonable to relate the increase in strain rate to the rate of crack advance and to the time or cycles to failure. The average strain rate in any cycle is proportional to the inverse of the hold time for that cycle. Hold time is plotted for test Ree 305 and test Ree 208 against cycle number in Figures 37 and 38 respectively and against elapsed time in Figures 39 and 40 respectively. As can be seen, hold time is proportional to the elapsed time which suggests that crack growth is a function of time

rather than a function of cycle number. Hold time could not be related to cycle number with an exponential function or a power function.

It should be noted that the quantity (ε_{creep}/hold time) represents the average strain rate in a cycle. However, as seen in Figures 34 though 36, the strain does not vary linearly with time. The most accurate functional representation takes the following form:

$$\varepsilon = \varepsilon_0 + \beta t^m + kt \qquad [15]$$

where ε = total strain

ε_0 = initial strain upon loading

β, m, and k = constants

considering the small amount of inelastic strain achieved in the secondary creep regime, the following simplified form of Eq. [15] is adequate:

$$\varepsilon = \varepsilon_0 + \beta t^m \qquad [16]$$

in terms of the inelastic strain

$$(\varepsilon - \varepsilon_0) = \beta t^m \qquad [17]$$

where $(\varepsilon - \varepsilon_0)$ = inelastic strain achieved during the hold.

The constants β and m were determined for the stain-time records of cycles 6 through 31 for test Ree 208. Agreement with Eq. [17] was evident in the correlation coefficients which ranged from 0.95 to 1.00. As can be seen in Figure 41, β varies little in successive cycles and both the cycle-averaged and time-averaged value of β = 0.058. As can be seen in Figure 42, m increases steadily as a function of cycle number or as a function of time.

In the preceeding discussion it has been shown that the progression of damage (i.e. crack growth as manifested by an increasing strain rate during a stress hold) could be related empirically to elapsed time in a few tests. The information available for the SRP tests presently being investigated is insufficient to explain these observations in more fundamental terms. Perhaps the most important question to be answered is; how m in Eq. [17] is related to cycle number or elapsed time and in what way does this relationship depend on the holding load and the total inelastic strain range.

Being able to predict the cyclic stress-strain-time response of a material is obviously important in predicting the life of a laboratory test specimen if damage is time dependent (i.e. oxidation or time dependent crack growth). Expressing the stress-strain-time relationship for a SRP test in a manner which could be easily incorporated into a life prediction methodology is not a simple undertaking. The strain-time response for a single cycle was accurately represented by Eq. [17]. The steadily increasing strain rate throughout the course of the test resulted in a steady increase in the constant m. It would

be expected that the stress dependency of strain rate be reflected by m, $^{dm}/dt$ or $^{dm}/dN$. Note that Eq. [17] with consideration of the changing m is a phenomenological representation of what is believed to be an increasing specimen compliance and an increasing true stress resulting from the presence of cracks in the specimen gauge section. Also, metallurgical changes result in structural softening. A more fundamental representation of the strain-time response for a single cycle would include several terms to represent the rate at which each of these physical processes accommodate strain. Each of these physical processes may have a unique stress dependency.

In view of the importance of strain rate in cyclic creep tests, the average strain rate during the stress hold is related to the holding stress in Figures 43 through 49.

The strain rate data for uncoated René 80 tested in vacuum at 1000C (TRW) is plotted in Figure 43. Note the three datum marked with an asterick, test numbers 26u-PC-8, 23u-PC-6, and 9u-PC-1, probably represent erroneous strain and/or load readings as already mentioned. In general the data follows an often observed relationship of the form:

$$\dot{\varepsilon}_{avg} = C\ \sigma^{n} \qquad [18]$$

where $\dot{\varepsilon}_{avg}$ = time averaged strain rate during the stress hold ($\varepsilon_{hold} \times N_f/t_f$)

σ = holding stress (i.e. initial stress)

C and n = constants.

The same trend can be noted for coated René 80 tested in vacuum at 1000C (TRW) as seen in Figure 44. Stain rate is plotted against holding stress for uncoated and coated René 80 tested in vacuum at 871C (TRW) in Figures 45 and 46 respectively. The TRW data will not be closely scrutinized for reasons given in Appendix B.

Strain rate is plotted against holding stress for uncoated and coated René 80 tested in air at 1000C (NASA) in Figures 47 and 48 respectively and for uncoated IN 100 tested in Air at 925C (NASA) in Figure 49. The number adjacent to each datum represents the inelastic strain achieved during the hold at constant load. The general trend for each data set can be described by Eq. [18]. There seems to be little difference in the stress-strain rate behavior for coated or uncoated data. It was noted that it is only approximate to express strain rate in this simplified manner. However, it is encouraging that this empirical correlation does exist.

In Figures 47 and 48 the data which exhibits a very high strain rate represents tests performed at low holding loads and a relatively small inelastic strain achieved during the hold. Since the maximum stress is relatively low, the specimen can tolerate larger cracks. Such a compliant specimen could accumulate a considerable number of cycles rather rapidly resulting in a high, calculated, average strain rate. The strain-time records for two such TCCR (CP) tests performed on René 80 in air at 1000C (NASA) were presented in Figures 35 and 36. In Figure 35 it can be seen that test Ree 305 has essentially failed in 31 cycles. The failure life reported in the AGARD conference proceedings

(see Table II) was 35 cycles. In Figure 36 it can be seen that test Ree 208 has essentially failed in 30 cycles. The reported value was 48 cycles.

Also in the early cycles where the strain-time records resemble a monotonic curve with considerable time spent in the secondary creep regime, a test in which total inelastic strain is small achieves a greater portion of the inelastic strain in the more rapid primary creep regime.

C. Crack Initiation and Propagation

In this section the results of an extensive microscopic investigation of tested specimens will be presented. SEM and optical microscopy were found to reveal the physical nature of crack initiation and propagation quite adequately. TEM was performed on a few select specimens.

The majority of the specimens examined were of the tubular hour glass type (NASA and TRW) as shown in Figure 6. Most of the failures occurred very near the center of the guage section at the location of minimum load bearing area. In either direction from the center the cross sectional area becomes larger and reaches a maximum 7.5 mm from the center. The maximum area is 12.8% greater than at the center of the gauge section and the nominal stress is correspondingly 12.8% less. Due to this gradual change in stress, the entire gauge section experiences nearly the same stress and strain as does the center. For this reason, damage observed below the fracture is nearly the same as that observed at the critical center of the gauge section.

1. Untested Microstructure

The untested microstructure of René 80 specimens (NASA and TRW) can be seen in Figures 50 through 52. The originating laboratories report an ASTM grain size number of 3, which means that grain dimensions would be approximately 0.1 to 0.2 mm. However, as can be seen in Figure 50, grain dimensions on the order of 2 mm could be found, particularly in the radial direction. Note in Figure 6 that the tube is only 1.5 mm thick at the center of the gauge section. Consequently, single grains can easily transverse the specimen wall. Also note the irregularity of grain boundaries as seen in Figure 50. Such gross irregularities greatly impede grain boundary sliding at high temperatures. Dendrites which result from microsegregation of elements during solidification can also be seen.

The nature of grain boundary carbides in René 80 can be seen in Figures 51 and 52. Note the discontinuous small carbides and the intermitent larger carbides. This irregularity in grain boundary carbide morphology is partly responsible for the good creep resistance of this alloy. The course γ' precipitates can be seen clearly in Figure 52. The small γ' precipitates, which should have resulted from the pre-test heat treatment, could not be resolved by SEM. Carbides approximately the size of the larger γ' residing at the grain boundaries could be found throughout the matrix (Figure 51).

The microstructure of IN 100 is considerably different than René 80 as can be seen in Figure 53. The grain boundary carbides occur at random intervals and are generally small. The matrix γ' is

generally small and irregular but large irregular γ' can be found throughout the matrix and at grain boundaries.

Except for small regions near the origin, the majority of fracture surfaces were interdendritic. These interdendritic regions reveal little about the damage process controlling life but represents a rapid propagation stage. In Figure 54, it can be seen that the periodicity of undulations on the fracture surface are the same as the dendrite arm spacing.

Micrographs documenting the various forms of damage can be seen in Figures 55 though 88. Most of the figures represent two tests and are designated A and B. The A-test is generally a high inelastic strain test and the B-test is generally a low inelastic strain test. The test conditions and failure data are given below each figure. The last two letters in the identification of each micrograph represents a particular feature of the specimen: FS = fracture surface, OS = outside surface, IS = inside surface and DS = diametral section made in the longitudinal direction. The longitudinal axis is in the vertical direction in each figure.

Uncoated René 80 Tested in Vacuum at 1000C (TRW)

The HRSC (PP) test specimens are shown in Figures 55 and 56. The low strain test, B, exhibits a relatively large region of slow crack propagation compared to the high strain test, A. Due to higher tensile stresses in the high strain test, 191 MPa compared to 117.2 MPa for the low strain test, a crack can initiate and propagate more rapidly. Also, the high strain test, having a higher maximum tensile stress, requires a

much smaller crack to cause specimen separation.

Delineation of grain boundaries is evident on the outside surface of these specimens. This delineation may be a result of two physical phenomena. It may result from grain boundary carbides "popping out" due to mechanical incompatibility with the matrix. Such an explaination should account for a greater or lesser delineation on boundaries with different orientations with respect to the longitudinal axis. In micrographs A3 and B3 of Figure 55 and in many figures which will follow (those representing vacuum tested specimens), it can be seen that the amount of grain boundary delineation is uniform, showing no perference for boundaries with a specific orientation. Also, elements found in greater concentrations at grain boundaries may have higher vapor pressures than the average for matrix elements. Such is the case with the element Cr, present in high concentrations in grain boundary carbides. Elemental Cr has a vapor pressure ten times greater than elemental Ni at the testing temperature of 1000C. The relative vapor pressures of Ni and Cr present in the matrix and in carbides, in René 80, may be different. The observations bear greater support for the second explanation. A more conclusive determination cannot be made with the evidence available.

Internal damage as revealed in the diametral sections shown in Figure 56 is generally grain boundary decohesion. The grain boundary cavity in micrograph B1 appears to have been a casting defect, probably present before testing. Triple point cracking, as seen in micrograph A2, is a mode of damage generally associated with hold times and creep.

The CCCR (PC) test specimens are shown in Figure 57. Damage takes the form of "thermal etching" and sliding at grain boundaries. Crack initiation and propagation are intergranular. Note the more extensive grain boundary sliding with grain extrusions in the low strain specimen. The low strain test was performed with an initial holding stress of -78.6 MPa compared to -103.4 MPa for the high strain test. The times-to-failure were 15.9 hours and 4.9 hours respectively. If grain boundary sliding is time dependent, it is reasonble that the low-strain long-lived specimen would exhibit more extensive grain boundary sliding. Secondly, the low strain test specimen experienced a lower maximum tensile stress, 176.5 MPa compared to 270.3 MPa for the high strain test specimen. Therefore, the low strain specimen would require a greater degree of grain boundary damage to cause separation. Micrograph A3 exhibits a common observation for compression hold tests, that is, grain boundary sliding without decohesion along the boundary.

The TCCR (CP) test specimens are shown in Figures 58 through 60. Damage was again found principally at grain boundaries and was evident on the inside and outside surfaces of the specimens along the "thermally etched" boundaries. Micrograph B3 exhibits a cross section through a "thermally etched boundary". In view of the fact that little grain boundary sliding is observed for the tensile hold tests, it is unlikely that this material loss could be attributed to mechanically induced loss of grain boundary carbides. Grain boundary cracks initiate at the surface and propagate along boundaries oriented approximately normal to the longitudinal axis as can be seen in Figure 59, micrograph 1. Grain

boundary decohesion also occurs internally as can be seen in Figure 59, micrographs 2 through 4 and in Figure 60, micrograph 3, particularly on boundary segments normal to the longitudinal axis. The stereo pair of a surface initiated crack (Figure 60 and micrographs 2 and 4) illustrates that cracks propagate along the carbide matrix interface.

Coated René 80 Tested in Vacuum at 1000C (TRW)

The CCCR (PC) test specimens are shown in Figure 61. In micrograph B1, the grain extrusions at grain boundaries are evident even through the aluminide coating. Note the similarity to the uncoated low strain specimen shown in Figure 57. Cracks generally initiated in the coating as seen in micrograph B3, but were also observed to initiate in the coating substrate as seen in micrograph B-4.

The TCCR (CP) test specimens are shown in Figure 62. Although cracks initiated in the coating, they appeared to have assumed a grain boundary pattern. Note particularly micrograph B1.

Uncoated René 80 Tested in Vacuum at 871C (TRW)

The HRSC (PP) test specimens are shown in Figure 63. Only a very moderate amount of grain boundary delineation was observed compared to the 1000C-vacuum tested specimens. Initiation likely occurred at transverse segments of grain boundaries as seen in micrograph B2. Also note the pit like defects at a region away from grain boundaries. These occur at matrix carbides which intersect the specimen surface. These pits, like the grain boundary delineation previously discussed, are likely due to high vapor pressure of carbide forming elements or to mechanical incompatibility between matrix and carbides. Although not

common, cracked carbides were occasionally found in the matrix as seen in micrograph A3.

The CCCR (PC) test specimens are shown in Figures 64 through 66. Note once again the larger region of slow crack propagation on the fracture surface of the low strain specimen. The majority of specimens examined were free of gross casting defects. Small casting pores such as those seen in Figure 65, micrograph 2, had no effect on crack initiation or propagation. However, in a few specimens, casting defects did play a role in the cracking process as can be seen in Figure 66. The relationship between grain boundary and matrix carbides and the pit-like surface defects is especially clear in Figure 66, micrograph 4.

The TCCR (CP) test specimens are shown in Figure 67. Crack initiation and propagation was intergranular.

Coated René 80 Tested in Vacuum at 871C (TRW)

The HRSC (PP) test specimens are shown in Figure 68. As suggested by the larger region of slow propagation in micrograph B1 and B2, and the deep crack into the bulk of the specimen, micrograph B3, the low inelastic strain-low maximum stress test required a larger crack to cause failure.

Consider the CCCR (PC) test specimen shown in Figure 69 and the TCCR (CP) test specimens shown in Figure 70. Cracks were initiated in the aluminide coating.

Uncoated René 80 Tested in Air at 1000C (NASA)

The HRSC (PP) test specimens are shown in Figure 71. Again, a larger region of slow crack propagation was found on the low inelastic

strain-low maximum stress specimen. Cracks initiated at oxide cracks in the specimen surface as can be seen in micrograph B3. As these cracks propagated into the matrix, the newly formed surfaces oxidized. This oxide, which could have potentially reduced the rate of further environmental attack, was continually cracked by repeated strain reversals providing a path for easy oxygen penetration. As a result of this process, many oxide-filled cracks can be found in the gauge section.

The CCCR (PC) test specimens are shown in Figures 72 and 73. Cracks in the oxide gave rise to cracks in the matrix. Note that these cracks have assumed parallel arrays of nearly equivalent spacing for a particular test. Diametral sections of these specimens revealed a γ' depleted zone near the surface as well as around the crack as can be seen in Figure 73, micrographs 3 and 4. The γ' depleted zone is associated with the diffusion of Ti and Al to the surfaces. The fact that this γ' depleted zone has different mechanical properties than the matrix means that oxidation may affect the rate of crack advance under specific test conditions. The crack shown in micrograph B4 may be an arrested crack or a slow moving crack experiencing general oxidation. The rate of growth of the principal crack may have exceeded the rate of development of the γ' depleted zone.

The TCCR (CP) test specimens are shown in Figure 74. There is a considerable difference in the behavior of the oxide compared to the CCCR tests. The oxide has spalled rather than cracked. Crack initiation and propagation was intergranular.

The BCCR (CC) test specimens are shown in Figure 75. Note once

again that the cracks in the oxide have assumed regular parallel arrays.

The behavior of the oxide played an important role in crack initiation for uncoated specimens tested in air. Consider a test where the specimen is held in tension (i.e. TCCR test). When the strain limit is achieved, the cycle is reversed. The compressive strain is accommodated in the bulk material by plastic deformation. However, the oxide which has formed during the hold is brittle and can tolerate only small elastic strains and therefore must spall. On the other hand, during a compression hold test (CCCR or BCCR), the oxide forms during the relatively long hold and to accommodate the strain on the tension going portion of the cycle, the oxide simply cracks. These oxide cracks give rise to cracks in the matrix, one of which will ultimately be responsible for failure of the specimen.

It has been observed that the cracks in the oxide assumed a very regular spacing on the gauge section surfaces. It is possible to relate the spacing of cracks to the total strain imposed during the test. As the plot in Figure 89 suggests, there exists a minimum total strain range below which we would expect an infinite spacing of cracks, that is, no cracks present in the oxide. The few tests performed with a total strain range below this minimum (around 0.3%) resulted in cyclic lives greater by a factor of two or three than would be predicted by extrapolation of the high strain range data. This possibility for error should be considered when using high strain-short lived tests to predict behavior at lower strains and longer lives.

Coated René 80 Tested in Air at 1000C (NASA)

The HRSC test specimens are shown in Figure 76. Note once again the larger region of slow propagation on the fracture surface of the low inelastic strain-low maximum stress specimen. The low inelastic strain, test specimen (micrograph B2) exhibits an intergranular character at the origin but a transition to transgranular propagation. Initiation generally occurred at coating cracks.

The CCCR (PC) test specimens are shown in Figure 77. Cracks initiated in the coating. Note also the rumpled appearance of the coating.

The TCCR (CP) test specimens are shown in Figure 78. Although there are numerous coating cracks, the preferred path for crack propagation is intergranular. Note also the cavity adjacent to a grain boundary carbide in micrograph A3. Such cavities are generally associated with carbides because their formation is favored by the high resolved shear stresses which are present there during testing[47].

The BCCR (CC) test specimens are shown in Figure 79. Note once again that the low inelastic strain-low maximum stress specimen exhibits a larger region of slow propagation.

René 80 Tested in Air at 1000C (U of C)

The TCCR (CP) test specimens are shown in Figures 80 and 81. Each of the three specimens represented in these two figures were tested under identical conditions. Test GR-1 (Figure 80) was cycled to failure, t = 16.6 hours and N = 130. Hence the damage seen in Figure 80 represents approximately the state of damage (cracking) necessary to cause failure under the imposed test conditions. The maximum damage

logically occurred at the location of failure. Crack initiation and propagation are intergranular. Most of the intergranular cracks originated at the surface but were also found internally at grain boundary segments normal to the tensile axis.

Specimen GR-2 (Figure 81-A) was cycled to t = 3.31 hours and N = 7. Note that in this early stage of the test, cracks have already initiated at grain boundaries.

Specimen GR-3 (Figure 81-B) was cycled to t = 7.39 hours N = 27. Grain boundary cracks were numerous in this specimen and on average longer than in specimen GR-2. Note also a deeper general oxidation at the surface and also note that oxidation of the cracked surfaces is similar to the general oxidation at the specimen surface. Note that the cracks in Figure 81-B are not longer than those in Figure 81-A, yet the testing time is 2.2 times longer. These cracks have obviously arrested because the particular grain boundaries in which they reside deviate from a normal-to-the-principal-stress direction. Oxidation also served to blunt the crack tip. The evidence presented above supports a contention that cracking is initiated at grain boundaries in René 80 tested at 1000C because they possess poorer mechanical strength than the matrix and not because of a rapid penetration of an "oxide spike".[3,38,54] Considerable oxidation product subsequently accumulates at the crack because repeated strain reversals continually breaks the potentially protective oxide. More accurately stated; cracking in HTLCF of René 80 occurs at grain boundaries, particularly when hold times are included. The poorer mechanical strength of grain boundaries for nickel-base

alloys may be attributed to oxygen poisoning of the boundaries as was demonstrated by Bricknel and Woodford[102]. Given the fact that grain boundaries have poorer mechanical strength (for whatever reason) and given the fact that initiation and propagation will occur along favorably oriented grain boundaries, the important question still remains; what parameters govern the rate of crack advance down such a boundary to achieve the critical crack size for failure under the prevailing maximum stress.

These tests serve to point out a possible fallacy in the interpretation of post mortum specimens.

Consider the strain hold (CP) test specimen shown in Figure 82. The depth of cracks observed in this specimen tested to failure were considerably less than that observed for the stress hold test specimen shown in Figure 80. The hysteresis loops for these two tests can be seen in Figure 27. Note the higher maximum stress for the strain hold test.

Uncoated IN 100 Tested in Air at 925C (NASA)

The test specimens are shown in Figures 83 through 86. The general mode of damage was intergranular initiation and propagation regardless of cycle type. The behavior of the oxide exhibited a dependency on cycle type similar to that observed for René 80. Again, the natural selection of grain boundaries as a site of crack initiation and propagation is due to their inferior mechanical strength rather than being a site of rapid environmental attack.

Consider the TCCR (CP) test specimen shown in Figure 85. Note the

general depth of cracking in micrograph B2 along boundaries oriented favorably to the principal stress direction. Note in micrograph B3, a crack in the same specimen is very short because the boundary in which it resides deviates from a favorable stress orientation. Oxidation has served to blunt the crack tip. If grain boundary penetration was due to intense localized oxidation of grain boundaries, there is no reason that this particular crack should be halted. The driving force for crack advance appears to be the component of stress normal to the crack plane.

Coated IN 100 (ONERA)

Consider the creep rupture test and the pure fatigue test specimen shown in Figure 87. The origin of failure in the creep rupture tested specimen could not be indentified. The fracture surface suggests a microvoid coalescence mechanism. The origin of failure in the pure fatigue test can be easily identified in micrographs B1 and B2. Crack initiation and propagation to the critical crack size was transgranular. Note the differences in the appearance of the gauge section surfaces in micrographs A3 and B3. The numerous cracks in the coating for the monotonic creep rupture test reflects the greater amount of strain which was necessarily accommodated by the coating.

Consider the LRSC and BCCR test specimens shown in Figure 88. Note that an origin could be located on the LRSC test specimen but not on the BCCR test specimen.

Transmission Electron Microscopy

(Uncoated René 80 Tested in Air at 1000C)

A cursory examination of dislocation substructure was performed on

a few specimens selected from those tested at U of C. The principal objective was to determine if the increasing strain rates observed during TCCR testing (Figure 34) could be explained in terms of structural softening. A few representative TEM micrographs are shown in Figure 90.

The starting microstructure was characterized by examination of foils taken from the head of a test specimen. This starting microstructure is shown in micrograph F. As stated in the Experimental section, it was discovered that the specimens used in this U of C test program had not been heat treated. Instead of the duplex γ' structure which would have resulted from the intended heat treatment, the coarse γ' structure seen in micrograph F is that which resulted from Hot Isostatic Pressing.

Micrographs A, B and C represent three TCCR tests performed under identical conditions (see Table II-13). Micrograph A represents the substructure in a specimen stopped very early in life, N = 7 and t = 3.31 hours. Micrograph B represents the substructure in a specimen stopped at an intermediate point in the life, N = 27 and t = 7.39 hours. Micrograph C represents the substructure in a specimen tested to failure, N = 130 and t = 16.56 hours. These three micrographs illustrate a similarity in microstructure and dislocation arrangement which indicates that the increasing strain rates observed thoughout the course of TCCR tests connot be attributed to structural softening.

Micrograph D represents the strain hold test GR-4 tested to failure. Note the similarity in microstructure and dislocation arrange-

ment compared to the TCCR test to failure, Micrograph C.

Micrograph E represents a grain boundary in the strain hold test specimen GR-4. There was no evidence of any particular grain boundary damage mechanism such as cavitation.

D. A Model For High-Temperature Low-Cycle Fatigue

In view of the evidence presented, it is apparent that HTLCF damage in René 80 and IN 100 takes the form of crack initiation and propagation. The observation of cracks in a René 80 test specimen (U of C) stopped very early in cyclic life supports a contention made by previous investigators that LCF life represents principally a crack propagation stage. The most consistent observation made of the failed specimens was that there exists a particular combination of maximum tensile stress and crack size necessary to cause failure (the higher the maximum tensile stress, the smaller the crack necessary to cause failure). Considering the nature of the tests investigated (i.e. TCCR tests in which specimens were held under a prescribed static load) and the findings that increasing strain rates during the hold were a function of elapsed time in such tests, it is surmised that crack growth was a function of time rather than cycle number. Based on the above stated premises, a methodology for analysis and prediction of fatigue life will be presented.

Several investigators have attempted to describe creep crack growth in HTLCF. A brief discussion of some of this work can be found in the Literature Review. One approach was expressed as follows:[69,70,73,74]

$$\frac{da}{dt} = AK^n \qquad [19]$$

where a = crack length
K = stress intensity
A,n = constants

This power law relationship, similar to the Paris equation, represents data for crack growth in a compact tension specimen under static load. Crack growth rate, da/dt, is a function of crack length, a, because the greater is the crack length, the greater is the stress and strain intensity at the crack tip and therefore the driving force for crack extension. In HTLCF testing, the entire bulk of the specimen is experiencing inelastic strains. Hence, employing a linear elastic fracture mechanics concept such as stress intensity is not strictly correct. Equation [19] has been employed from a purely empirical standpoint to describe creep crack growth quite satisfactorily.

Huang and Pelloux[66] studied fully plastic crack growth rates in Hastelloy-X at 25C and 760C and found da/dN to correlate most satisfactorily with ΔJ. It should be noted that these tests were continuous cycling tests performed at 0.2 Hz. There is no apparent justification for applying this approach to the present investigation which involved long hold times and where crack growth is suspected to have been a function of time.

Jones and Tetelman[73] have correlated crack growth, da/dt, with both net section stress and the apparent stress intensity factor for 304 stainless steel over the temperature range from 650C to 800C. Their results indicated that the stress intensity correlation is strongly dependent on specimen geometry, whereas the net section stress correlation appeared to be generally valid. The correlation may be expressed as follows:

$$\frac{da}{dt} = A\,\sigma^m \qquad [20]$$

where a = crack length
σ = net sections stress
A,m = constant

It was shown that time-dependent crack growth rate could be described by a power function of the net section stress because the net section stress is proportional to the local (crack tip) stress. The strain rate in the net section was also shown to be proportional to the local strain rate. This net section stress expression will be used in the following development. Considering that net section stress varies as a function of time in a HTLCF test, Eq. [20] becomes:

$$\frac{da}{dt} = A\,\sigma(t)^m \qquad [21]$$

Consider da/dt for any given cycle in a HTLCF test:

da = crack extension during the cycle

dt = elapsed time during which the crack was extending.

The crack does not extend at all times throughout a given cycle but only when the stress is positive. Taking this one step futher, we can surmise that the crack extends only when $\sigma(t) > \sigma_T$ (a threshold stress for crack extension by the mechanism of creep crack growth) and hence for $t = t(\sigma(t) > \sigma_T)$. Creep crack growth in any given cycle of a HTLCF test may be determined by integration of Eq. [21] between the appropriate limits.

$$\int_{a\ (\text{prior to cycle})}^{a\ (\text{after cycle})} da = \int_{t(\sigma(t) > \sigma_T)}^{t(\sigma(t) < \sigma_T)} A\ (\sigma(t) - \sigma_T)^m dt \qquad [22]$$

The principal point of interest in HTLCF testing is to be able to predict cyclic life or time to failure given the imposed conditions of the test (i.e., $\Delta\varepsilon_T$, $\Delta\varepsilon_p$, ε_{hold}, t_{hold}, ...etc.) Depending on the type of control, stress range, stain range or both, a given test may accumulate quite a number of cycles after the damage process (cracking) has ran its course. The number of cycles or time accumulated from this point to the end of the test can represent a significant fraction of N_f and/or t_f since it is usually reported for specimen separation. Therefore, a meaningful presentation of a method for the analysis and prediction of HTLCF life should define N_f and t_f as the cycle number and time for which the damage process is completed. This matter may be somewhat complicated when applying a definition for failure to tests with different controls. For example: In a total strain control-strain hold test, actual failure will manifest itself as a marked decay in the maximum stress. In a total strain control-stress hold test, actual failure may manifest itself as a very rapid attainment of the inelastic strain, resulting in very short hold times. Defining an equivalence between the two requires a judgement.

The physical significance of a definition for failure was quite adequately demonstrated in the previous section. Failure in a HTLCF test has occurred when the principal crack exhibits a transition from slow propagation to rapid crack advance (which was charac-

teristically interdendritic for the materials and test conditions studied). The transition may have been marked by specimen separation in a single cycle if the maximum tensile stress was high or by the observations described above. The fact that the transition to a rapid propagation stage occurs at a particular combination of crack size and maximum tensile stress suggests that fracture mechanics considerations and therefore an "apparent stress intensity factor" defines an operative failure criterion. Such a criterion may be expressed as follows:

$$K_f = S\,\sigma_{max}\,(a)^{1/2} \qquad [23]$$

where K_f = apparent stress intensity factor
S = shape factor, depends primarily on specimen geometry
σ_{max} = maximum tensile stress
a = crack length at the onset of rapid propagation

As was presented in Eq. [22]:

$$a/\text{cycle} = \int_{t(\sigma(t) > \sigma_T)}^{t(\sigma(t) < \sigma_T)} A(\sigma(t) - \sigma_T)^m \, dt \qquad [24]$$

For the nickel-base superalloy René 80, the value for m was found by inspection to be equal to 2. The crack length for failure of René 80 as defined above may be expressed as follows:

$$a_f = (N_f)(a/\text{cycle}) = N_f \int_{t(\sigma(t) > \sigma_T)}^{t(\sigma(t) < \sigma_T)} A(\sigma(t) - \sigma_T)^2 \, dt \qquad [25]$$

Eq. [25] is valid when $\sigma(t)$ does not change much with cycle number. If $\sigma(t)$ changes significantly with cycle number, the change should be accounted for. The condition for failure when the mechanism of damage in HTLCF is creep crack growth may be stated as follows:

$$K_f = S\ \sigma_{max}\ [a_f]^{1/2} = \text{Constant} \qquad [26]$$

$$K_f = S\ \sigma_{max} \left[N_f \int_{t(\sigma(t) > \sigma_T)}^{t(\sigma(t) < \sigma_T)} A\ (\sigma(t) - \sigma_T)^2\ dt \right]^{1/2} \qquad [27]$$

Application of this failure criterion to three tests performed on uncoated René 80 at 1000C in air (U of C) will be demonstrated explicitly. The test conditions are described in detail in Table II-13. The hysteresis loops for these three tests can be seen in Figure 27. Note particularly the similarities in the imposed test conditions. In each test the total strain limits were identically 0.93%. The time required for strain reversal in each leg of the hysteresis loops was approximately 30 seconds in each test. The resulting inelastic strain range in each test was approximately 0.6%.

Case I, Strain Hold Test

Consider the strain hold test designated GR-4. The hysteresis loop taken at approximately half life can be seen in Figure 27. Portions of the stress-time record can be seen in Figure 91. The hold time at the positive strain limit was 390 seconds. This hold time was the cycle-averaged hold time for the stress hold test designated GR-1. (This test

will be considered in Case II). Application of Eq. [27] requires an appropriate expression for $\sigma(t)$ and a determination of σ_T and N_f.

It was determined that $\sigma(t)$ for the strain hold could be expressed in the classical manner for exponential decay of stress. Note that Eq. [27] requires an expression for $\sigma(t)$ only for the time during which $\sigma(t)$ is greater than σ_T.

In lieu of a direct determination of the threshhold stress for creep crack growth, the following rationale was used to approximate the value of σ_T. Cyclic life correlates very well with inelastic strain (i.e. Coffin-Manson equation) for a given type and condition of testing. Inelastic strain, therefore, must correlate with damage (cracking) in HTLCF. An exponential decay of stress with a corresponding increase in inelastic strain was observed in Case I. The stress levels off at a stress of about 151.7 MPa for cyclically stablized René 80 tested under these conditions. Inelastic strain (damage) is no longer accrued below this value of stress (approximately the back stress). σ_T will therefore be taken as 151.7 MPa.

The next concern is the determination of N_f. As previously discussed, failure in HTLCF occurs when the damage process (cracking) has run its course. This was defined as the transition to a rapid propagation stage. Since a direct determination of the transition cannot be made, consider how such a transition would manifest itself in the cyclic stress response. Stress versus cycle number is plotted for the strain hold test presently being discussed in Figure 92. The maximum and minimum stress in each cycle as well as the minimum stress achieved

during the strain hold are plotted. The presence of cracks in the specimen was manifested by a reduction in the maximum stress and the relaxed stress. Metallurgical changes such as structural coarsing were also partly responsible for this decay in maximum stresses. Without the necessary basis for making a determination, a judgement must be made. A rapid change in slope is noted in the maximum stress at a stress of approximately 207 MPa. The corresponding cycle number is 160. N_f by definition is therefore 160. Employing the cycle-averaged values of the maximum tensile stress and the minimum stress in the strain hold, the following expression represents the quantity $(\sigma(t)-\sigma_T)$ for Case I.

$$(\sigma(t)-151.7) = 91.50\ e^{-t/24} \qquad [28]$$

Now the appropriate substitutions can be made into Eq. [27].

$$K_f = S(207)\left[A(160)\int_{t=o}^{t=390}[91.50\ e^{-t/24}]^2\ dt\right]^{1/2} \qquad [29]$$

$$K_f = SA^{1/2}\ 8.3 \times 10^5 \qquad [30]$$

Case II, Tensile Cyclic Creep Rupture Test

Consider the stress hold test designated GR-1. The hysteresis loop taken at approximately half life can be seen in Figure 27. Portions of the stress-time record can be seen in Figure 93. The hold time varied in each cycle and was as long as necessary to achieve the positive

strain limit (see Figure 34).

Due to the imposed conditions of the test; $\sigma(t)$ = constant = 172 MPa. The value of σ_T is again taken as 151.7 MPa. Consequently the quantity ($\sigma(t)-\sigma_T$) = constant = 20.3 MPa. The presence of cracks in this specimen was manifested by the rapid attainment of inelastic strain as can be seen in Figures 34 and 93. Failure was judged to have occurred at N=130 and t=16.56 hours. Recall that in the development of Eq. [27], the integral represents the crack growth per cycle. After multiplying by N_f, the resulting expression represents the crack length at failure. This approach cannot be applied directly to the present case because the hold time decreases throughout the test. Consequently, the time for crack growth decreases in each successive cycle. The integration can be performed for the cycle-averaged hold time in which case the quantity (total hold time) is substituted for the quantity (N_f x cycle-averaged hold time). With the appropriate substitutions Eq. [27] reduces to:

$$K_f = S(172)[A(51166)(20.3)^2]^{1/2} \qquad [31]$$

$$K_f = SA^{1/2}\ 7.9 \times 10^5 \qquad [32]$$

Continuous Cycling Test, Case III

Consider the low rate continuous cycling test, GR-5. The hysteresis loop taken at approximately half life can be seen in Figure 27. A schematic of the stress time record for a few cycles can be seen in Figure 94. Note that the cycle period was 60 seconds. It is expected that crack growth was time dependent at such a low rate of cycling.

Due to the imposed conditions of the test; σ (t) approximately fits an equation of the form $\sigma(t) = at + b$. The value of σ_T is again taken as 151.7 MPa. Consider the determination of N_f for this test. The maximum and minimum stress is plotted against cycle number in Figure 95. Failure will be defined in a manner equivalent to the strain hold test considered in Case I. Failure occurred when the maximum stress fell to 207 MPa. The corresponding cycle number is 260. With the appropriate substitutions Eq. [27] becomes:

$$K_f = S(207)\left[A(260)\int_{t=0}^{t=13.6}[6/76t]^2\,dt + A(260)\int_{t=13.6}^{t=15.8}[659-41.7t]^2\,dt\right]^{1/2} \qquad [33]$$

$$K_f = SA^{1/2}\ 7.1 \times 10^5 \qquad [34]$$

Considering Cases I through III, the failure criterion was calculated to be nearly identical in every case. Once again:

Case I, $K_f = SA^{1/2}\ 8.3 \times 10^5$

Case II, $K_f = SA^{1/2}\ 7.9 \times 10^5$

Case III, $K_f = SA^{1/2}\ 7.1 \times 10^5$

The general applicability of this failure criterion to tests representing such varied cycle character strongly suggests that the precepts on which it was founded are correct.

René 80 Tested in Air at 1000C (NASA)

The model expressed in Eq. [27] was applied to René 80 tests performed by NASA. The value for σ_T was determined by applying Eq. [27] to a small group of data and employing an interation technique to achieve the lowest deviation of K_f. σ_T was found to be 132 MPa. This value of σ_T was used in Eq. [27] to calculate values of K_f for many of the tests performed by NASA. The results are reported in Table III. Note that these values of K_f are not numerically equivalent to those just calculated for the tests performed at U of C. This is due to the fact that a different specimen geometry and hence a different shape factor, S', was employed. Furthermore, there is not a numerical equivalence between tests of different cycle types because Eq. [27] was necessarily applied in approximate form for most of the tests. Comparisons should be made only within a particular cycle type.

Calculation of K_f for the TCCR tests presented in Table III was performed in the manner demonstrated in Case II. Note particularly tests Ree 315 and Ree 305. The calculated values for K_f are $S'A^{1/2}$ 1.49 X 10^4 and $S'A^{1/2}$ 1.44 X 10^4 respectively. K_f was not calculated for TCCR tests in which the holding stress was below σ_T, 132 MPa.

In view of the fact that strain reversals occur at a very high rate for HRSC and CCCR tests, the time for which σ (t) is greater than σ_T is very small, usually less than one second. Consequently, crack growth under these conditions was more likely to have been cycle dependent than time dependent. To arrive at a convenient form for the cycle dependent

crack growth expression, consider the following: The imposed condition in all of these HTLCF tests was total strain control. Also, in nearly every case, multiple cracking was observed in the specimen gauge sections. The appropriate expression for the crack driving force becomes[103]:

$$G = \frac{\sigma_{eff}^{2}\, h}{2E} = \frac{K^2}{E} \qquad [35]$$

where G = Griffith crack driving force
h = specimen guage length
σ_{eff} = effective stress
K = effective stress intensity factor
E = elastic modulus

In Eq. [35] it can be seen that the effective stress intensity at the crack tip is proportional to the effective stress. Since cyclic crack growth under these conditions has been expressed in the form:

$$\frac{da}{dN} \propto (K)^n \qquad [36]$$

Then it follows that:

$$\frac{da}{dN} \propto (\sigma_{eff})^n \qquad [37]$$

Expressing the effective stress in a form which incorporates a threshold stress for cycle dependent crack growth, Eq. (37) becomes:

$$\frac{da}{dN} = A'(\sigma_{max} - \sigma_T)^n \qquad [38]$$

where σ_{max} = maximum tensile stress
σ_T = threshold stress for cycle dependent crack growth

Assuming a value of 2 for n, and following the same formulation used for time dependent crack growth, the failure criterion for the cycle dependent case becomes.

$$K_f' = S'A'^{1/2} (\sigma_{max})[(\sigma_{max} - \sigma_T)^2 N_f]^{1/2} \qquad [39]$$

Most of the calculations presented in Table III represent application of K_f' by Eq. [39]. Note the excellent agreement within any cycle type. The correlation is expressed as the (standard deviation/average value of K_f') for each cycle type. The possiblity that expressions for time dependent and cycle dependent crack growth may be similar in form is interesting since the Coffin-Manson equation, or some modification of it, generally serves to correlate cyclic life for both time dependent and cycle dependent fatigue.

It has been shown that, for a particular cycle type and test conditions, there is a good correlation between $\Delta\varepsilon_p$ and N_f. That is to say, the Coffin-Manson equation applies. Therefore any mechanistically based model should represent a form approximate to the Coffin-Manson equation. Consider the case of the continuous cycling tests performed on René 80 in air at 1000C (NASA). (Each datum considered is identified by an asterisk in Table III). The Coffin-Manson equation representing the data of interest is:

$$\Delta\varepsilon_p = 4.23\ N_f^{-.45} \qquad [40]$$

The coefficient of correlation is 0.96. Since the frequency of cycling is one hertz, the cycle dependent failure criterion, Eq. [39], will be employed.

$$(\sigma_{max})[(\sigma_{max} - 132)N_f]^{1/2} = \frac{K'_f}{S'A'^{1/2}} = 1.085 \times 10^6 \qquad [41]$$

Note that Eq. [41] is expressed in terms of maximum stress and cycles to failure. The equivalence between this equation and the Coffin-Manson equation representing the same data is not directly apparent. Consider Figure 30 in which the maximum stress is plotted against the inelastic strain range for this data. The relationship between the maximum stress and the inelastic strain range may be expressed by the familiar Holloman equation:

$$\sigma_{max} = 487.6\ \Delta\varepsilon_p^{.346} \qquad [42]$$

The coefficient of correlation is 0.99. Despite the excellent correlation, this equation is inaccurate at low values of $\Delta\varepsilon_p$. For example, when $\Delta\varepsilon_p = 0$ the calculated value of $\sigma_{max} = 0$ according to Eq. [42]. The true material behavior exhibits a nonzero maximum stress at $\Delta\varepsilon_p = 0$ when the specimen is cycled within the elastic limits. By extrapolating the curve in Figure 30 to $\Delta\varepsilon_p = 0$, the expression relating the maximum stress in the cycle to inelastic strain can take on greater physical significance.

$$\sigma_{max} = 132 + 417.1 \quad \Delta\varepsilon_p^{.710} \qquad [43]$$

The coefficient of correlation is 0.99.

Now with Eqs. [42] and [43] the appropriate substitutions can be made into Eq. [41].

$$(487.6 \quad \Delta\varepsilon_p^{.346})[(417.1 \quad \Delta\varepsilon_p^{.710})^2 N_f]^{1/2} = 1.085 \times 10^6 \qquad [41]$$

With the appropriate rearrangements Eq. [38] becomes:

$$\Delta\varepsilon_p = 4.87 \; N_f^{-.47} \qquad [44]$$

This equation is nearly identical to the Coffin-Manson equation representing the same data (see Eq. [40]).

IN 100 Tested in Air at 925C (NASA)

The failure criteria expressed in Eqs. [27] and [39] were applied to the IN 100 tests performed by NASA. The value for σ_T was determined by applying Eq. [39] to a small group of data and employing an iteration technique to achieve the lowest deviation in K'_f. σ_T was found to be 126 MPa. This value of σ_T was used in Eqs. [27] and [39] to calculate values of K_f and K_f' which appear in Table IV. The TCCR, BCCR and Verification tests were evaluated using Eq. [27]. Eq. [39] was used for the HRSC and CCCR tests since the time for which $\sigma(t)$ was greater than σ_T was very short in each cycle.

The same general observations made for the René 80 tests also apply for these IN 100 tests. There is, however, greater variation in K_f and K'_f for any given cycle type. This may be due to a significant

environmental interaction. The role of environment in crack growth in HTLCF was not treated explicitly in the development of Eqs. [27] or [39].

Consider the HRSC tests identified with an asterisk in Table IV. The Coffin-Manson equation representing this data is:

$$\Delta\varepsilon_p = 4.24\ N_f^{-.55} \qquad [45]$$

The coefficient of correlation is 0.98. With the appropriate substitutions for σ_{max}, Eq. [39] becomes:

$$\Delta\varepsilon_p = 4.08\ N_f^{-.54} \qquad [46]$$

Once again an equivalence between the Coffin-Manson equation (a phenomenological approach) and Eq. [39] a mechanistic approach has been demonstrated.

It should be noted that this model is in a development stage. Future work will address:

1) The physical significance of the crack growth expressions, particularly the physical significance of σ_T.
2) The apparent dichotomy in using an expression for crack growth which is independent of crack length and using a quasi-fracture mechanics failure criterion which is dependent on crack length*.
3) Application of the model to a variety of available data to test its general applicability.

*For example, as the crack grows the net section stress increases and at some point failure occurs when the net section stress reaches a critical value.

SUMMARY AND CONCLUSIONS

In summary, the evidence presented in this work indicates that damage in HTLCF of René 80 and IN 100 in the temperature range from 871C to 1000C is principally initiation and propagation of a crack or cracks to such a size that failure ensures. Failure was defined as the time and cycle number at which there is a transition to rapid propagation (characteristically interdendritic for the materials and test conditions studied). The transition (failure) occurred at a particular combination of crack size and maximum stress; the higher the maximum stress, the smaller was the crack size.

Cracks were generally found to initiate and propagate along grain boundaries oriented normal to the direction of loading. The driving force for crack advance was the component of stress normal to the crack plane. This propagation stage may be time dependent or cycle dependent in accordance with the cycle character. Hence the cyclic stress-strain-time response for any given test proved to be valuable. A model was developed to incorporate these observations into a failure criterion. In this model the cycles to initiation were not accounted for. The intention was not to disregard them, but an adequate basis to account for them was not available. Consider the range of inelastic strains imposed on the test specimens studied; approximately 0.05% to 2.0%. the attending maximum stress was generally greater than the time independent flow stress. For most of the test specimens studied in this regime, the contention that a crack or cracks initiated very early in cyclic life appeared to be valid. For low

inelastic strain tests (~0.05%) or for those tests where the maximum stress was relatively low (TCCR or BCCR tests), the cycles to initiation may have been significant.

Considerable attention was given to modes of crack initiation. In vacuum it was found that a form of damage existed that was not readily apparent in air tested specimens. Grain boundary delineation and pit like defects at the specimen surface were believed to be a result of the higher vapor pressure of carbide forming elements. These surface irregularities could potentially aid crack initiation. However, similarity between cyclic lives for coated and uncoated specimens precludes a straightforward assessment of this damage.

To give the proper weight to the environmental interaction, consider the following: Crack initiation and propagation generally occurred at grain boundaries, logically because they posess poorer mechanical strength. This poorer mechancial strength may be attributed to oxygen or nitrogen embrittlement of these boundaries or simply due to poorer inherent strength compared to the matrix. Specimens tested in air were found to have comparable cyclic lives for coated and uncoated specimens. This suggests that the environment did not play a major role in the initiation event for most of the tests investigated. However, oxidation can influence the cyclic life provided the inelastic strain and the maximum stress are low by affecting the cycles to initiation. It was found that below the critical strain for cracking of the oxide, a significant improvement in life was noted for uncoated specimens tested in air. The manner in which the environment affects the rate of

propagation of an initiated crack to a critical size could not be determined quantitatively from the present investigation. There were observations which indicate that oxidation served to blunt the crack tip. However, work by previous investigators suggest that propagation is likely enhanced by the environmental interaction. Oxidation as a mechanism of penetration of the material to achieve a crack like entity of a size necessary to cause failure was not observed in this investigation.

The following specific conclusions can be made from this work. They are applicable to René 80 and IN 100 in the regime of testing studied.

1. HTLCF of René 80 and IN 100 represents principally propagation of a crack to a size necessary to bring about failure under the prevailing maximum stress.
2. Crack initiation and propagation were generally intergranular.
3. Those degradation processes which degrade the specimen surface influence crack initiation. They affect life in the low inelastic strain - low maximum stress regime.
4. Vacuum tested specimens exhibited a form of damage unique to that enviroment.
5. The principal environmental interaction in air is related to the effect on crack initiation, particularly in the low inelastic strain - low maximum stress regime.

APPENDIX A

The TCCR tests performed at U of C were accomplished with the aid of a relay device borrowed from NASA Lewis. The tests were preformed in load control using the 50 kps MTS at U of C. The relay device was connected to Programmer 2 at location J226 on the 422 Controller as illustrated in Figure A-1. The rate of load reversals was controlled by the Resistance-Capacitance circuit also illustrated in Figure A-1. The holding load was achieved by increasing the Span 2 setting on the 422 Controller. Since these tests have a negative mean stress, it is necessary to impose a negative Set Point in such a way that (Set Point) + (Span 2) equals the holding load and (Set Point) - (Span 2) is less than the peak negative load required to reverse the cycle. The value for (Set Point) + (Span 2) should be just below the negative peak. If it is too low, it will effect a greater rate of load reversal since the command is essentially (%/sec) of (Set Point) $\pm$ (Span 2). This was illustrated in Figures 25 and 26 where higher rates of load reversal were achieved by clocking in a more negative value for the Set Point. Strain overshoot was noted at the negative strain limit for the high rate reversals. This was due to the inherent limitations of the relay device employed. The fastest rate which could be exployed without producing a significant strain overshoot was the rate illustrated by loop 4; about 35 seconds (see Figures 25 and 26). NASA reported reversal times of 1 second using the same device.

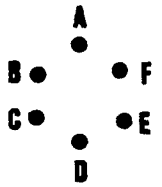

Location (J226)
422 Controller

On Programmer 2

A Ground
B High External Command (tension)
C Low External Command (compression)
D Reference Voltage (+10V)
E + Excitation
F - Excitation

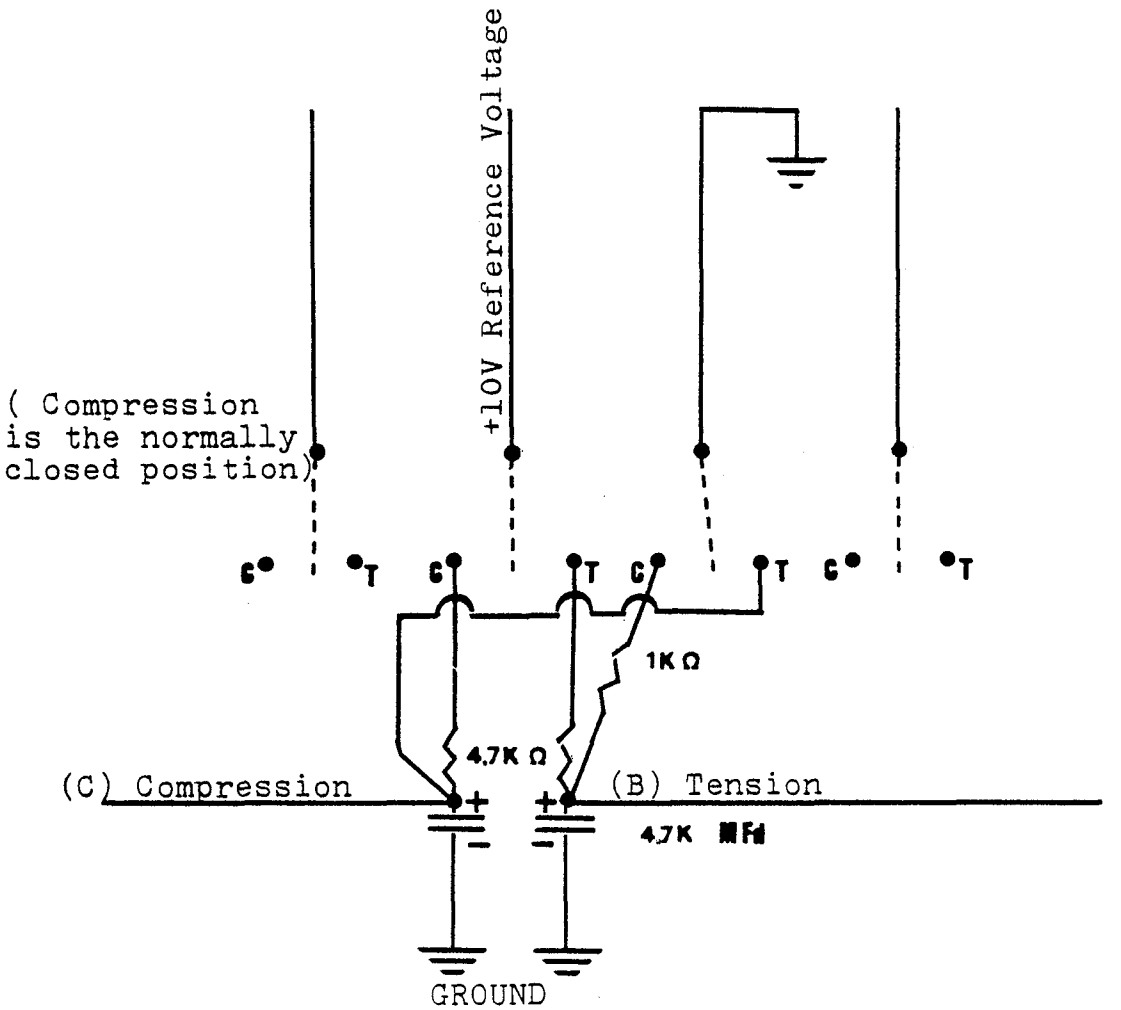

Figure A-1 Circuit modification made to the NASA relay device to control the rate of load reversals.

APPENDIX B

As was noted in the text, the stress response reported for the TRW tests appeared to be erroneous. The most likely explanation was the possibility of a scale factor error. Another discrepancy was noted in the flow stress for a number of tests. The stress-strain hysteresis loops reported by TRW in Report No. TRW ER-7861 for two tests can be seen in Figure B-1. The testing temperature was 871C for both tests. There is no plausible explanation for such a difference in stress-strain response.

Suspicions that the TRW tests were not well controlled were confirmed by a cursory examination of strain-time charts. A segment from two typical tests can be seen in Figure B-2. Note that the total strain limits are not equivalent in every cycle. Also note that there is not the steady decrease in the hold times that was observed for the NASA and U of C tests. This may be due to the shifting strain limits. There also appears to be considerable "noise" in the strain signal which could have caused the strain limits to be reached prematurely, especially where the strain-time curve is "flat" as it is in the early cycles in the test.

The uncertainties introduced by the poor test control described above precluded a rigorous analysis of the test data for the TRW tests. However, all observations of a general nature, such as those described in the section on microscopic observations are valid.

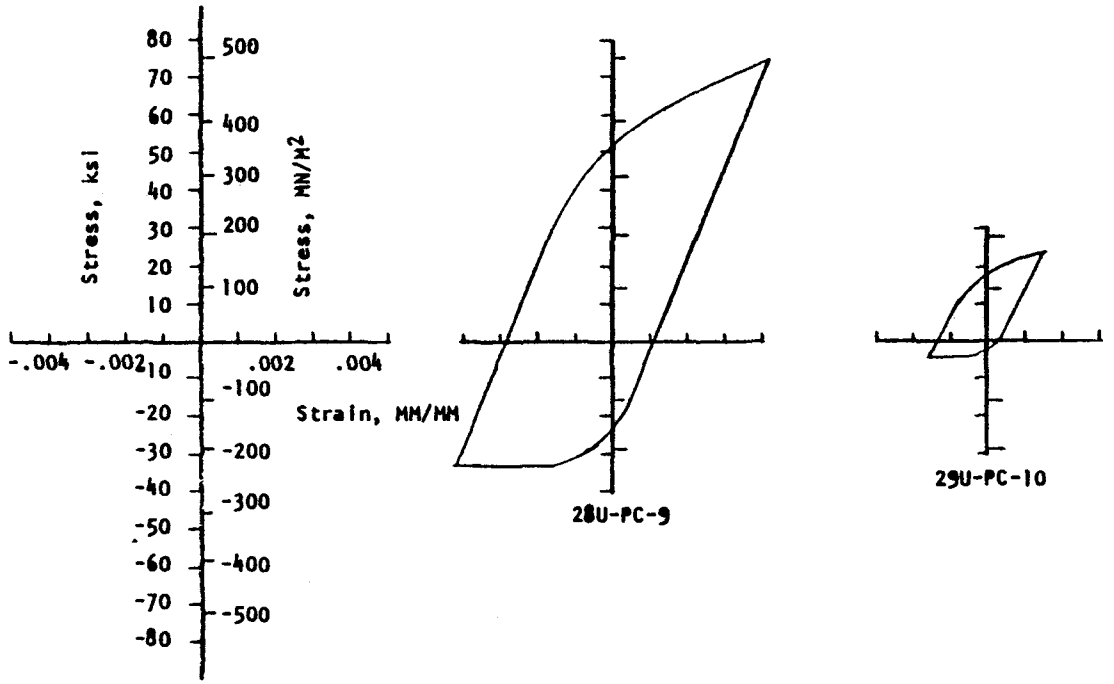

Figure B-1 Hysteresis loops for two tests performed on René 80 in Vacuum at 871C (TRW).

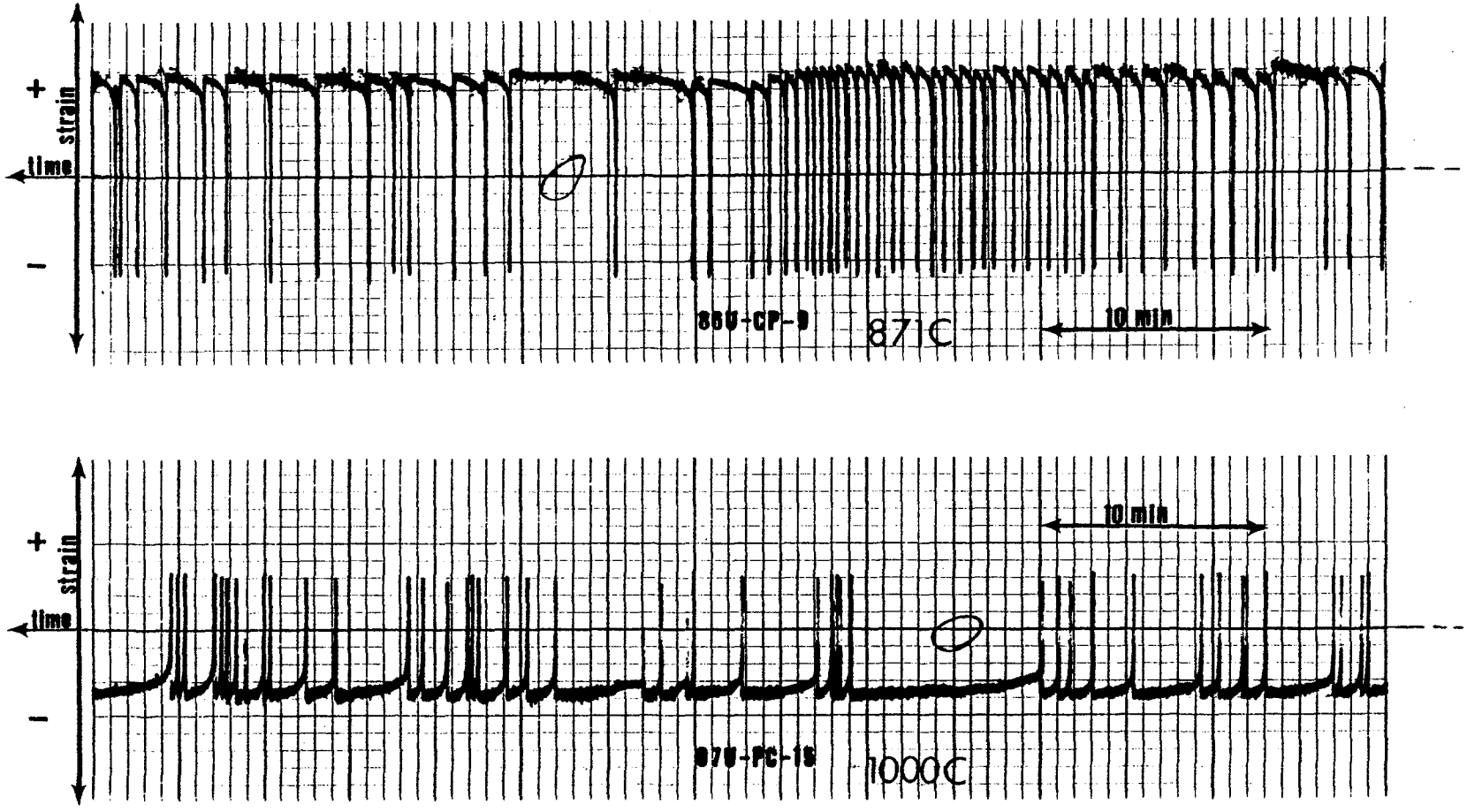

Figure B-2 Segments of the strain time charts for two tests performed on René 80 in Vacuum (TRW).

REFERENCES

1. T.D. Cooper and C.A. Kelto: Fatigue and Microstructure, ASM 1979, pp. 29-30.

2. M.H. Hirschberg: Seminar at the University of Cincinnati, December 1978.

3. S.D. Antolovich: Metallurgical Aspects of High Temperature Fatigue, based on a lecture given at the International Summer School, "Fatigue in Materials and Structures" held in Sherbrooke (Quebec, Canada), 1978.

4. C.T. Sims: Journal of Metals, October 1966, pp. 1119-30.

5. J.V. Vaccari: Assoc. Ed. Materials Eng., May 1969.

6. R.F. Decker: International Nickel Company, Steel Strengthening Mechanisms Sympsium, Zurich, Switzerland, May 1969.

7. C.T. Sims and W.C. Hagel: The Superalloys, John Wiley and Sons, 1972.

8. C.D. DesForges: Revue Internationale des Houtes Temperatures et Refractaues, Vol. 14, 1977.

9. J.R. Mihalisin and D.L. Pasquine: "Phase Transformations in Nickel-Base Superalloys, International Symposium on Structural Stability in Superalloys, Seven Springs, Pa., 1968, I, p. 134.

10. O.H. Kriege and J.M. Baris: Trans. ASM 62, 1969, p. 195.

11. W.T. Loomis, The Influence of Molybdenum on the γ' Phase Formed in a Systematic Series of Experimental Nickel-Base Superalloys, Ph.D Thesis, University of Michigan, 1969.

12. R.M. Pelloux and N.J. Grant: Trans. AIME 218, 1960, p. 232.

13. E.R. Parker and T.H. Hazlett: Principles of Solution Hardening, ASM, 1954, p. 30.

14. B.E. Beeston, I.L. Dillamore and R.E. Smallman, Metal Sci. J. 2, 1968, p. 12.

15. B.E. Beeston and L.K. France, J. Inst. Metal 96, 1968, p. 105.

16. M.V. Pridanstev: Izv. Akad. Nauk SSSR, Metal., 1967, (5), p. 115.

17. H. Gleiter: Z. Metallk, 58, 1967, p. 306.

18. R.O. Williams: Acta Met., 5, 1957, p. 241.

19. H.E. Collins: Metallurgical Transactions, 1974, Vol. 5, pp. 181-204.

20. L.R. Woodyatt, C.T. Sims, and H.J. Beattie, Jr.: Transactions of the Metallurgical Society of AIME, April 1966, Vol. 236, pp. 519-526.

21. R. Blower and G. Mayer: J. Iron and Steel Inst., 1963, (London) 201, p. 933.

22. K Bungardt and G. Lennartz: Arch. Eisenhuttenwes, 1962, 33, p. 251.

23. E.G. Richards: J. Inst. Metals, 1968, 96, p. 365.

24. L.F. Coffin, Jr., S.S. Manson, A.E. Carden, L.K. Severud, W.L. Greenstreet: Time-Dependent Fatigue of Structural Alloys, Oak Ridge National Laboratory, ORNL 5073 (June 1977).

25. M. Gell, G.R. Leverant, and C.H. Wells: ASTM STP 467, American Society for Testing and Materials, 1970, pp. 113-153.

26. C.H. Wells, C.P. Sullivan, and M. Gell: ASTM STP 495, American Society for Testing and Materials, 1971, pp. 61-122.

27. L.F. Coffin, Jr.: ASTM STP 520, American Society for Testing and Materials, 1973, pp. 5-34.

28. M. Gell and G.R. Leverant: ASTM STP 520, American Society for Testing and Materials, 1973, pp. 37-67.

29. D.A. Woodford and D.F. Mowbray: Materials Science and Engineering, 1974, vol. 16, pp. 5-43.

30. R.M. Pelloux and N.S. Stoloff, Ed.: Creep-Fatigue - Environment Interactions, The Metallurgical Society of AIME, 1980.

31. L.F. Coffin, Jr.: Metal Science, Feb. 1977, pp.68-72.

32. M. Gell and G.R. Leverant: Transactions of the Metallurgical Society of AIME, 1968, Vol. 242, pp. 1869-79.

33. G.R. Leverant and M. Gell: Metallurgical Transactions A, 1975, Vol 6A, pp.367-371.

34. D. Fournier and A. Pineau: Metallurgical Transactions A, 1977, Vol. 8A, pp. 1095-1105.

35. H.F. Merrick: Metallurgical Transactions, 1974, Vol. 5, pp. 891-97.

36. M.N. Menon and W.H. Reimann: Journal of Materials Science, 1975, Vol. 10, 1571-81.

37. C.H. Wells and C.P. Sullivan: Transactions of the ASM, 1968, Vol. 61, pp. 149-155.

38. S.D. Antolovich, P. Domas, and J.L. Strudel: Metallurgical Transactions A, 1979, Vol. 10A, pp. 1859-68.

39. M. Clavel, C. Levaillant and A. Pineau: Creep-Fatigue-Environment Interactions, 1980 The Metallurgical Society of AIME, pp. 24-45.

40. H.F. Merrick, D.H. Maxwell and R.C. Gibson: ASTM STP 520, American Society for Testing and Materials, 1973, pp. 285-99.

41. D.M. Moon and G.P. Sabol: ASTM STP 520, American Society for Testing and Materials, 1973, pp. 438-50.

42. G.R. Leverant and M. Gell: Transactions of the Metallurgical Society of AIME, 1969, Vol. 245, pp. 1167-73.

43. L.F. Coffin, Jr.: Creep-Fatigue-Environment Interactions, 1980, The Metallurgical Society of AIME, pp. 1-23.

44. C.H. Wells and C.P. Sullivan: Transactions of the ASM, 1967, Vol. 600, pp. 217-22.

45. C.H. Wells and C.P. Sullivan: Transactions of the ASM, 1965, Vol. 58, pp. 391-402.

46. C.H. Wells and C.P. Sullivan: ASTM STP 459, American Society for Testing and Materials, 1969, pp. 59-74.

47. B.K. Min and R. Raj: Acta Metallurgica, 1978, Vol. 26, pp. 1007-22.

48. L.F. Coffin, Jr.: Transactions of the ASM, 1963, Vol. 56, 339-45.

49. C.J. McMahon and L.F. Coffin, Jr.: Metallurgical Transactions, 1970, Vol. 1, pp. 3443-50.

50. H. Teranishi and A.J. McEvily: Metallurgical Transactions A, 1979, Vol. 10A, pp. 1806-08.

51. L.F. Coffin, Jr.: "The Effect of Vacuum on the High Temperature Low Cycle Fatigue Behavior of Structural Metals", 1971, General Electric Report 71-C-108.

52. L.F. Coffin, Jr.: "The Effect of High Vacuum on the Low Cycle Fatigue Law", 1972, General Electric Report 72CRD005.

53. L.F. Coffin, Jr.: Metallurgical Transactions, 1974, Vol. 5, pp. 1053-60.

54. S.D. Antolovich: "Microstructural Effects and Fatigue Life Predictions of Notched and Un-notched Nickel-Base Superalloys at Elevated Temperatures", 1979, Final Report AFOSR-76-2952.

55. M.N. Menon: Journal of Materials Science, 1976, Vol. 11, pp. 984-88.

56. J.P. Dennison, P.D., Holmes, and B. Wilshire: Materials Science and Engineerfing, 1978, Vol. 33, pp. 35-47.

57. P.N. Chaku and C.J. McMahon, Jr.: Metallurgical Transactions, 1974, Vol. 5, pp. 441-50.

58. D.H. Boone and C.P. Sullivan: ASTM STP 520, American Society for Testing and Materials, 1973, pp. 401-415.

59. B. Tomkins: Phil. Mag., 1971, Vol. 23, p. 687.

60. H.D. Solomon: J. Mater., 1972, Vol. 7, p. 299.

61. H.D. Solomon and L.F. Coffin, Jr.: ASTM STP 520, American Society for Testing and Materials, 1973, p. 112.

62. J. Wareing: Metallurgical Transactions A, 1975, Vol. 6A, p. 1367.

63. Skelton: Mater. Sci. and Eng., 1978, Vol. 32., p. 211.

64. N.E. Dowling: ASTM STP 637, American Society for Testing and Materials, 1977, p. 97.

65. B. Tomkins: Phil Mag., 1968, Vol. 18, pp. 1041-66.

66. J.S. Huang and R.M. Pelloux: Metallurgical Transactions A, 1980, Vol. 11A, pp. 899-904.

67. H.D. Solomon: Metallurgical Transactions, 1973, Vol. 4, pp. 341-47.

68. J. Wareing: Metallurgical Transactions A, 1977, Vol. 8A, pp. 711-21.

69. K. Sadananda and P. Shahinian: Journal of Materials Science, 1978, Vol. 13, pp. 2347-57.

70. K. Sadananda and P. Shahinian: Metallurgical Transactions A, 1978, Vol. 9A, pp. 79-83.

71. K. Sadananda and P. Shahinian: Metallurgical Transactions A, 1977, Vol. 8A, pp. 439-49.

72. E.G. Ellison and C.P. Sullivan: Transactions of the ASM, 1968, p. 88.

73. P.L. Jones and A.S. Tetelman: Engineering Fracture Mechanics, 1979, Vo. 12, pp. 79-97.

74. H.P. Van Leeuwen: Engineering Fracture Mechanics, 1977, Vol. 9, pp. 951-74.

75. S. Floreen: Creep-Fatigue-Environmental Interactions, The Metallurgical Society of AIME, 1980, pp. 112-28.

76. L.F. Coffin, Jr.: Transactions of the ASME, 1954, Vol. 76, pp. 931-50.

77. S.S. Manson: NASA-TN-2933, 1953.

78. L.F. Coffin, Jr.: J. Mater., 1971, Vol. 6, p. 388.

79. L.F. Coffin, Jr.: ASME NPC-3, 1976, Symposium on Creep-Fatigue Interactions.

80. W.J. Ostergren: Journal of Testing and Evaluation, 1976, Vol. 4, No. 5, pp. 327-39.

81. W.J. Ostergren: ASME NPC-3, 1976, Symposium on Creep-Fatigue Interactions.

82. S. Majumdar and P.S. Maiya: ASME - NPC-3, 1976, Symposium on Creep-Fatigue Interactions.

83. G.R. Halford: In Metals Handbook, 9th ed., American Society for Metals, 1975.

84. G.R. Halford and S.S. Manson: ASTM STP 612, American Society for Testing and Materials, 1976, pp. 239-54.

85. G.R. Halford, M.H. Hirschberg and S.S. Manson: ASTM STP 520, American Society for Testing and Materials, 1973, pp. 658-69.

86. S.S. Manson: ASTM STP 520, American Society for Testing and Materials, 1973, pp. 744-82.

87. S.S. Manson and G.R. Halford: AGARDO-CP-155, NATO, Advisory Group for Aerospace Research and Development, 1974.

88. S.S. Manson and G.R. Halford: ASME-MPC-3 Symposium on Creep-Fatigue Interactions, 1976, pp. 299-322.

89. J.F. Saltsman and G.R. Halford: Transactions of the ASME, 1977, Series J 99, pp. 267-71.

90. J.F. Saltsman and G.R. Halford: ASME-MPC-3, Symposium on Creep-Fatigue Interactions, 1976, pp. 283-98.

91. K.D. Sheffler: ASTM STP 612, American Society for Testing and Materials, 1976, pp. 214-26.

92. S.D. Antolovich: TM77-565, General Electric, 1974, Schenectady, N.Y.

93. J.M. Drapier: AGARD-R-618, NATO, Advisory Group for Aerospace Research and Development, 1974.

94. C.E. Jaske, H. Mindlin, and J.S. Perrin: Proceedings of the ASTM, ASME, IME International Conference on Creep and Fatigue in Elevated Temperature Applications, 1973, pp. 23-8.

95. C.E. Jaske and R.C. Rice: ASME MPC-3, Symposium on Creep-Fatigue Interaction, 1976, pp. 101-28.

96. D.F. Mowbray and J.E. McConnelee: ASTM STP 612, American Society for Testing and Materials, 1976, pp. 10-29.

97. Characterization of Low Cycle High Temperature Fatigue by the Strainrange Partitioning Method, AGARD-CP-243, Advisory Group for Aerospace Research and Development, 1978.

98. M.H. Hirschberg: Manual on Low-Cycle Fatigue Testing, ASTM STP 465, American Society for Testing and Materials, 1969, pp. 67-86.

99. C.E. Feltner: Acta Metallurgica, 11, July 1963, pp. 817-828.

100. C.B. Coutinho, D.K. Matlock and W.L. Bradley: Materials Science and Engineering, 21, 1975, pp. 239-47.

101. W.L. Bradley, S.W. Nam and D.K. Matlock: Metallurgical Transactions, 7A, March 1976, pp. 425-30.

102. R.H. Bricknell and D.A. Woodford: Metallurgical Transactions, 12A, March 1981, pp. 425-33.

103. S.D. Antolovich: Lectures on Engineering Fracture Mechanics, University of Cincinnati.

TABLE I: CHEMICAL COMPOSITION - WT % (97)

LAB	MATERIAL	Al	Au	B	C	Co	Cb	Cb+Ta	Cr	Cu	Fe	Hf	Mo	Mn	Ni
		P	Si	S	Ta	Ti	V	W	Zr	W2	O2	N	Al+Ti		
TRW	RENE' 80	2.990	---	0.015	0.170	9.730	---	---	13.800	---	0.130	---	4.110	<0.020	BAL
NASA		---	<0.050	---	---	4.870	---	3.940	0.043	---	---	---	---		
NASA	IN100	5.450	---	0.016	0.170	15.100	---	---	10.300	---	---	---	2.960	<0.020	BAL
		---	0.110	---	---	4.760	0.970	---	0.084	---	---	---	---		
ONERA	IN100	5.500	---	0.014	0.180	15.000	---	---	10.000	---	---	---	3.000	---	BAL
		---	---	---	---	4.700	1.000	---	0.060	---	---	---	---		

Table II-1 (97)

LABORATORY: TRW
MATERIAL: RENE' 80, UNCOATED

CREEP-FATIGUE DATA

RATE DATA & STRESSES

SPEC NO	TEST TYPE	TEMP-C TEN/COMP	RATE DATA(HALF-LIFE VALUES) FREQ HZ	STRAIN-RATE-%/SEC TEN	STRAIN-RATE-%/SEC COMP	HOLD TIME-SEC TEN	HOLD TIME-SEC COMP	STRESSES(HALF-LIFE VALUES) TEN MAX	COMP MAX	RANGE MAX	RELAXATION TEN	RELAXATION COMP	SPA CYCLIC STRAIN HARDENING %
110U-PP-25	HRSC	25/25	1.0E 00	2.0E 00	2.0E 00	0	0	810.2	900.4	1710.6	0.0	0.0	--
99U-PP-14	HRSC	25/25	1.0E 00	1.3E 00	1.3E 00	0	0	628.8	545.4	1174.2	0.0	0.0	--
101U-PP-16	HRSC	204/204	1.0E 00	1.5E 00	1.5E 00	0	0	668.8	662.6	1331.4	0.0	0.0	--
102U-PP-17	HRSC	204/204	1.0E 00	1.5E 00	1.5E 00	0	0	674.3	712.3	1386.6	0.0	0.0	--
1U-PP-1	HRSC	538/538	1.0E 00	1.7E 00	1.7E 00	0	0	664.0	735.6	1399.6	0.0	0.0	--
2U-PP-2	HRSC	538/538	1.0E 00	1.5E 00	1.5E 00	0	0	568.2	615.7	1183.9	0.0	0.0	--
105U-PP-20	HRSC	649/649	1.0E 00	1.6E 00	1.6E 00	0	0	576.4	589.6	1166.0	0.0	0.0	--
107U-PP-22	HRSC	649/649	1.0E 00	1.3E 00	1.3E 00	0	0	495.7	444.8	940.5	0.0	0.0	--
104U-PP-19	HRSC	760/760	1.0E 00	1.6E 00	1.6E 00	0	0	536.4	568.2	1104.6	0.0	0.0	--
103U-PP-18	HRSC	760/760	1.0E 00	1.2E 00	1.2E 00	0	0	424.1	388.2	812.3	0.0	0.0	--
74-U-PP-13	HRSC	871/871	1.0E 00	2.5E 00	2.5E 00	0	0	521.2	510.2	1031.4	0.0	0.0	--
21U-PP-8	HRSC	871/871	1.0E 00	1.7E 00	1.7E 00	0	0	417.2	413.7	830.9	0.0	0.0	--
41U-PP-10	HRSC	871/871	1.0E 00	1.3E 00	1.3E 00	0	0	350.9	357.1	708.0	0.0	0.0	--
22U-PP-9	HRSC	871/871	1.0E 00	4.8E-01	4.8E-01	0	0	180.7	156.5	337.2	0.0	0.0	--
42U-PP-11	HRSC	871/871	1.0E 00	5.9E-01	5.9E-01	0	0	162.1	222.0	384.1	0.0	0.0	--
6U-PP-5	HRSC	1000/1000	1.0E 00	2.5E 00	2.5E 00	0	0	278.6	243.4	522.0	0.0	0.0	--
4U-PP-3	HRSC	1000/1000	1.0E 00	1.9E 00	1.9E 00	0	0	279.3	264.8	544.1	0.0	0.0	--
109U-PP-24	HRSC	1000/1000	1.0E 00	1.2E 00	1.2E 00	0	0	210.9	192.4	403.3	0.0	0.0	--
7U-PP-6	HRSC	1000/1000	1.0E 00	1.1E 00	1.1E 00	0	0	191.0	191.0	382.0	0.0	0.0	--
108U-PP-23	HRSC	1000/1000	1.0E 00	6.8E-01	6.8E-01	0	0	156.5	137.9	294.4	0.0	0.0	--
5U-PP-4	HRSC	1000/1000	1.0E 00	5.5E-01	5.5E-01	0	0	92.4	84.1	176.5	0.0	0.0	--
8U-PP-7	HRSC	1000/1000	1.0E 00	4.9E-01	4.9E-01	0	0	117.2	124.8	242.0	0.0	0.0	--
92U-PC-13	CCCR	871/871	1.0E-02	--	--	0	97.0	553.7	246.1	799.8	0.0	0.0	--
26U-PC-9	CCCR	871/871	1.4E-02	--	--	0	71.0	519.9	231.0	750.9	0.0	0.0	--
91U-PC-12	CCCR	871/871	1.7E-02	--	--	0	60.0	438.5	194.7	633.2	0.0	0.0	--
96U-PC-16	CCCR	871/871	2.6E-03	--	--	0	389.0	390.2	147.6	537.8	0.0	0.0	--
29U-PC-10	CCCR	871/871	5.3E-02	--	--	0	19.0	168.3	29.0	197.3	0.0	0.0	--
10U-PC-2	CCCR	1000/1000	5.3E-03	--	--	0	190.0	478.6	159.3	637.9	0.0	0.0	--
12U-PC-4	CCCR	1000/1000	4.2E-03	--	--	0	240.0	490.2	151.7	641.9	0.0	0.0	--
89U-PC-11	CCCR	1000/1000	1.1E-02	--	--	0	94.0	270.3	103.4	373.7	0.0	0.0	--
94U-PC-14	CCCR	1000/1000	2.0E-02	--	--	0	50.0	239.2	115.2	354.4	0.0	0.0	--
9U-PC-1	CCCR	1000/1000	3.5E-02	--	--	0	29.0	226.8	48.3	275.1	0.0	0.0	--
97U-PC-15	CCCR	1000/1000	2.0E-02	--	--	0	49.0	188.3	72.4	260.7	0.0	0.0	--
23U-PC-6	CCCR	1000/1000	1.6E-01	--	--	0	6.2	176.5	78.6	255.1	0.0	0.0	--
26U-PC-8	CCCR	1000/1000	1.5E-01	--	--	0	6.8	195.9	48.3	244.2	0.0	0.0	--
112U-CP-11	TCCR	871/871	1.6E-02	--	--	64.0	0	284.8	519.2	804.0	0.0	0.0	--
86U-CP-9	TCCR	871/871	1.2E-02	--	--	83.0	0	216.5	474.3	690.8	0.0	0.0	--
30U-CP-5	TCCR	871/871	4.1E-02	--	--	24.0	0	251.0	451.0	702.0	0.0	0.0	--
31U-CP-6	TCCR	871/871	3.1E-02	--	--	32.0	0	193.1	402.7	595.8	0.0	0.0	--
36U-CP-7	TCCR	871/871	1.6E-02	--	--	62.3	0	128.2	269.9	397.1	0.0	0.0	--
14U-CP-1	TCCR	1000/1000	6.7E-03	--	--	150.0	0	201.3	271.2	472.5	0.0	0.0	--
111U-CP-10	TCCR	1000/1000	2.2E-02	--	--	46.0	0	128.2	226.1	354.3	0.0	0.0	--
39U-CP-8	TCCR	1000/1000	1.7E-02	--	--	59.0	0	98.6	180.0	278.6	0.0	0.0	--
16U-CP-3	TCCR	1000/1000	2.2E-02	--	--	46.0	0	128.2	175.2	303.4	0.0	0.0	--

LABORATORY: TRW
MATERIAL: RENE' 80, UNCOATED

Table II-2[97]
CREEP-FATIGUE DATA (CONTINUED)

STRAINS & FAILURE DATA

SPEC NO	STRAINRANGES (HALF-LIFE VALUES) % TOTAL	PL	IN	PR	PC	CP	CC	FAILURE DATA-CICLES NO	NI	N5	NF	TF-HRS
110U-PP-25	0.979	0.828	0.151	0.151	0.000	0.000	0.000	--	--	--	1306	0.50
99U-PP-14	0.639	0.568	0.071	0.071	0.000	0.000	0.000	--	--	--	6900	2.00
101U-PP-16	0.741	0.667	0.074	0.074	0.000	0.000	0.000	--	--	--	1674	0.50
102U-PP-17	0.769	0.698	0.071	0.071	0.000	0.000	0.000	--	--	--	2170	0.60
1U-PP-1	0.874	0.773	0.101	0.101	0.000	0.000	0.000	--	--	--	1621	0.60
2U-PP-2	0.747	0.654	0.093	0.093	0.000	0.000	0.000	--	--	--	1950	0.50
105U-PP-20	0.784	0.669	0.115	0.115	0.000	0.000	0.000	--	--	--	744	0.20
107U-PP-22	0.642	0.539	0.103	0.103	0.000	0.000	0.000	--	--	--	4402	1.30
104U-PP-19	0.792	0.663	0.129	0.129	0.000	0.000	0.000	--	--	--	496	0.10
103U-PP-18	0.604	0.488	0.116	0.116	0.000	0.000	0.000	--	--	--	4216	1.20
74-U-PP-13	1.262	0.657	0.605	0.605	0.000	0.000	0.000	--	--	--	145	0.04
21U-PP-8	0.851	0.529	0.322	0.322	0.000	0.000	0.000	--	--	--	642	0.20
41U-PP-10	0.630	0.451	0.179	0.179	0.000	0.000	0.000	--	--	--	1410	0.40
22U-PP-9	0.241	0.215	0.026	0.026	0.000	0.000	0.000	--	--	--	163533	44.00
42U-PP-11	0.296	0.245	0.051	0.051	0.000	0.000	0.000	--	--	--	217620	59.50
6U-PP-5	1.250	0.363	0.887	0.887	0.000	0.000	0.000	--	--	--	103	0.02
4U-PP-3	0.944	0.378	0.566	0.566	0.000	0.000	0.000	--	--	--	306	0.10
109U-PP-24	0.576	0.280	0.296	0.296	0.000	0.000	0.000	--	--	--	1240	0.30
7U-PP-6	0.561	0.265	0.296	0.296	0.000	0.000	0.000	--	--	--	2298	0.60
108U-PP-23	0.343	0.204	0.139	0.139	0.000	0.000	0.000	--	--	--	5766	1.50
5U-PP-4	0.277	0.122	0.055	0.055	0.000	0.000	0.000	--	--	--	6302	1.70
8U-PP-7	0.247	0.169	0.078	0.078	0.000	0.000	0.000	--	--	--	22115	5.90
92U-PC-13	1.064	0.510	0.554	0.094	0.460	0.000	0.000	--	--	--	41	1.10
28U-PC-9	0.856	0.478	0.378	0.095	0.283	0.000	0.000	--	--	--	148	2.90
91U-PC-12	0.659	0.402	0.257	0.048	0.209	0.000	0.000	--	--	--	356	5.90
98U-PC-16	0.601	0.343	0.258	0.075	0.183	0.000	0.000	--	--	--	396	42.50
29U-PC-10	0.330	0.126	0.204	0.040	0.164	0.000	0.000	--	--	--	1415	7.40
10U-PC-2	1.999	0.443	1.556	0.218	1.338	0.000	0.000	--	--	--	19	1.00
12U-PC-4	1.809	0.445	1.364	0.109	1.255	0.000	0.000	--	--	--	30	2.00
89U-PC-11	0.579	0.259	0.319	0.048	0.271	0.000	0.000	--	--	--	187	4.90
94U-PC-14	0.464	0.246	0.218	0.031	0.187	0.000	0.000	--	--	--	418	5.80
9U-PC-1	0.944	0.191	0.753	0.038	0.715	0.000	0.000	--	--	--	479	3.30
97U-PC-15	0.292	0.181	0.111	0.022	0.089	0.000	0.000	--	--	--	1978	25.30
23U-PC-6	0.386	0.177	0.209	0.015	0.194	0.000	0.000	--	--	--	9810	15.30
26U-PC-8	0.409	0.169	0.240	0.023	0.217	0.000	0.000	--	--	--	10164	19.10
112U-CP-11	0.907	0.512	0.385	0.077	0.000	0.308	0.000	--	--	--	101	1.30
86U-CP-9	0.772	0.440	0.332	0.026	0.000	0.306	0.000	--	--	--	147	3.40
30U-CP-5	0.736	0.447	0.289	0.035	0.000	0.254	0.000	--	--	--	193	1.30
31U-CP-6	0.588	0.380	0.208	0.006	0.000	0.202	0.000	--	--	--	530	4.70
36U-CP-7	0.364	0.253	0.111	0.019	0.000	0.092	0.000	--	--	--	3705	64.10
14U-CP-1	1.595	0.328	1.267	0.280	0.000	0.987	0.000	--	--	--	12	0.50
111U-CP-10	0.957	0.246	0.711	0.178	0.000	0.533	0.000	--	--	--	79	1.00
39U-CP-8	0.436	0.193	0.243	0.016	0.000	0.227	0.000	--	--	--	527	3.60
16U-CP-3	0.589	0.211	0.378	0.114	0.000	0.264	0.000	--	--	--	601	7.60

Table II-3[97]

CREEP-FATIGUE DATA (CONTINUED)

LABORATORY: TRW
MATERIAL: RENE' 80, UNCOATED

RATE DATA & STRESSES

SPEC	TEST	TEMP-C	RATE DATA (HALF-LIFE VALUES) FREQ	STRAIN-RATE-%/SEC	HOLD TIME-SEC		STRESSES (HALF-LIFE VALUES) MPA TEN	COMP	RANGE	RELAXATION	CYCLIC	STRAIN
17U-CP-4	TCCR	1000/1000	4.5E-02	--	--	22.0	0	80.0	163.4	243.4	0.0	0.0	--
71U-CC-7	UCCR	871/871	4.5E-03	--	--	110.0	110.0	351.0	285.5	636.5	0.0	0.0	--
73U-CC-8	UCCR	871/871	4.4E-03	--	--	110.0	110.0	344.7	320.7	665.4	0.0	0.0	--
76U-CC-9	UCCR	871/871	2.6E-03	--	--	190.0	190.0	289.0	245.4	534.4	0.0	0.0	--
120U-CC-12	UCCR	871/871	7.6E-03	--	--	66.0	66.0	213.0	206.1	419.1	0.0	0.0	--
79U-CC-10	UCCR	871/871	3.3E-03	--	--	150.0	150.0	222.7	189.7	412.4	0.0	0.0	--
119U-CC-11	UCCR	1000/1000	7.4E-03	--	--	68.0	68.0	186.9	174.5	361.4	0.0	0.0	--
67U-CC-6	UCCR	1000/1000	2.9E-03	--	--	170.0	170.0	80.7	53.8	134.5	0.0	0.0	--
19U-CC-3	UCCR	1000/1000	2.3E-03	--	--	220.0	220.0	128.9	100.0	228.9	0.0	0.0	--
40U-CC-5	UCCR	1000/1000	8.7E-03	--	--	38.0	76.0	100.7	68.3	169.0	0.0	0.0	--
20U-CC-4	UCCR	1000/1000	3.2E-02	--	--	16.0	16.0	85.5	56.5	142.0	0.0	0.0	--

LABORATORY: TRW
MATERIAL: RENE' 80, UNCOATED

STRAINS & FAILURE DATA

SPEC NO	STRAINRANGES (HALF-LIFE VALUES) % TOTAL	EL	IN	PP	PC	CP	CC	FAILURE DATA-CICLES NO	NI	N5	NF	TF-HRS
17U-CP-4	0.409	0.169	0.240	0.030	0.000	0.210	0.000	--	--	--	1385	8.60
71U-CC-7	1.368	0.405	0.963	0.241	0.067	0.000	0.655	--	--	--	25	1.60
73U-CC-8	1.193	0.424	0.769	0.085	0.084	0.000	0.600	--	--	--	35	2.20
76U-CC-9	0.784	0.340	0.444	0.013	0.031	0.000	0.400	--	--	--	166	17.60
120U-CC-12	0.622	0.267	0.355	0.071	0.007	0.000	0.277	--	--	--	181	6.60
79U-CC-10	0.507	0.263	0.244	0.029	0.010	0.000	0.205	--	--	--	637	53.10
119U-CC-11	0.973	0.251	0.722	0.079	0.029	0.000	0.614	--	--	--	69	2.60
67U-CC-6	0.599	0.093	0.506	0.101	0.025	0.000	0.380	--	--	--	257	24.80
19U-CC-3	0.457	0.159	0.298	0.060	0.029	0.000	0.209	--	--	--	420	51.00
40U-CC-5	0.273	0.118	0.155	0.031	0.008	0.000	0.116	--	--	--	4783	152.60
20U-CC-4	0.233	0.099	0.134	0.013	0.007	0.000	0.114	--	--	--	8154	70.50

Table II-4[97]

CREEP-FATIGUE DATA (CONTINUED)

LABORATORY: TRW
MATERIAL: RENE' 80, COATED

RATE DATA & STRESSES

SPEC NO	TEST TYPE	TEMP-C TEN/COMP	RATE DATA (HALF-LIFE VALUES) FREQ HZ	STRAIN-RATE-%/SEC TEN	STRAIN-RATE-%/SEC COMP	HOLD TIME-SEC TEN	HOLD TIME-SEC COMP	STRESSES (HALF-LIFE VALUES) MPA TEN MAX	COMP MAX	RANGE MAX	RELAXATION TEN	RELAXATION COMP	CYCLIC STRAIN HARDENING %
77C-PP-11	HRSC	871/871	1.0E 00	2.0E 00	2.0E 00	0	0	452.3	441.3	893.6	0.0	0.0	--
52C-PP-7	HRSC	871/871	1.0E 00	1.5E 00	1.5E 00	0	0	409.6	394.4	804.0	0.0	0.0	--
51C-PP-6	HRSC	871/871	1.0E 00	1.3E 00	1.3E 00	0	0	355.1	355.1	710.2	0.0	0.0	--
54C-PP-8	HRSC	871/871	1.0E 00	8.2E-01	8.2E-01	0	0	231.0	277.2	508.2	0.0	0.0	--
55C-PP-9	HRSC	871/871	1.0E 00	3.8E-01	3.8E-01	0	0	112.4	113.1	225.5	0.0	0.0	--
75C-PP-10	HRSC	1000/1000	1.0E 00	1.9E 00	1.9E 00	0	0	285.5	273.7	559.2	0.0	0.0	--
45C-PP-3	HRSC	1000/1000	1.0E 00	9.8E-01	9.8E-01	0	0	178.6	177.2	355.8	0.0	0.0	--
47C-PP-4	HRSC	1000/1000	1.0E 00	6.9E-01	6.9E-01	0	0	128.9	126.2	255.1	0.0	0.0	--
49C-PP-5	HRSC	1000/1000	1.0E 00	4.5E-01	4.5E-01	0	0	116.5	113.1	229.6	0.0	0.0	--
43C-PP-1	HRSC	1000/1000	1.0E 00	3.0E-01	3.0E-01	0	0	71.7	74.4	146.1	0.0	0.0	--
90C-PC-7	CCCR	871/871	5.1E-03	--	--	0	195.0	566.8	233.7	800.5	0.0	0.0	--
59C-PC-4	CCCR	871/871	1.0E-02	--	--	0	103.0	628.8	210.3	839.1	0.0	0.0	--
95C-PC-9	CCCR	871/871	1.3E-02	--	--	0	80.0	493.6	233.0	726.6	0.0	0.0	--
61C-PC-5	CCCR	871/871	1.2E-02	--	--	0	84.0	520.1	232.3	752.4	0.0	0.0	--
88C-PC-6	CCCR	871/871	7.8E-03	--	--	0	128.0	326.2	193.1	519.3	0.0	0.0	--
56C-PC-1	CCCR	1000/1000	1.5E-02	--	--	0	65.0	348.2	153.8	502.0	0.0	0.0	--
58C-PC-3	CCCR	1000/1000	1.7E-02	--	--	0	59.0	297.2	117.2	414.4	0.0	0.0	--
96C-PC-10	CCCR	1000/1000	1.3E-02	--	--	0	77.0	282.7	133.1	415.8	0.0	0.0	--
57C-PC-2	CCCR	1000/1000	1.3E-02	--	--	0	76.0	242.0	106.2	348.2	0.0	0.0	--
93C-PC-8	CCCR	1000/1000	4.7E-03	--	--	0	215.0	304.8	66.2	371.0	0.0	0.0	--
84C-CP-6	TCCR	871/871	5.4E-03	--	--	190.0	0	358.5	608.1	966.6	0.0	0.0	--
115C-CP-11	TCCR	871/871	2.1E-02	--	--	47.0	0	340.6	495.7	836.3	0.0	0.0	--
62C-CP-1	TCCR	871/871	1.5E-02	--	--	65.0	0	275.8	505.4	781.2	0.0	0.0	--
83C-CP-5	TCCR	871/871	1.0E-02	--	--	95.7	0	198.0	530.9	728.9	0.0	0.0	--
64C-CP-2	TCCR	871/871	1.5E-02	--	--	66.5	0	240.6	322.0	562.6	0.0	0.0	--
113C-CP-9	TCCR	1000/1000	2.5E-02	--	--	40.0	0	200.0	330.3	530.3	0.0	0.0	--
66C-CP-4	TCCR	1000/1000	1.8E-02	--	--	55.0	0	171.0	344.7	515.7	0.0	0.0	--
85C-CP-7	TCCR	1000/1000	8.3E-03	--	--	120.0	0	145.5	205.4	350.9	0.0	0.0	--
65C-CP-3	TCCR	1000/1000	1.8E-02	--	--	55.0	0	115.8	293.7	409.5	0.0	0.0	--
87C-CP-8	TCCR	1000/1000	4.3E-02	--	--	23.0	0	124.1	197.2	321.3	0.0	0.0	--
72C-CC-3	UCCR	871/871	3.7E-03	--	--	140.0	140.0	446.1	406.8	852.9	0.0	0.0	--
69C-CC-2	UCCR	871/871	5.0E-03	--	--	100.0	100.0	341.9	317.2	659.1	0.0	0.0	--
78C-CC-4	UCCR	871/871	4.5E-03	--	--	110.0	110.0	347.5	301.3	648.8	0.0	0.0	--
80C-CC-5	UCCR	871/871	2.6E-03	--	--	200.0	200.0	333.0	300.6	633.6	0.0	0.0	--
118C-CC-10	UCCR	871/871	4.9E-03	--	--	100.0	100.0	263.4	232.3	495.7	0.0	0.0	--
68C-CC-1	UCCR	1000/1000	4.3E-03	--	--	160.0	80.0	208.9	179.3	388.2	0.0	0.0	--
81C-CC-6	UCCR	1000/1000	5.6E-03	--	--	90.0	90.0	178.6	150.3	328.9	0.0	0.0	--
116C-CC-8	UCCR	1000/1000	5.1E-03	--	--	100.0	100.0	195.5	148.9	344.8	0.0	0.0	--
117C-CC-9	UCCR	1000/1000	5.2E-03	--	--	130.0	60.0	160.7	141.4	302.1	0.0	0.0	--
82C-CC-7	UCCR	1000/1000	4.0E-03	--	--	120.0	120.0	155.2	120.7	275.9	0.0	0.0	--

Table II-5[97]

CREEP-FATIGUE DATA (CONTINUED)

LABORATORY: TRW
MATERIAL: RENE' 80, COATED

STRAINS & FAILURE DATA

SPEC NO	STRAINRANGES (HALF-LIFE VALUES) % TOTAL	EL	IN	PP	PC	CP	CC	FAILURE DATA-CYCLES NO	NI	NS	NF	TF-HRS
77C-PP-11	1.011	0.569	0.442	0.442	0.000	0.000	0.000	--	--	--	293	0.10
52C-PP-7	0.742	0.512	0.230	0.230	0.000	0.000	0.000	--	--	--	1365	0.40
51C-PP-6	0.672	0.452	0.220	0.220	0.000	0.000	0.000	--	--	--	1860	0.50
54C-PP-8	0.410	0.324	0.086	0.086	0.000	0.000	0.000	--	--	--	71982	19.40
55C-PP-9	0.191	0.145	0.046	0.046	0.000	0.000	0.000	--	--	--	426870	114.50
75C-PP-10	0.961	0.388	0.573	0.573	0.000	0.000	0.000	--	--	--	233	0.10
45C-PP-3	0.490	0.247	0.243	0.243	0.000	0.000	0.000	--	--	--	2188	0.60
47C-PP-4	0.343	0.177	0.166	0.166	0.000	0.000	0.000	--	--	--	9412	2.50
49C-PP-5	0.225	0.159	0.066	0.066	0.000	0.000	0.000	--	--	--	101184	27.20
43C-PP-1	0.152	0.101	0.051	0.051	0.000	0.000	0.000	--	--	--	206460	55.50
90C-PC-7	1.055	0.510	0.545	0.088	0.457	0.000	0.000	--	--	--	48	2.60
59C-PC-4	1.107	0.535	0.572	0.114	0.458	0.000	0.000	--	--	--	63	1.90
95C-PC-9	0.835	0.463	0.372	0.033	0.339	0.000	0.000	--	--	--	126	2.80
61C-PC-5	0.774	0.480	0.294	0.042	0.252	0.000	0.000	--	--	--	282	6.60
88C-PC-6	0.485	0.331	0.154	0.031	0.123	0.000	0.000	--	--	--	1855	66.00
56C-PC-1	0.819	0.348	0.471	0.132	0.339	0.000	0.000	--	--	--	55	1.00
58C-PC-3	0.581	0.288	0.293	0.038	0.255	0.000	0.000	--	--	--	240	3.90
96C-PC-10	0.585	0.289	0.296	0.044	0.252	0.000	0.000	--	--	--	262	5.50
57C-PC-2	0.450	0.242	0.208	0.019	0.189	0.000	0.000	--	--	--	386	9.20
93C-PC-8	0.424	0.257	0.167	0.025	0.142	0.000	0.000	--	--	--	691	41.20
84C-CP-6	1.145	0.616	0.529	0.096	0.000	0.433	0.000	--	--	--	29	1.50
115C-CP-11	0.907	0.533	0.374	0.034	0.000	0.340	0.000	--	--	--	77	1.00
62C-CP-1	0.995	0.498	0.497	0.040	0.000	0.457	0.000	--	--	--	150	2.70
83C-CP-5	0.709	0.464	0.245	0.035	0.000	0.210	0.000	--	--	--	455	12.10
64C-CP-2	0.490	0.358	0.132	0.016	0.000	0.116	0.000	--	--	--	1818	33.60
113C-CP-9	1.023	0.368	0.655	0.164	0.000	0.491	0.000	--	--	--	45	0.50
66C-CP-4	0.966	0.358	0.608	0.110	0.000	0.498	0.000	--	--	--	66	1.00
85C-CP-7	0.568	0.244	0.324	0.074	0.000	0.250	0.000	--	--	--	134	4.50
65C-CP-3	0.603	0.284	0.319	0.045	0.000	0.274	0.000	--	--	--	251	3.90
87C-CP-8	0.422	0.223	0.199	0.030	0.000	0.169	0.000	--	--	--	950	6.20
72C-CC-3	1.377	0.543	0.834	0.125	0.050	0.000	0.659	--	--	--	33	2.50
69C-CC-2	1.005	0.420	0.585	0.099	0.059	0.000	0.427	--	--	--	108	6.00
78C-CC-4	0.917	0.413	0.504	0.071	0.085	0.000	0.348	--	--	--	109	6.70
80C-CC-5	0.824	0.404	0.420	0.017	0.000	0.013	0.390	--	--	--	171	10.60
118C-CC-10	0.582	0.316	0.266	0.050	0.016	0.000	0.200	--	--	--	544	31.70
68C-CC-1	1.135	0.269	0.865	0.069	0.060	0.000	0.736	--	--	--	17	1.10
81C-CC-6	0.790	0.228	0.562	0.045	0.133	0.000	0.384	--	--	--	76	3.80
116C-CC-8	0.754	0.239	0.515	0.031	0.000	0.026	0.458	--	--	--	77	4.20
117C-CC-9	0.555	0.210	0.345	0.069	0.017	0.000	0.259	--	--	--	225	12.00
82C-CC-7	0.445	0.191	0.254	0.015	0.016	0.000	0.223	--	--	--	621	42.30

Table II-6[97]

CREEP-FATIGUE DATA (CONTINUED)

LABORATORY: NASA
MATERIAL: RENE80, UNCOATED, TESTED IN AIR

RATE DATA & STRESSES

SPEC NO	TEST TYPE	TEMP-C TEN/COMP	RATE DATA (HALF-LIFE VALUES) FREQ HZ	STRAIN-RATE-%/SEC TEN	STRAIN-RATE-%/SEC COMP	HOLD TIME-SEC TEN	HOLD TIME-SEC COMP	STRESSES (HALF-LIFE VALUES) MPA TEN MAX	COMP MAX	RANGE MAX	RELAXATION TEN	RELAXATION COMP	CYCLIC STRAIN HARDENING %
REE205	HRSC	1000/1000	1.0E 00	--	--	0	0	420.9	420.9	841.8	0.0	0.0	--
REE215	HRSC	1000/1000	1.0E 00	--	--	0	0	370.9	370.9	741.8	0.0	0.0	--
REE206	HRSC	1000/1000	1.0E 00	--	--	0	0	358.2	358.2	716.4	0.0	0.0	--
REE204	HRSC	1000/1000	1.0E 00	--	--	0	0	206.2	206.2	412.4	0.0	0.0	--
REE200	CCCR	1000/1000	6.8E-05	--	--	0	--	467.1	179.3	646.4	0.0	0.0	--
REE219	CCCR	1000/1000	7.0E-04	--	--	0	--	355.0	136.0	491.0	0.0	0.0	--
REE213	CCCR	1000/1000	9.9E-04	--	--	0	--	321.7	179.5	501.2	0.0	0.0	--
REE210	CCCR	1000/1000	7.6E-03	--	--	0	--	183.3	119.7	303.0	0.0	0.0	--
REE223	TCCR	1000/1000	6.4E-05	--	--	--	0	127.7	405.7	533.4	0.0	0.0	--
REE208	TCCR	1000/1000	5.4E-04	--	--	--	0	172.6	341.4	514.0	0.0	0.0	--
REE201	TCCR	1000/1000	5.5E-04	--	--	--	0	172.0	276.7	448.7	0.0	0.0	--
REE221	TCCR	1000/1000	4.2E-03	--	--	--	0	110.4	250.2	360.6	0.0	0.0	--
REE220	TCCR	1000/1000	2.2E-02	--	--	--	0	89.0	225.6	314.6	0.0	0.0	--
REE211	BCCR	1000/1000	1.8E-03	--	--	--	--	244.1	244.1	488.3	0.0	0.0	--
REE212	BCCR	1000/1000	6.2E-04	--	--	--	--	157.8	135.2	293.0	0.0	0.0	--
REE217	BCCR	1000/1000	9.2E-03	--	--	--	--	156.3	112.7	269.0	0.0	0.0	--

STRAINS & FAILURE DATA

SPEC NO	STRAINRANGES (HALF-LIFE VALUES) % TOTAL	EL	IN	PP	PC	CP	CC	FAILURE DATA-CICLES NO	NI	N5	NF	TF-HRS
REE205	1.525	0.656	0.869	0.869	0.000	0.000	0.000	--	42	30	42	0.01
REE215	1.557	0.578	0.979	0.979	0.000	0.000	0.000	--	55	27	55	0.01
REE206	0.989	0.558	0.431	0.431	0.000	0.000	0.000	--	177	152	202	0.06
REE204	0.410	0.321	0.089	0.089	0.000	0.000	0.000	--	4890	4890	9226	2.46
REE200	2.612	0.504	2.108	0.222	1.866	0.000	0.000	--	--	--	10	40.75
REE219	1.007	0.383	0.624	0.268	0.356	0.000	0.000	--	--	--	63	23.53
REE213	0.916	0.391	0.525	0.258	0.267	0.000	0.000	--	--	--	130	36.64
REE210	0.339	0.237	0.102	0.031	0.071	0.000	0.000	--	--	--	3980	145.00
REE223	1.472	0.416	1.056	0.299	0.000	0.757	0.000	--	--	--	13	56.00
REE208	1.098	0.400	0.698	0.218	0.000	0.480	0.000	--	--	--	35	17.97
REE201	0.927	0.350	0.577	0.195	0.000	0.382	0.000	--	--	--	70	35.63
REE221	0.534	0.281	0.253	0.089	0.000	0.164	0.000	--	--	--	416	27.26
REE220	0.354	0.245	0.109	0.055	0.000	0.054	0.000	--	--	--	1600	19.85
REE211	2.214	0.381	1.833	0.276	0.000	0.000	1.557	--	--	--	10	1.56
REE212	0.531	0.228	0.303	0.071	0.000	0.000	0.232	--	--	--	191	85.10
REE217	0.461	0.211	0.250	0.067	0.000	0.000	0.183	--	--	--	548	16.60

Table II-7[97]

CREEP-FATIGUE DATA (CONTINUED)

LABORATORY: NASA
MATERIAL: RENE80, COATED, TESTED IN AIR

RATE DATA & STRESSES

SPEC NO	TEST TYPE	TEMP-C TEN/COMP	RATE DATA(HALF-LIFE VALUES) FREQ HZ	STRAIN-RATE-%/SEC TEN	STRAIN-RATE-%/SEC COMP	HOLD TIME-SEC TEN	HOLD TIME-SEC COMP	STRESSES(HALF-LIFE VALUES) MPA TEN MAX	COMP MAX	RANGE MAX	RELAXATION TEN	RELAXATION COMP	CYCLIC STRAIN HARDENING %
REE322	HRSC	1000/1000	1.0E 00	--	--	0	0	481.5	481.5	963.0	0.0	0.0	--
REE317	HRSC	1000/1000	1.0E 00	--	--	0	0	394.6	394.6	789.2	0.0	0.0	--
REE310	HRSC	1000/1000	1.0E 00	--	--	0	0	440.4	440.4	880.8	0.0	0.0	--
REE304	HRSC	1000/1000	1.0E 00	--	--	0	0	375.2	375.2	750.4	0.0	0.0	--
REE306	HRSC	1000/1000	1.0E 00	--	--	0	0	298.6	298.6	597.2	0.0	0.0	--
REE300	HRSC	1000/1000	1.0E 00	--	--	0	0	239.5	239.5	479.0	0.0	0.0	--
REE323	HRSC	1000/1000	1.0E 00	--	--	0	0	198.2	198.2	396.4	0.0	0.0	--
REE311	HRSC	1000/1000	1.0E 00	--	--	0	0	178.2	178.2	356.4	0.0	0.0	--
REE312	CCCR	1000/1000	5.0E-04	--	--	0	--	365.6	178.1	543.7	0.0	0.0	--
REE301	CCCR	1000/1000	2.2E-03	--	--	0	--	323.5	172.7	496.2	0.0	0.0	--
REE303	CCCR	1000/1000	3.4E-03	--	--	0	--	234.1	84.8	318.9	0.0	0.0	--
REE328	CCCR	1000/1000	1.3E-01	--	--	0	--	210.1	77.3	287.4	0.0	0.0	--
REE315	TCCR	1000/1000	9.1E-04	--	--	--	0	169.1	353.2	522.3	0.0	0.0	--
REE305	TCCR	1000/1000	1.1E-03	--	--	--	0	152.9	349.9	502.8	0.0	0.0	--
REE308	TCCR	1000/1000	1.9E-03	--	--	--	0	100.0	298.7	398.7	0.0	0.0	--
REE302	TCCR	1000/1000	1.1E-03	--	--	--	0	90.3	210.6	300.9	0.0	0.0	--
REE309	BCCR	1000/1000	5.4E-04	--	--	--	--	203.1	236.9	440.0	0.0	0.0	--
REE316	BCCR	1000/1000	4.9E-04	--	--	--	--	169.1	165.3	334.4	0.0	0.0	--
REE313	BCCR	1000/1000	2.6E-03	--	--	--	--	115.9	136.1	252.0	0.0	0.0	--
REE314	BCCR	1000/1000	4.8E-02	--	--	--	--	103.4	118.3	221.7	0.0	0.0	--

Table II-8[97]

CREEP-FATIGUE DATA (CONTINUED)

LABORATORY: NASA
MATERIAL: RENE80, COATED, TESTED IN AIR

STRAINS & FAILURE DATA

SPEC	STRAINRANGES(HALF-LIFE VALUES) %							FAILURE DATA-CYCLES				
NO	TOTAL	EL	IN	PP	PC	CP	CC	NO	NI	N5	NF	TF-HRS
REE322	1.917	0.751	1.166	1.166	0.000	0.000	0.000	--	43	24	43	0.01
REE317	1.091	0.615	0.476	0.476	0.000	0.000	0.000	--	69	69	69	0.02
REE310	1.399	0.687	0.712	0.712	0.000	0.000	0.000	--	65	58	85	0.02
REE304	1.101	0.585	0.516	0.516	0.000	0.000	0.000	--	93	93	93	0.03
REE306	0.696	0.465	0.231	0.231	0.000	0.000	0.000	--	99	76	650	0.18
REE300	0.515	0.385	0.130	0.130	0.000	0.000	0.000	--	1666	640	1666	0.46
REE323	0.397	0.309	0.088	0.088	0.000	0.000	0.000	--	2228	2228	3820	1.06
REE311	0.324	0.278	0.046	0.046	0.000	0.000	0.000	--	6715	6970	15000	4.28
REE312	2.410	0.424	1.986	0.330	1.656	0.000	0.000	--	--	--	24	13.20
REE301	1.007	0.387	0.620	0.228	0.392	0.000	0.000	--	--	--	159	20.47
REE303	0.387	0.248	0.139	0.063	0.076	0.000	0.000	--	--	--	1200	97.25
REE328	0.312	0.224	0.088	0.044	0.044	0.000	0.000	--	--	--	1900	4.10
REE315	1.369	0.407	0.962	0.238	0.000	0.724	0.000	--	--	--	14	4.25
REE305	1.022	0.392	0.630	0.134	0.000	0.496	0.000	--	--	--	48	11.58
REE308	0.631	0.311	0.320	0.088	0.000	0.232	0.000	--	--	--	432	63.47
REE302	0.337	0.235	0.102	0.058	0.000	0.044	0.000	--	--	--	3928	45.45
REE309	2.133	0.343	1.790	0.342	0.000	0.000	1.448	--	--	--	11	5.52
REE316	0.984	0.261	0.723	0.141	0.000	0.036	0.546	--	--	--	36	20.44
REE313	0.492	0.197	0.295	0.035	0.000	0.000	0.260	--	--	--	620	65.23
REE314	0.266	0.173	0.093	0.011	0.000	0.000	0.082	--	--	--	4457	25.92

Table II-9[97]

CREEP-FATIGUE DATA (CONTINUED)

LABORATORY: NASA
MATERIAL: IN-100, CAST

RATE DATA & STRESSES

SPEC NO	TEST TYPE	TEMP-C TEN/COMP	RATE DATA (HALF-LIFE VALUES) FREQ HZ	STRAIN-RATE-%/SEC TEN	STRAIN-RATE-%/SEC COMP	HOLD TIME-SEC TEN	HOLD TIME-SEC COMP	STRESSES (HALF-LIFE VALUES) MPA TEN MAX	COMP MAX	RANGE MAX	RELAXATION TEN	RELAXATION COMP	CYCLIC STRAIN HARDENING %
INN-2	HRSC	925/925	5.0E-01	--	--	0	0	736.0	774.0	1510.0	0.0	0.0	--
INN-32	HRSC	925/925	5.0E-01	--	--	0	0	573.6	619.2	1192.8	0.0	0.0	--
INN-3	HRSC	925/925	5.0E-01	--	--	0	0	483.0	520.0	1003.0	0.0	0.0	--
INN-17	HRSC	925/925	5.0E-01	--	--	0	0	548.7	564.1	1112.8	0.0	0.0	--
INN-18	HRSC	925/925	5.0E-01	--	--	0	0	385.3	400.7	786.0	0.0	0.0	--
INN-36	HRSC	925/925	5.0E-01	--	--	0	0	224.1	228.2	452.3	0.0	0.0	--
INN-24	HRSC	925/925	5.0E-01	--	--	0	0	172.4	172.4	345.9	0.0	0.0	--
INN-12	BCCR	925/925	1.6E-05	--	--	--	--	228.2	228.2	456.4	0.0	0.0	--
INN-16	BCCR	925/925	1.4E-04	--	--	--	--	171.0	171.0	342.0	0.0	0.0	--
INN-89	BCCR	925/925	3.0E-03	--	--	--	--	200.7	200.7	401.4	0.0	0.0	--
INN-99	TCCR	925/925	2.7E-04	--	--	--	0	322.7	674.3	997.0	0.0	0.0	--
INN-11	TCCR	925/925	1.0E-04	--	--	--	0	169.6	594.3	763.9	0.0	0.0	--
INN-9	TCCR	925/925	1.9E-03	--	--	--	0	142.0	360.6	502.6	0.0	0.0	--
INN-74	CCCR	925/925	5.1E-04	--	--	0	--	504.7	241.3	746.0	0.0	0.0	--
INN-13	CCCR	925/925	4.4E-04	--	--	0	--	486.8	140.6	627.4	0.0	0.0	--
INN-15	CCCR	925/925	7.1E-04	--	--	0	--	412.3	141.3	553.6	0.0	0.0	--
INN-73**	VERF	925/925	2.8E-03	--	--	6.0	116.0	621.5	655.0	1276.5	28.6	223.2*	--
INN-72**	VERF	925/925	2.8E-03	--	--	6.0	116.0	366.1	355.1	721.2	51.4	214.5*	--
INN-47**	VERF	925/925	2.8E-03	--	--	6.0	116.0	345.4	259.2	604.6	46.7	113.9*	--
INN-75**	VERF	925/925	2.8E-03	--	--	116.0	6.0	436.4	582.6	1019.0	207.8*	54.1	--
INN-68**	VERF	925/925	2.8E-03	--	--	116.0	6.0	375.1	462.6	837.7	225.4*	20.0	--
INN-66**	VERF	925/925	2.8E-03	--	--	116.0	6.0	247.5	352.0	599.8	101.3*	32.8	--

* STRESS IS SUM OF THREE RELAXATION PERIODS
** VERIFICATION TESTS

Table II-10[97]

CREEP-FATIGUE DATA (CONTINUED)

LABORATORY: NASA
MATERIAL: IN-100, CAST

STRAINS & FAILURE DATA

SPEC NO	STRAINRANGES (HALF-LIFE VALUES) % TOTAL	EL	IN	PP	PC	CP	CC	FAILURE DATA-CYCLES NO	NI	NS	NF	TF-HRS
INN-2	2.170	0.924	1.246	1.246	0.000	0.000	0.000	--	--	--	15	0.01
INN-32	1.351	0.769	0.582	0.582	0.000	0.000	0.000	--	--	--	50	0.03
INN-3	0.920	0.638	0.282	0.282	0.000	0.000	0.000	--	--	--	96	0.05
INN-17	1.125	0.708	0.417	0.417	0.000	0.000	0.000	--	--	--	160	0.11
INN-18	0.640	0.500	0.140	0.140	0.000	0.000	0.000	--	--	--	300	0.17
INN-36	0.332	0.292	0.040	0.040	0.000	0.000	0.000	--	--	--	4015	2.23
INN-24	0.236	0.222	0.014	0.014	0.000	0.000	0.000	--	--	--	51261	28.36
INN-12	1.208	0.290	0.918	0.108	0.000	0.000	0.810	--	--	--	17	301.50
INN-16	0.650	0.218	0.432	0.039	0.019	0.000	0.374	--	--	--	102	203.37
INN-89	0.402	0.258	0.144	0.045	0.000	0.000	0.099	--	--	--	840	73.33
INN-99	2.300	0.643	1.657	0.369	0.000	1.288	0.000	6	6	6	5	6.09
INN-11	0.899	0.485	0.414	0.182	0.000	0.232	0.000	--	--	--	60	163.92
INN-9	0.414	0.320	0.094	0.047	0.000	0.047	0.000	--	--	--	1100	159.32
INN-74	1.324	0.481	0.643	0.207	0.436	0.000	0.000	19	20	20	22	12.02
INN-13	0.577	0.399	0.178	0.076	0.102	0.000	0.000	--	--	--	139	87.31
INN-15	0.450	0.352	0.098	0.034	0.064	0.000	0.000	--	--	--	332	129.11
INN-73**	1.625	0.823	0.802	0.677	0.107	0.000	0.018	--	--	--	17	1.73
INN-72**	0.822	0.465	0.357	0.219	0.105	0.000	0.033	--	--	--	84	8.40
INN-47**	0.517	0.390	0.127	0.054	0.043	0.000	0.030	--	--	--	454	47.11
INN-75**	1.502	0.657	0.845	0.724	0.000	0.099	0.022	--	--	--	15	1.55
INN-68**	0.866	0.540	0.326	0.181	0.000	0.132	0.013	--	--	--	79	7.97
INN-66**	0.505	0.387	0.118	0.053	0.000	0.044	0.021	--	--	--	1400	140.00

** VERIFICATION TESTS

LABORATORY: ONERA
MATERIAL: IN-100, COATED

Table II-11 (97)

CREEP-FATIGUE DATA (CONTINUED)

RATE DATA & STRESSES

SPEC NO	TEST TYPE	TEMP-C TEN/COMP	FREQ HZ	RATE DATA (HALF-LIFE VALUES) STRAIN-RATE-%/SEC TEN	COMP	HOLD TIME-SEC TEN	COMP	STRESSES (HALF-LIFE VALUES) TEN MAX	COMP MAX	RANGE MAX	RELAXATION TEN	COMP	SPA CYCLIC STRAIN HARDENING %
7	HRSC	900/900	5.0E 00	--	--	0	0	515.0	515.0	1030.0	0.0	0.0	--
6	HRSC	900/900	5.0E 00	--	--	0	0	479.5	479.5	959.0	0.0	0.0	--
1	HRSC	900/900	5.0E 00	--	--	0	0	445.0	445.0	890.0	0.0	0.0	--
2	HRSC	900/900	5.0E 00	--	--	0	0	411.0	411.0	822.0	0.0	0.0	--
3	HRSC	900/900	1.0E 01	--	--	0	0	376.5	376.5	753.0	0.0	0.0	--
4	HRSC	900/900	1.0E 01	--	--	0	0	342.5	342.5	685.0	0.0	0.0	--
5	HRSC	900/900	1.0E 01	--	--	0	0	308.0	308.0	616.0	0.0	0.0	--
10	HRSC	900/900	1.0E 01	--	--	0	0	287.5	287.5	575.0	0.0	0.0	--
8	HRSC	900/900	1.0E 01	--	--	0	0	308.0	308.0	616.0	0.0	0.0	--
11	HRSC	900/900	1.0E 01	--	--	0	0	287.5	287.5	575.0	0.0	0.0	--
24	HRSC	1000/1000	5.0E 00	--	--	0	0	308.0	308.0	616.0	0.0	0.0	--
58	HRSC	1000/1000	5.0E 00	--	--	0	0	274.0	274.0	548.0	0.0	0.0	--
25	HRSC	1000/1000	5.0E 00	--	--	0	0	240.0	240.0	480.0	0.0	0.0	--
26	HRSC	1000/1000	5.0E 00	--	--	0	0	205.5	205.5	411.0	0.0	0.0	--
H12	CHSC	900/900	3.0E-03	4.5E-02	4.5E-02	--	300.0	512.0	295.0	807.0	0.0	54.0	-6.00
H10	CHSC	900/900	3.0E-03	3.3E-02	3.3E-02	--	300.0	420.0	252.0	672.0	0.0	32.5	-5.00
H9	CHSC	900/900	1.7E-02	3.3E-02	3.3E-02	--	30.0	357.0	264.0	621.0	0.0	31.0	-6.80
37	CHSC	1000/1000	2.8E-03	5.2E-02	5.2E-02	--	330.0	336.0	245.0	581.0	0.0	76.0	-5.50
H13	CHSC	1000/1000	3.0E-03	4.0E-02	4.0E-02	--	300.0	336.0	195.0	531.0	0.0	53.0	-4.00
39	THSC	900/900	2.8E-03	4.2E-02	4.2E-02	330.0	--	302.0	438.0	740.0	43.0	0.0	-6.50
H8	THSC	900/900	3.0E-03	3.3E-02	3.3E-02	300.0	--	247.0	394.0	641.0	27.0	0.0	-4.50
36	THSC	1000/1000	2.8E-03	5.2E-02	5.2E-02	330.0	--	257.0	326.0	583.0	71.0	0.0	-4.50
H36	THSC	1000/1000	3.0E-03	3.0E-02	3.0E-02	300.0	--	185.0	248.0	433.0	41.0	0.0	-8.00
H37	THSC	1000/1000	3.0E-03	2.2E-02	2.2E-02	300.0	--	135.0	212.0	347.0	26.0	0.0	-3.00
44	TCCR	900/900	2.8E-03	--	--	330.0	--	342.4	342.4	684.8	0.0	0.0	--
45	TCCR	1000/1000	2.8E-03	--	--	330.0	--	171.0	171.0	342.0	0.0	0.0	--
54	BCCR	900/900	2.8E-03	--	--	165.0	165.0	342.4	342.4	684.8	0.0	0.0	--
H5	BCCR	900/900	1.4E-02	--	--	20.0	20.0	416.0	416.0	832.0	0.0	0.0	--
H6	BCCR	900/900	2.6E-03	--	--	180.0	180.0	312.0	312.0	624.0	0.0	0.0	--
56	BCCR	900/900	1.7E-02	--	--	15.0	15.0	342.4	342.4	684.8	0.0	0.0	--
51	BCCR	1000/1000	5.5E-04	--	--	870.0	870.0	188.0	188.0	376.0	0.0	0.0	--
55	BCCR	1000/1000	2.8E-03	--	--	165.0	165.0	171.0	171.0	342.0	0.0	0.0	--
H32	BCCR	1000/1000	2.6E-02	--	--	180.0	180.0	171.0	171.0	342.0	0.0	0.0	--
57	BCCR	1000/1000	1.7E-02	--	--	15.0	15.0	171.0	171.0	342.0	0.0	0.0	--
H35	BCCR	1000/1000	2.6E-03	--	--	180.0	180.0	154.0	154.0	308.0	0.0	0.0	--
H34	BCCR	1000/1000	1.4E-02	--	--	20.0	20.0	154.0	154.0	308.0	0.0	0.0	--
40	LRSC	900/900	3.3E-02	--	--	--	--	411.0	411.0	822.0	0.0	0.0	--
26	LRSC	900/900	3.3E-02	4.5E-02	4.5E-02	--	--	426.0	419.0	845.0	0.0	0.0	-1.70
42	LRSC	900/900	3.3E-02	--	--	--	--	342.4	342.4	684.8	0.0	0.0	--
49	LRSC	900/900	3.3E-02	--	--	--	--	274.0	274.0	548.0	0.0	0.0	--
33	LRSC	1000/1000	3.3E-02	4.5E-02	4.5E-02	--	--	295.0	295.0	590.0	0.0	0.0	-1.50
27	LRSC	1000/1000	3.3E-02	3.0E-02	3.0E-02	--	--	233.0	218.0	451.0	0.0	0.0	-3.00
34	LRSC	1000/1000	3.3E-02	2.0E-02	2.0E-02	--	--	175.0	169.0	344.0	0.0	0.0	-4.00

LABORATORY: ONERA
MATERIAL: IN-100, COATED

Table II-12[97]
CREEP-FATIGUE DATA (CONTINUED)

STRAINS & FAILURE DATA

SPEC NO	STRAINRANGES(HALF-LIFE VALUES) % TOTAL	EL	IN	PP	PC	CP	CC	FAILURE DATA-CYCLES NO	NI	N5	NF	TF-HRS
7	0.771	0.643	0.129	0.129	0.000	0.000	0.000	--	--	--	635	0.04
6	0.720	0.600	0.121	0.121	0.000	0.000	0.000	--	--	--	900	0.05
1	0.694	0.556	0.138	0.138	0.000	0.000	0.000	--	--	--	1260	0.07
2	0.600	0.513	0.086	0.086	0.000	0.000	0.000	--	--	--	2120	0.12
3	0.530	0.470	0.059	0.059	0.000	0.000	0.000	--	--	--	3670	0.10
4	0.478	0.428	0.050	0.050	0.000	0.000	0.000	--	--	--	9460	0.26
5	0.416	0.385	0.031	0.031	0.000	0.000	0.000	--	--	--	12210	0.34
10	0.385	0.359	0.026	0.026	0.000	0.000	0.000	--	--	--	17340	0.48
8	0.413	0.385	0.028	0.028	0.000	0.000	0.000	--	--	--	27260	0.76
11	0.372	0.359	0.014	0.014	0.000	0.000	0.000	--	--	--	48320	1.34
24	0.571	0.419	0.152	0.152	0.000	0.000	0.000	--	--	--	520	0.03
58	0.468	0.372	0.095	0.095	0.000	0.000	0.000	--	--	--	1520	0.08
25	0.371	0.326	0.045	0.045	0.000	0.000	0.000	--	--	--	5450	0.30
26	0.297	0.279	0.018	0.018	0.000	0.000	0.000	--	--	--	24380	1.35
N12	0.700	0.504	0.196	0.055	0.098	0.000	0.041	--	235	187	250	23.00
N10	0.525	0.420	0.105	0.010	0.025	0.000	0.070	--	744	738	763	70.00
N9	0.490	0.388	0.102	0.011	0.020	0.000	0.071	--	910	888	943	15.70
37	0.785	0.395	0.390	0.200	0.085	0.000	0.105	--	--	--	107	10.70
N13	0.616	0.361	0.255	0.077	0.107	0.000	0.072	--	253	234	268	24.60
39	0.642	0.462	0.180	0.056	0.000	0.045	0.079	--	190	194	239	23.90
N8	0.480	0.400	0.080	0.008	0.000	0.010	0.062	--	--	1110	1495	137.00
36	0.788	0.396	0.392	0.210	0.000	0.082	0.100	--	57	48	63	6.40
N36	0.474	0.294	0.180	0.054	0.000	0.038	0.088	--	172	198	243	22.30
N37	0.332	0.236	0.096	0.050	0.021	0.000	0.025	--	500	560	870	80.00
44	0.578	0.428	0.150	0.034	0.000	0.030	0.086	--	--	--	115	11.60
45	0.378	0.232	0.146	0.024	0.000	0.022	0.100	--	--	100	111	11.10
54	0.686	0.428	0.258	0.090	0.000	0.000	0.168	--	--	138	159	15.90
N5	0.715	0.520	0.245	0.085	0.000	0.000	0.160	--	--	--	200	3.89
N6	0.555	0.390	0.165	0.032	0.000	0.000	0.133	--	--	268	293	29.40
56	0.592	0.428	0.164	0.054	0.000	0.000	0.110	--	--	300	338	5.60
51	0.776	0.256	0.520	0.110	0.000	0.000	0.410	--	--	17	24	12.00
55	0.408	0.233	0.175	0.044	0.000	0.000	0.131	--	--	225	263	2.63
N32	0.406	0.234	0.172	0.036	0.000	0.000	0.136	--	--	505	568	61.50
57	0.344	0.233	0.111	0.023	0.000	0.000	0.088	--	--	720	800	13.30
N35	0.325	0.210	0.138	0.017	0.000	0.000	0.121	--	--	790	958	103.40
N34	0.279	0.210	0.078	0.011	0.000	0.000	0.067	--	--	3040	3109	60.40
40	0.688	0.514	0.174	0.106	0.000	0.000	0.068	--	--	290	299	2.50
28	0.684	0.528	0.156	0.066	0.000	0.000	0.090	--	280	270	300	2.50
42	0.510	0.428	0.082	0.029	0.000	0.000	0.053	--	--	--	1130	9.40
49	0.384	0.342	0.042	0.009	0.000	0.000	0.033	--	--	--	4018	33.45
33	0.700	0.400	0.300	0.225	0.000	0.000	0.075	--	269	255	275	2.30
27	0.447	0.307	0.140	0.070	0.000	0.000	0.070	--	--	--	850	7.10
34	0.300	0.234	0.066	0.013	0.000	0.000	0.053	--	2290	2220	2520	21.00

TABLE II - 13

UNCOATED RENÉ 80 TESTED IN AIR AT 1000C (U of C)

Test Type	Specimen #	[%] ε_T	[%] ε_{in}	[MPa] Holding Stress	[MPa] Maximum Stress	[MPa] Minimum Stress	[sec] Hold Time	[hours] N_f	[hours] t_f
TCCR	GR-1	0.927	0.597	172.0	172.0	299.0	varied	130	16.56
TCCR	GR-2	0.927	0.597	172.0	172.0	299.0	varied	interrupted at: N = 7	t = 3.31
TCCR	GR-3	0.927	0.597	172.0	172.0	299.0	varied	interrupted at: N - 27	t = 7.39
Strain Hold	GR-4	0.927	0.671	-	243.4	297.3	390	160	17.33
Continuous Cycling	GR-5	0.927	0.561	-	243.4	252.5	-	260	4.33

Spectrum Creep-Rupture	GR-6	[MPa] Stress	[hours] t_o	[hours] t_f	[%] ε_o	[%] ε_f	[5/hour]
		89.0	0	5	0.0658	0.1152	9.88×10^{-3}
		110.4	5	10	0.1341	0.2098	1.51×10^{-2}
		129.3	10	20.08	0.2304	0.3538	1.22×10^{-2}
		172.4	20.08	25.08	0.4196	1.1313	1.42×10^{-1}

TABLE III

Failure Criterion for Rene' 80 Tested in Air at 1000C (NASA)

	Specimen #	MPa Maximum Stress	N_f	$K'_f/S'A'^{1/2}$	
Uncoated HRSC	Ree 205 Ree 215 Ree 206* Ree 204*	420.9 370.9 358.2 206.2	42 55 202 9226	0.79×10^6 0.66×10^6 1.15×10^6 1.47×10^6	$x = 1.02 \times 10^6$ $s = 3.66 \times 10^5$ $s/x = 0.36$
Coated HRSC	Ree 322 Ree 317* Ree 310* Ree 304* Ree 306* Ree 300* Ree 323* Ree 311*	481.5 394.6 440.4 375.2 298.6 239.5 198.2 178.2	43 69 85 93 650 1666 3820 15000	1.10×10^6 0.86×10^6 1.25×10^6 0.88×10^6 1.27×10^6 1.05×10^6 0.81×10^6 1.01×10^6	$x = 1.03 \times 10^6$ $s = 1.74 \times 10^5$ $s/x = 0.17$
Uncoated CCCR	Ree 200 Ree 219 Ree 213 Ree 210	467.1 355.0 321.7 183.3	10 63 130 3980	4.83×10^5 6.06×10^5 6.66×10^5 5.01×10^5	$x = 5.64 \times 10^5$ $s = 8.70 \times 10^4$ $s/x = 0.15$
Coated CCCR	Ree 312 Ree 310 Ree 303 Ree 328	365.6 323.5 234.1 210.1	24 159 1200 1900	4.18×10^5 7.81×10^5 8.28×10^5 7.15×10^5	excludingRee312 $x = 7.75 \times 10^5$ $s = 5.68 \times 10^4$ $s/x = 0.07$
			t_f	$K_f/SA^{1/2}$	
Uncoated TCCR Coated TCCR	Ree 208 Ree 201 Ree 315 Ree 305	172.6 172.0 169.1 152.9	17.97 35.63 5.62 20.44	3.0×10^4 4.1×10^4 1.49×10^4 1.44×10^4	

TABLE IV

Failure Criterion for IN100 Tested in Air at 925C (NASA)

	Specimen #	MPa Maximum Stress	N_f	$K'_f/S'A'^{1/2}$	
Uncoated HRSC	INN - 2 INN - 32 INN - 3 INN - 17 INN - 18 INN - 36 INN - 24	736.0 573.6 483.0 548.7 385.3 224.1 172.4	15 50 96 160 300 4015 51261	1.74×10^6 1.82×10^6 1.69×10^6 2.93×10^6 1.73×10^6 1.39×10^6 1.81×10^6	excludingINN-17 $x = 1.70 \times 10^6$ $s = 1.56 \times 10^5$ $s/x = 0.09$
Uncoated CCCR	INN - 74 INN -13 INN - 15	504.7 486.8 412.3	22 139 332	8.96×10^5 2.07×10^6 2.15×10^6	$x = 1.71 \times 10^6$ $s = 7.02 \times 10^5$ $s/x = 0.41$
			[hours] t_f	$K_f/SA^{1/2}$	
Uncoated TCCR	INN - 99 INN - 11 INN - 9	322.7 169.6 142.0	6.09 163.92 159.32	1.57×10^5 9.47×10^4 2.87×10^4	$x = 9.35 \times 10^4$ $s = 6.42 \times 10^4$ $s/x = 0.69$

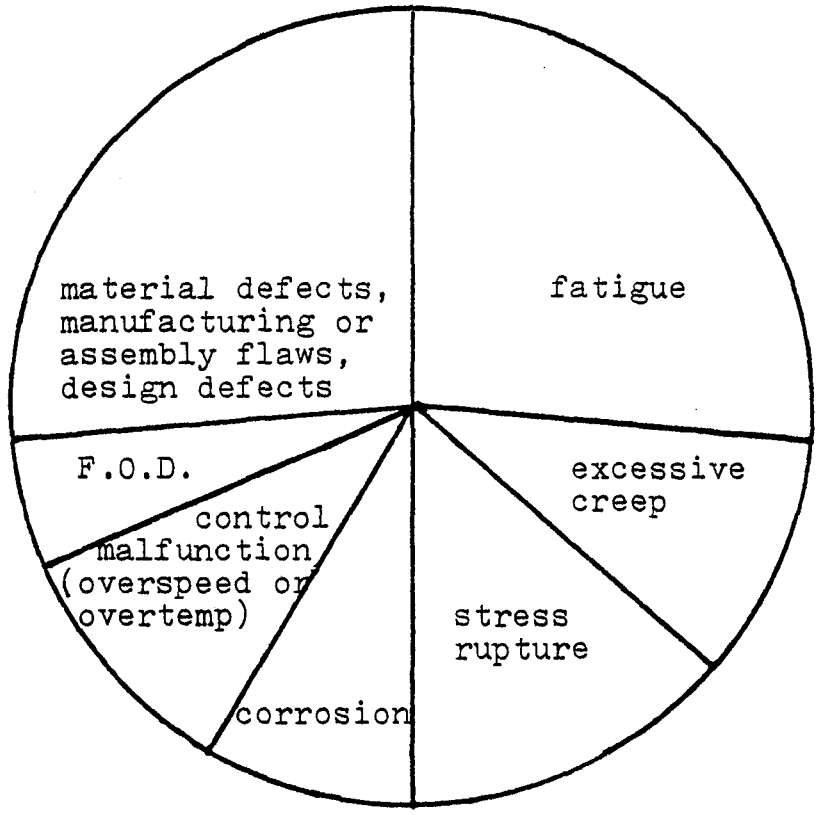

Figure 1. Causes of engine failure[1]

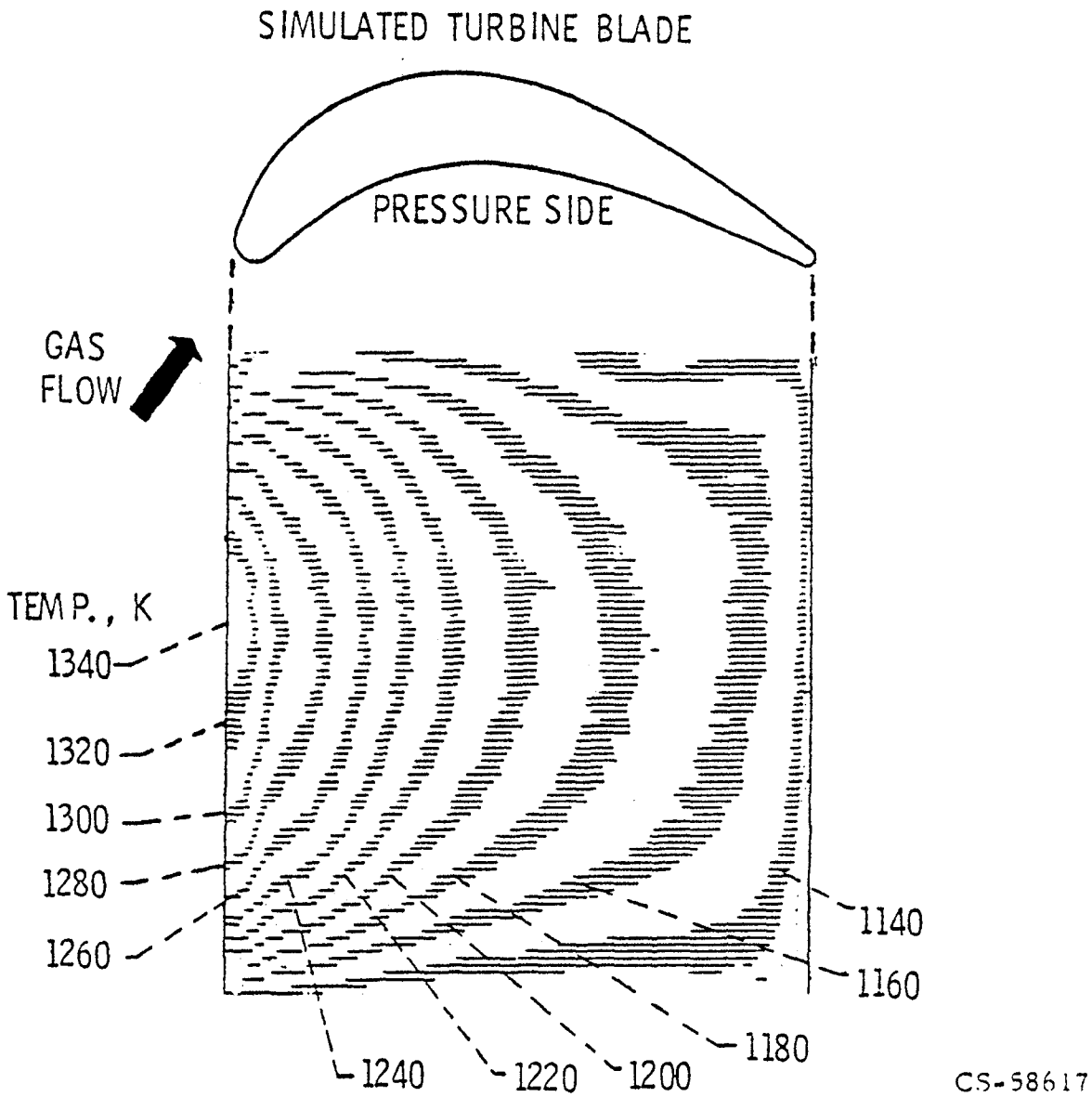

Figure 2. Steady-state temperature distribution for a simulated turbine blade[2]

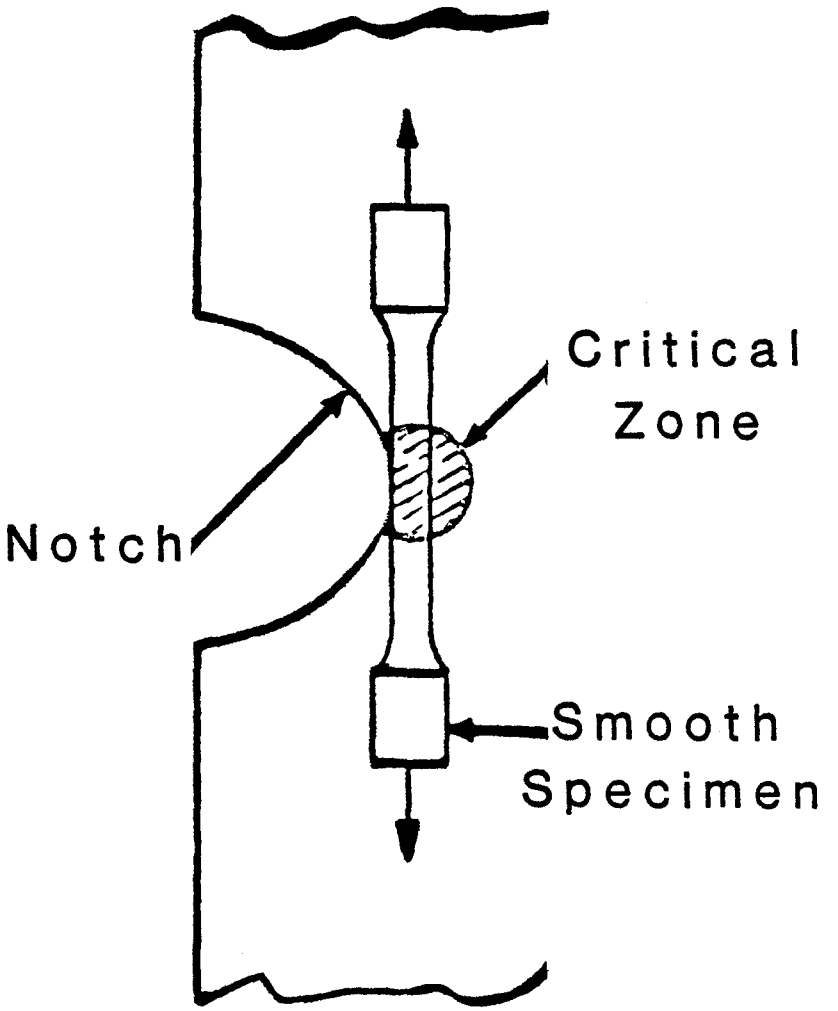

Figure 3. Relationship of local behavior of compoment to specimen life via low-cycle fatigue testing[2]

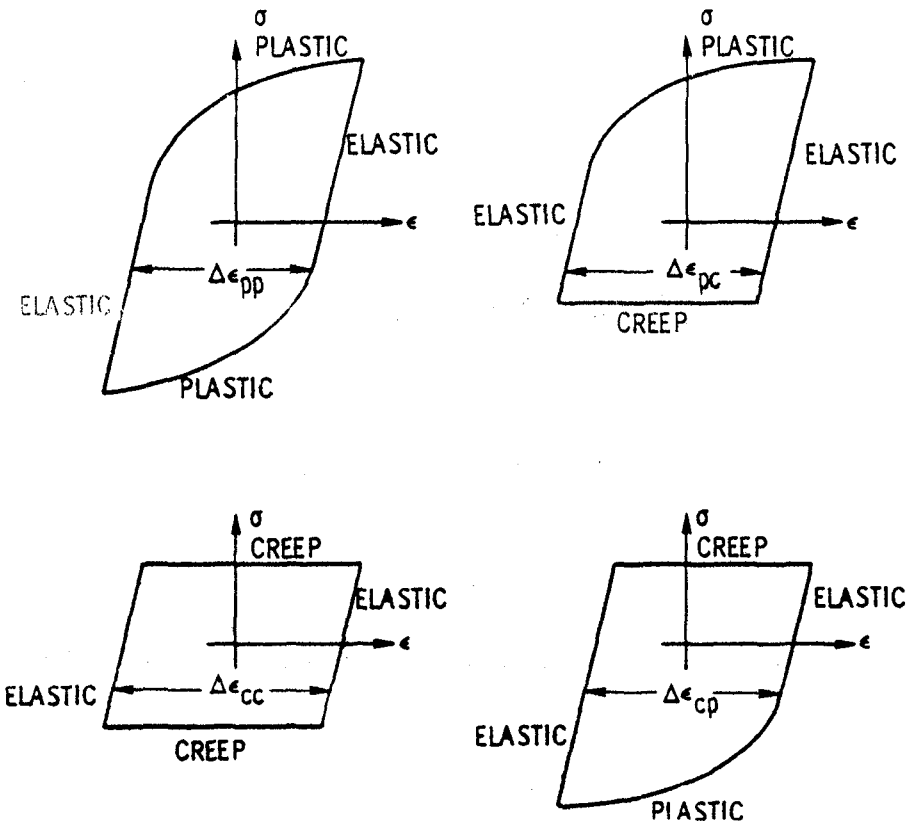

Figure 4. Idealized hysteresis loops for the four basic types of inelastic strainrange[97]

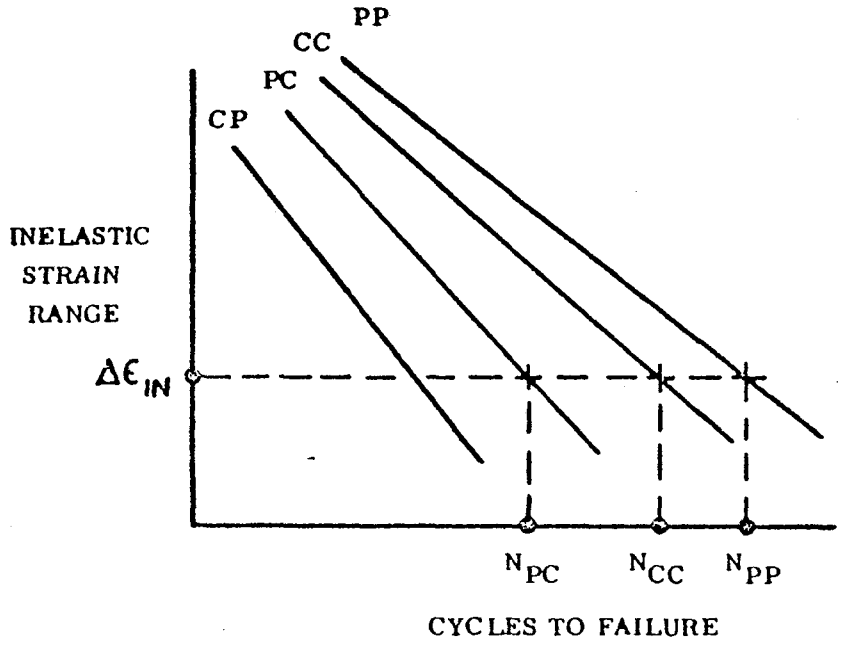

$$\frac{1}{N_F} = \frac{F_{PP}}{N_{PP}} + \frac{F_{CC}}{N_{CC}} + \frac{F_{PC}}{N_{PC}}$$

ENTER STRAINRANGE PARTITIONING
LIFE RELATIONSHIPS

APPLY INTERACTION DAMAGE RULE
SOLVE FOR PREDICTED LIFE, N_F

Figure 5. Technique for predicting lives for complex cycles[2]

Figure 5. Technique for predicting lives for complex cycles[2]

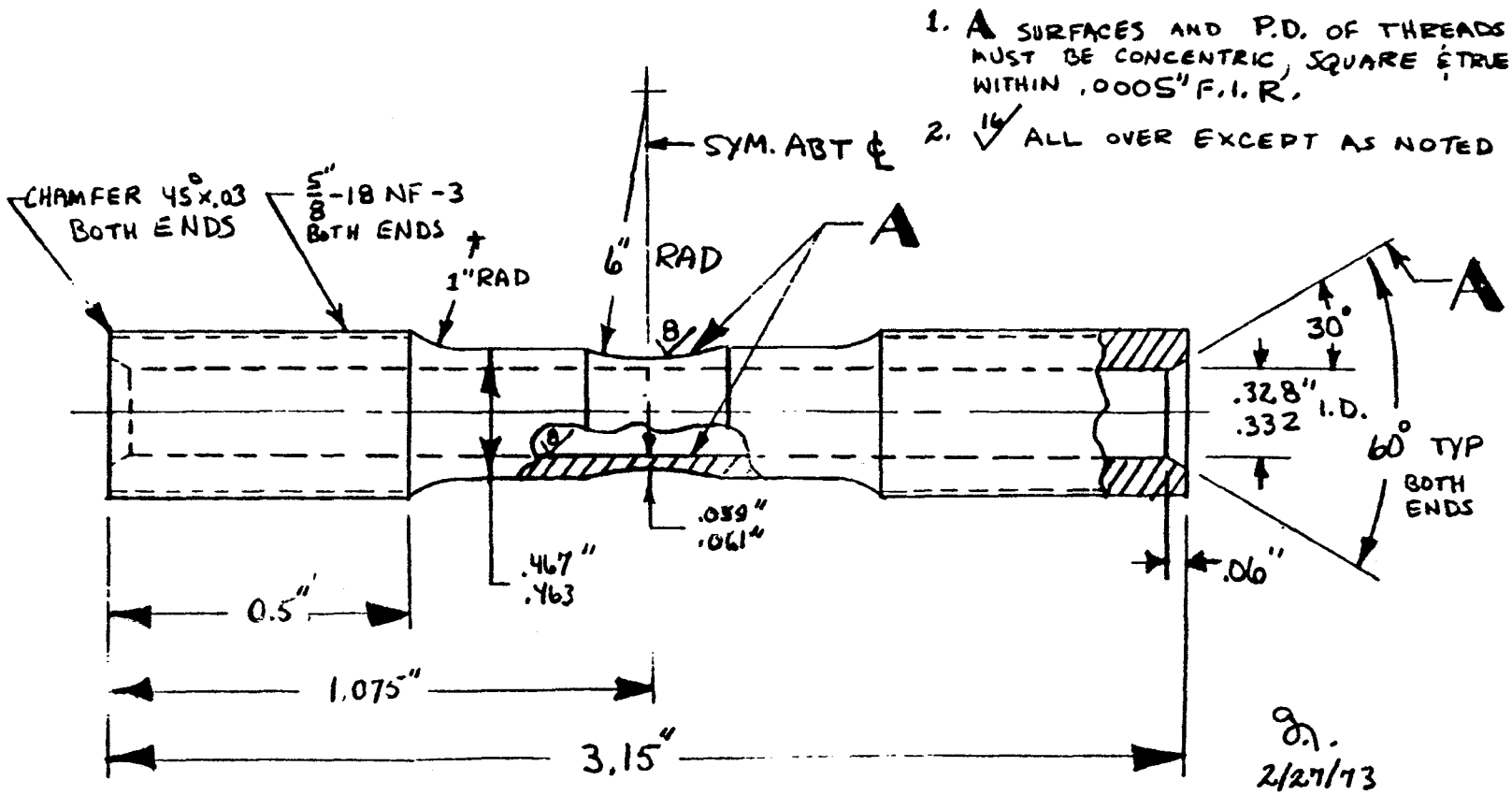

Figure 6. LCF test specimen geometry for René 80 (NASA & TRW) and IN 100 (NASA)[97]

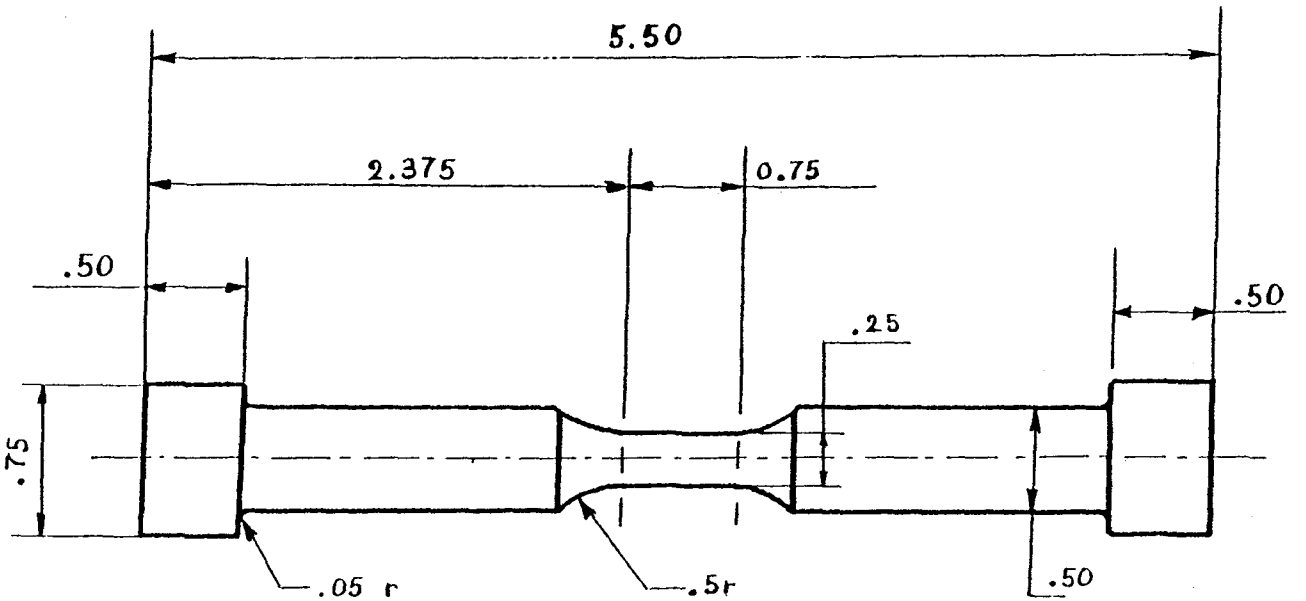

All dimensions in inches

Figure 7. LCF test specimen geometry for René 80 (U of C)

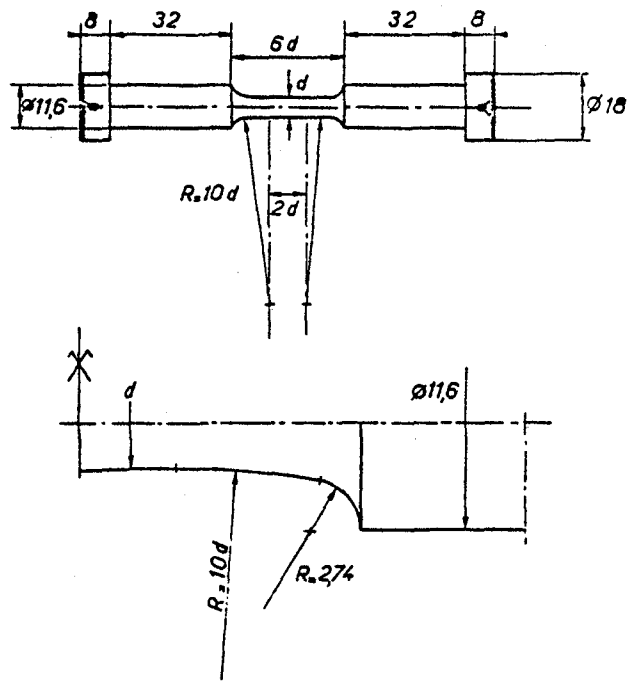

Figure 8. LCF test specimen geometry for IN 100 (ONERA)[97]

principal component of inelastic strain range	Temp	Uncoated	Coated
$\Delta\varepsilon_{pp}$	1000C	high strain low strain	high strain low strain
	871C	high strain low strain	high strain low strain

	Temp	Uncoated	Coated
$\Delta\varepsilon_{pc}$	1000C	high strain low strain	high strain low strain
	871C	high strain low strain	high strain low strain

	Temp	Uncoated	Coated
$\Delta\varepsilon_{cp}$	1000C	high strain low strain	high strain low strain
	871C	high strain low strain	high strain low strain

Figure 9-A. Test matrix for the examination of René 80 specimens tested in vacuum (TRW)

principal component of inelastic strain range	Temp	Uncoated	Coated
$\Delta\varepsilon_{pp}$	1000C	high strain low strain	high strain low strain

	Temp	Uncoated	Coated
$\Delta\varepsilon_{pc}$	1000C	high strain low strain	high strain low strain

	Temp	Uncoated	Coated
$\Delta\varepsilon_{cp}$	1000C	high strain low strain	high strain low strain

	Temp	Uncoated	Coated
$\Delta\varepsilon_{cc}$	1000C	high strain low strain	high strain low strain

Figure 9-B. Test maxtrix for the examination of René 80 specimens tested in air (NASA)

principal component of inelastic strain range	Temp	Uncoated
$\Delta\varepsilon_{pp}$	925C	high strain low strain

	Temp	Uncoated
$\Delta\varepsilon_{pc}$	925C	high strain low strain

	Temp	Uncoated
$\Delta\varepsilon_{cp}$	925C	high strain low strain

	Temp	Uncoated
$\Delta\varepsilon_{cc}$	925C	high strain low strain

Figure 9-C. Test matrix for the examination of IN 100 specimens tested in air (NASA)

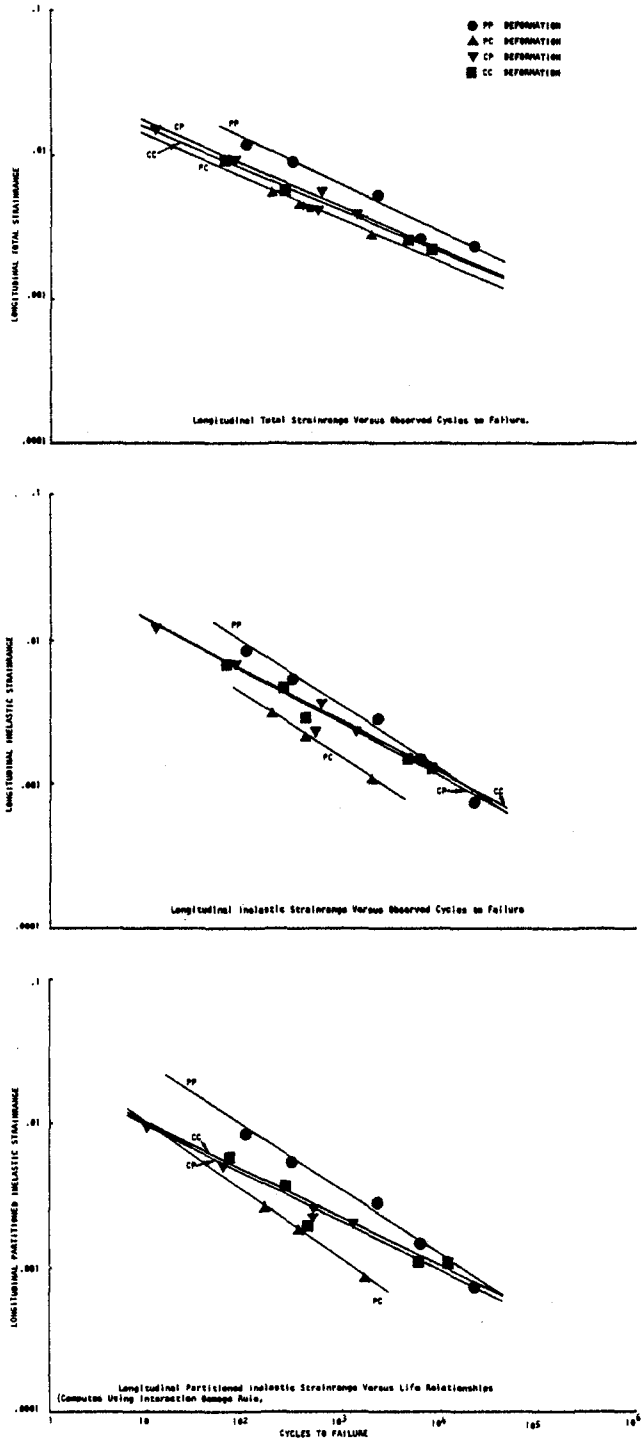

Figure 10. Uncoated René 80 (TRW); Fatigue test results in vacuum at 1000C

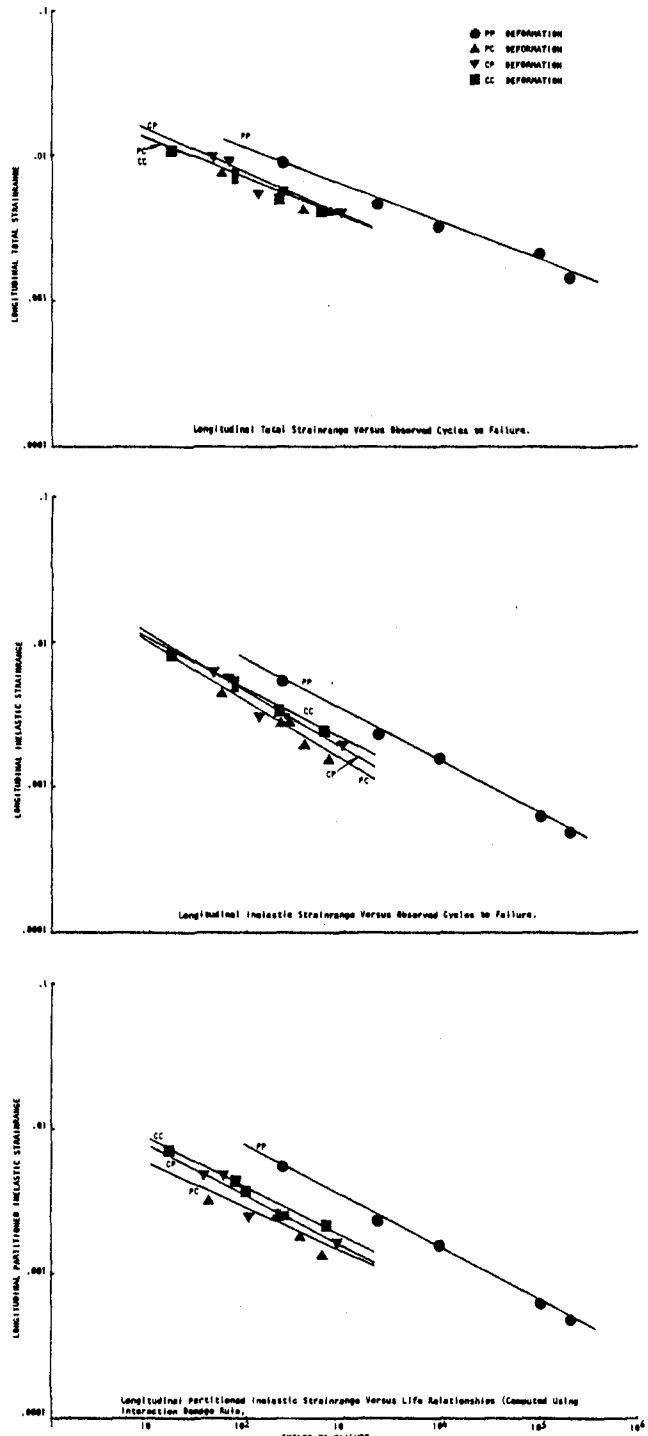

Figure 11. Coated René 80 (TRW); Fatigue test results in vacuum at 1000C

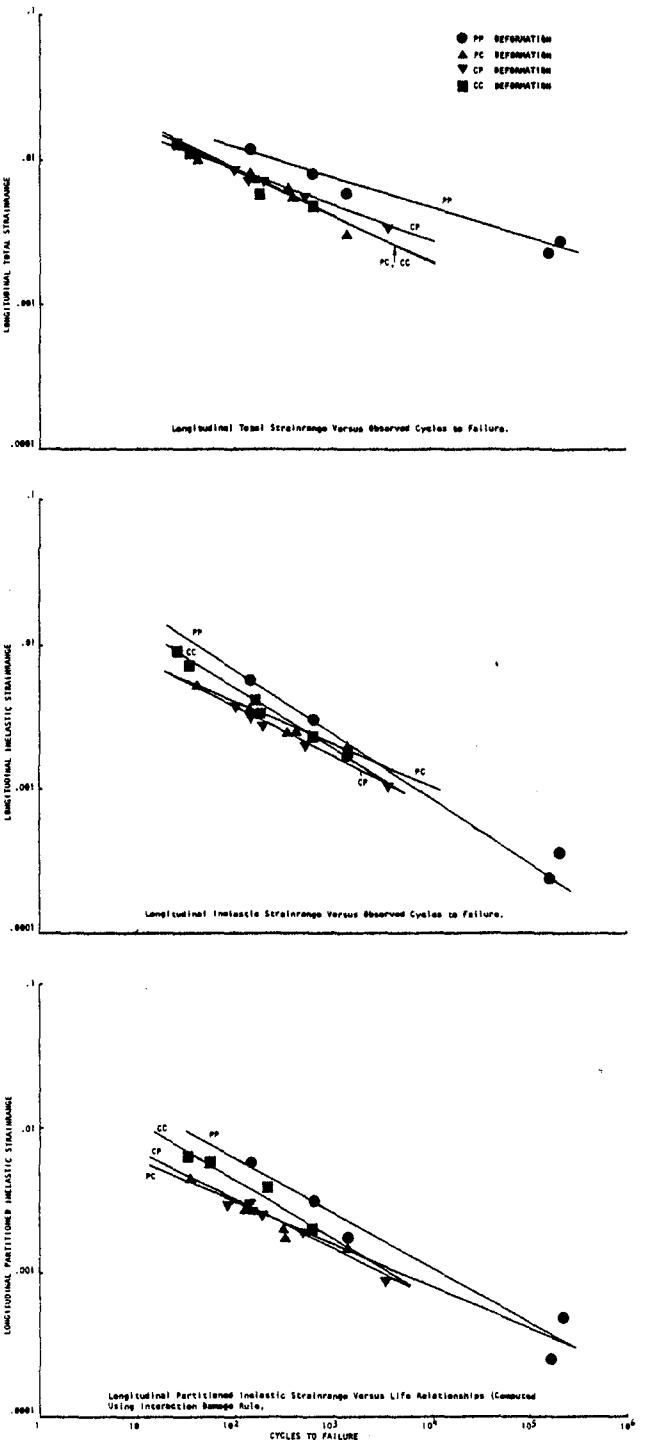

Figure 12. Uncoated René 80 (TRW); Fatigue test results in vacuum at 871C

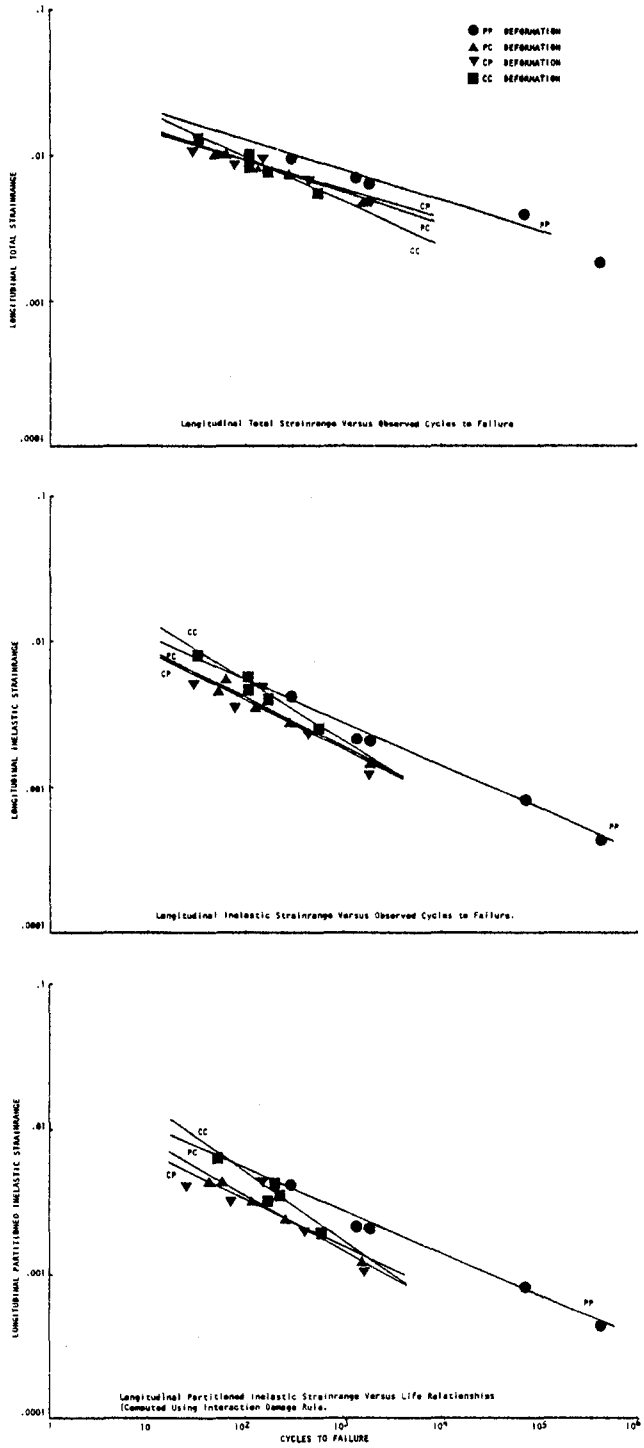

Figure 13. Coated René 80 (TRW); Fatigue test results in vacuum at 871C

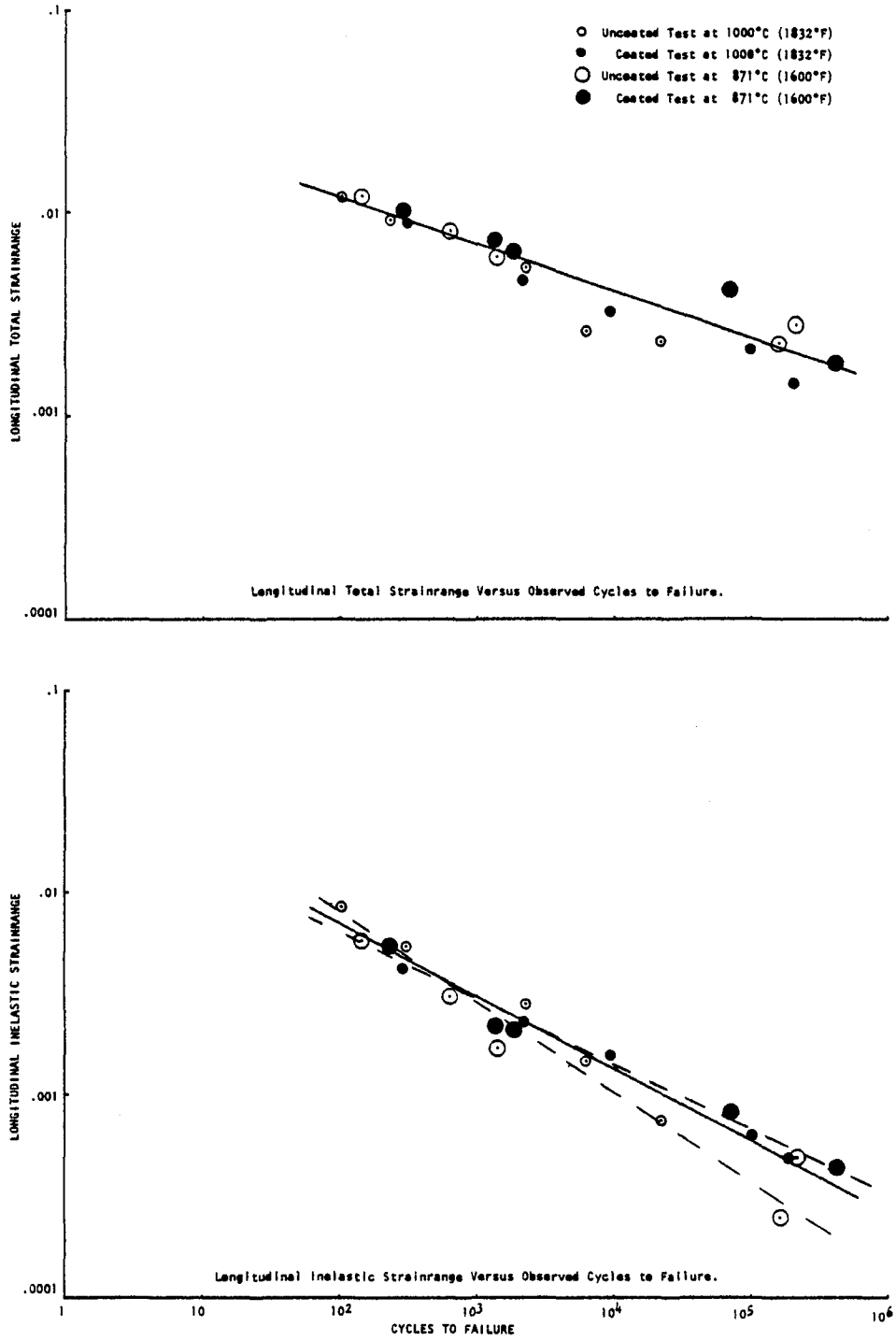

Figure 14. René 80 (TRW); HRSC fatigue test results in vacuum at 1000C and 871C for uncoated and coated specimens

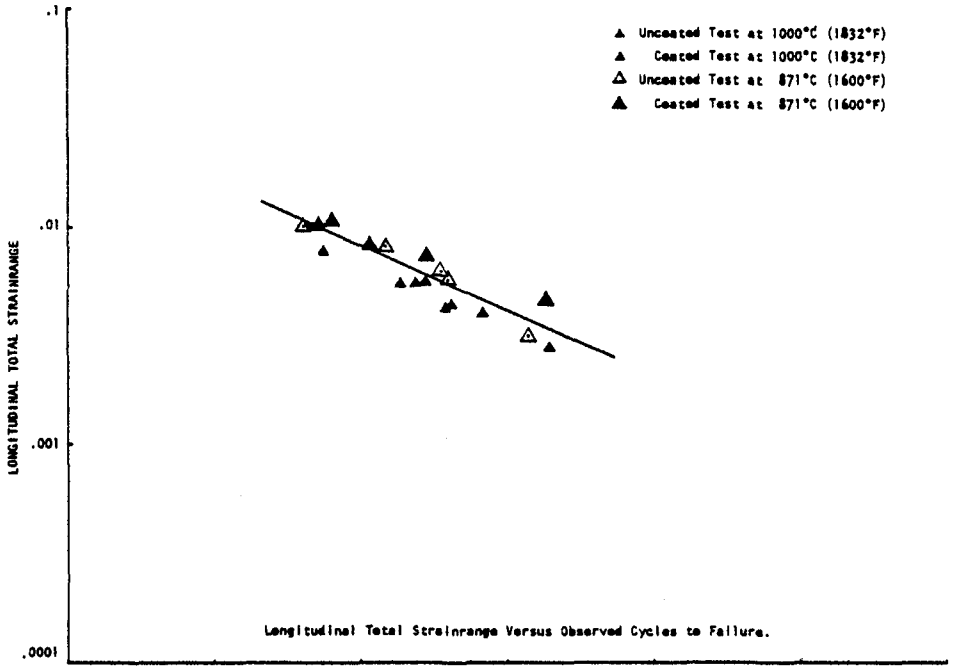

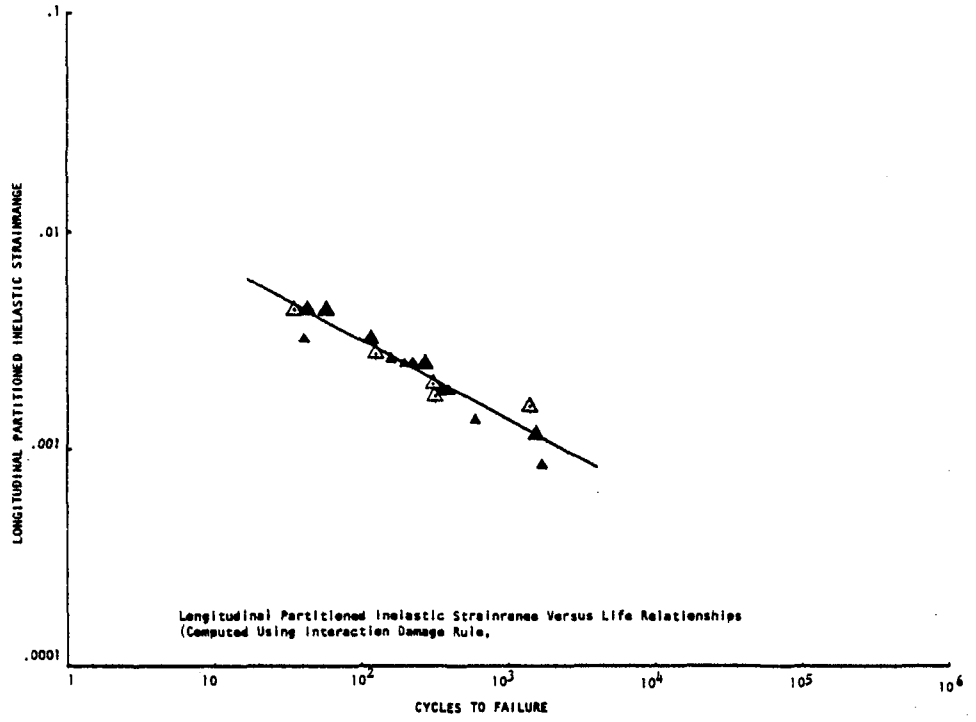

Figure 15. René 80 (TRW); CCCR fatigue test results in vacuum at 1000C and 871C for uncoated and coated specimens

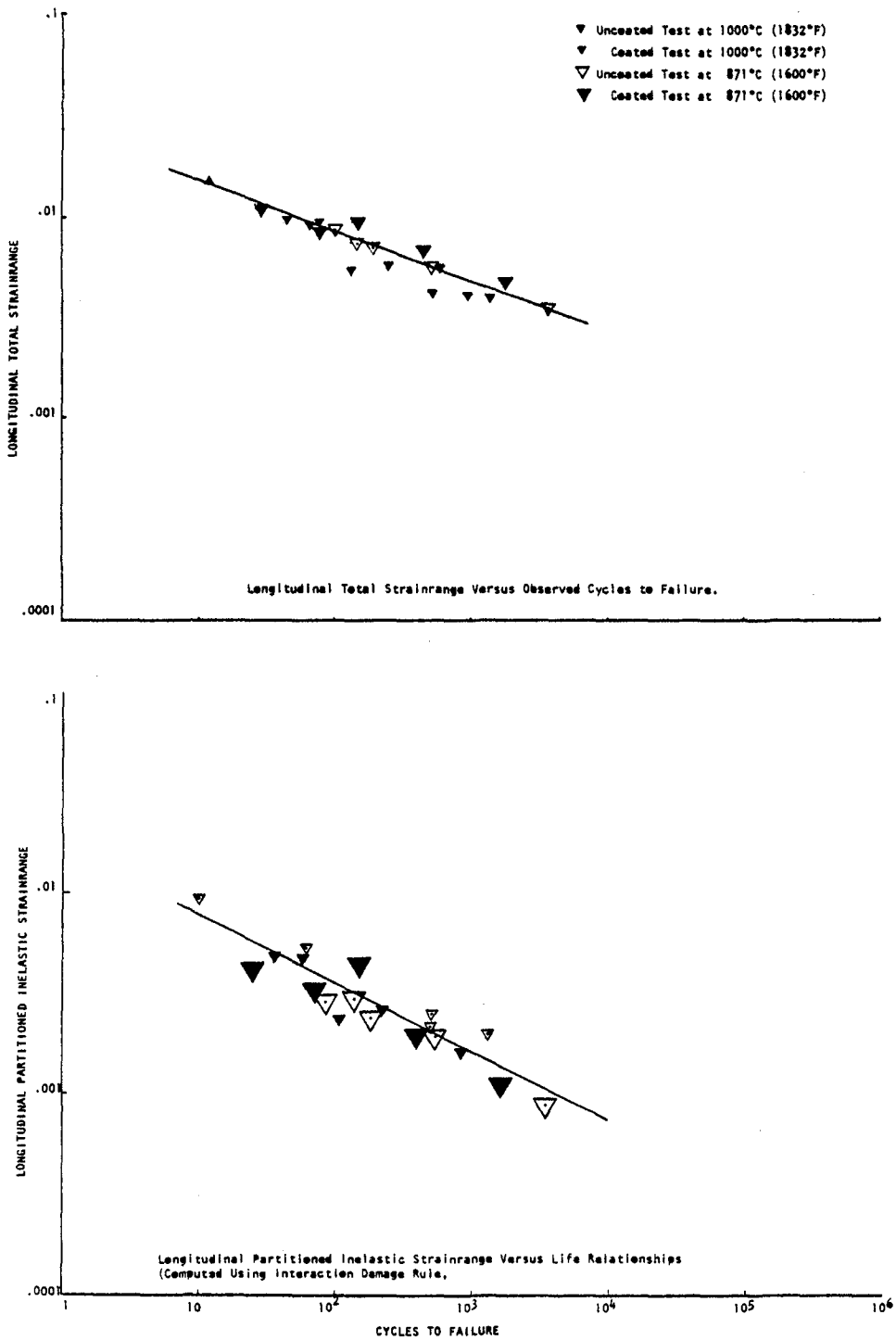

Figure 16. René 80 (TRW); TCCR fatigue test results in vacuum at 1000C and 871C for uncoated and coated specimens

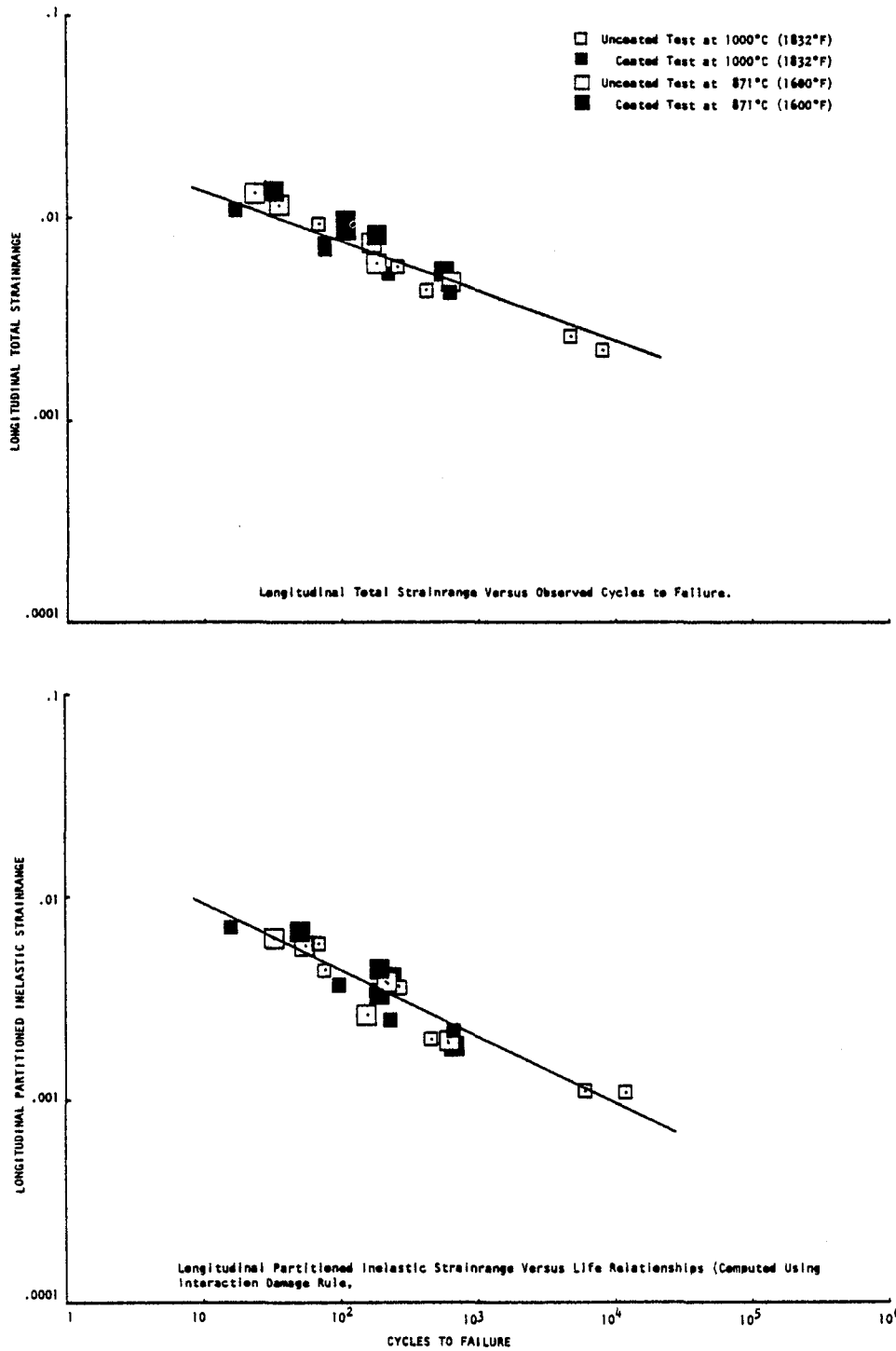

Figure 17. René 80 (TRW); BCCR fatigue test results in vacuum at 1000C and 871C for uncoated and coated specimens

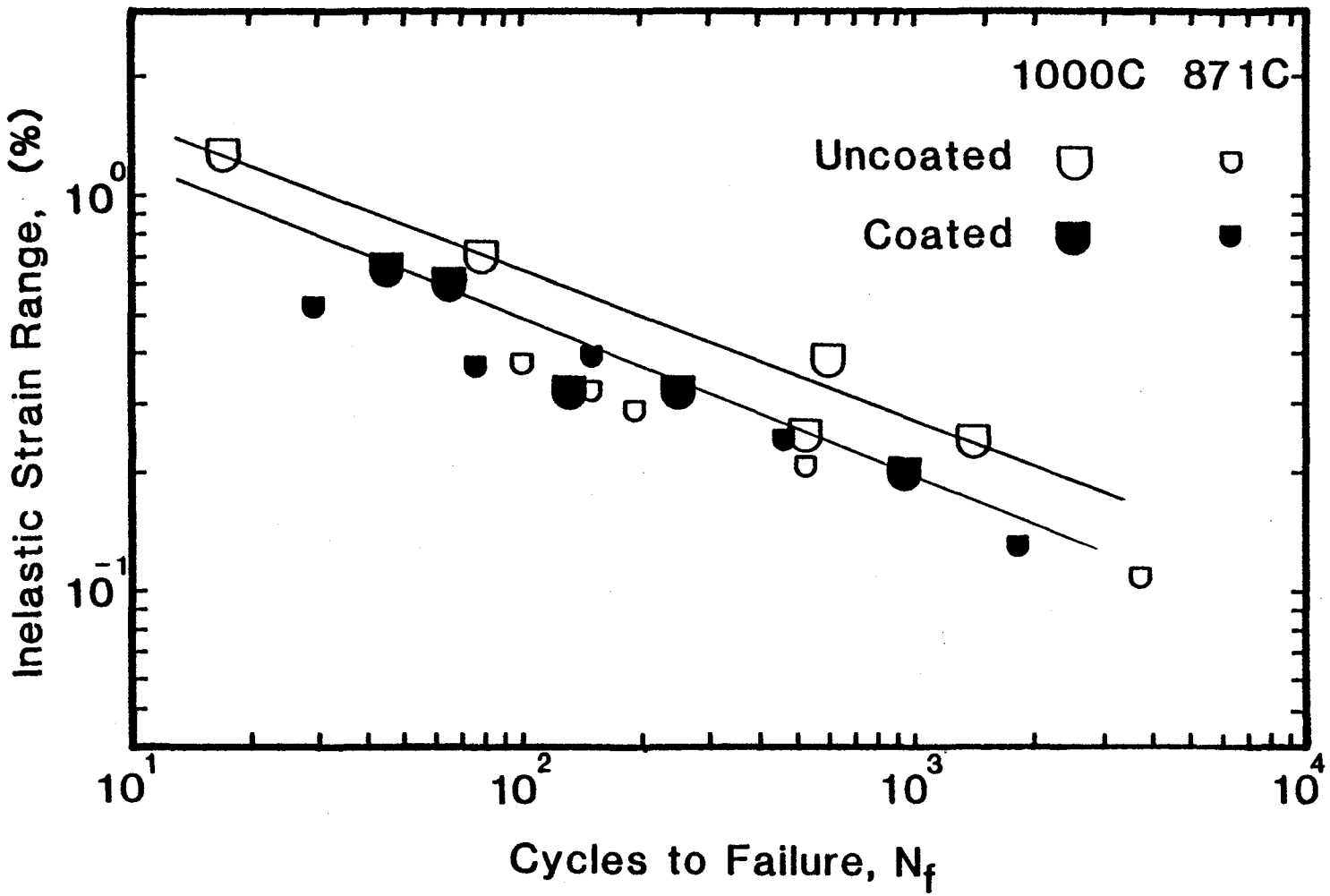

Figure 18. René 80 (TRW); TCCR fatigue test results in vacuum at 1000C and 871C for uncoated and coated specimens

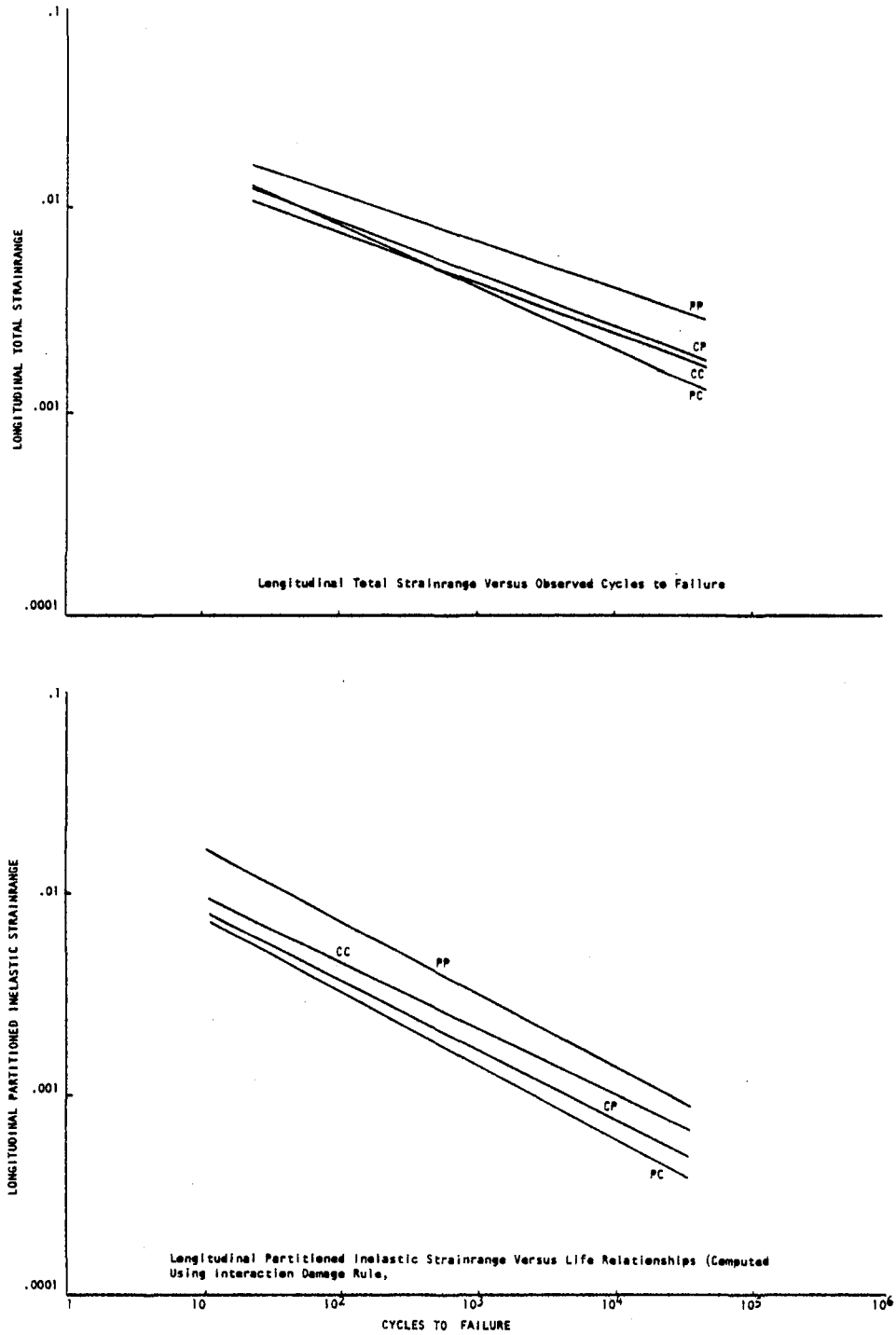

Figure 19. René 80 (TRW); Composite plot of least squares lines through the fatigue data shown in Figures 14 through 17

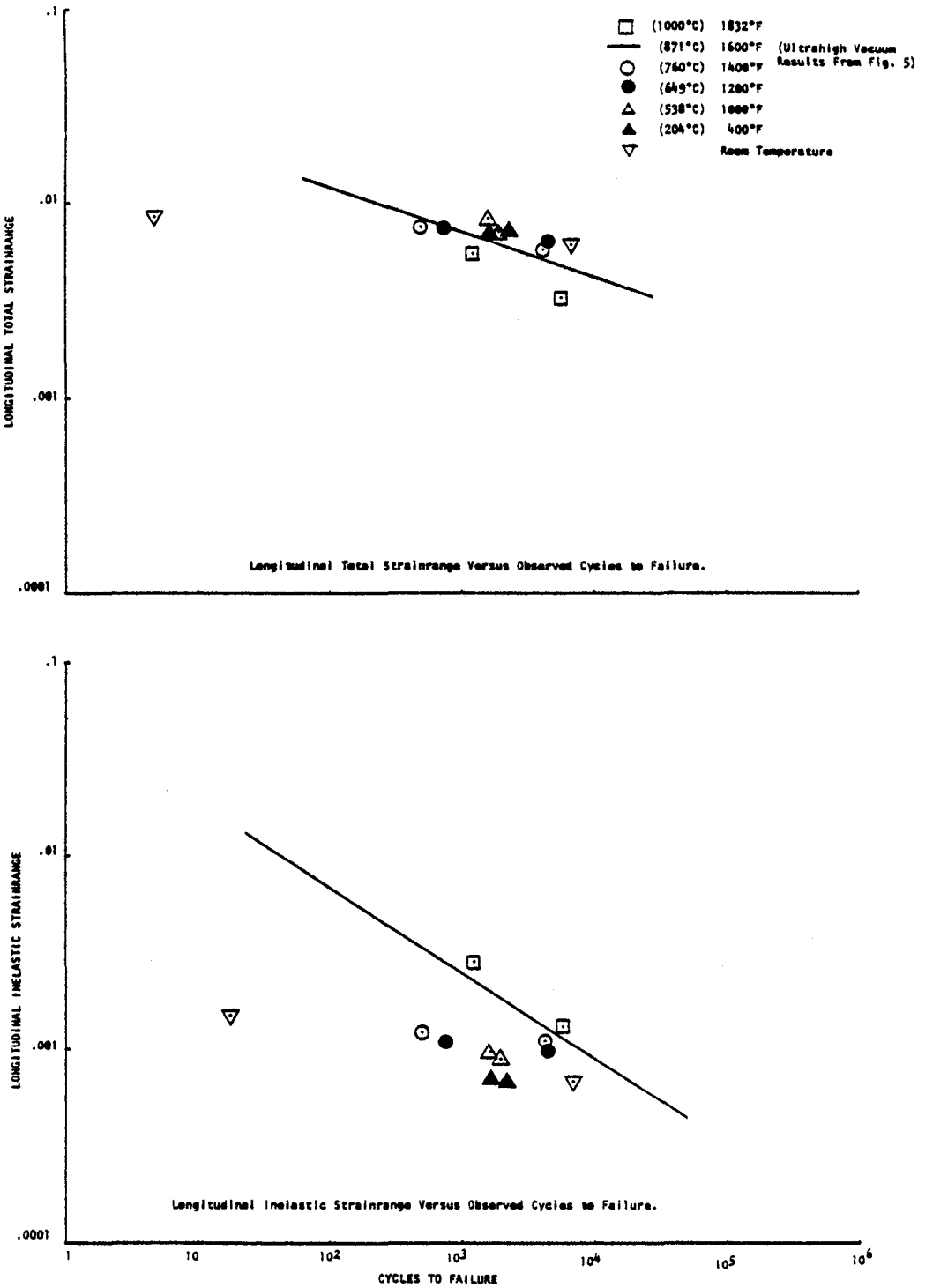

Figure 20. Uncoated René 80 (TRW); HRSC fatigue test results in vacuum at various temperatures

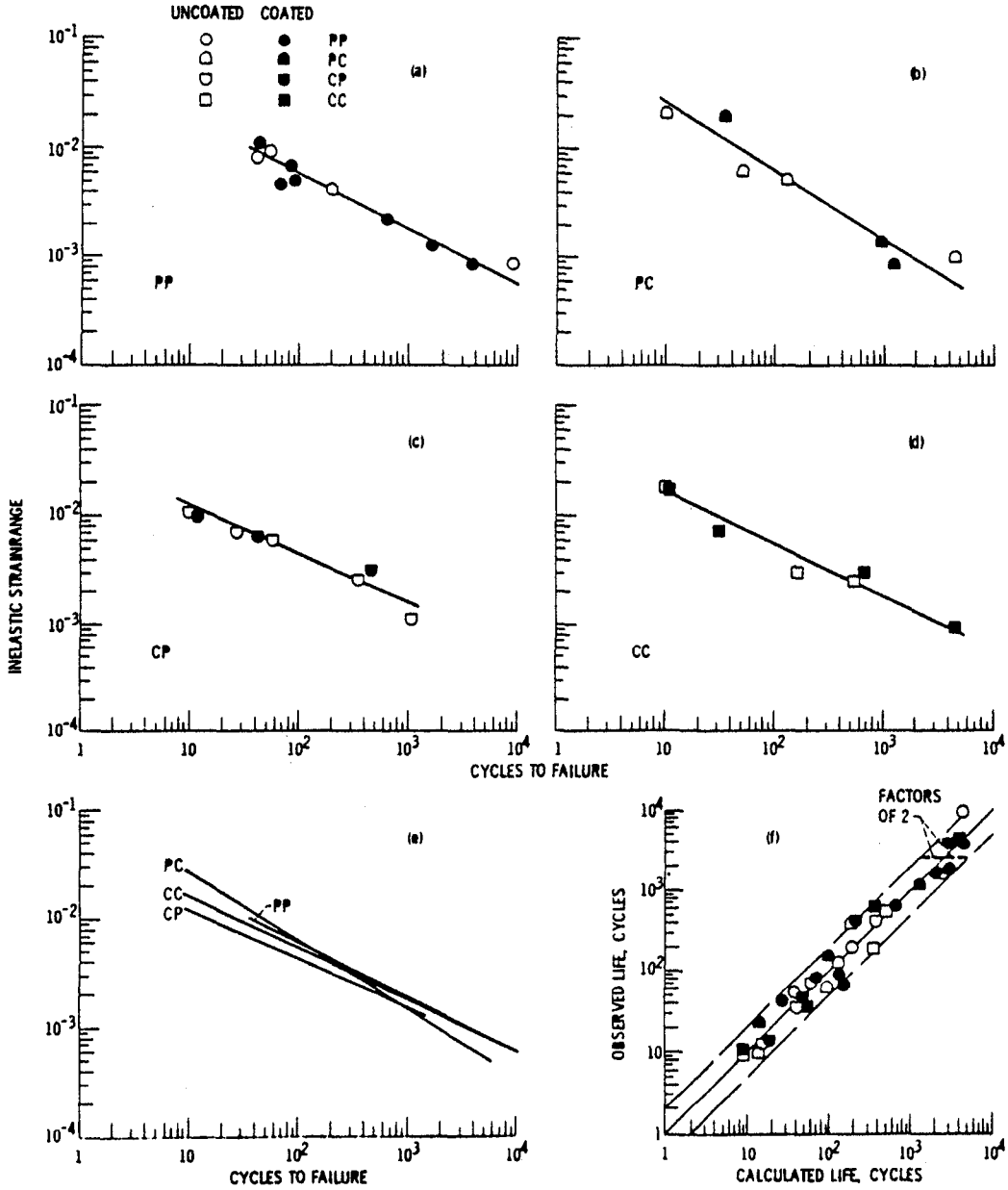

Figure 21. René 80 (NASA); Fatigue test results in air at 1000C for uncoated and coated specimens

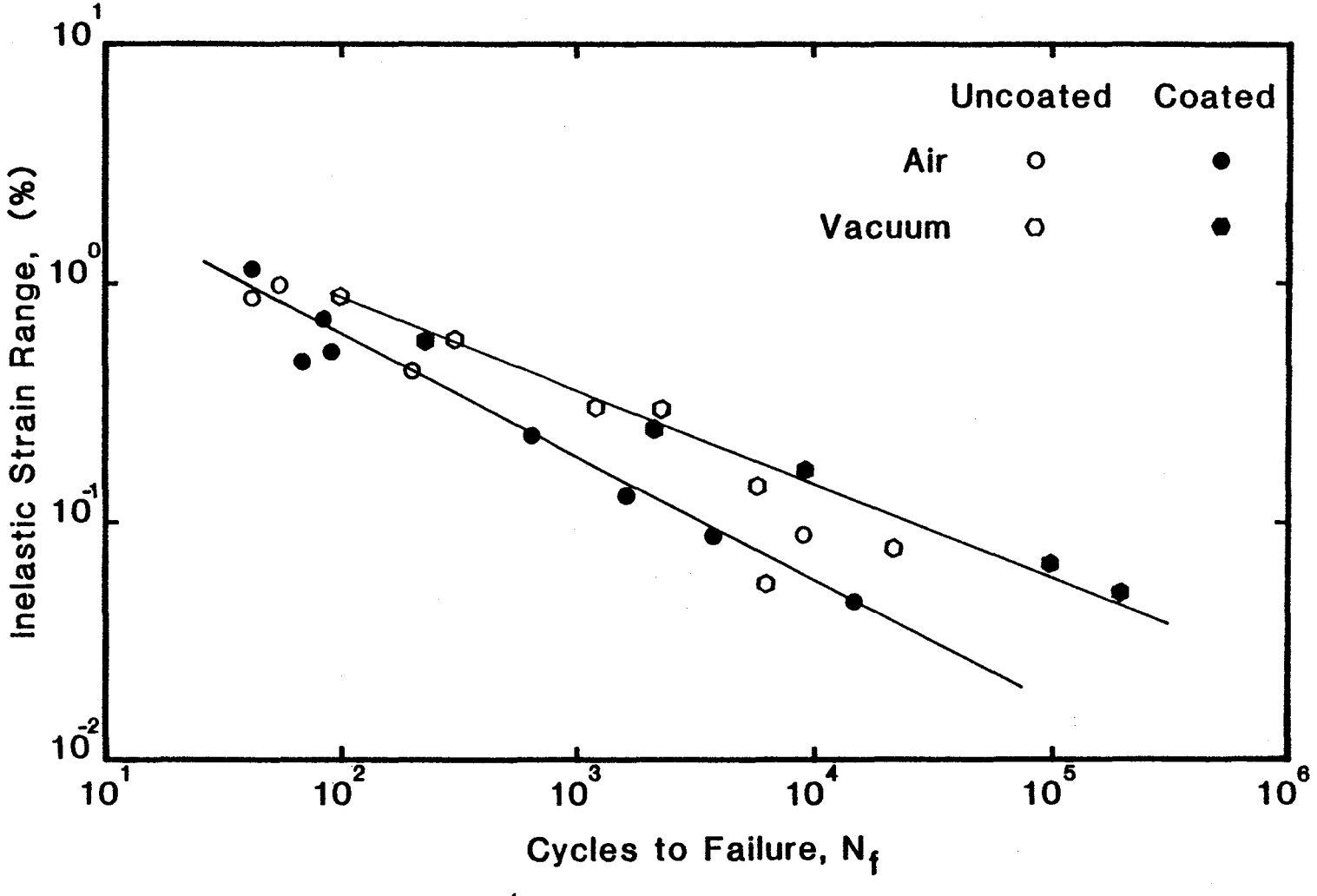

Figure 22. René 80; HRSC fatigue test results in vacuum (TRW) and in air (NASA) at 1000C for uncoated and coated specimens

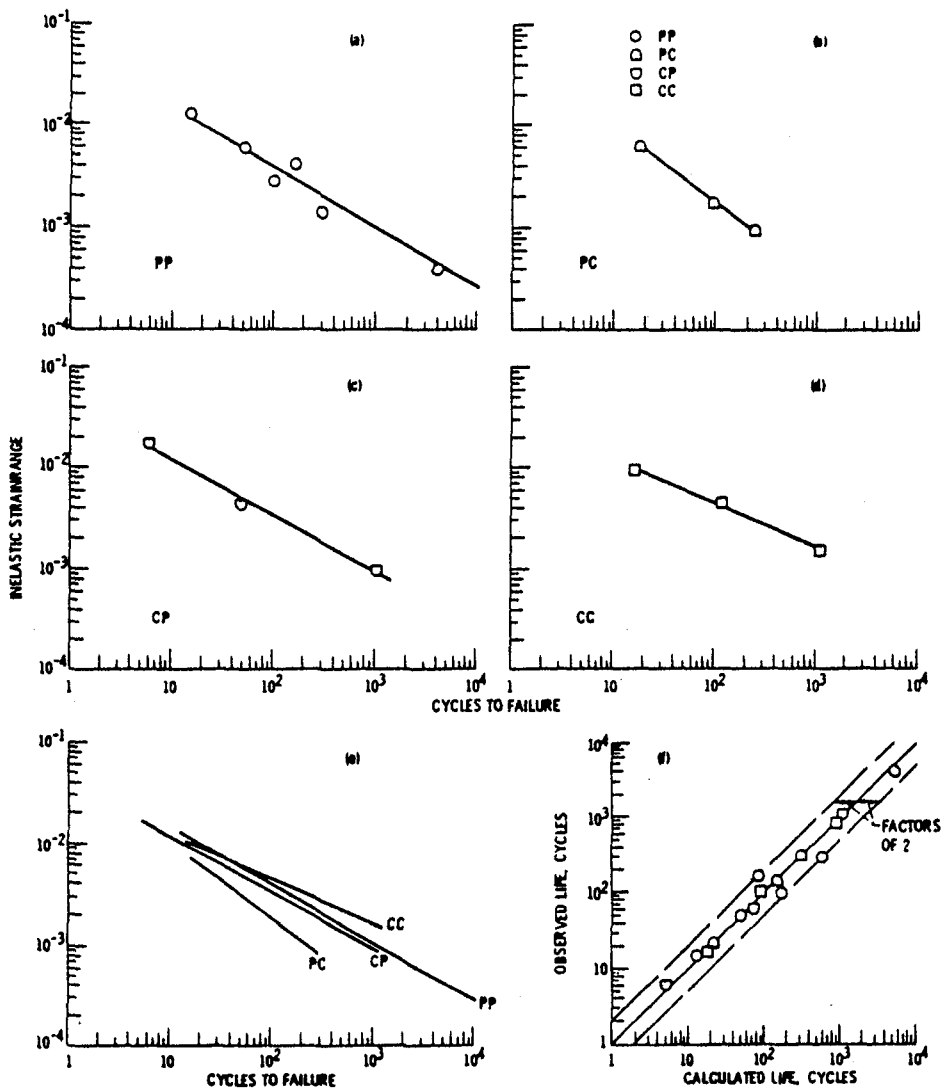

Figure 23. IN 100 (NASA); Fatigue test results in air at 925C for uncoated specimens

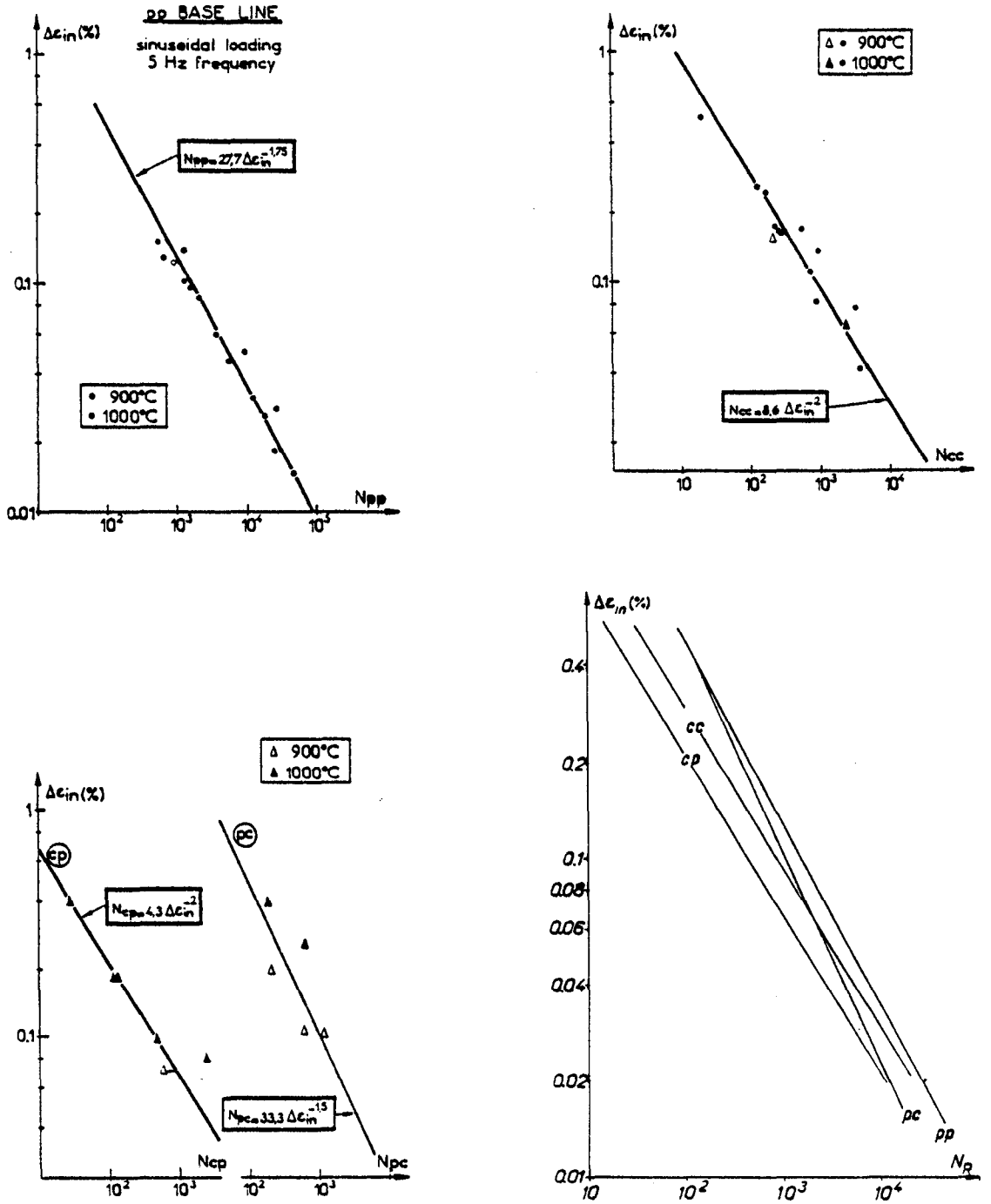

Figure 24. Coated IN 100 (ONERA); Fatigue test results in air at 1000C and 900C

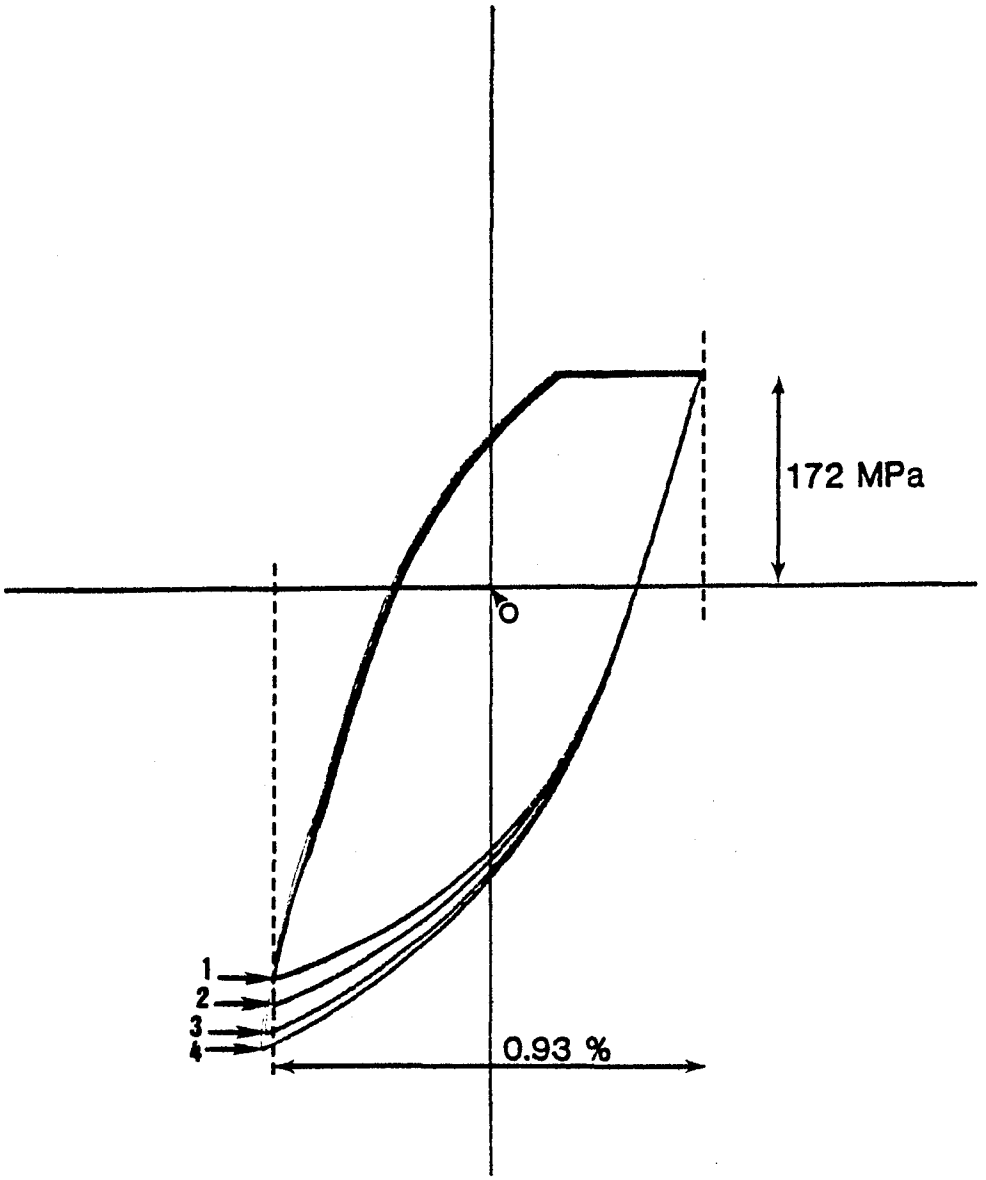

Figure 25. Uncoated René 80 (U of C); Hysteresis loops for a TCCR experiment in which the effect of strain rate on stress response was demonstrated. The nominal holding stress was 172 MPa

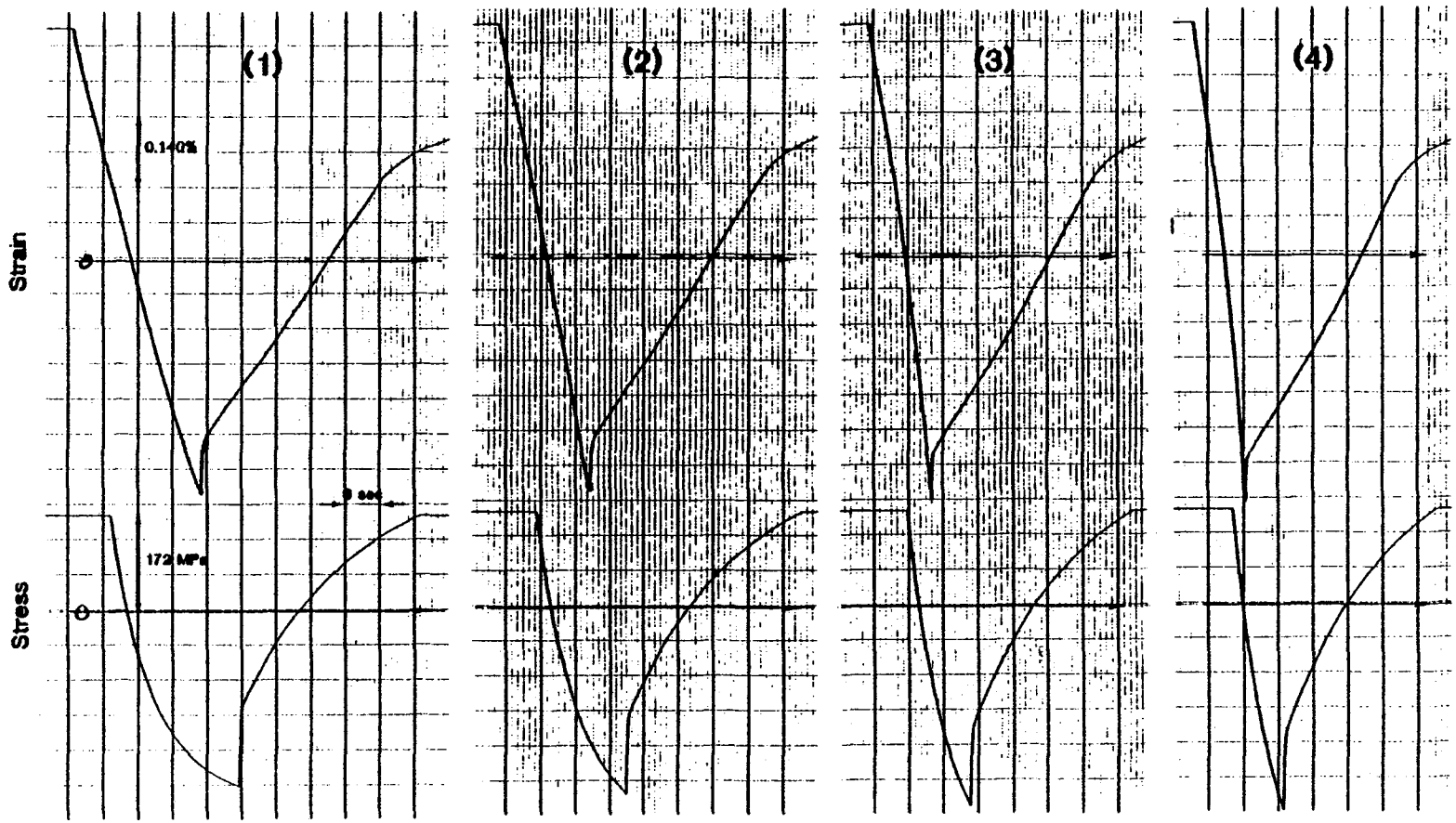

Figure 26. Uncoated René 80 (U of C); Strain time and stress time records for the TCCR experiment in which the effect of strain rate on stress response was demonstrated. The nominal holding stress was 172 MPa.

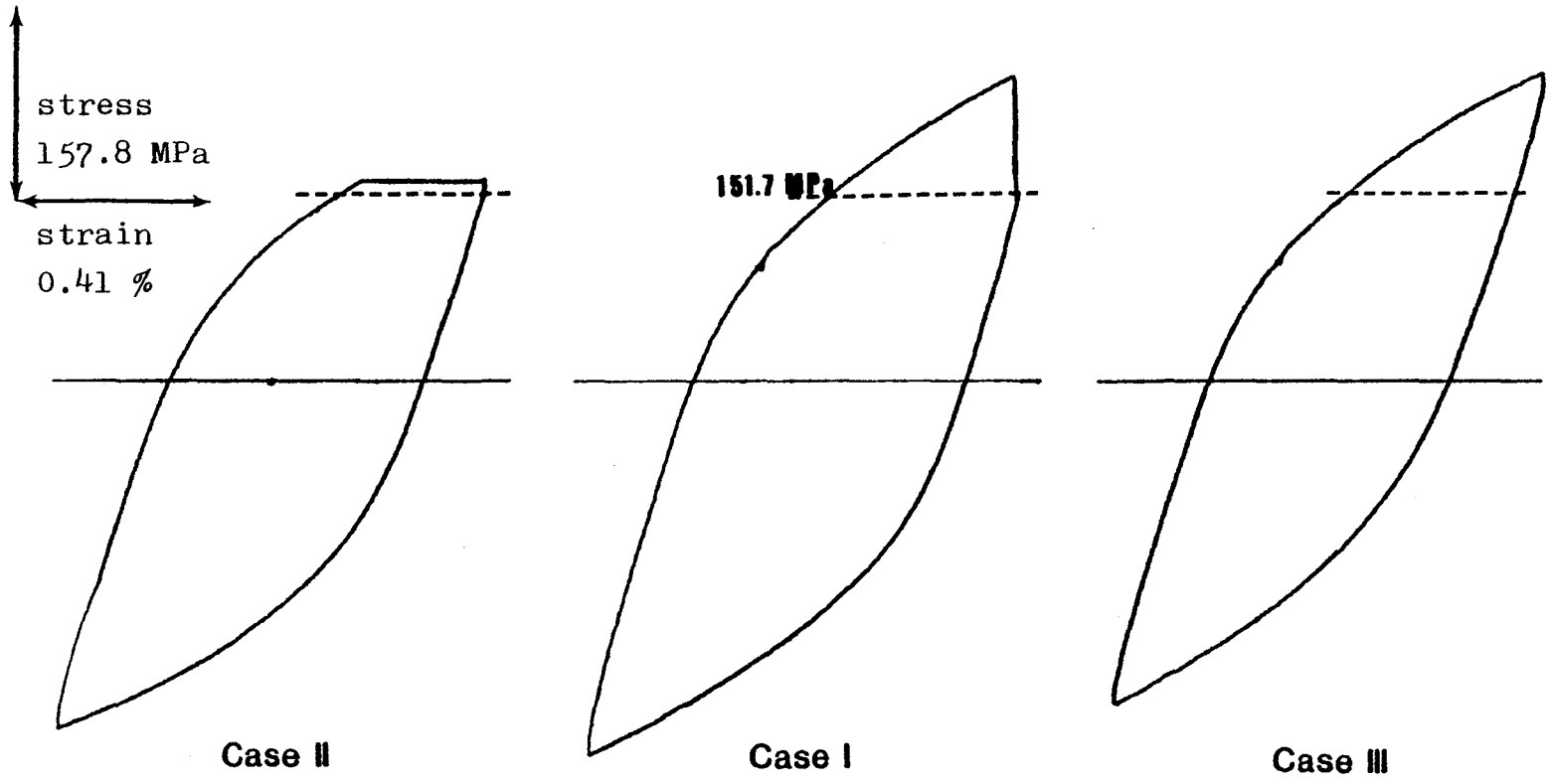

Figure 27. Uncoated René 80 (U of C); Hysteresis loops recorded for: Case I - a strain hold test, Case II - a tensile cyclic creep rupture test, Case III - a continuous cycling test

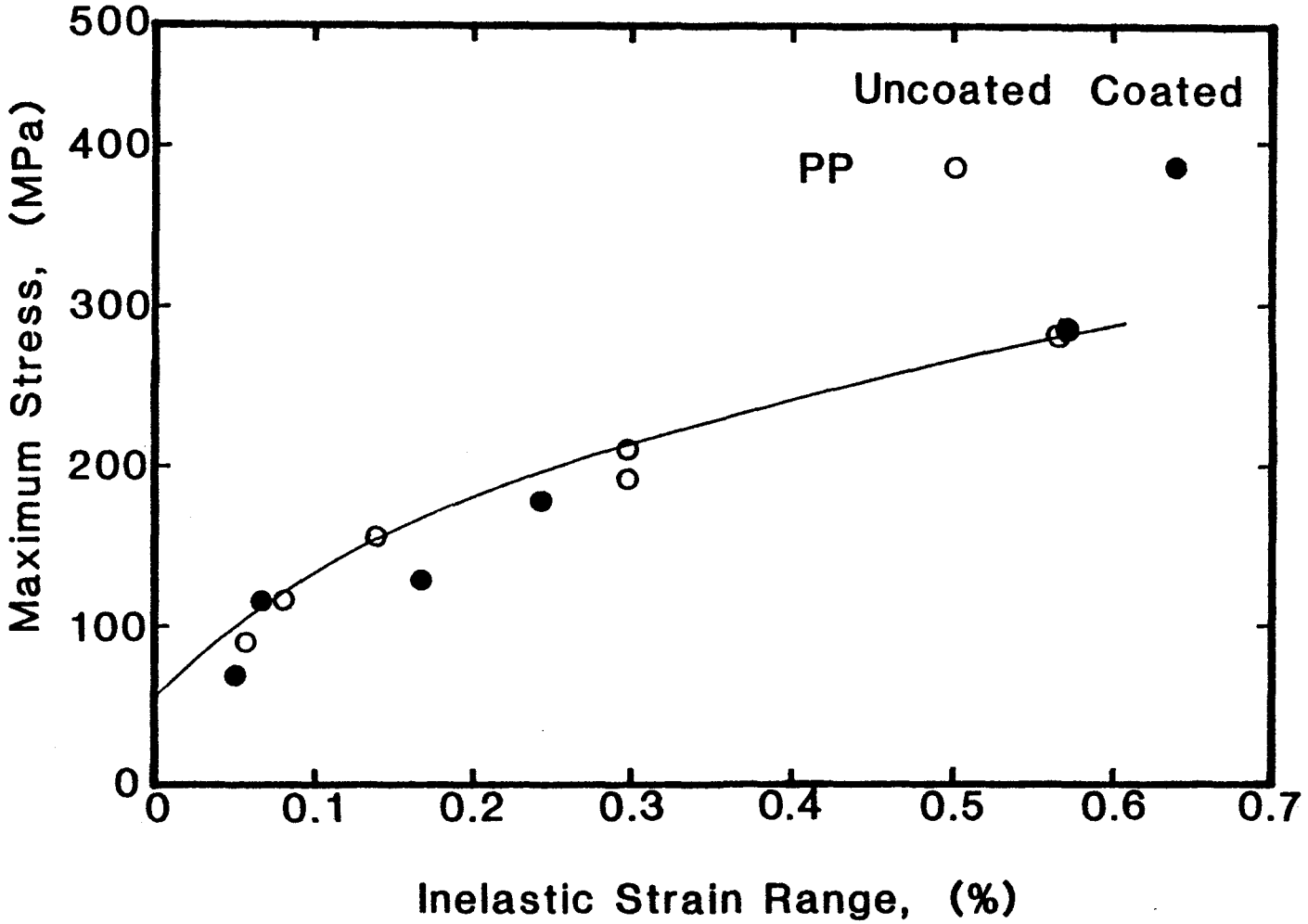

Figure 28. Maximum Stress versus Inelastic Strain Range for René 80 tested in vacuum at 1000C (TRW)

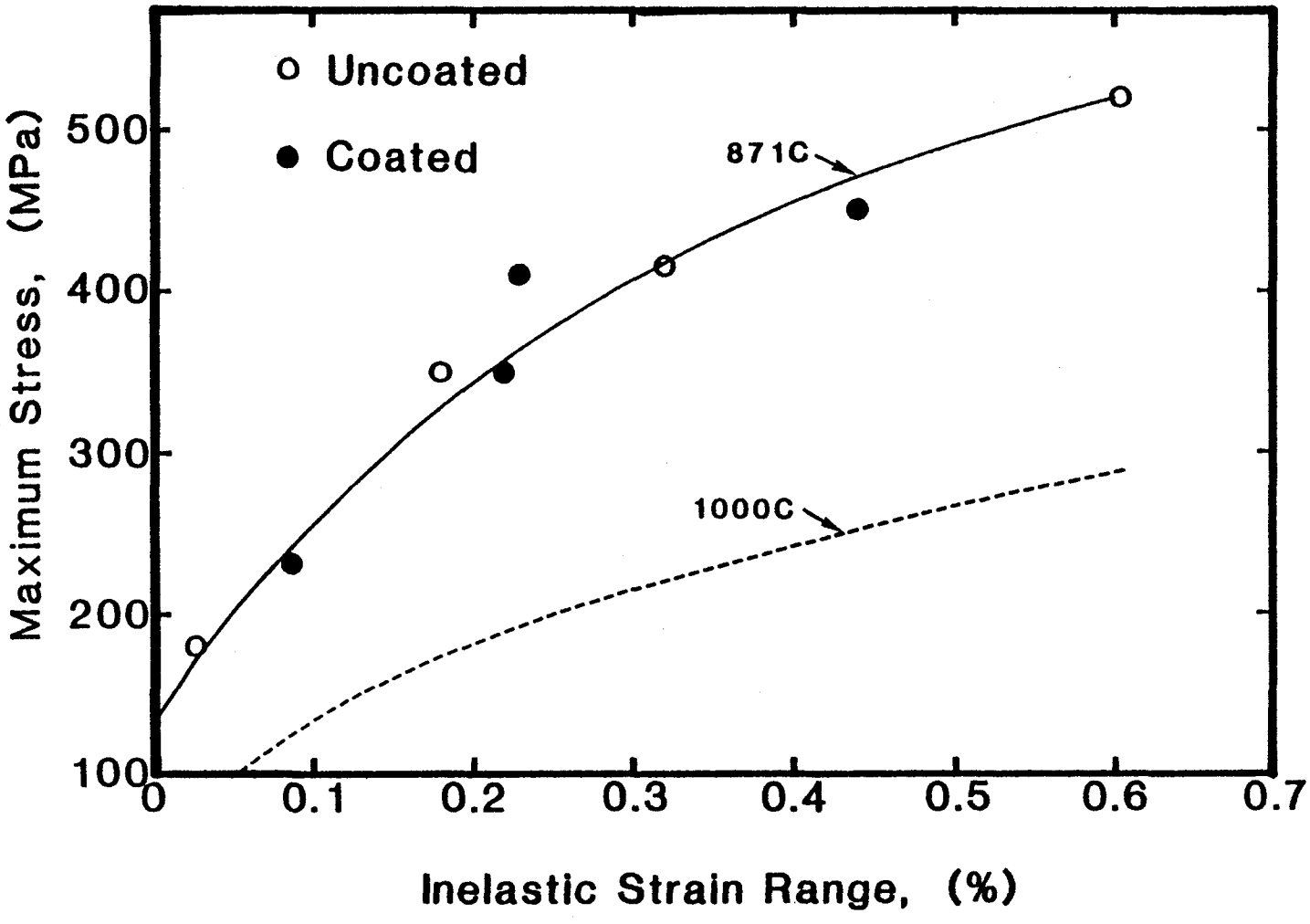

Figure 29. Maximum Stress versus Inelastic Strain Range for René 80 tested in vacuum at 871C (TRW)

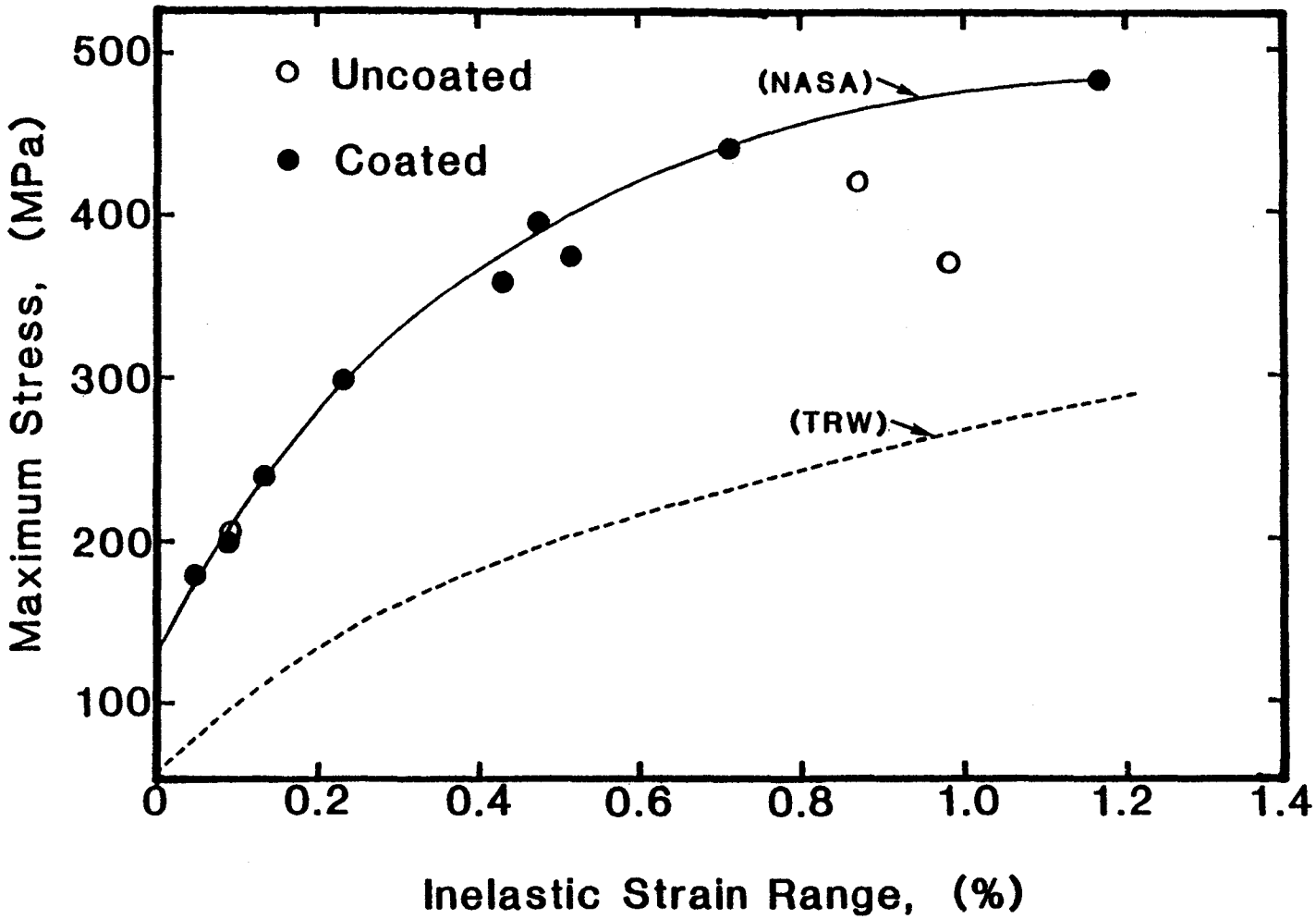

Figure 30. Maximum Stress versus Inelastic Strain Range for René 80 tested in air at 1000C (NASA)

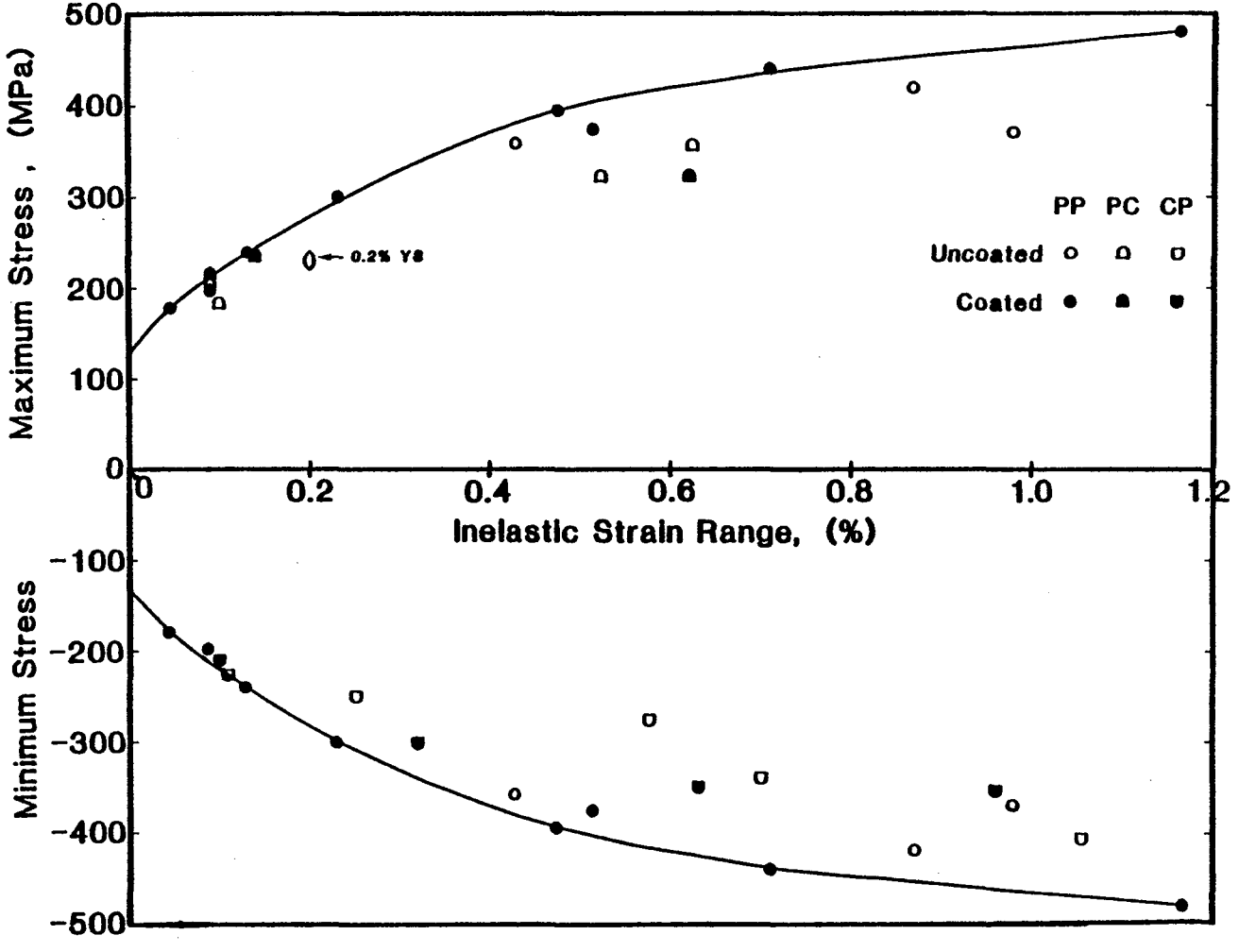

Figure 31. Maximum and Minimum Stress versus Inelastic Strain Range for René 80 tested in air at 1000C (NASA)

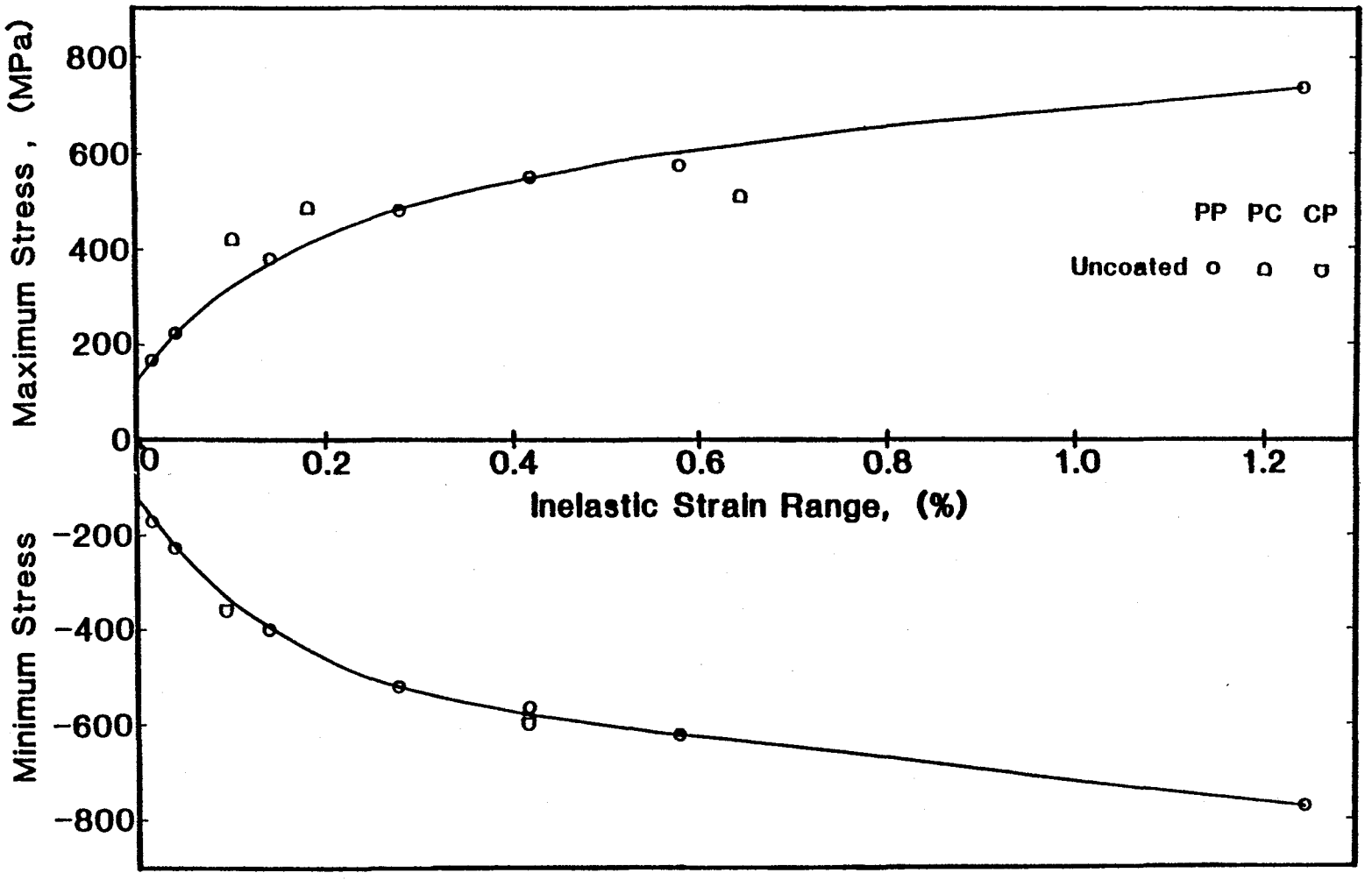

Figure 32. Maximum and Minimum Stress versus Inelastic Strain Range for IN 100 tested in air at 925C (NASA)

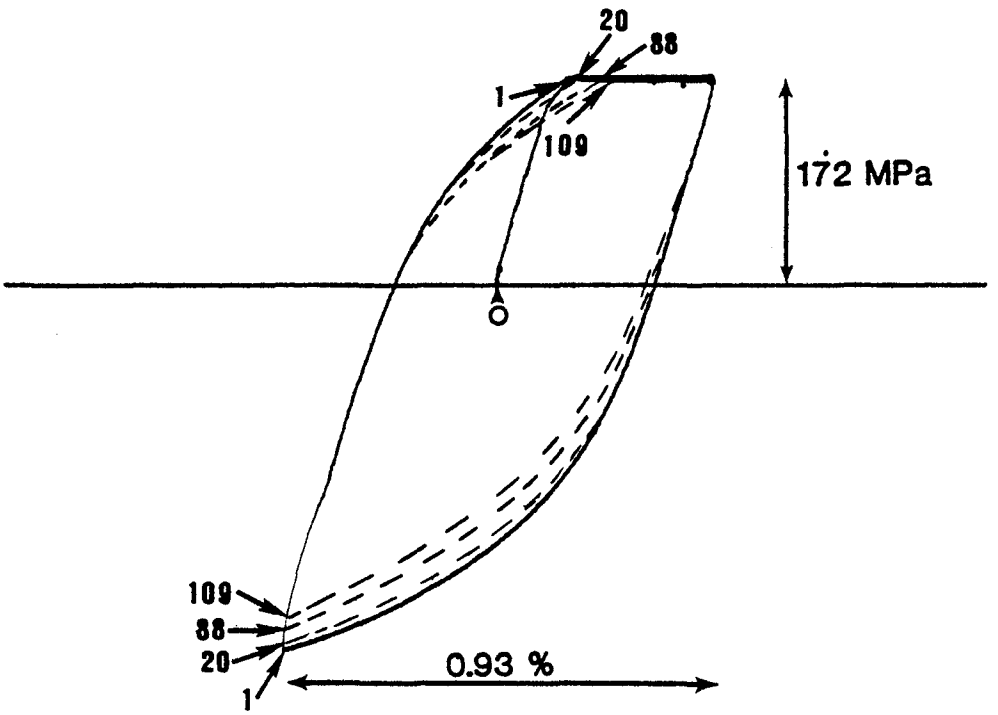

Figure 33. Uncoated René 80 (U of C); Hysteresis loops recorded for the TCCR test designated GR-1

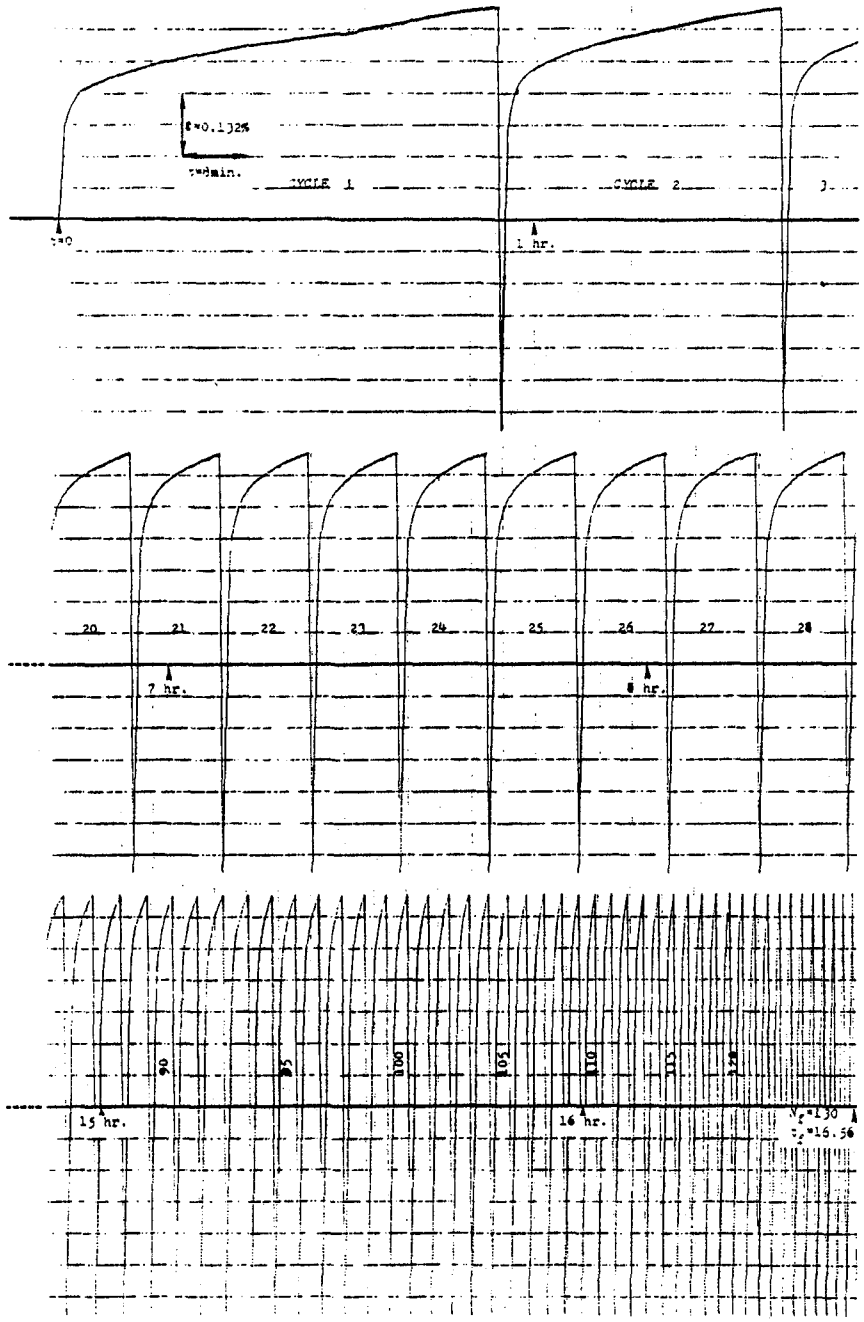

Figure 34. Uncoated René 80 (U of C); Segments of the Strain-time record for the TCCR test designated GR-1

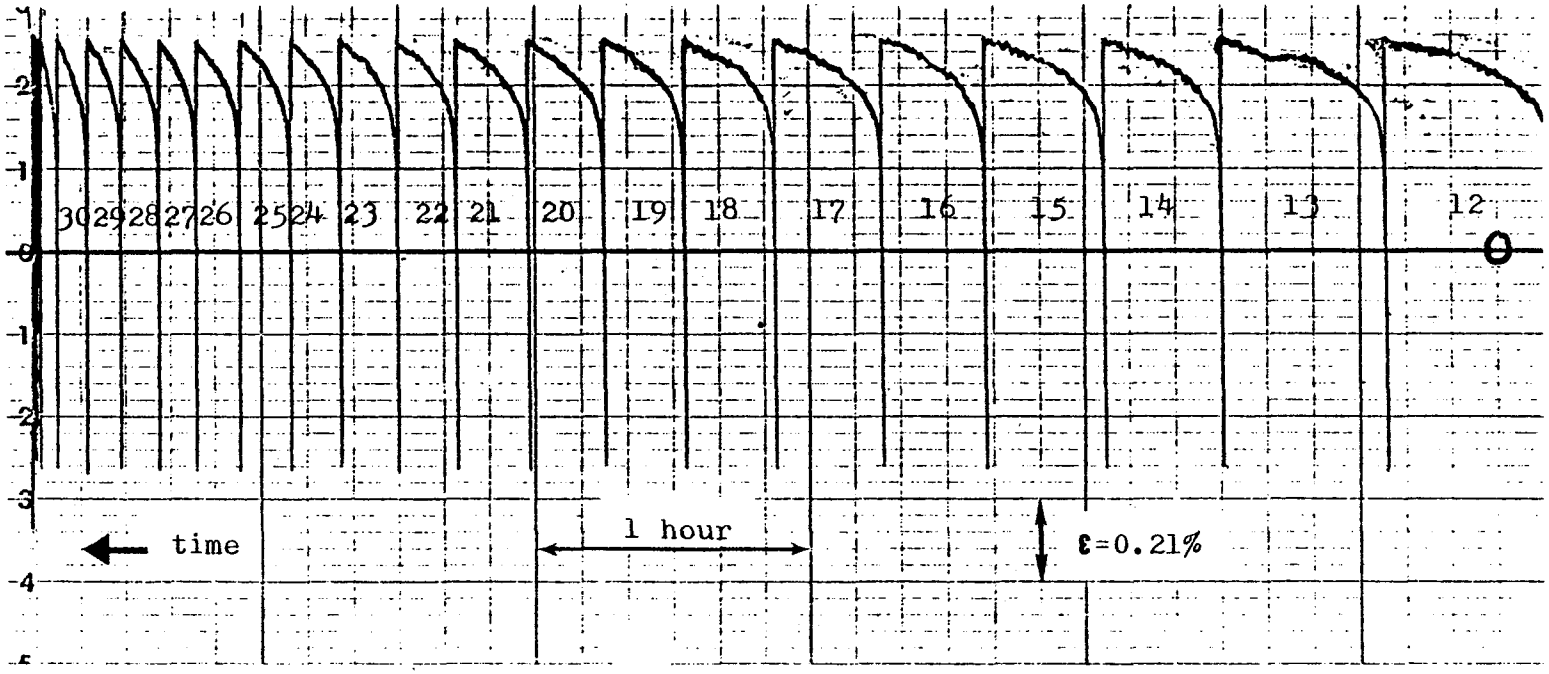

Figure 35. Coated René 80 (NASA); Segment of the strain-time record for the TCCR test designated Ree 305

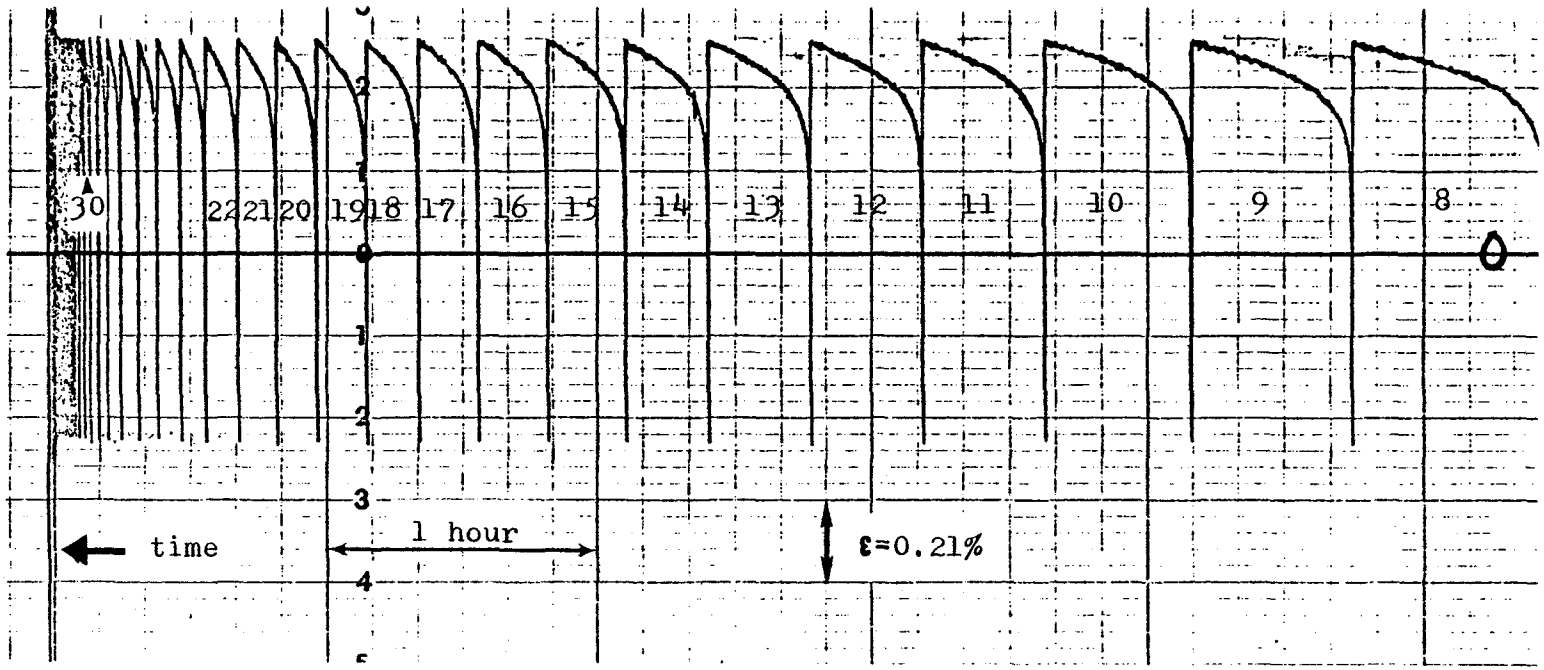

Figure 36. Uncoated René 80 (NASA); Segment of the strain-time record for the TCCR test designated Ree 208

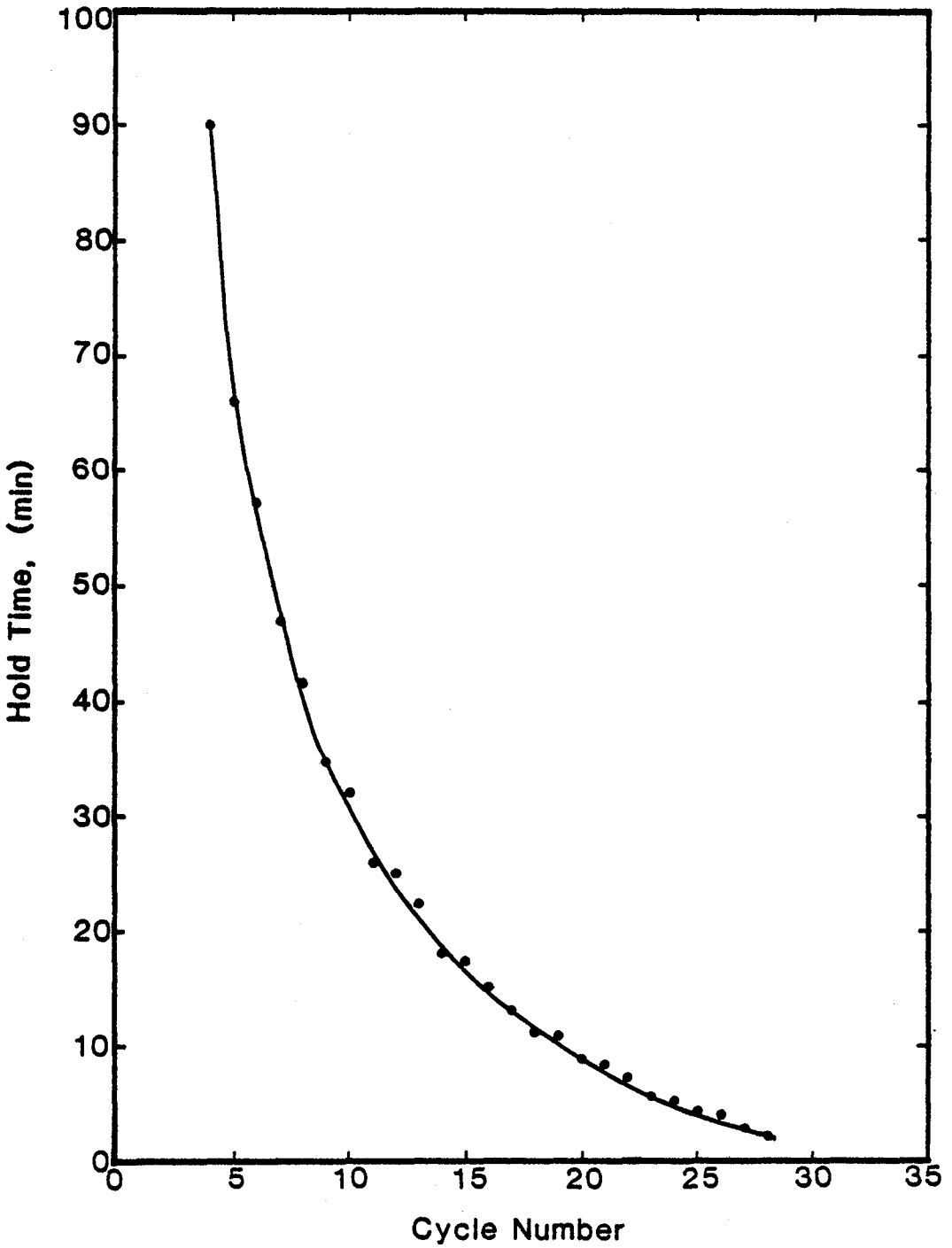

Figure 37. Hold Time versus Cycle Number for TCCR test Ree 305

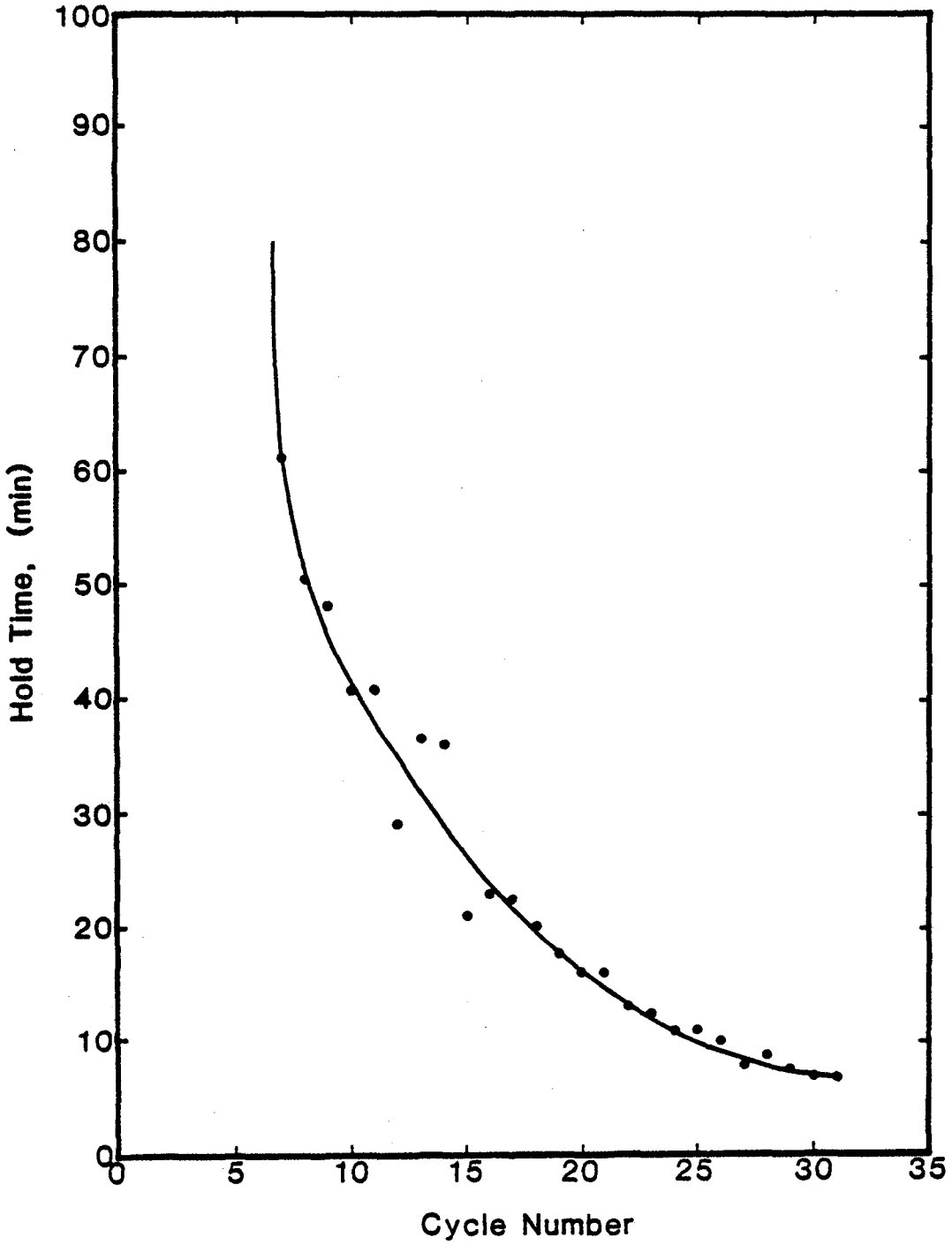

Figure 38. Hold Time versus Cycle Number for TCCR test Ree 208

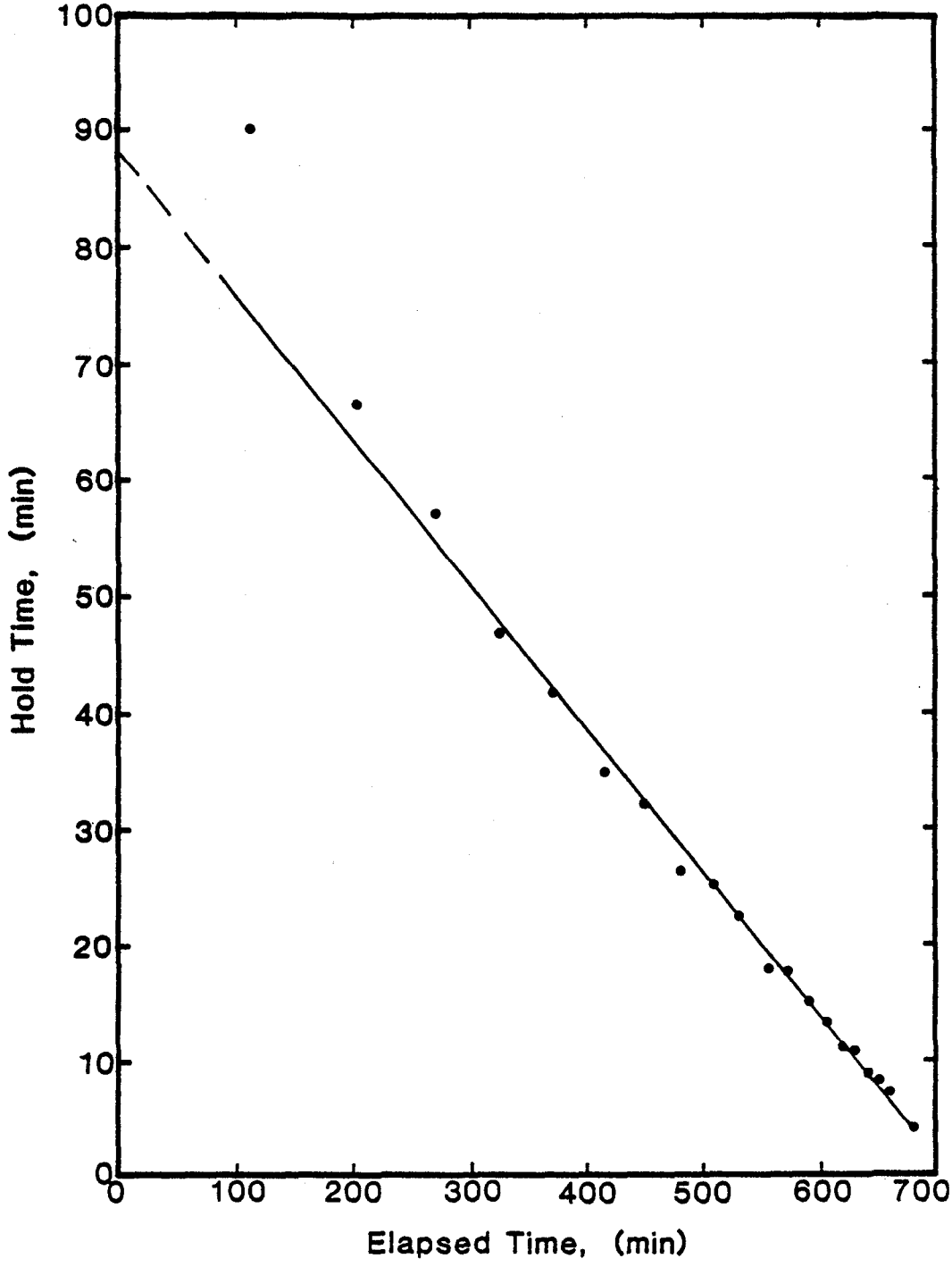

Figure 39. Hold Time versus Elapsed Time for TCCR test Ree 305

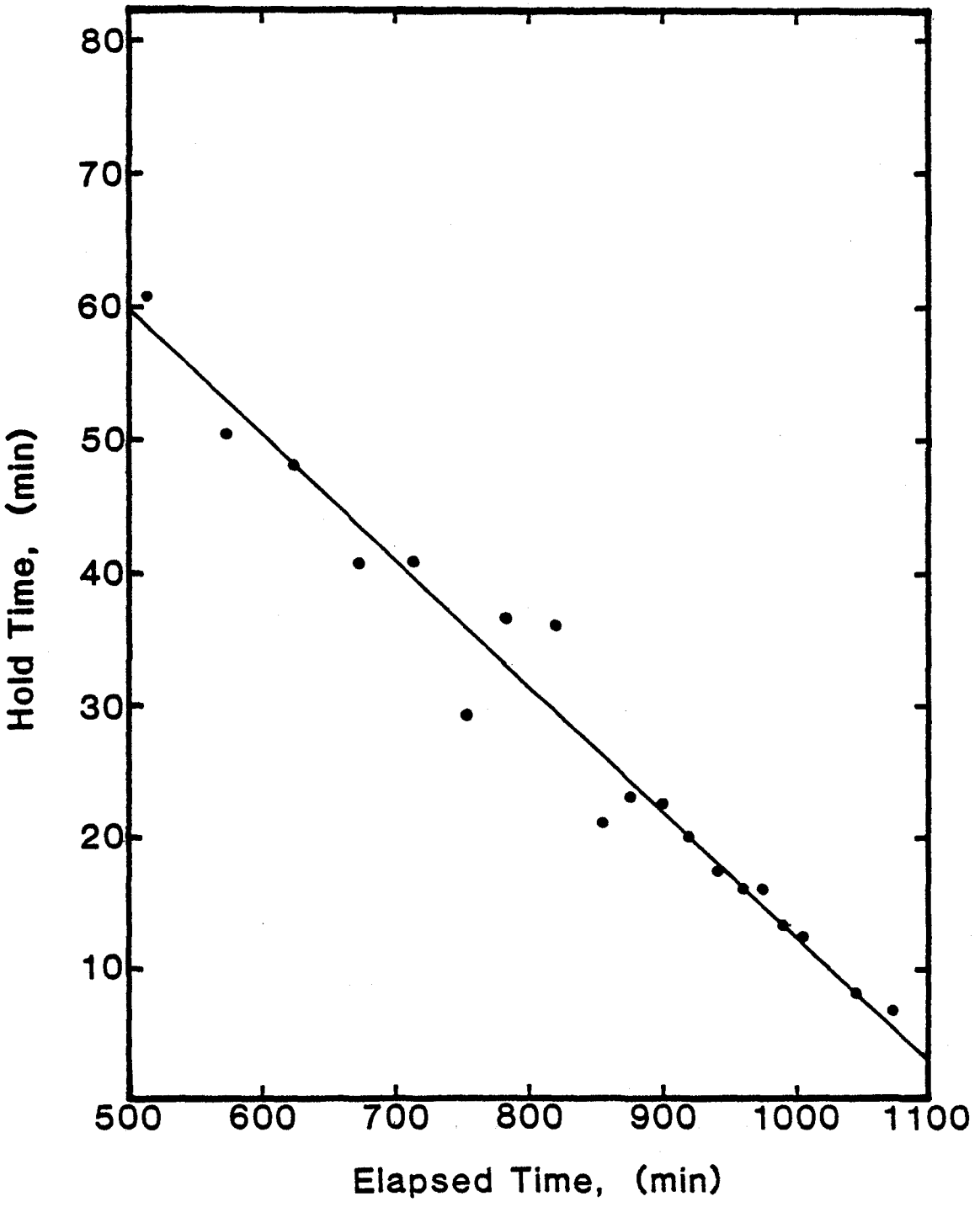

Figure 40. Hold Time versus Elapsed Time for TCCR test Ree 208

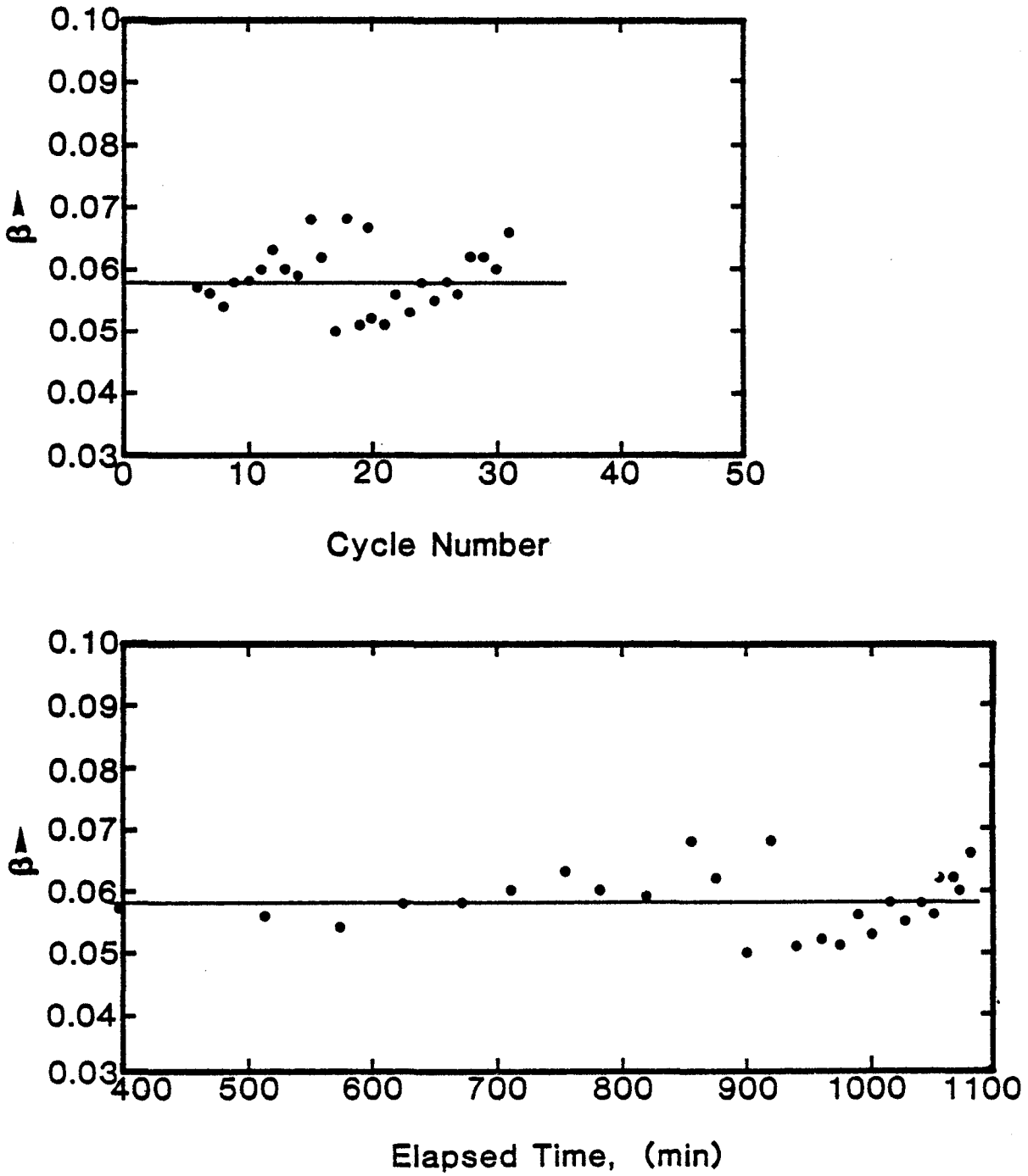

Figure 41. β versus Cycle Number and β versus Elapsed Time for the Eq. [17] representation of inelastic strain in TCCR test Ree 208

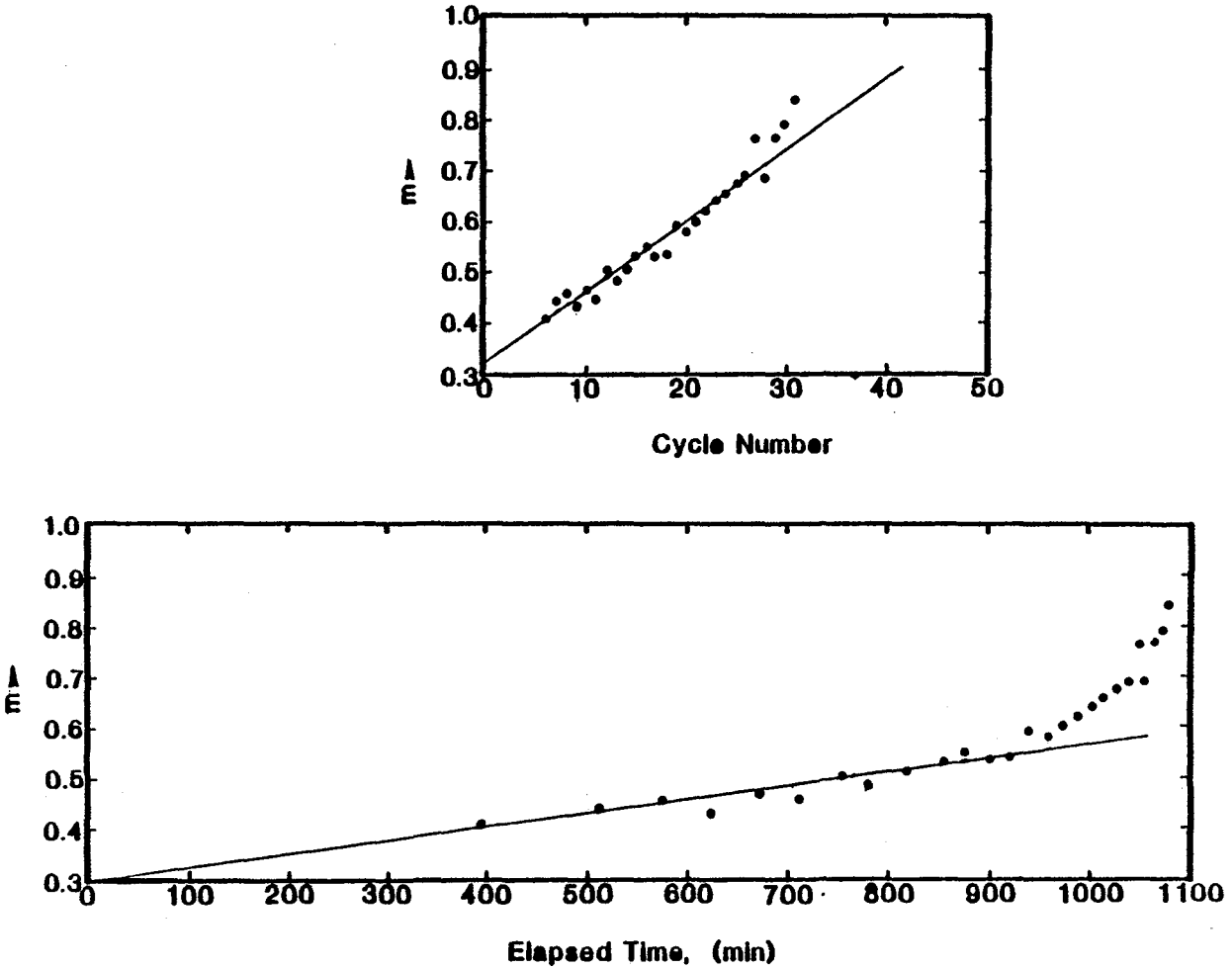

Figure 42. m versus Cycle Number and m versus Elapsed Time for the Eq. [17] representation of inelastic strain in TCCR test Ree 208

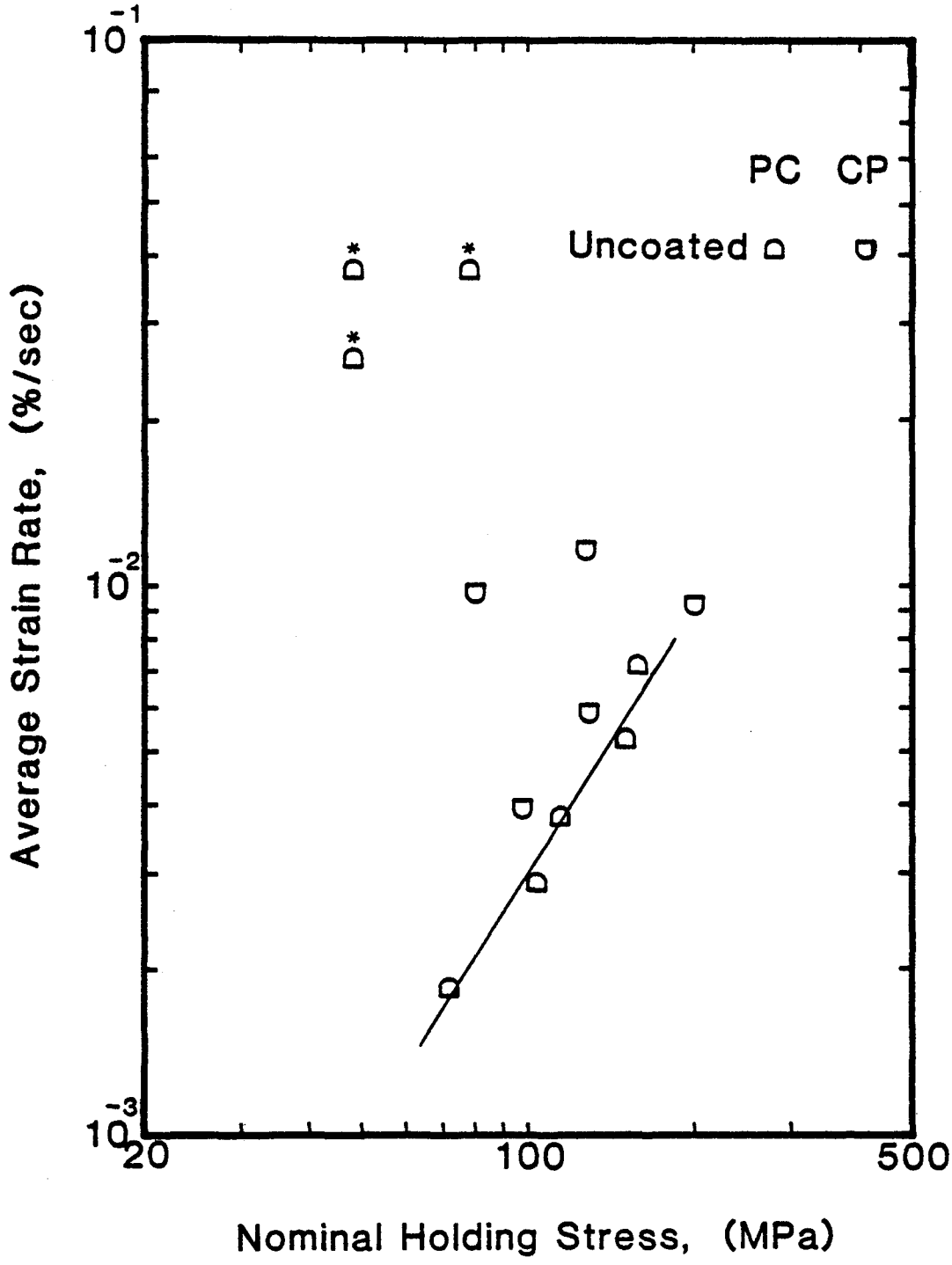

Figure 43. Average Strain Rate versus Nominal Stress for uncoated René 80 tested in vacuum at 1000C (TRW)

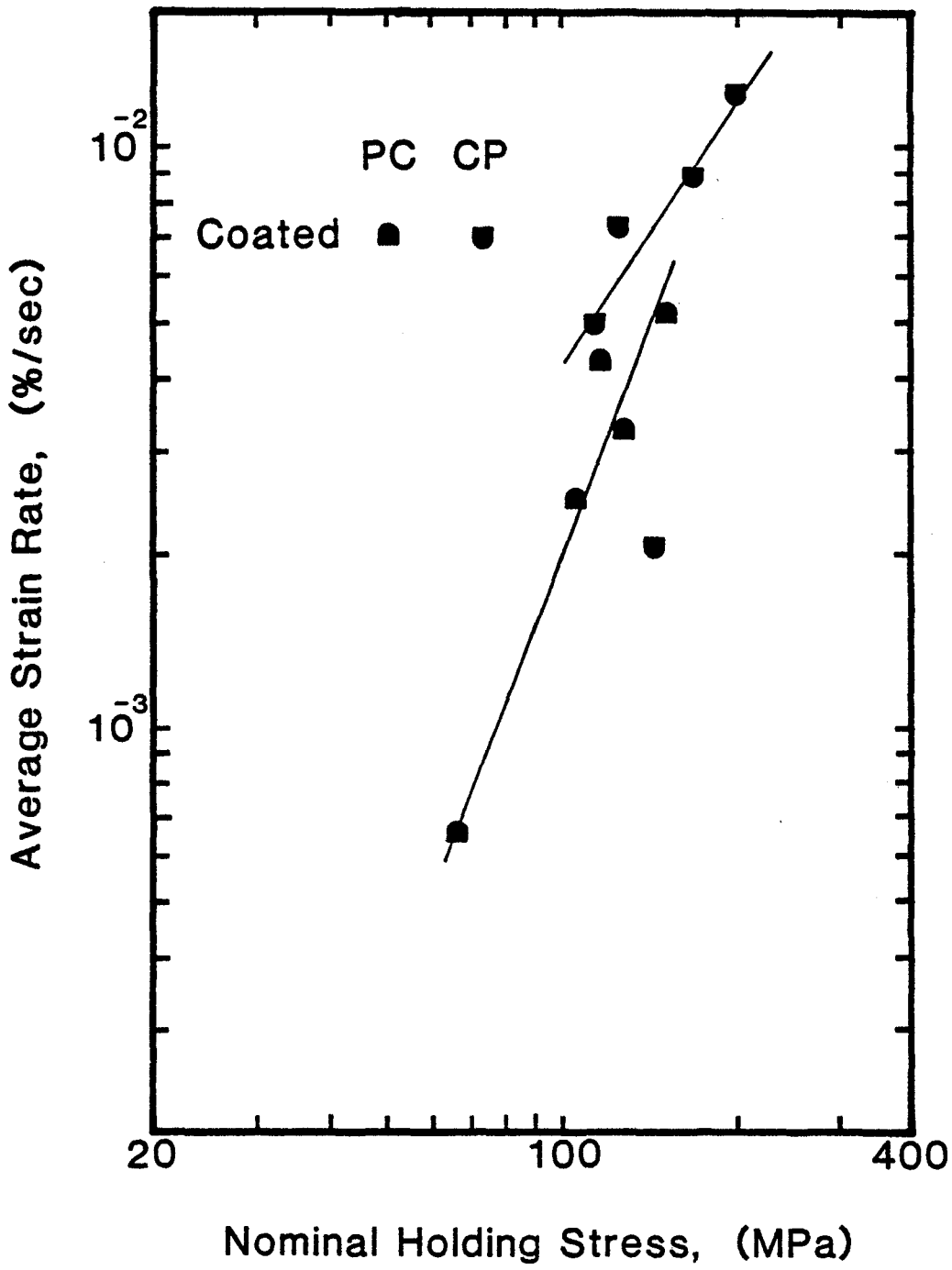

Figure 44. Average Strain Rate versus Nominal Stress for coated René 80 tested in vacuum at 1000C (TRW)

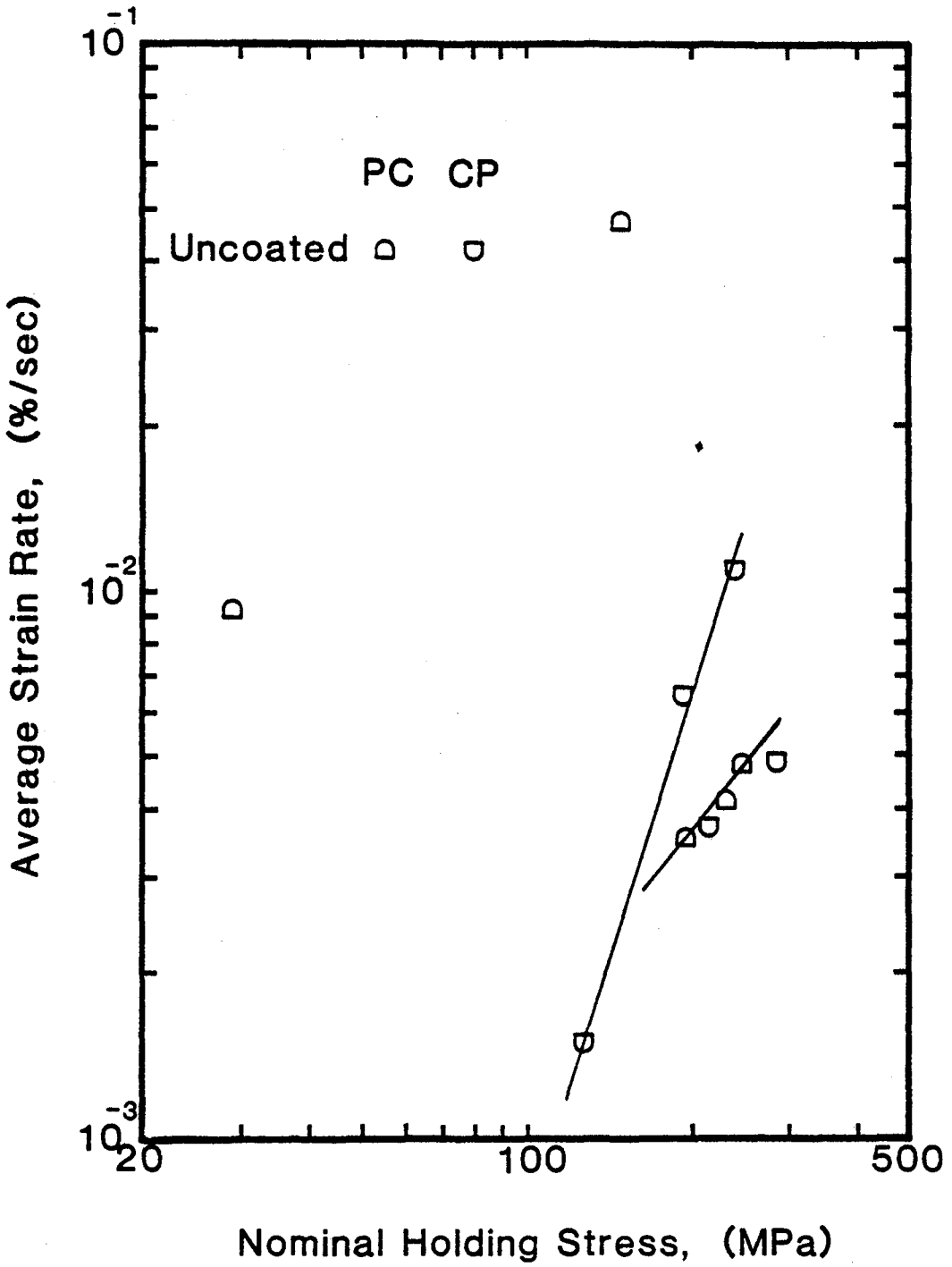

Figure 45. Average Strain Rate versus Nominal Stress for uncoated René 80 tested in vacuum at 871C (TRW)

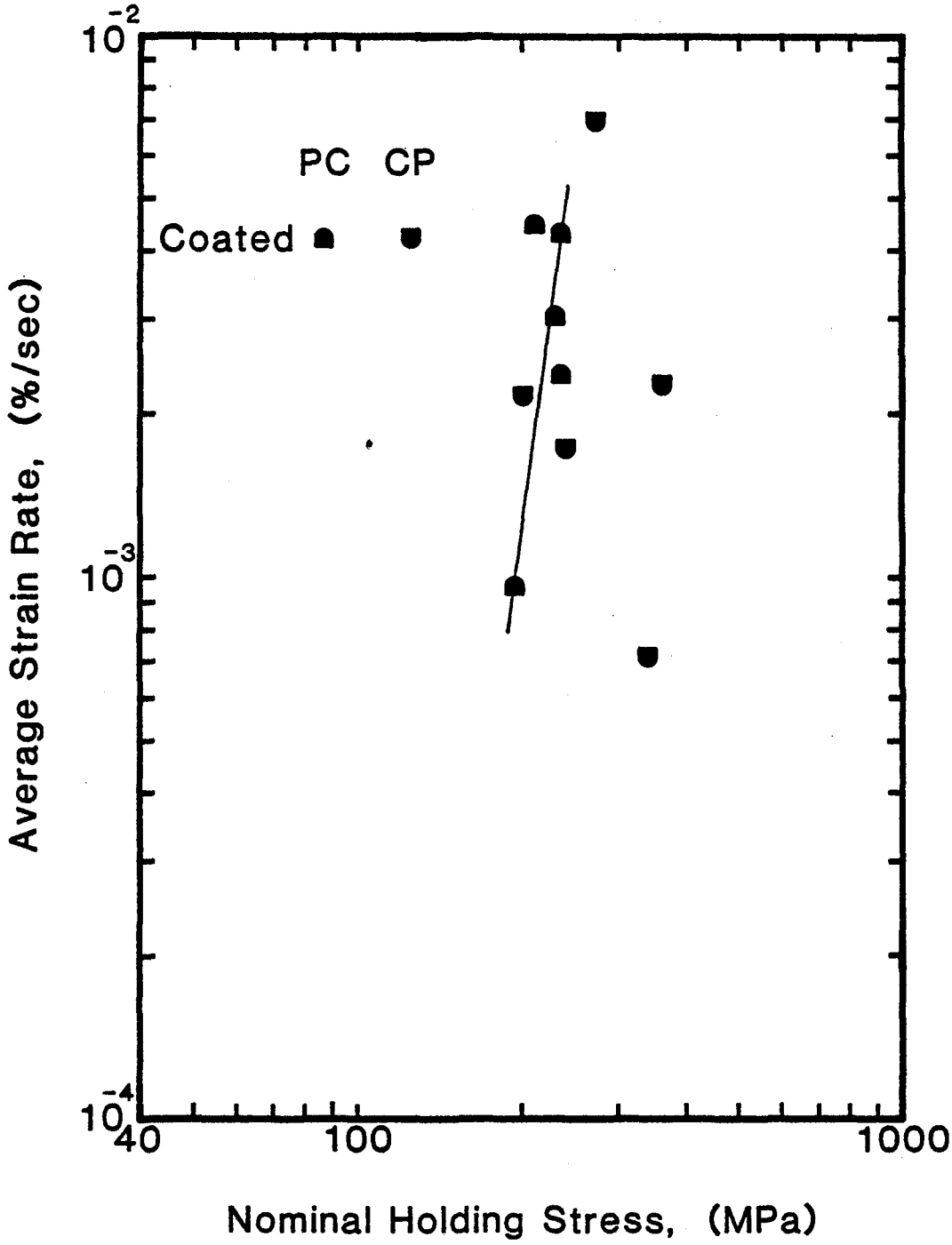

Figure 46. Average Strain Rate versus Nominal stress for coated René 80 tested in vacuum at 871C (TRW)

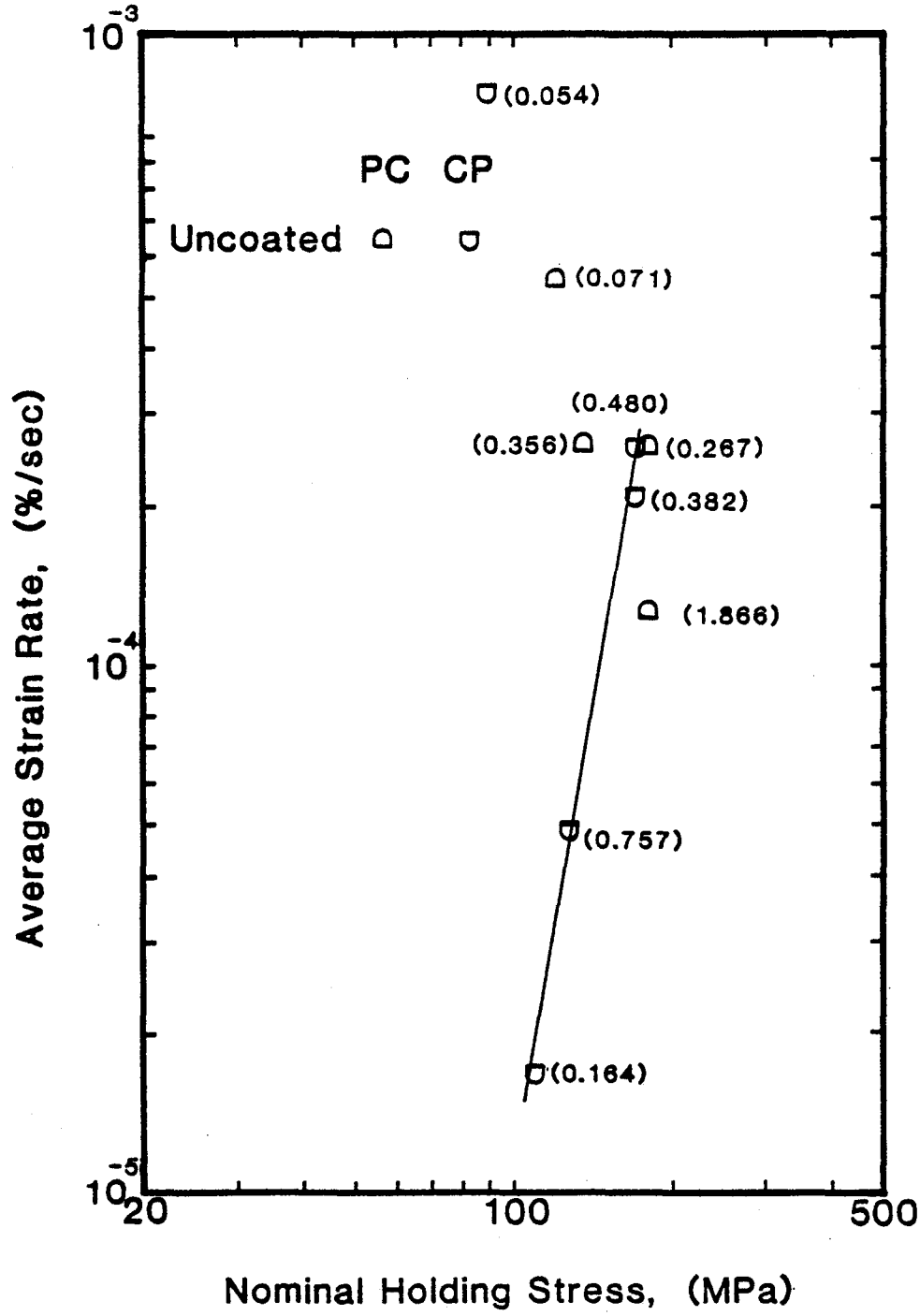

Figure 47. Average Strain Rate versus Nominal Stress for uncoated René 80 tested in air at 1000C (NASA)

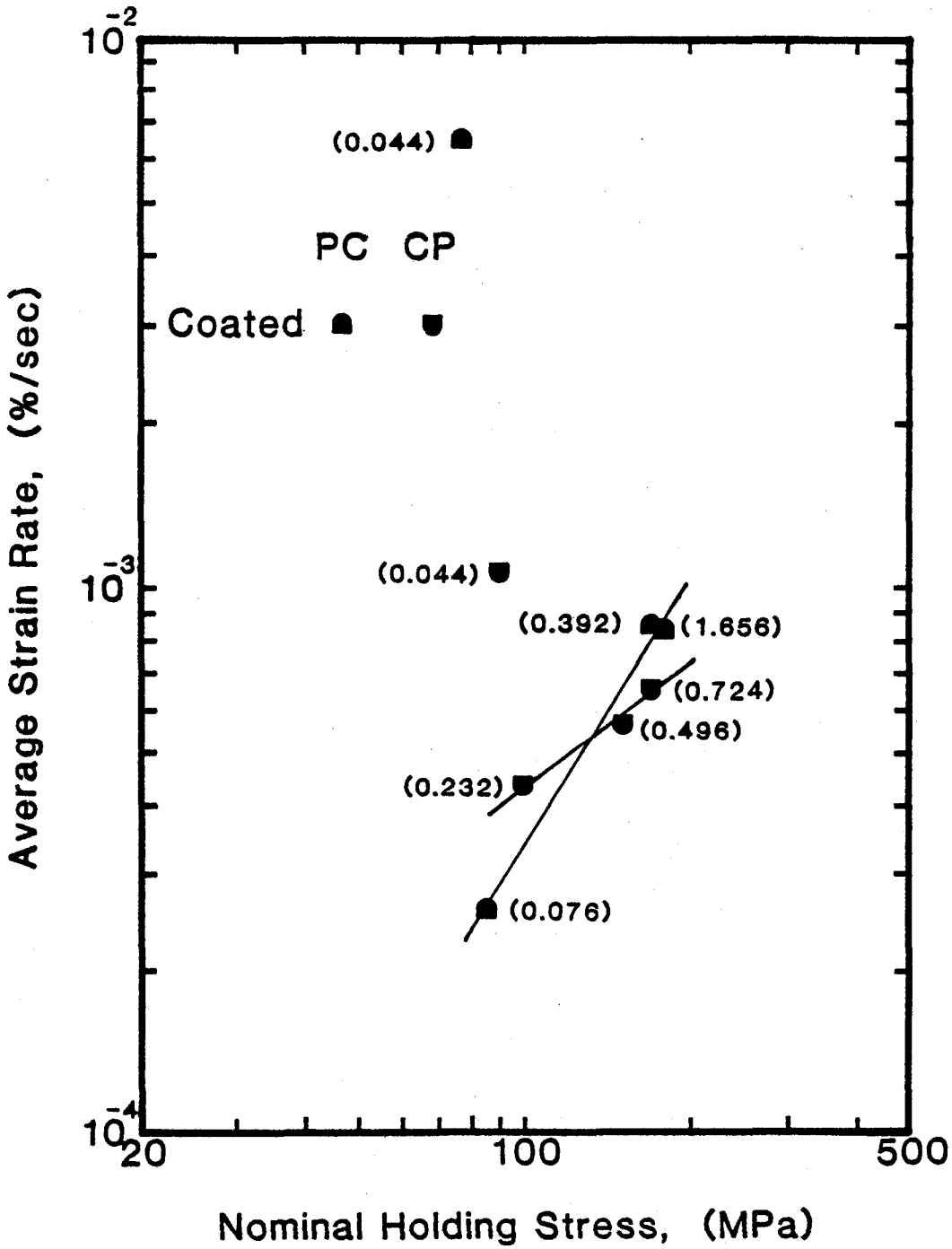

Figure 48. Average Strain Rate versus Nominal Stress for coated René 80 tested in air at 1000C (NASA)

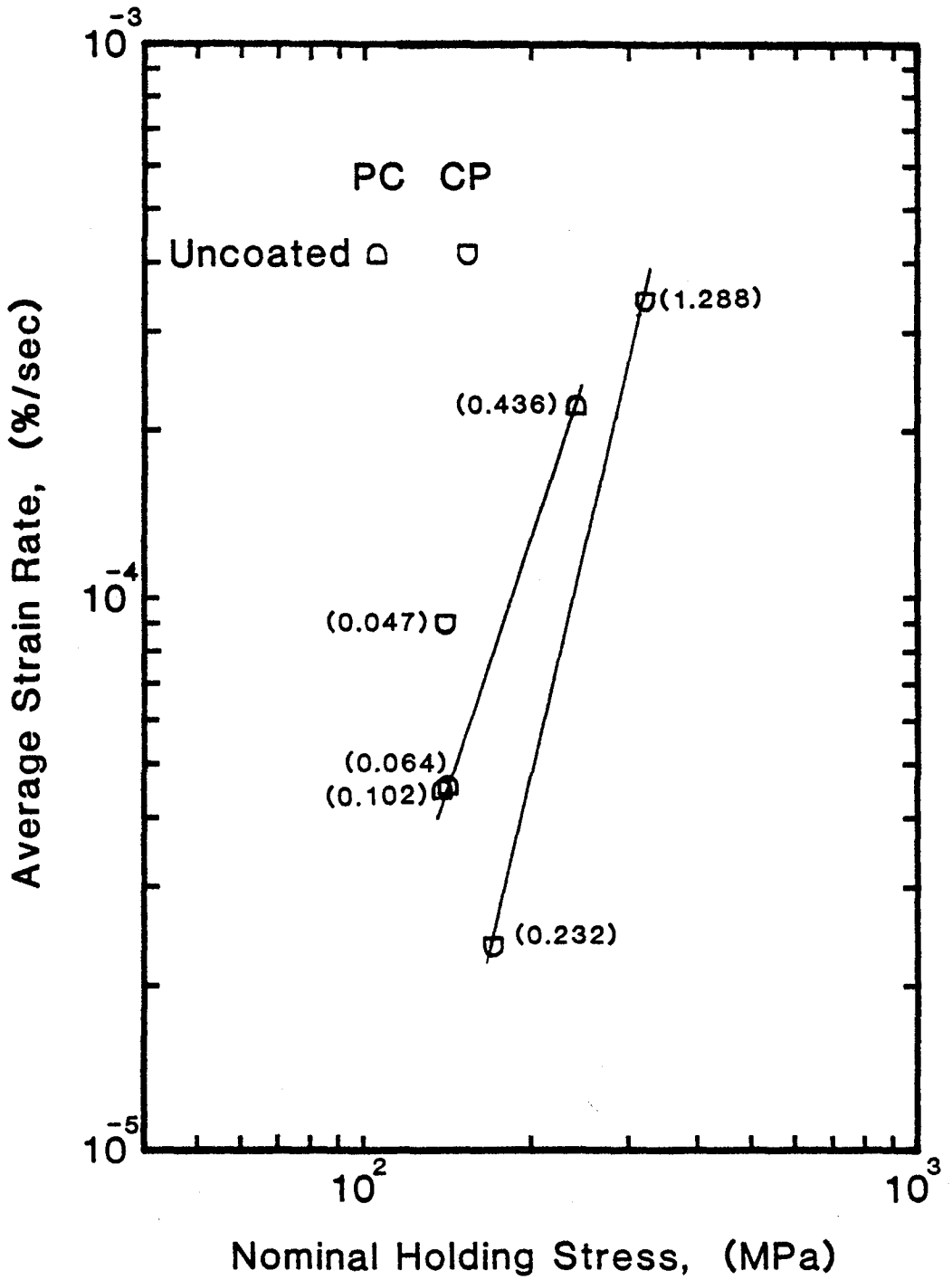

Figure 49. Average Strain Rate versus Nominal Stress for uncoated IN 100 tested in air at 925C (NASA)

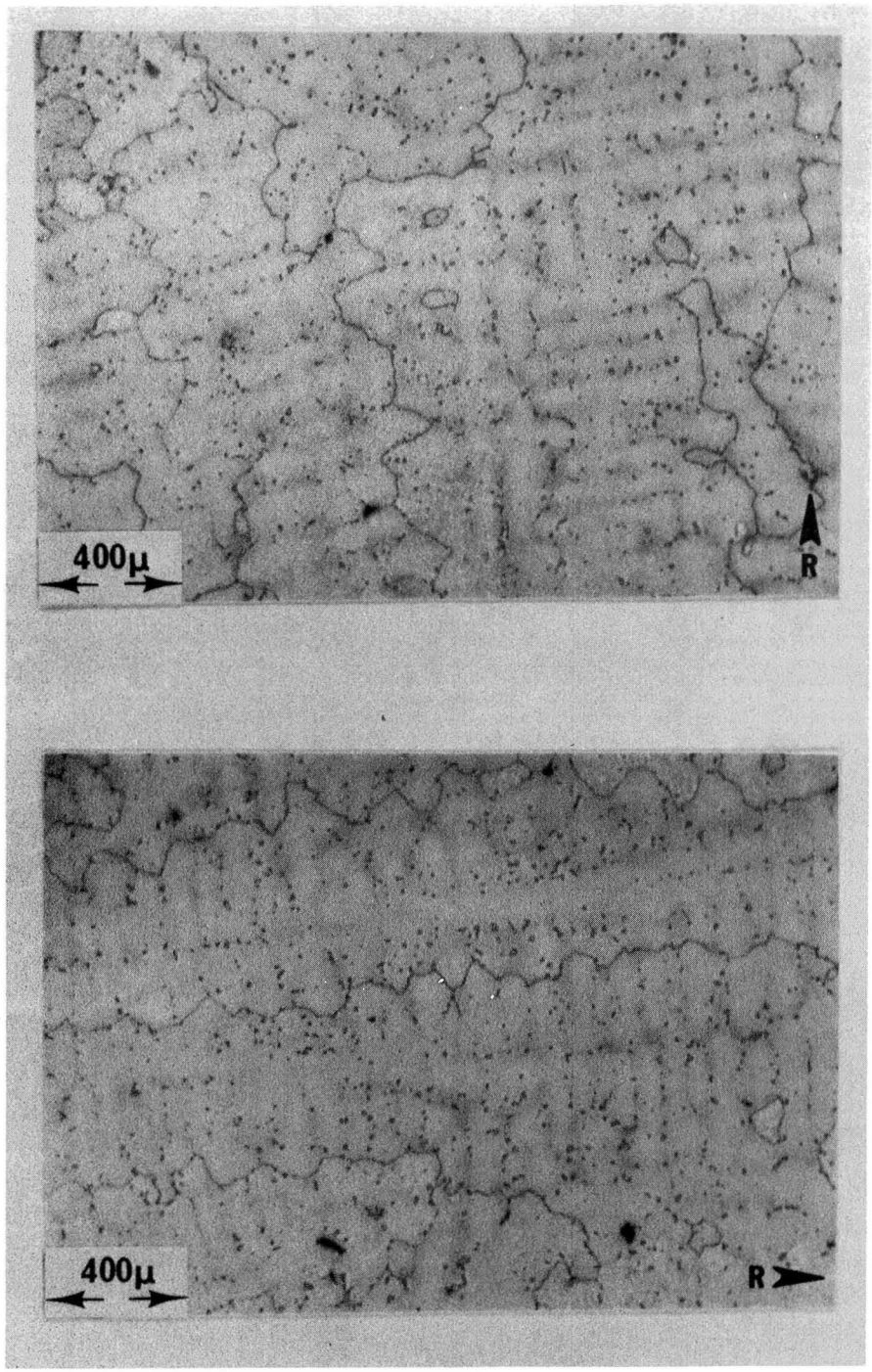

Figure 50. René 80 (NASA & TRW); untested microstructure from the head of a specimen. The arrow head indicates the radial direction.

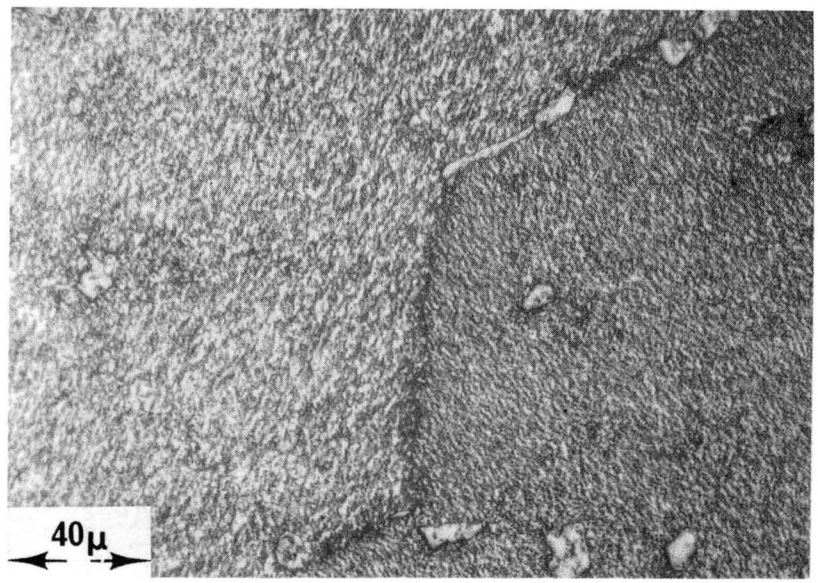

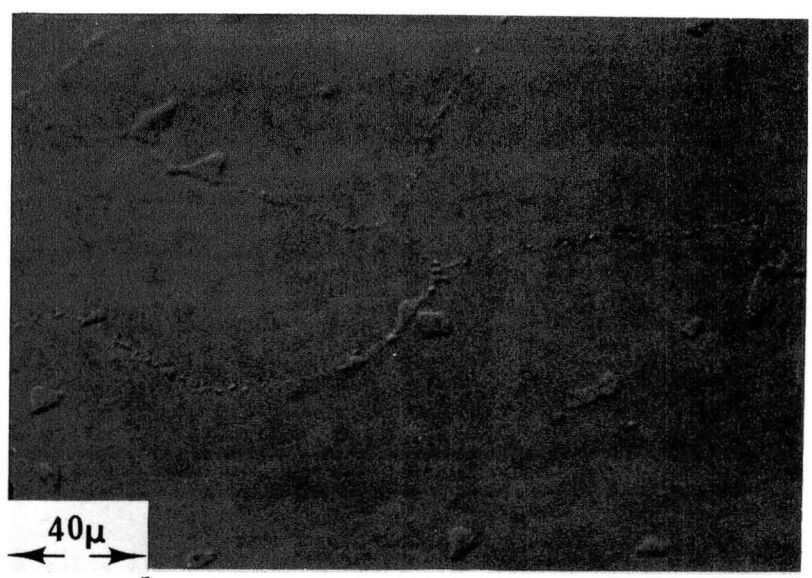

Figure 51. René 80 (NASA & TRW); untested microstructure from the head of a specimen.

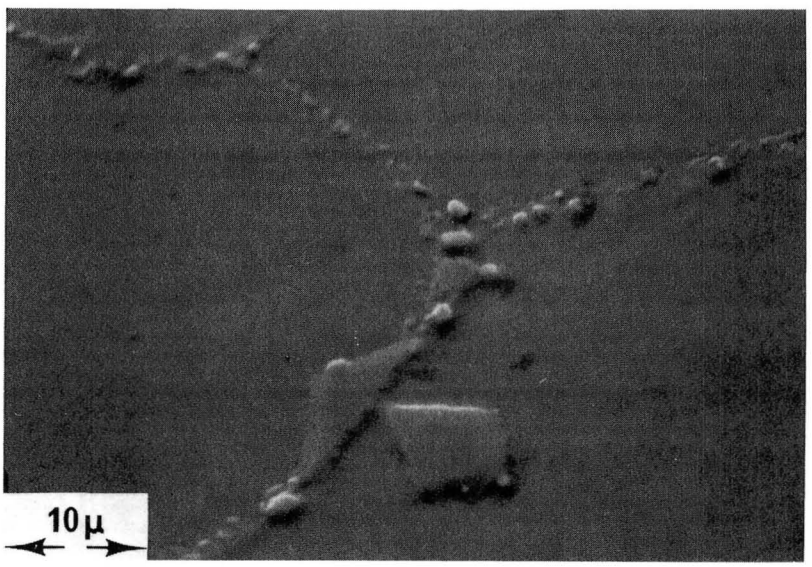

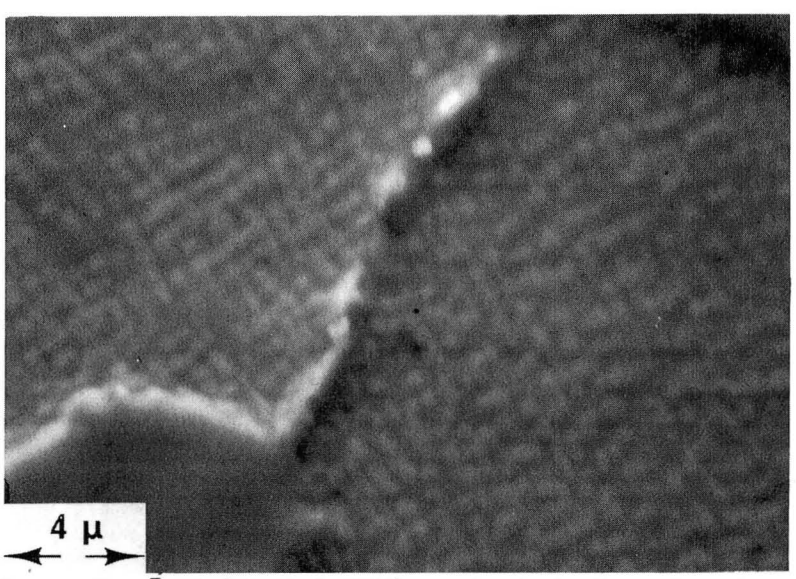

Figure 52. René 80 (NASA & TRW); untested microstructure from the head of a specimen.

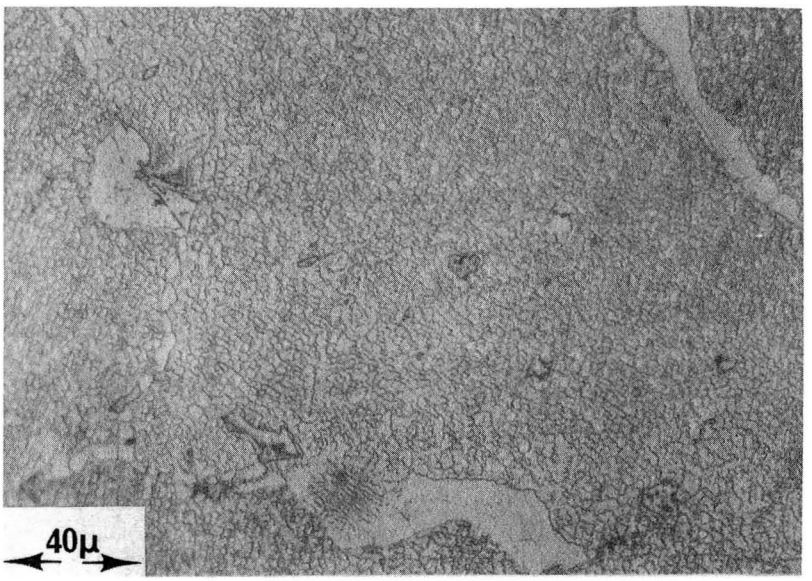

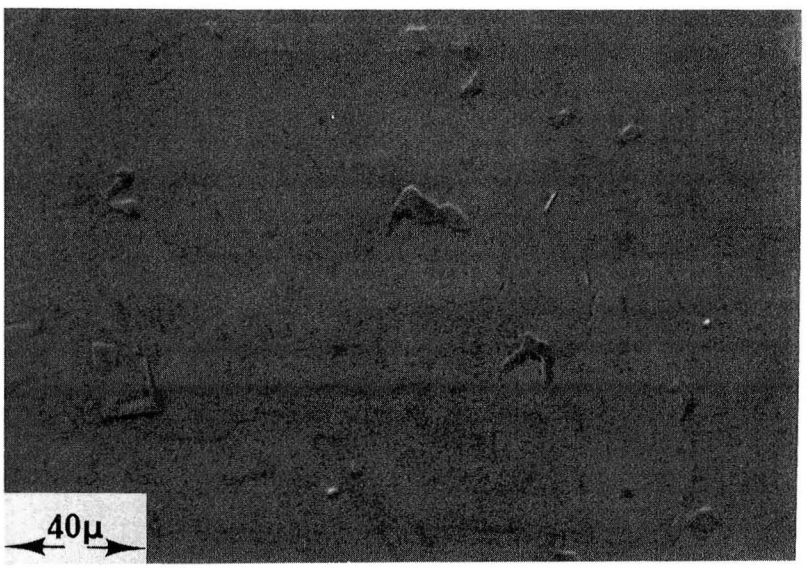

Figure 53. IN 100 (NASA); untested microstructure from the head of a specimen.

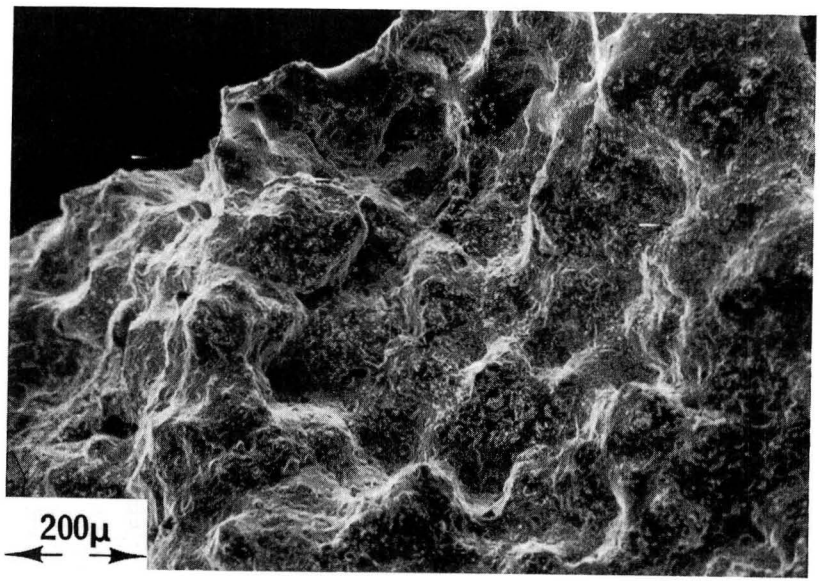

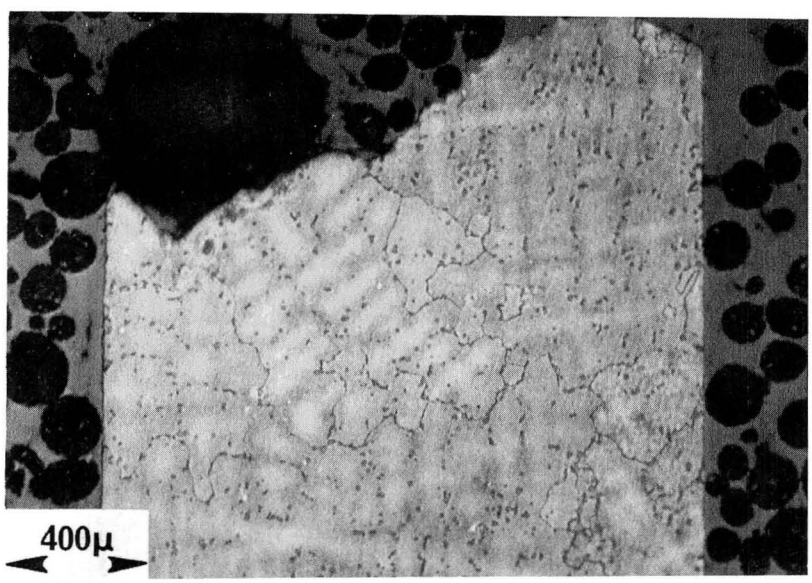

Figure 54. Specimen separation generally occurs by rapid crack propagation along an interdendritic path.

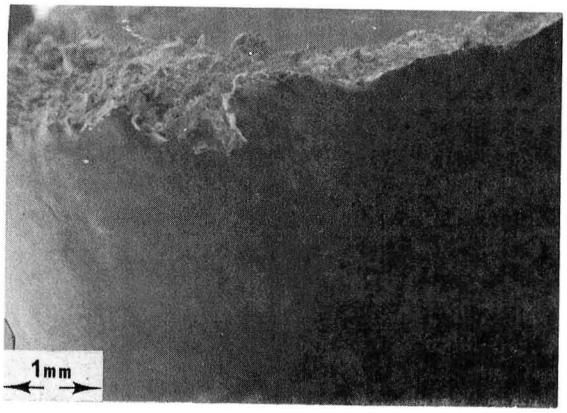

A1-OS

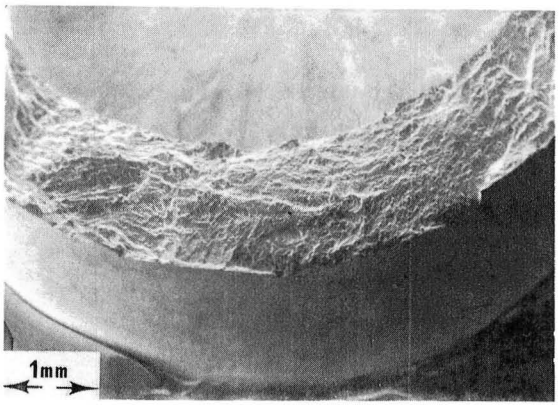

B1-FS

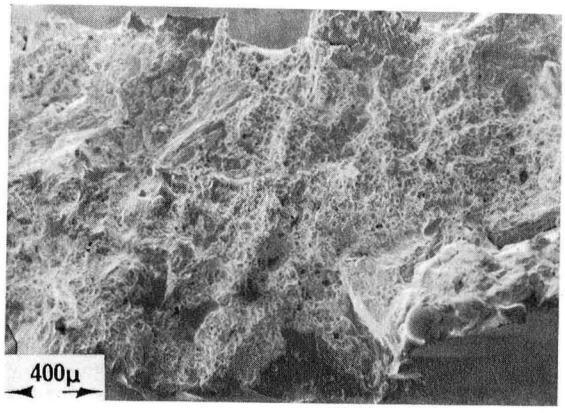

A2-FS

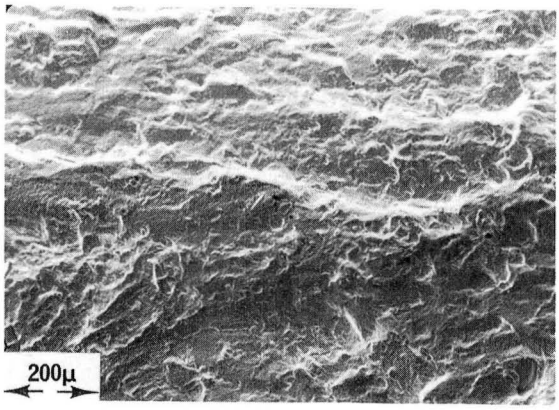

B2-FS

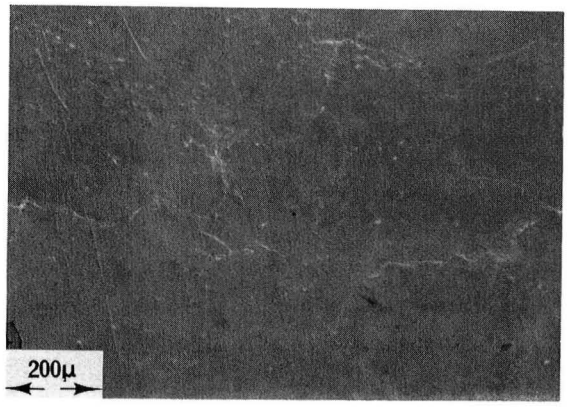

A3-OS

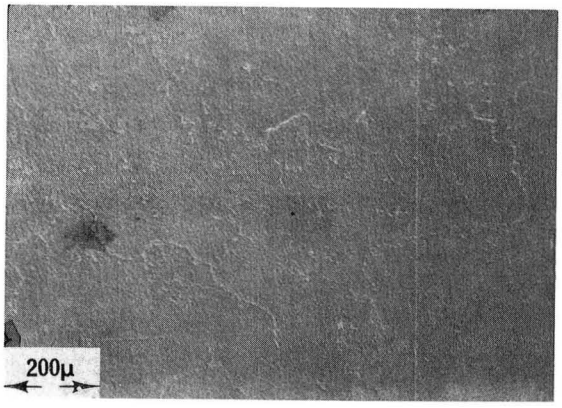

B3-OS

Figure 55. Uncoated René 80 (TRW); HRSC test in vacuum at 1000C.
A. 7U-PP-6: PP = 0.296%, N_f = 2,298, t_f = 0.60 hr., Maximum Tensile Stress = 191.0 MPa.
B. 8U-PP-7: PP = 0.078%, N_f = 22,115, t_f = 5.90 hr., Maximum Tensile Stress = 117.2 MPa.

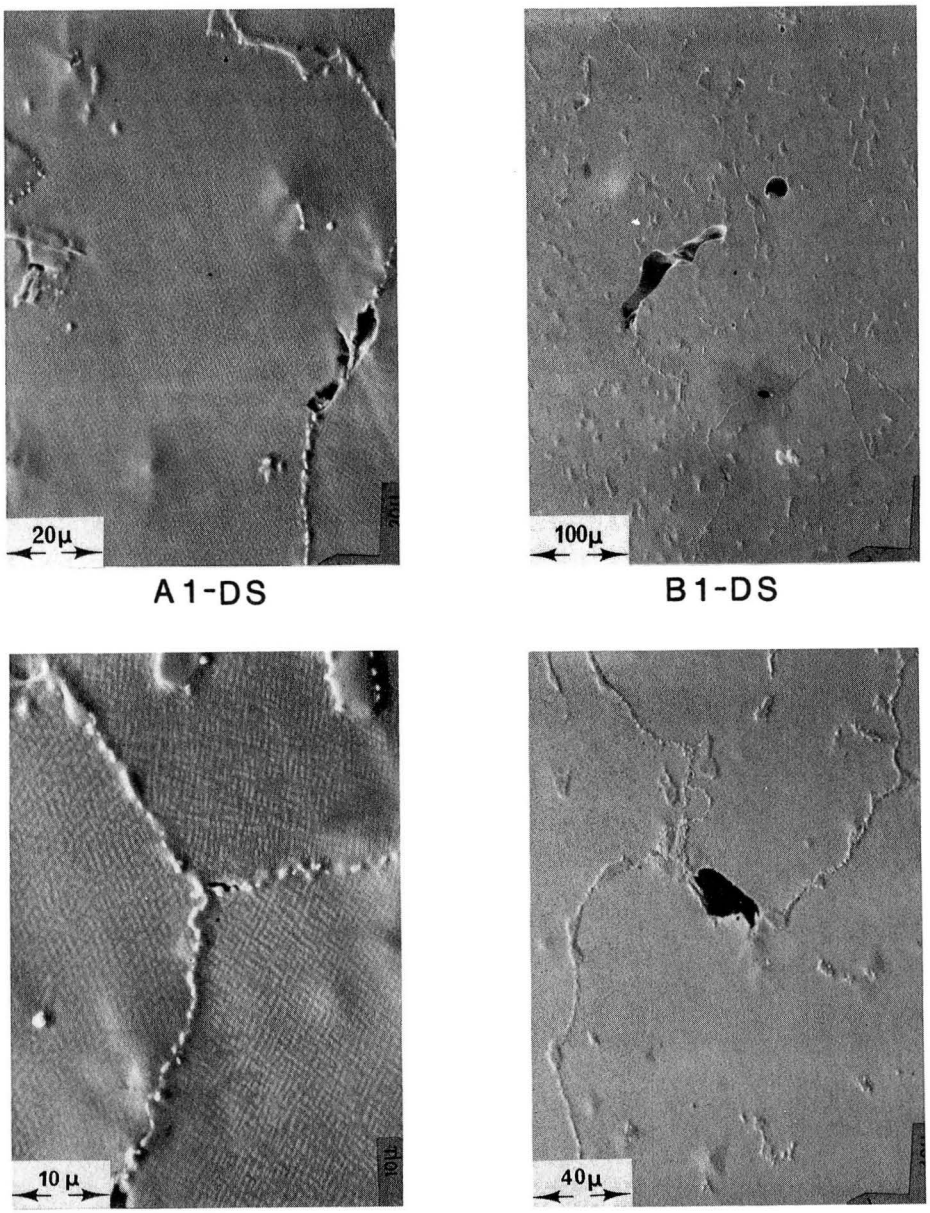

Figure 56. Uncoated René 80 (TRW); HRSC test in vacuum at 1000C.
A. 7U-PP-6: PP = 0.296%, N_f = 2,298, t_f = 0.60 hr., Maximum Tensile Stress = 191.0 MPa.
B. 8U-PP-7: PP = 0.078%, N_f = 22,115, t_f = r.90 hr., Maximum Tensile Stress = 117.2 MPa.

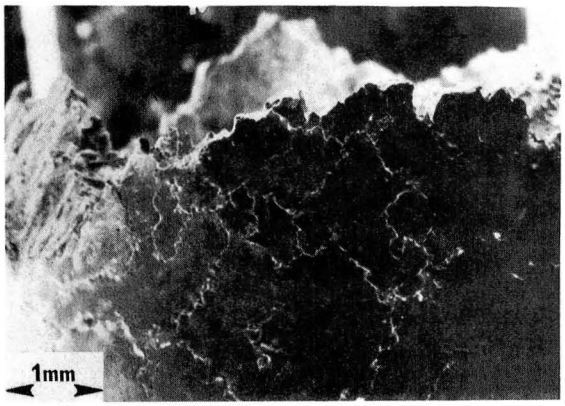

A1-OS

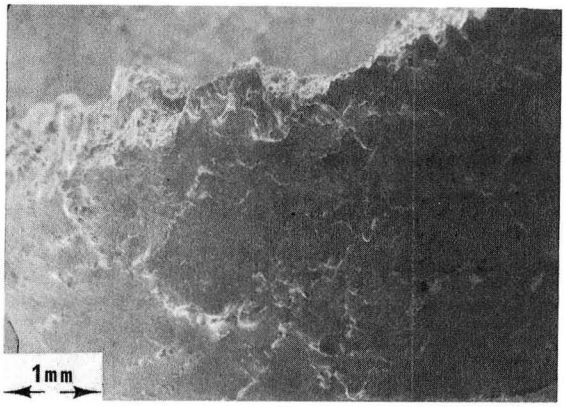

B1-OS

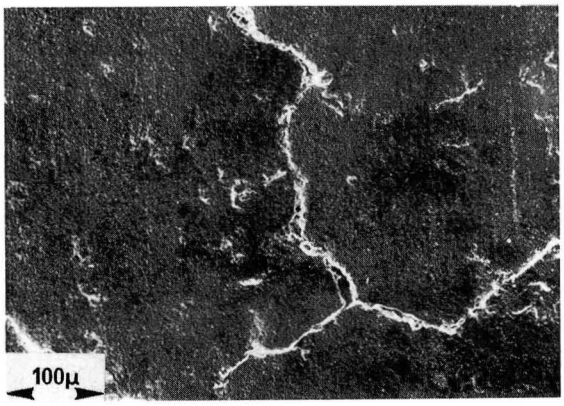

A2-OS

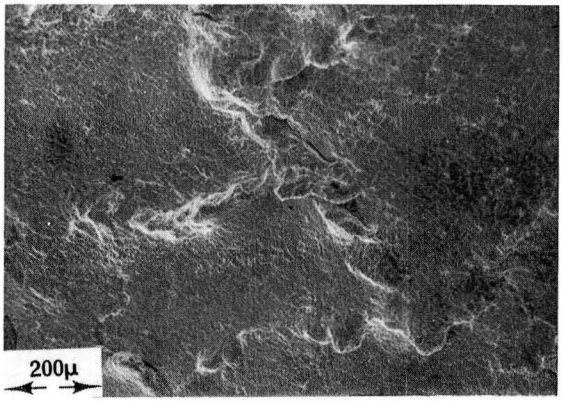

B2-OS

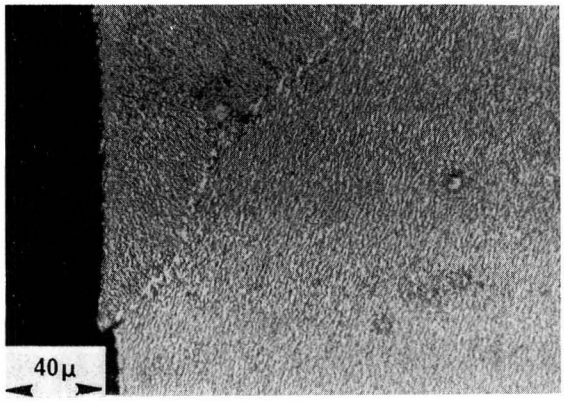

A3-DS

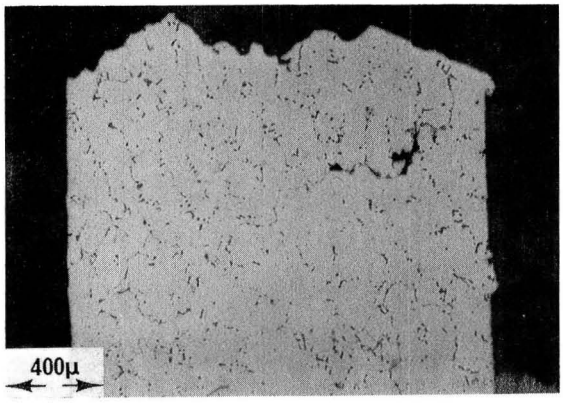

B3-DS

Figure 57. Uncoated René 80 (TRW); CCCR test in vacuum at 1000C.
A. 89U-PC-11: PP = 0.048%, PC = 0.271, N_f = 187, t_f = 4.90 hr., Maximum Tensile Stress = 270.3 MPa.
B. 23U-PC-6: PP = 0.015%, PC = 0.194%, N_f = 9810, t_f = 15.90 hr., Maximum Tensile Stress = 176.5 MPa.

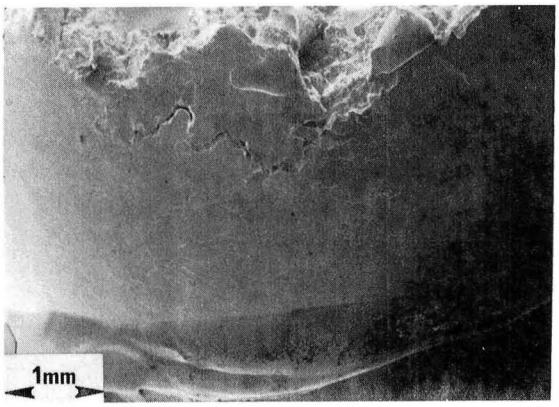

A1-OS

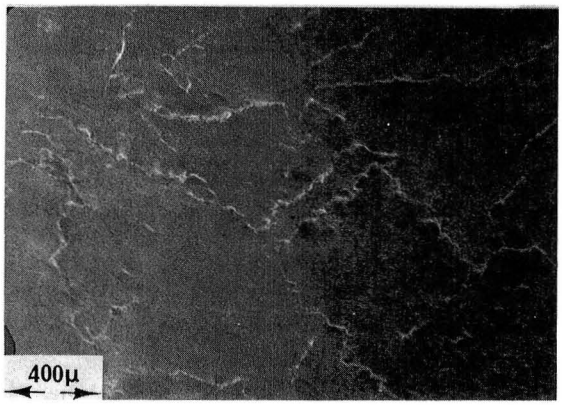

B1-OS

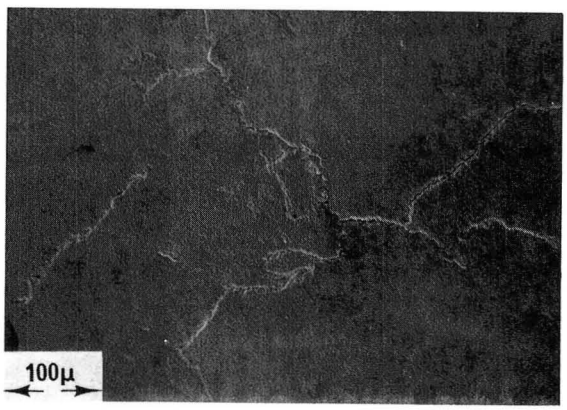

A2-OS

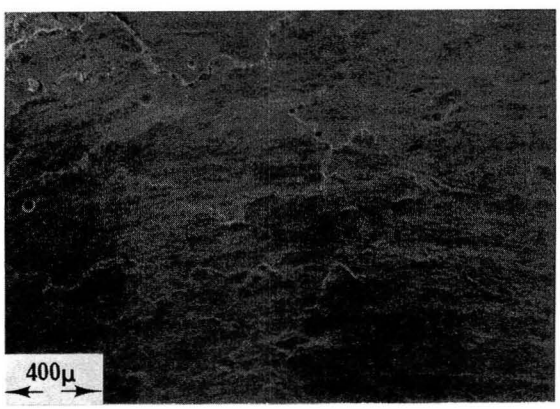

B2-IS

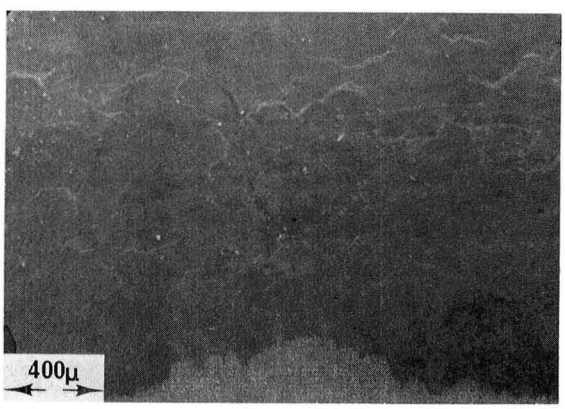

A3-IS

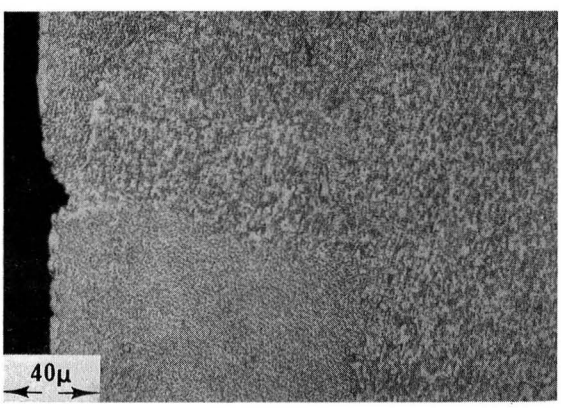

B3-DS

Figure 58. Uncoated René 80 (TRW); TCCR test in vacuum at 1000C.
A. 111U-CP-10: PP = 0.178%, CP = 0.533%, N_f, t_f = 1.00 hr., Maximum Tensile Stress = 128.2 MPa.
B. 17U-CP-4: PP = 0.030%, CP = 0.210%, N_f = 1385, t_f = 8.60 hr., Maximum Tensile Stress = 80.0 MPa.

1-DS

3-DS

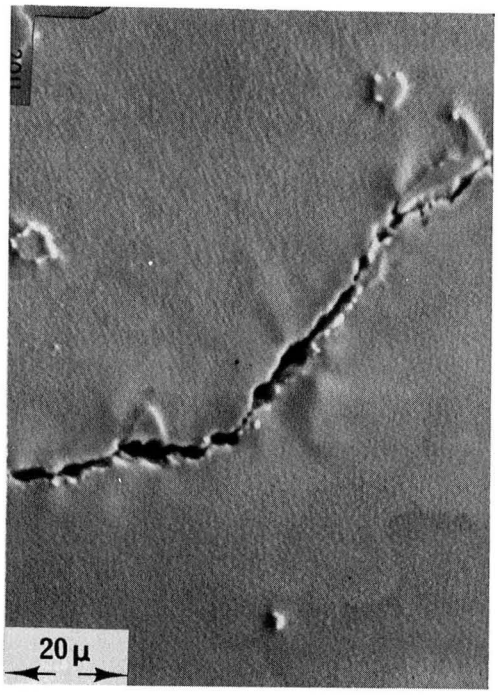

2-DS

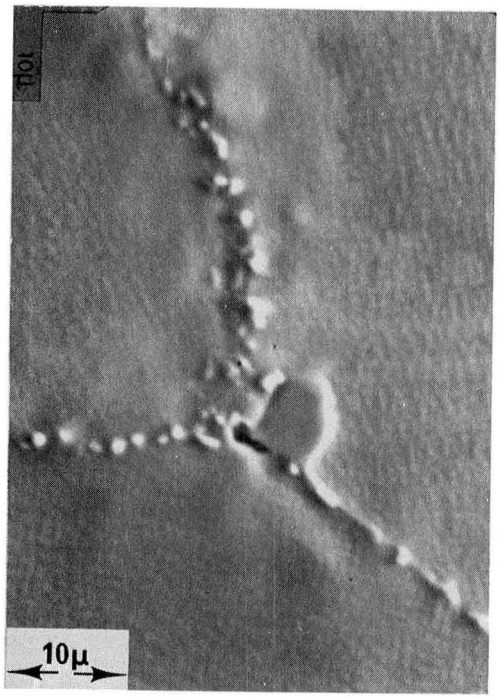

4-DS

Figure 59. Uncoated René 80 (TRW); TCCR test in vacuum at 1000C.
A. 111U-CP-10: PP = 0.178%, CP = 0.553%, N_f = 78, t_f = 1.00 hr., Maximum Tensile Stress = 128.2 MPa.

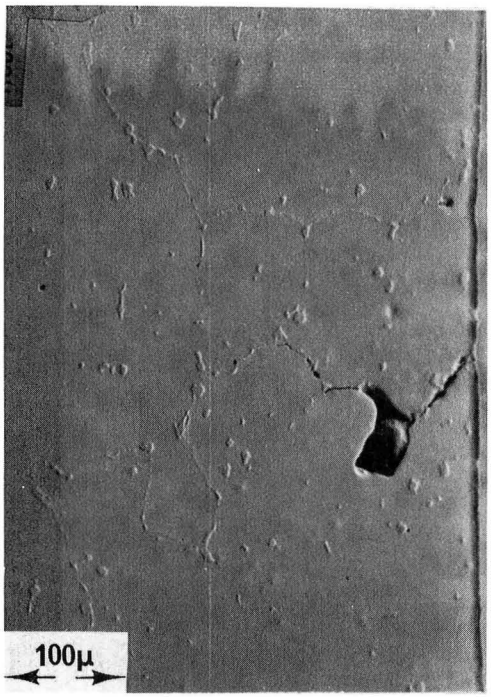

1-DS

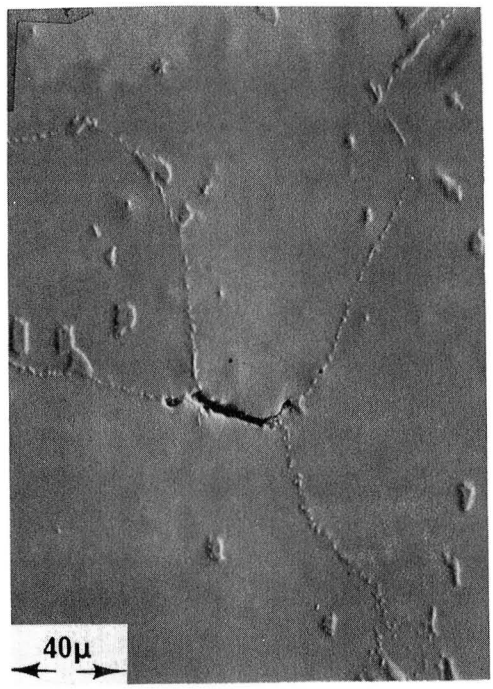

3-DS

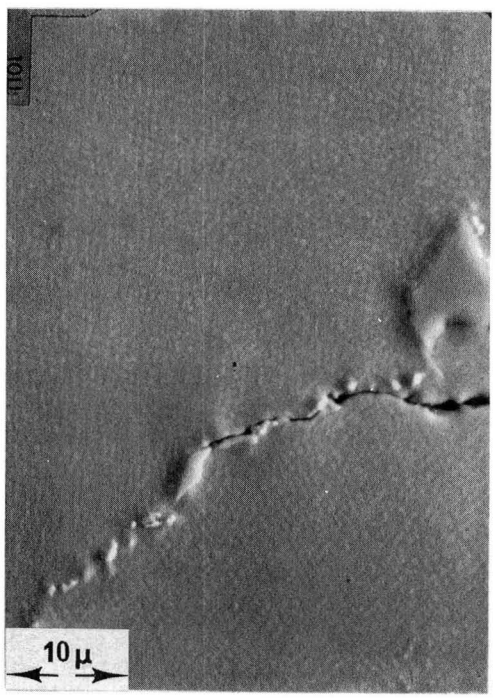

2-DS

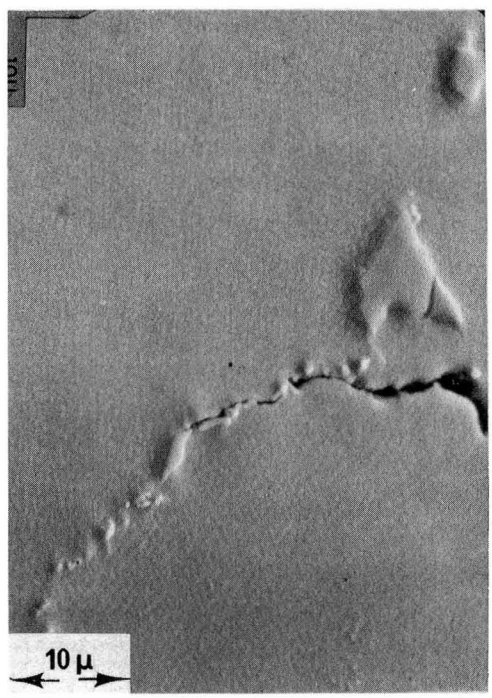

4-DS

Figure 60. Uncoated René 80 (TRW); TCCR test in vacuum at 1000C.
B. 17U-CP-4: PP = 0.030%, CP = 0.210%, N_f = 1385, t_f = 8.60 hr., Maximum Tensile Stress = 80.0 MPa.

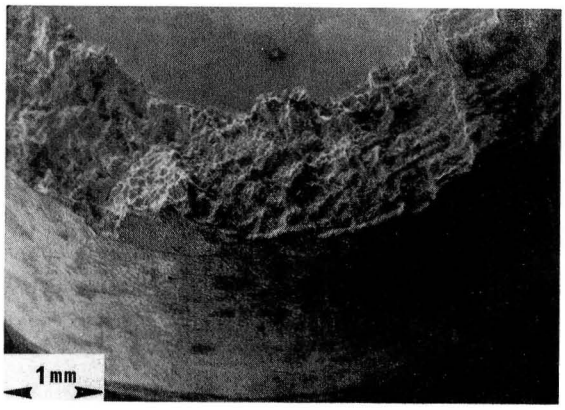

A1-FS

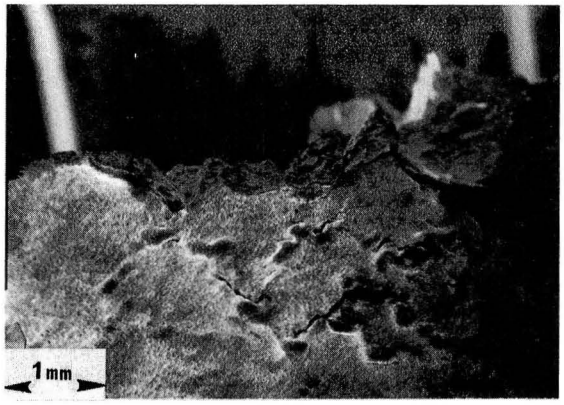

B1-OS

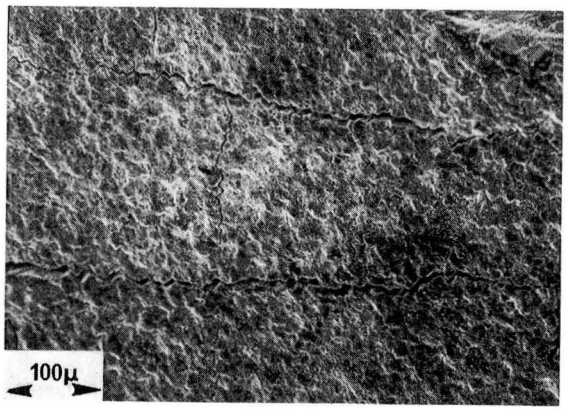

A2-OS

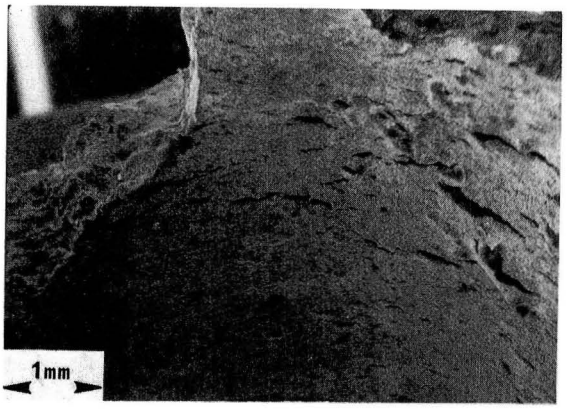

B2-IS

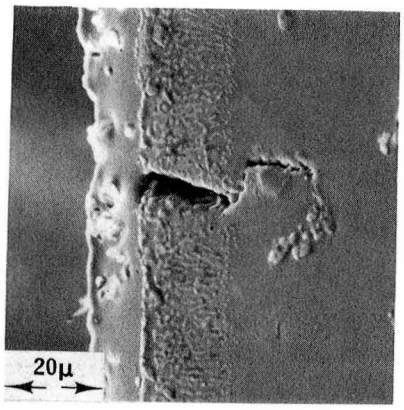

B4-DS

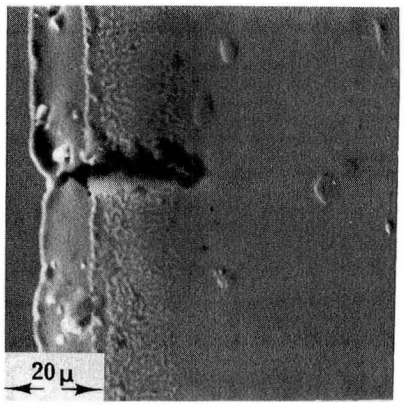

B3-DS

Figure 61. Coated René 80 (TRW); CCCR test in vacuum at 1000C.
A. 56C-PC-1: PP = 0.132%, PC = 0.339%, N_f = 55, t_f = 1.00 hr., Maximum Tensile Stress = 348.2 MPa.
B. 93C-PC-8: PP = 0.025, PC = 0.142, N_f = 691, t_f = 41.20 hr., Maximum Tensile Stress = 304.8 MPa.

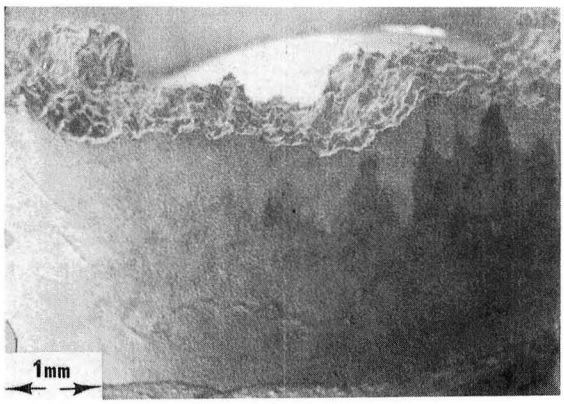

A1-OS

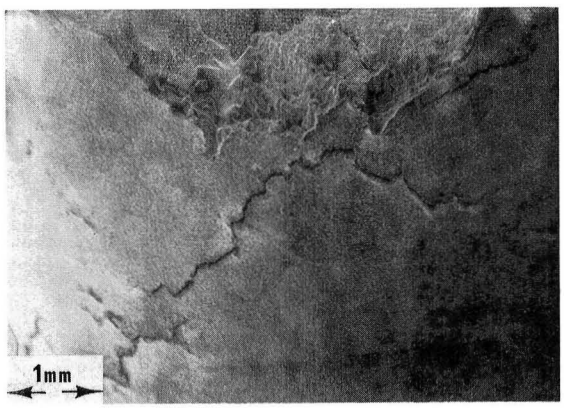

B1-OS

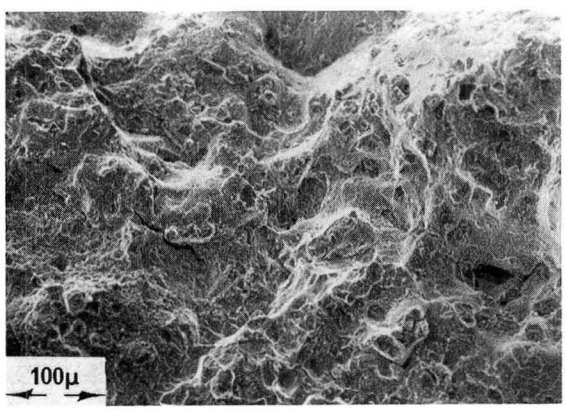

A2-FS

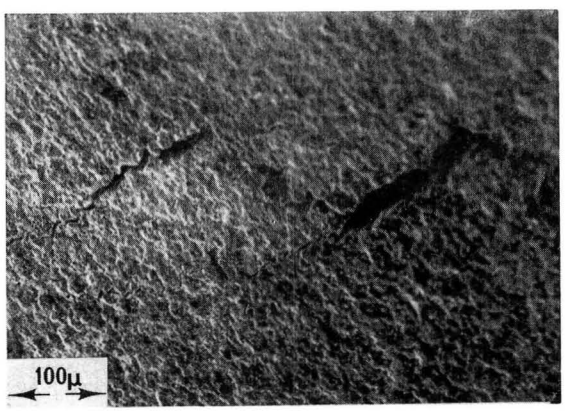

B2-OS

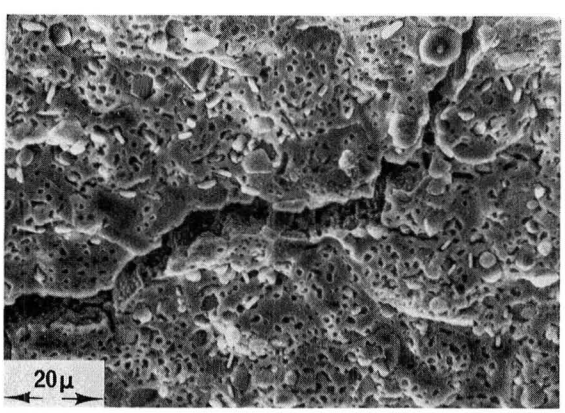

A3-OS

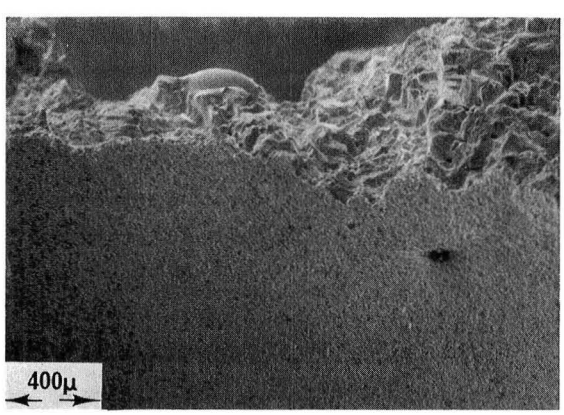

B3-IS

Figure 62. Coated René 80 (TRW); TCCR test in vacuum at 1000C.
A. 85C-CP-7: PP = 0.074%, CP = 0.250%, N_f = 134, t_f = 4.50 hr., Maximum Tensile Stress = 145.5 MPa.
B. 87C-CP-8: PP = 0.030%, CP = 0.169%, N_f = 950, t_f = 6.20 hr., Maximum Tensile Stress = 124.1 MPa.

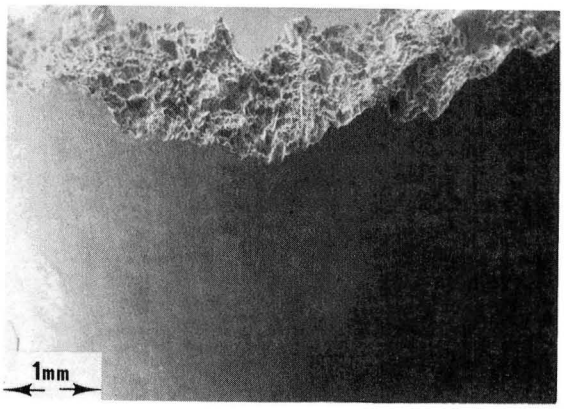

A1-OS

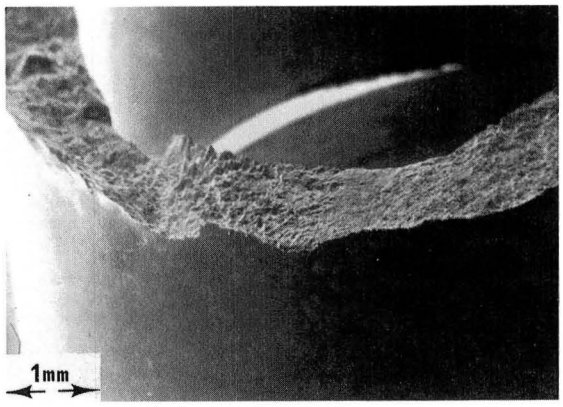

B1-FS

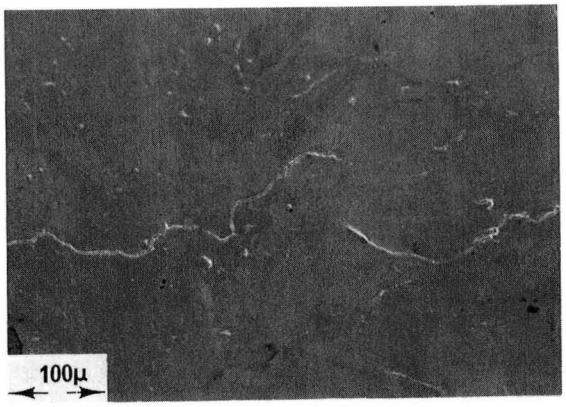

A2-OS

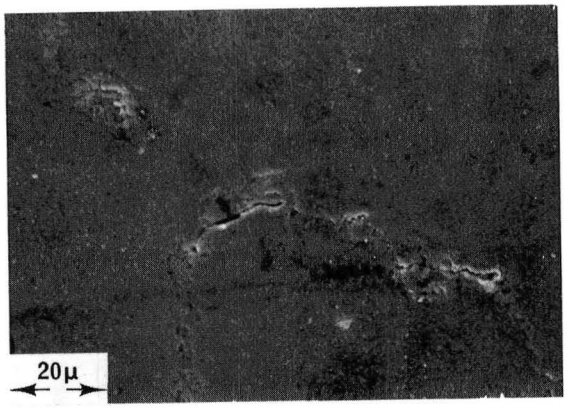

B2-OS

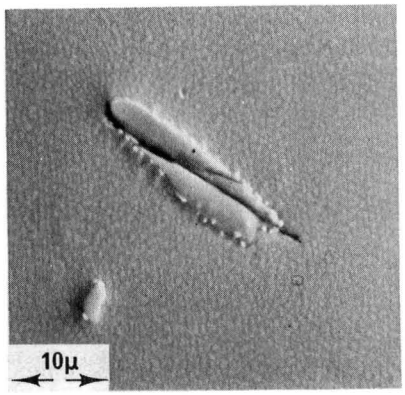

A3-DS

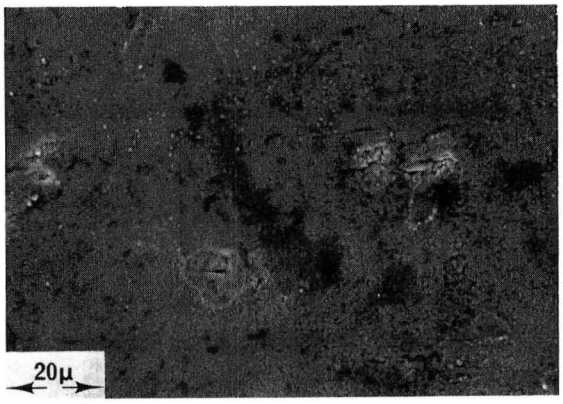

B3-OS

Figure 63. Uncoated René 80 (TRW); HRSC test in vacuum at 871C.
A. 21U-PP-8: PP = 0.322%, N_f = 642, t_f = 0.20 hr., Maximum Tensile Stress = 417.2 MPa.
B. 42U-PP-11: PP = 0.051%, N_f = 21,620, t_f = 58.50 hr., Maximum Tensile Stress = 162.1 MPa.

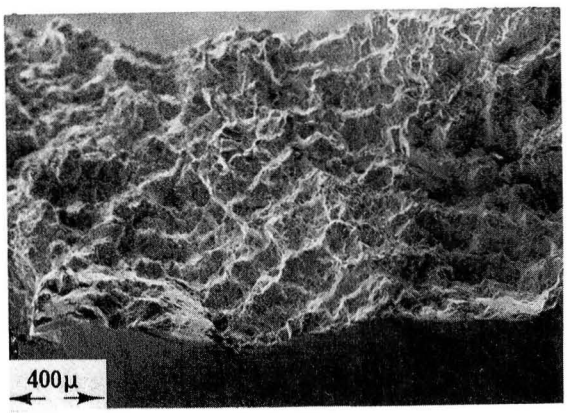

A1-FS

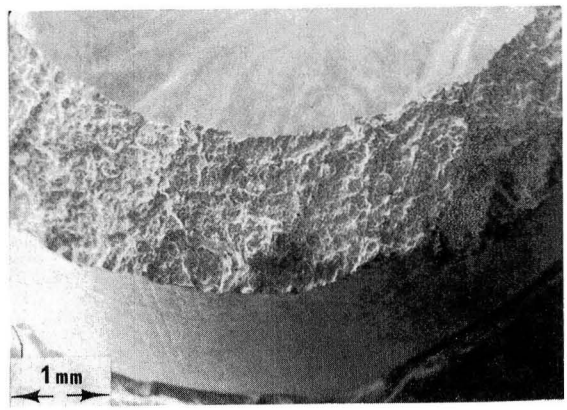

B1-FS

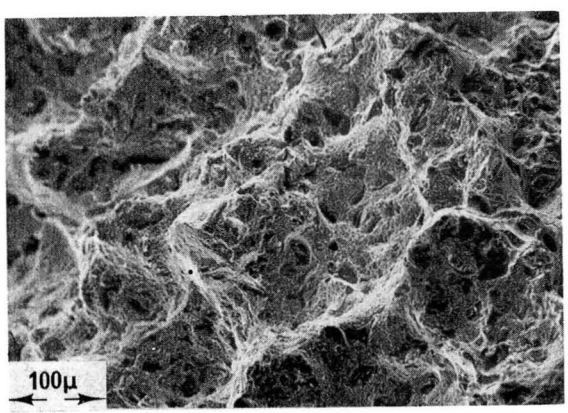

A2-FS

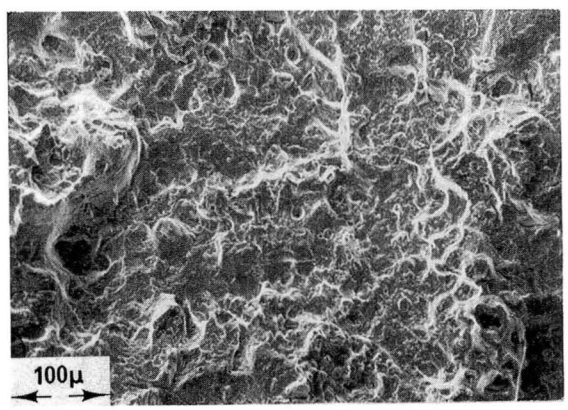

B2-FS

A3-OS

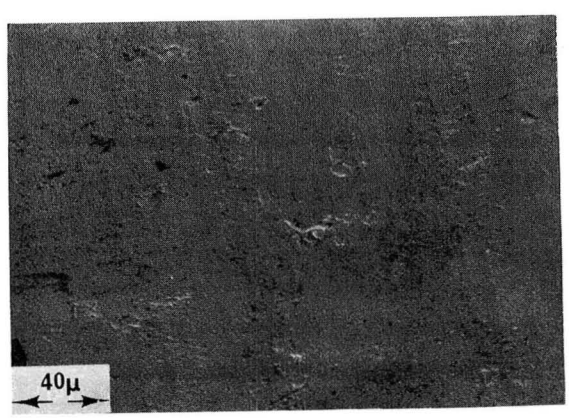

B3-OS

Figure 64. Uncoated René 80 (TRW); CCCR test in vacuum at 871C.
A. 92U-PC-13: PP = 0.094%, PC = 0.460%, N_f = 41, t_f = 1.10 hr., Maximum Tensile Stress = 553.7 MPa.
B. 29U-PC-10: PP = 0.040%, PC = 0.164%, N_f = 1415, t_f = 7.40 hr., Maximum Tensile Stress = 168.3 MPa.

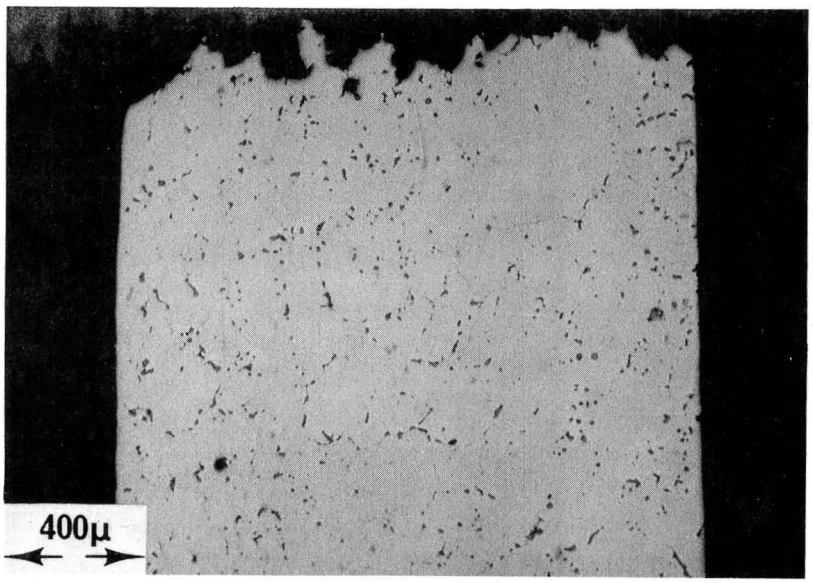

1-DS

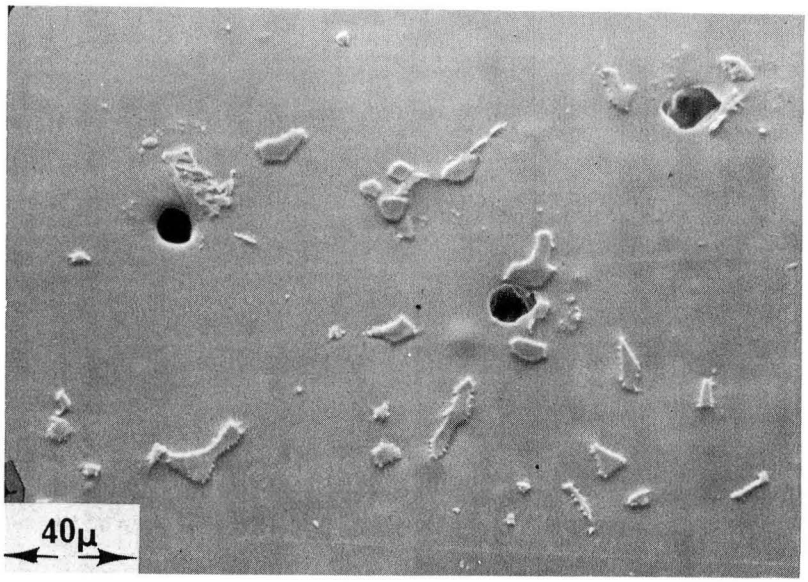

2-DS

Figure 65. Uncoated René 80 (TRW); CCCR test in vacuum at 871C.
A. 92U-PC-13: PP = 0.094%, PC = 0.460%, N_f = 41, t_f = 1.10 hr., Maximum Tensile Stress = 553.7 MPa.

1-DS

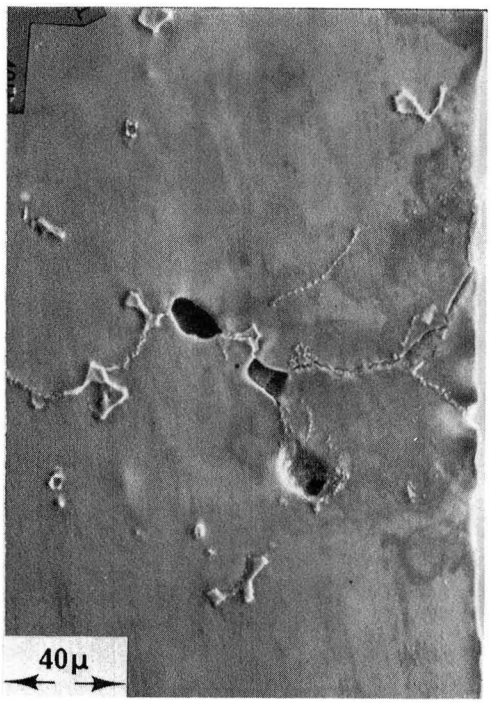

3-DS

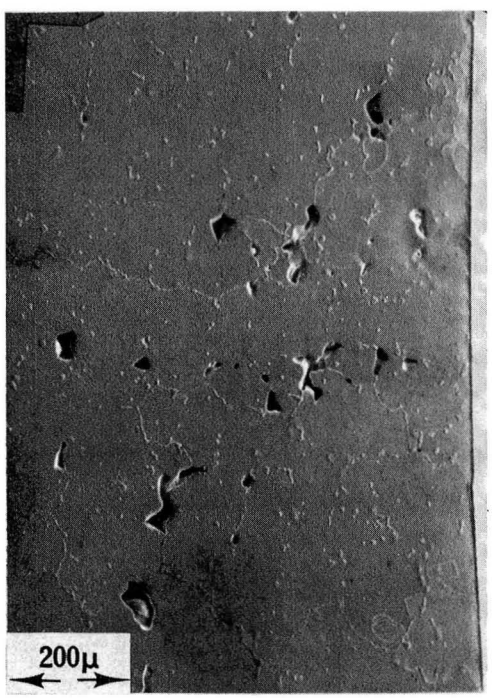

2-DS

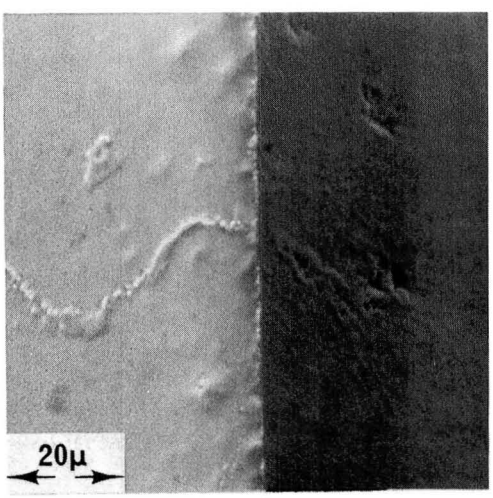

4-DS|OS

Figure 66. Uncoated René 80 (TRW); CCR test in vacuum at 871C.
B. 29U-PC-10: PP = 0.040%, PC = 0.164%, N_f = 1415, t_f = 7.40 hr., Maximum Tensile Stress = 168.3 MPa.

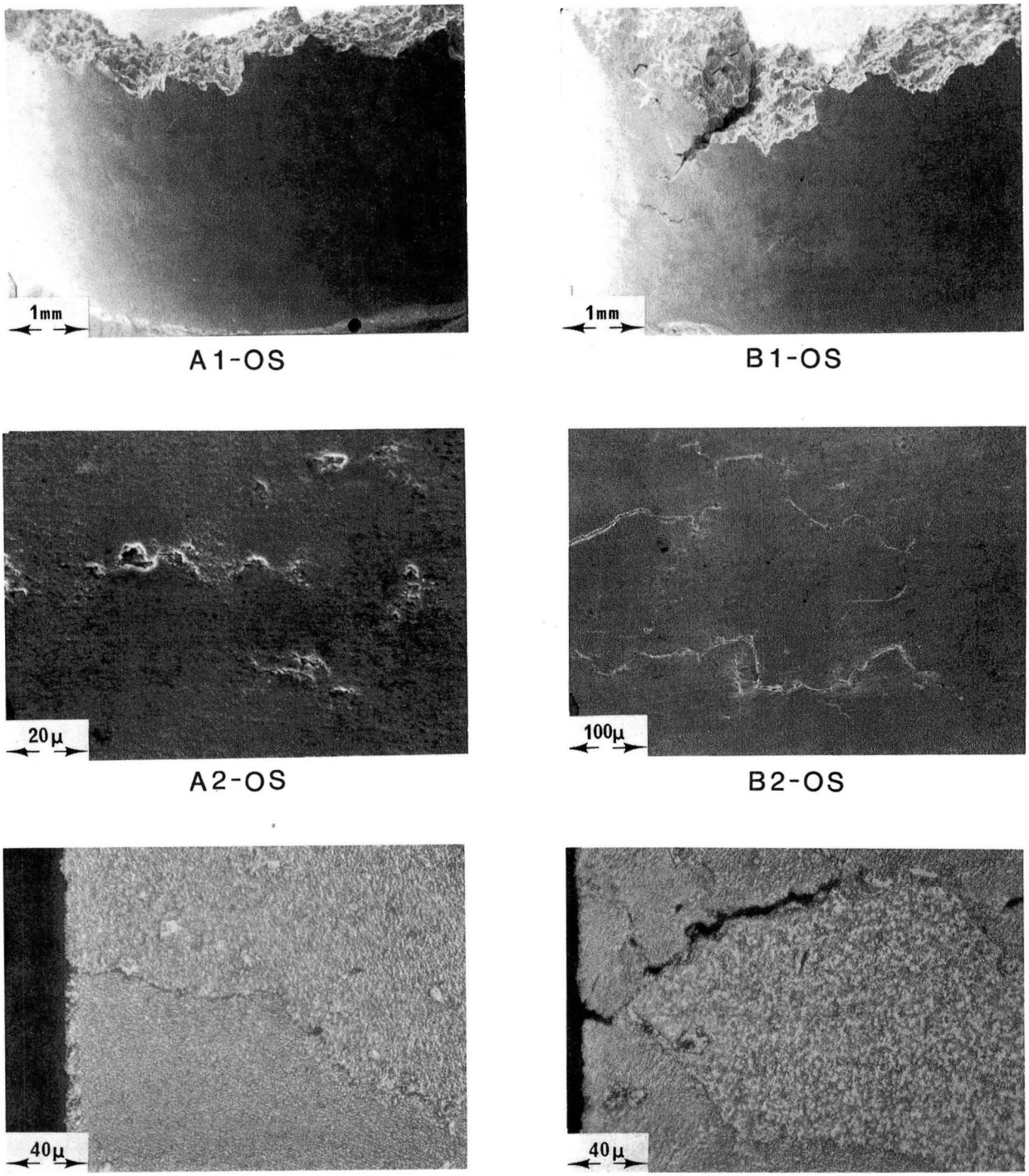

Figure 67. Uncoated René 80 (TRW); TCCR test in vacuum at 871C.
A. 112U-CP-11: PP = 0.077%, CP = 0.308%, N_f = 101, t_f = 1.80 hr., Maximum Tensile Stress = 284.8 MPa.
B. 30U0-CP-11: PP = 0.035%, CP = 0.254%, N_f = 193, t_f = 1.30 hr., Maximum Tensile Stress - 251 MPa.

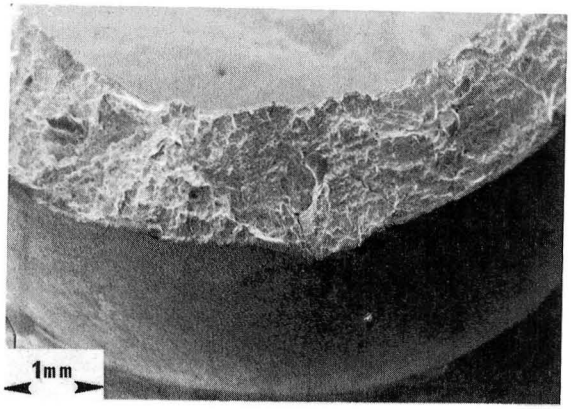

A1-FS

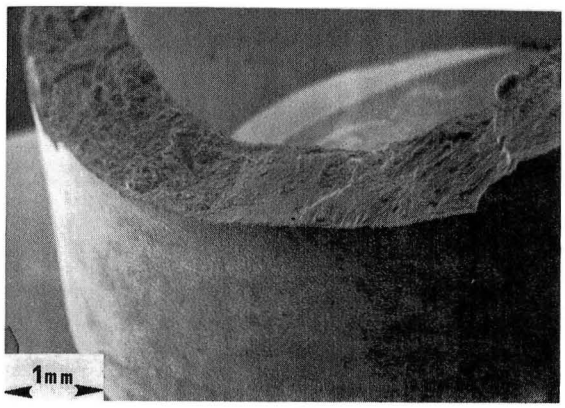

B1-FS

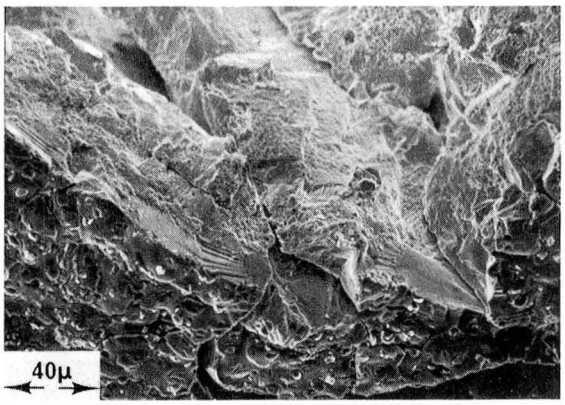

A2-FS

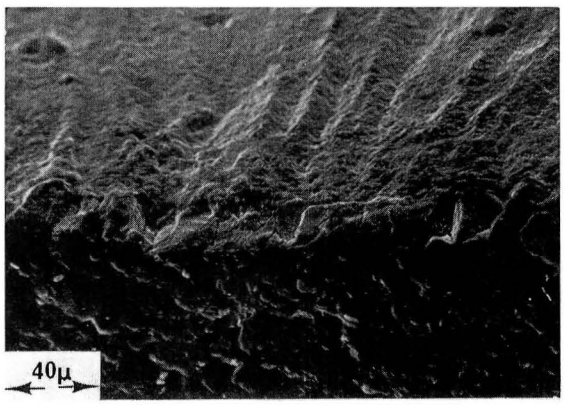

B2-FS

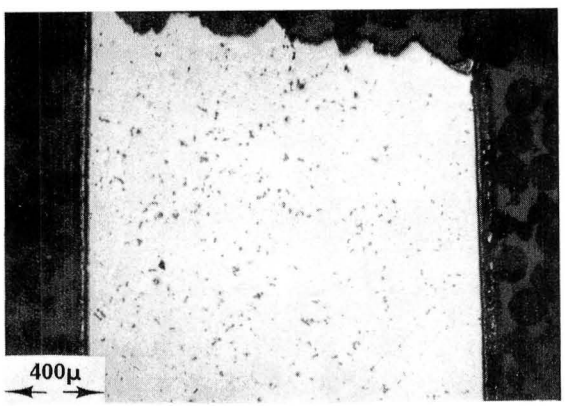

A3-DS

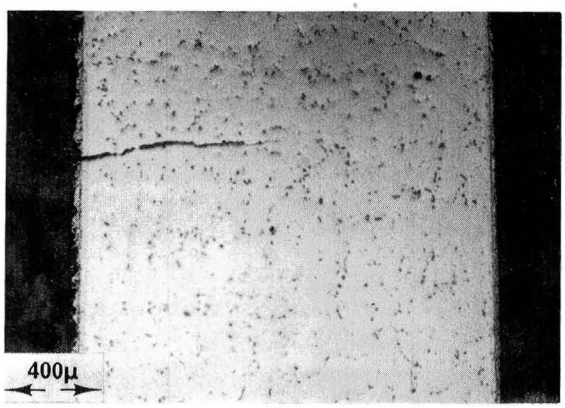

B3-DS

Figure 68. Coated René 80 (TRW); HRSC test in vaccum at 871C.
A. 52C-PP-7: PP = 0.230%, N_f = 1365, t_f = 0.04 hr., Maximum Tensile Stress = 409.6 MPa.
B. 54C-PP-8: PP = 0.086%, N_f = 71,982, t_f = 19.40 hr., Maximum Tensile Stress = 231.0 MPa.

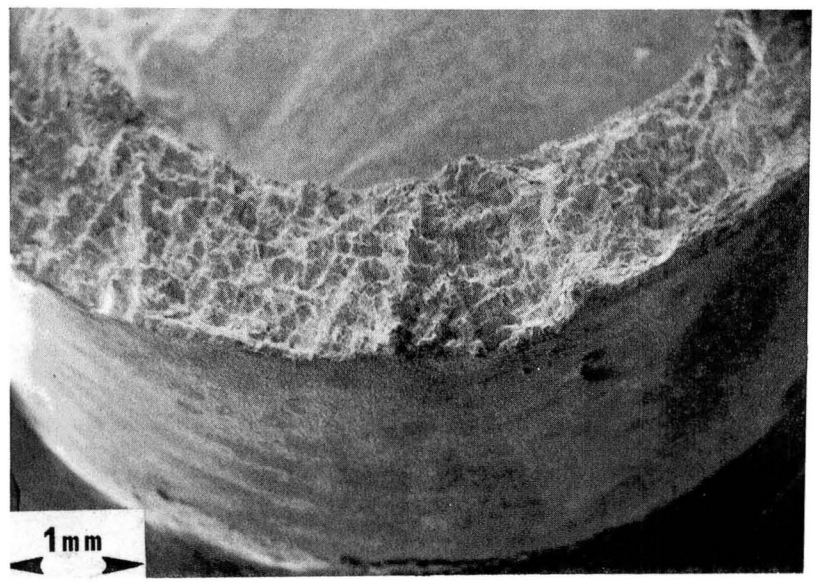

1-FS

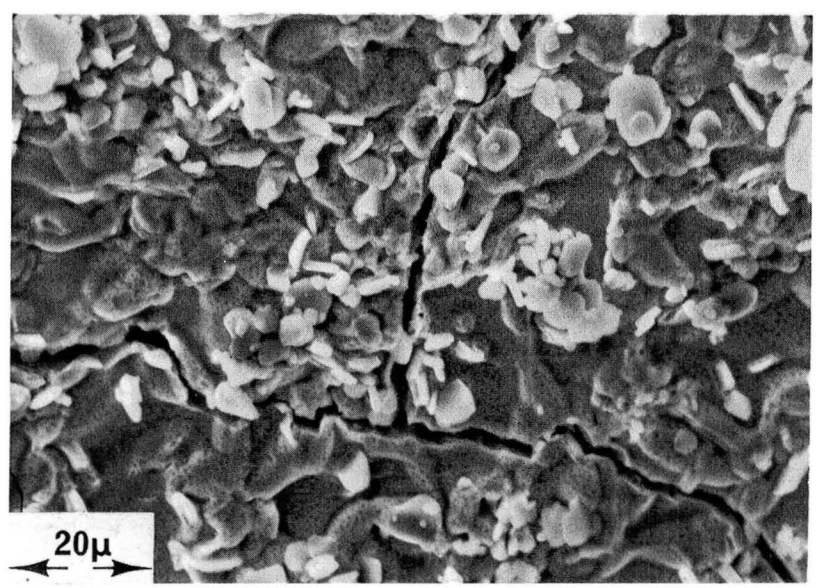

2-OS

Figure 69. Coated René 80 (TRW); CCCR test in vacuum at 871C. 95C-PC-9: PP = 0.033%, PC = 0.339%, N_f = 126, t_f = 2.80 hr., Maximum Tensile Stress = 493.6 MPa.

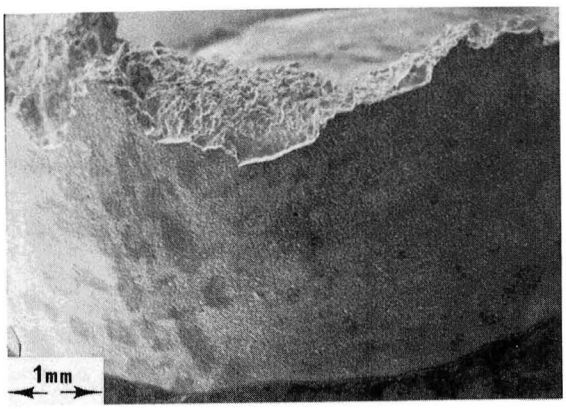

A1-OS

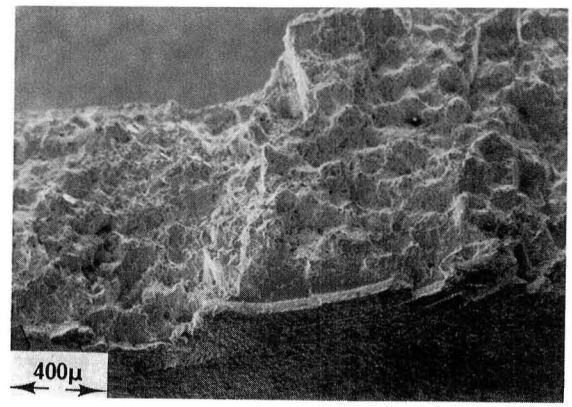

B1-FS

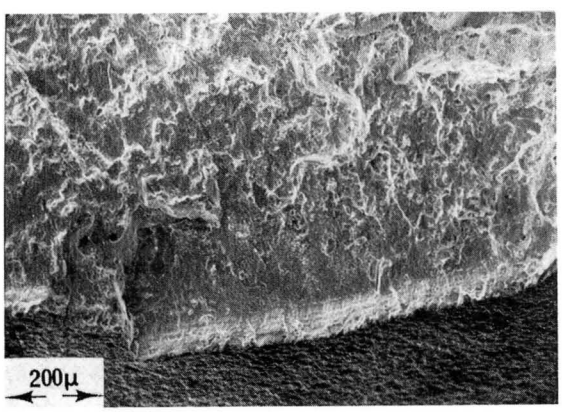

A2-FS

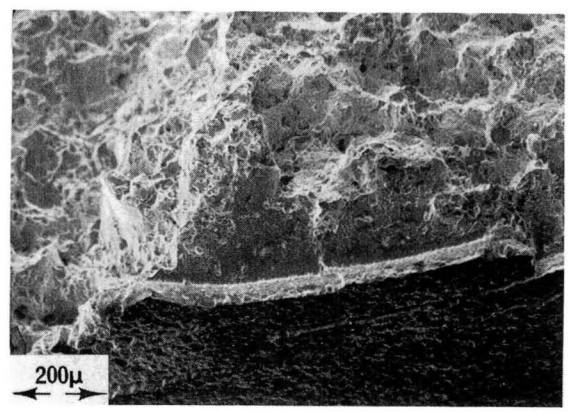

B2-FS

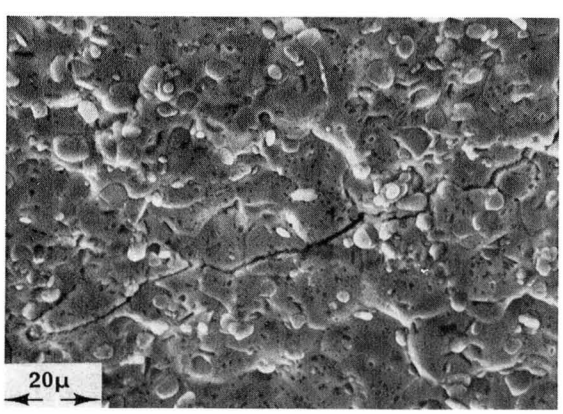

A3-OS

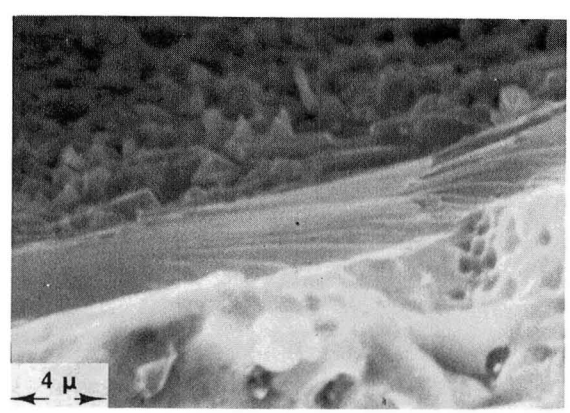

B3-OS

Figure 70. Coated René 80 (TRW); TCCR test in vacuum at 871C.
A. 83C-CP-5: PP = 0.035, CP = 0.210, N_f = 455, t_f = 12.10 hr., Maximum Tensile Stress = 198.0 MPa.
B. 115C-CP-11: PP = 0.034, CP = 0.034, N_f = 77, t_f = 1.00 hr., Maximum Tensile Stress = 340.6 MPa.

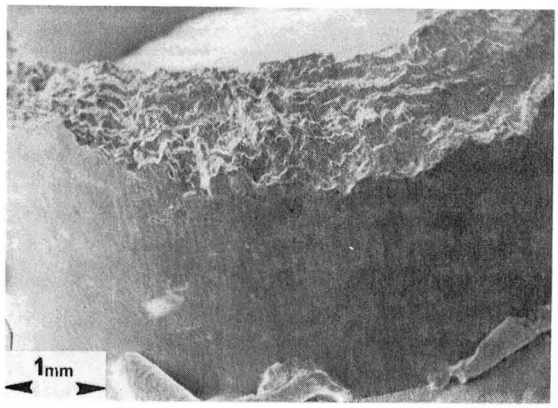

A1-OS

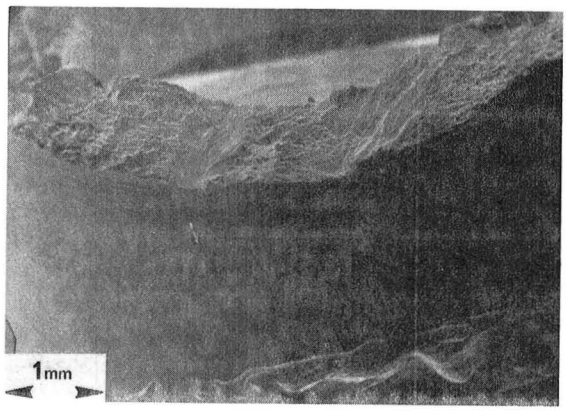

B1-OS

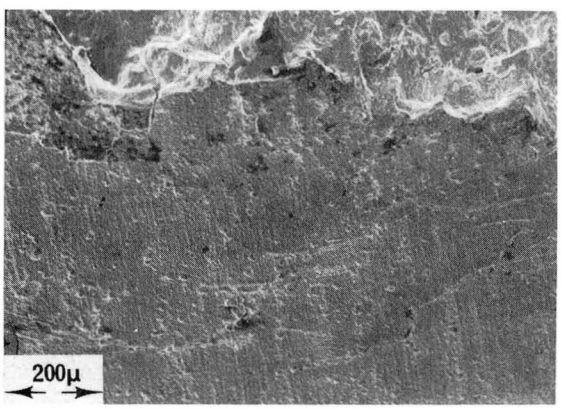

A2-OS

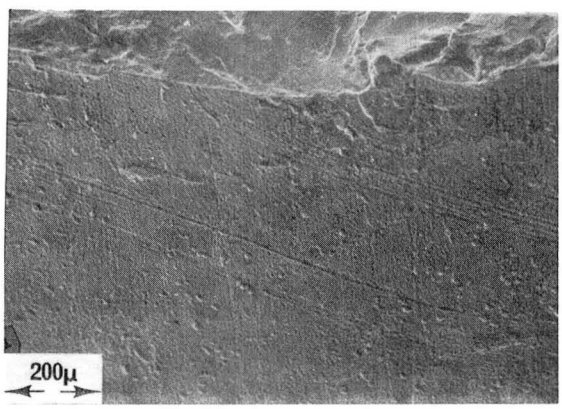

B2-OS

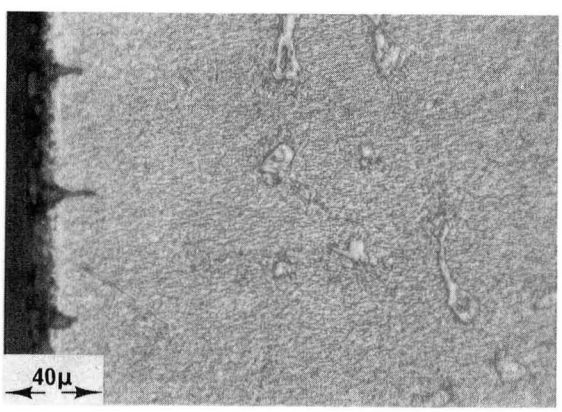

A3-DS

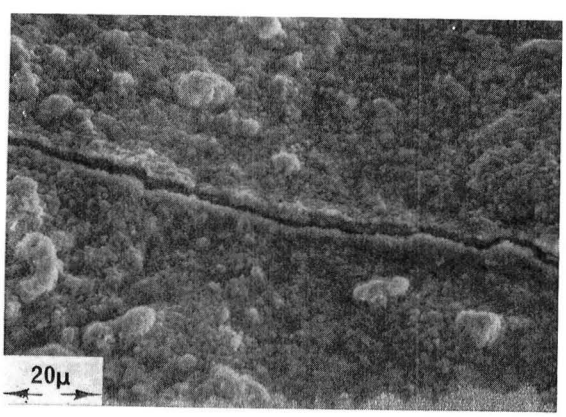

B3-OS

Figure 71. Uncoated René 80 (NASA); HRSC test in air at 1000C
A. Ree 206: PP = 0.431%, N_f = 202, t_f = 0.06 hr., Maximum Tensile Stress = 358.2 MPa.
B. Ree 204: PP = 0.089%, N_f = 9226, t_f = 2.46 hr., Maximum Tensile Stress = 206.2 MPa.

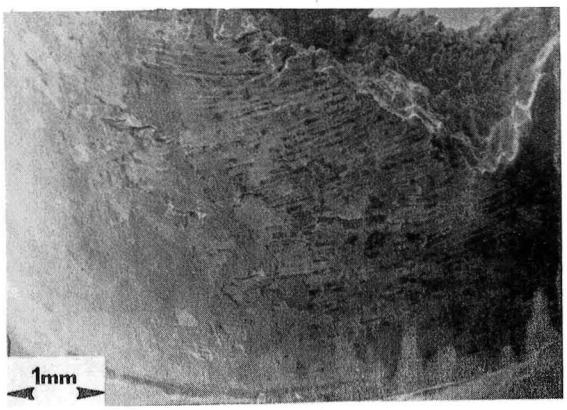

A1-OS

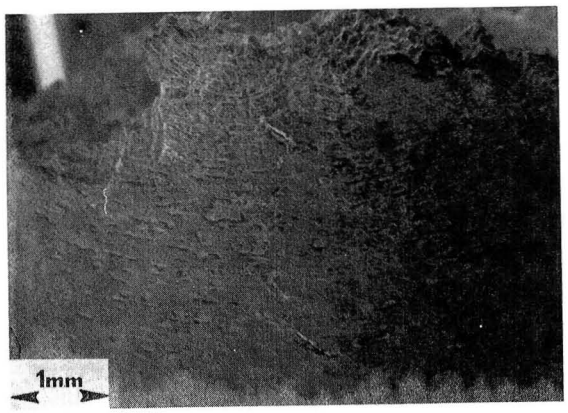

B1-OS

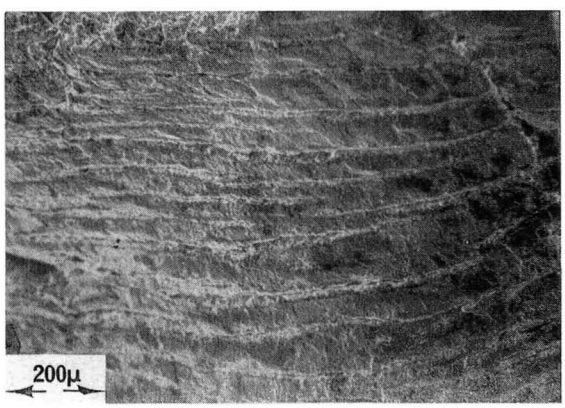

A2-OS

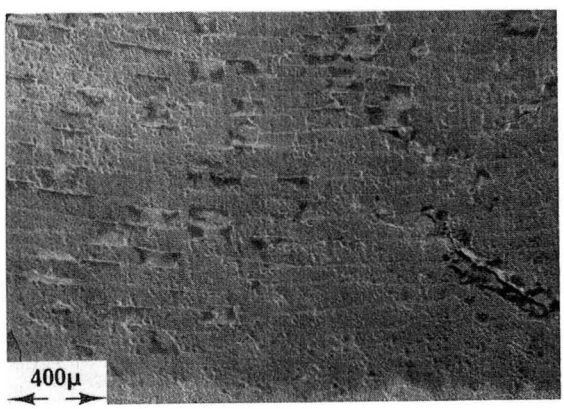

B2-OS

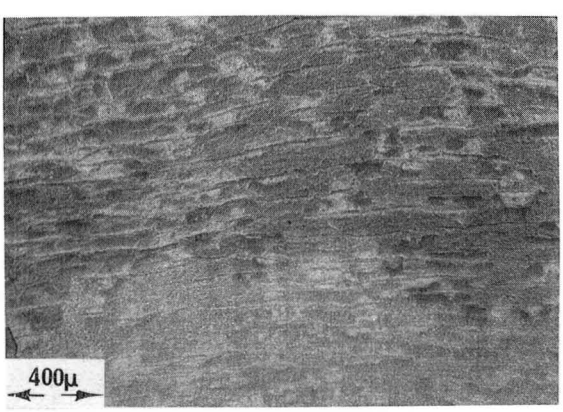

A3-IS

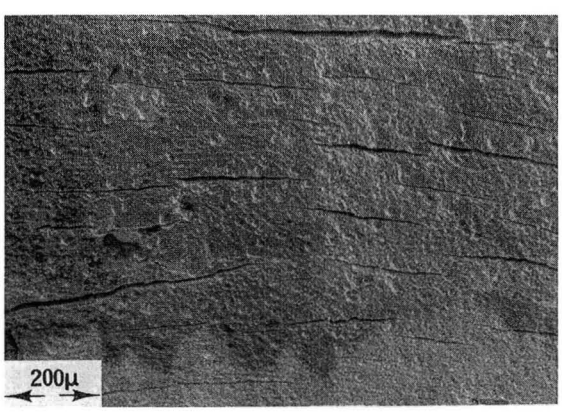

B3-IS

Figure 72. Uncoated René 80 (NASA); CCCR test in air at 1000C.
A. Ree 200; PP = 0.222%, PC = 1.866%, N_f = 10, t_f = 40.75 hr., Maximum Tensile Stress = 467.1 MPa.
B. Ree 219; PP = 0.268%, PC = 0.356%, N_f = 63, t_f = 23.53 hr., Maximum Tensile Stress = 355.0 MPa.

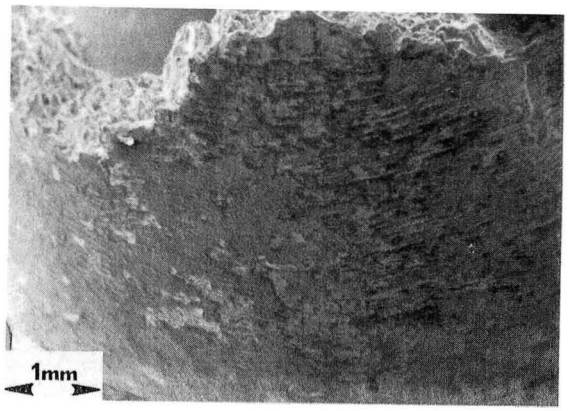

A1-OS

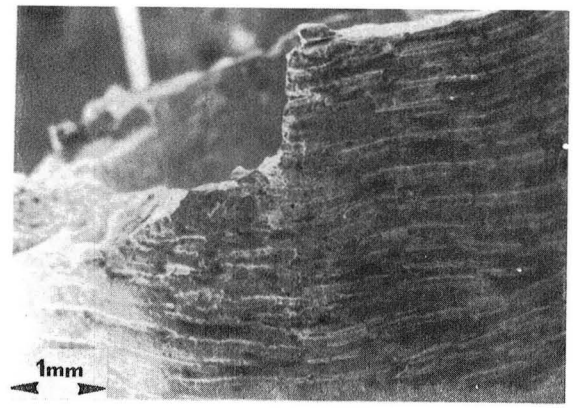

B1-OS

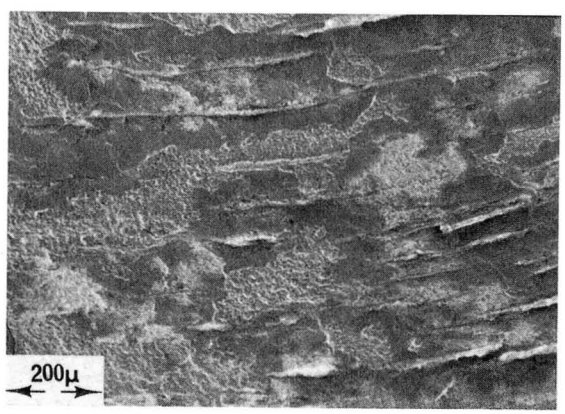

A2-OS

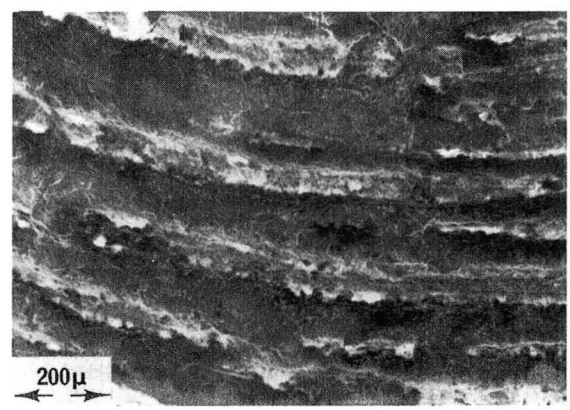

B2-OS

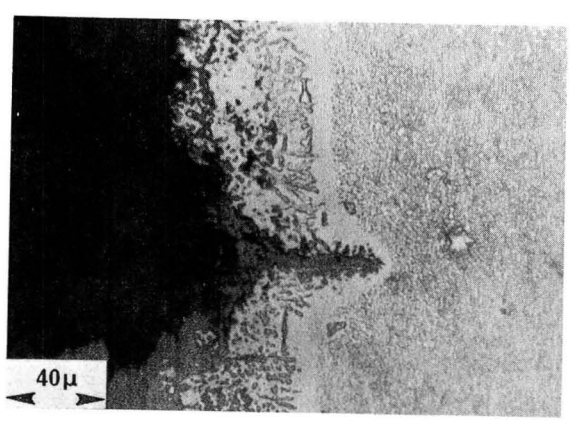

B4-DS

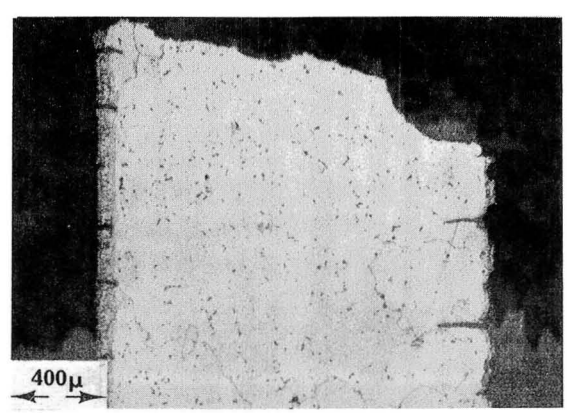

B3-DS

Figure 73. Uncoated René 80 (NASA); CCCR test in air at 1000C.
A. Ree 213: PP = 0.258%, PC = 0.267%, N_f = 130, t_f = 36.64 hr., Maximum Tensile Stress = 321.7 MPa.
B. Ree 210: PP = 0.031%, PC = 0.071%, Maximum Tensile Stress = 183.3 MPa.

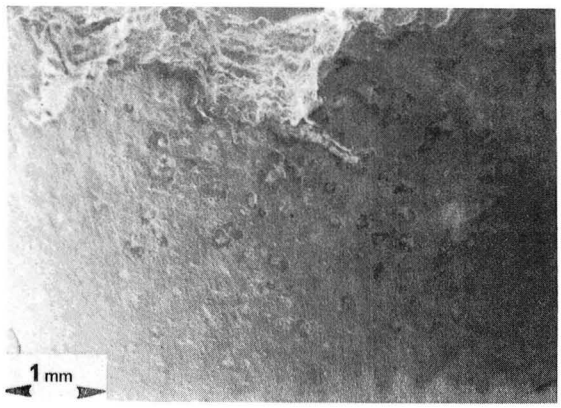

A1-OS

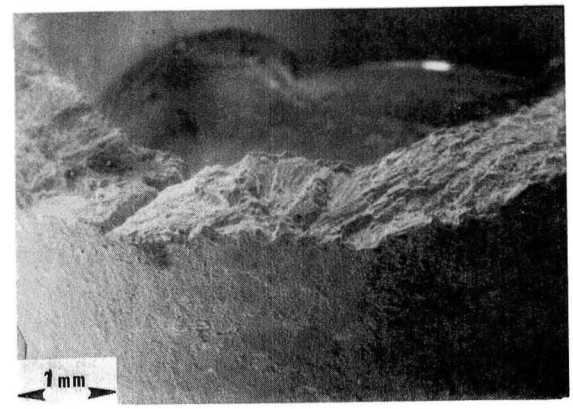

B1-FS

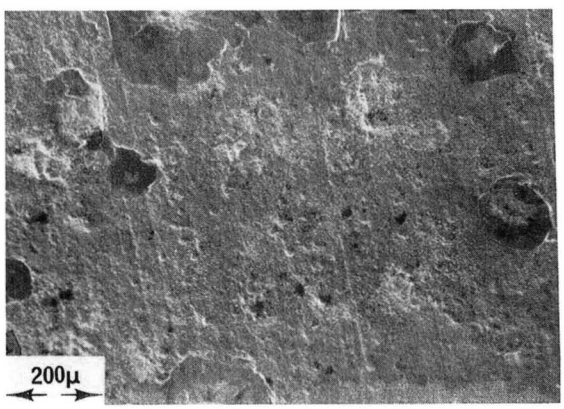

A2-OS

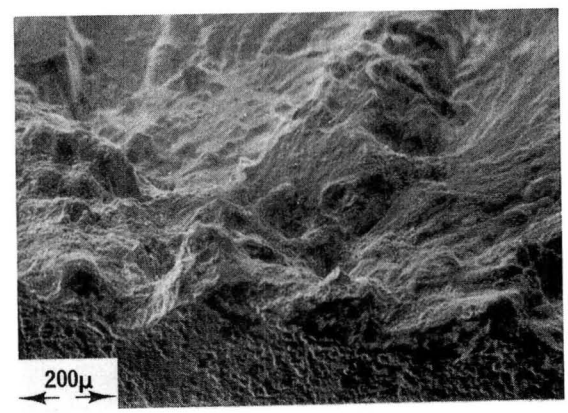

B2-FS

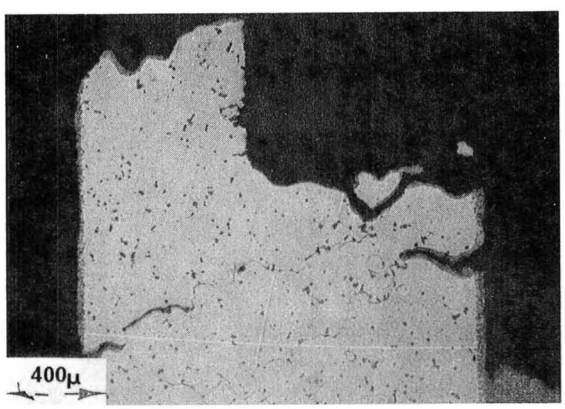

A3-DS

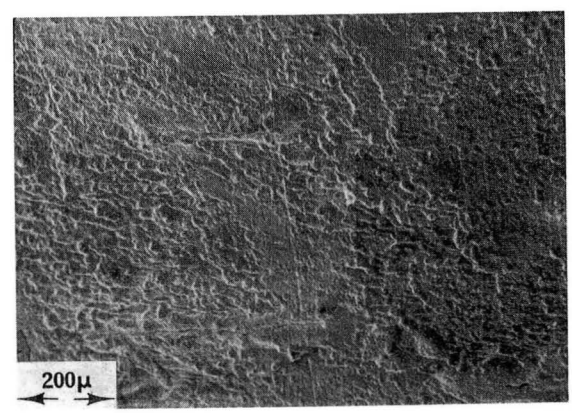

B3-OS

Figure 74. Uncoated René 80 (NASA); TCCR test in air at 1000C.
A. Ree 223: PP = 0.299%, CP = 0.757%, N_f = 13, t_f = 56.00 hr., Maximum Tensile Stress = 127.7 MPa.
B. Ree 220: PP = 0.055%, CP = 0.054%, N_f = 1600, t_f = 19.85 hr., Maximum Tensile Stress = 89.0 MPa.

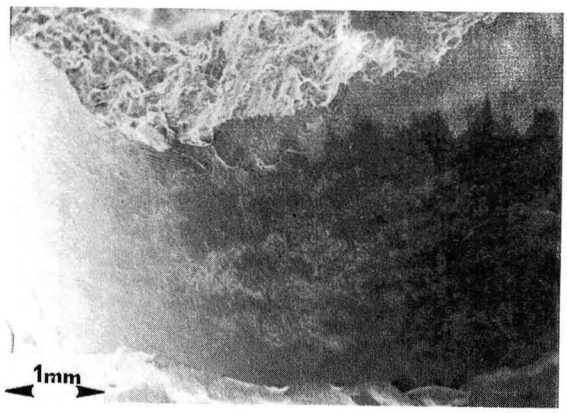

A1-OS

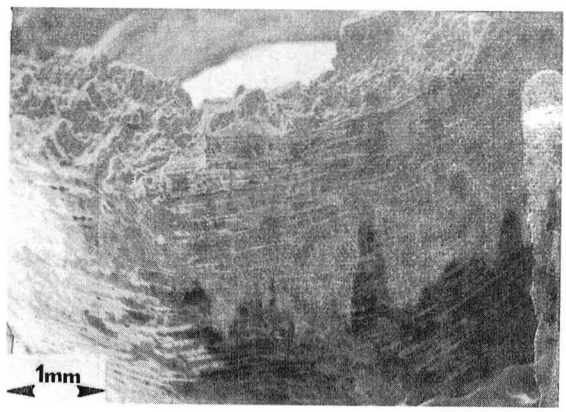

B1-OS

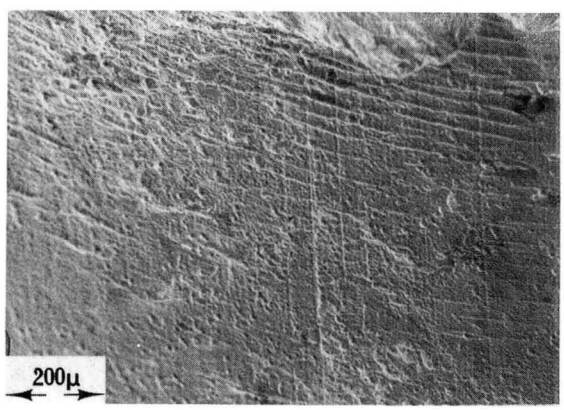

A2-OS

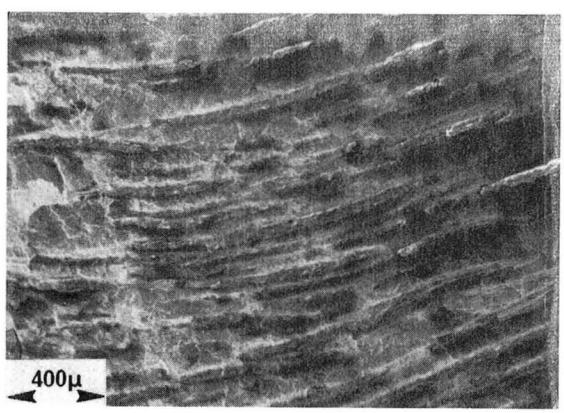

B2-OS

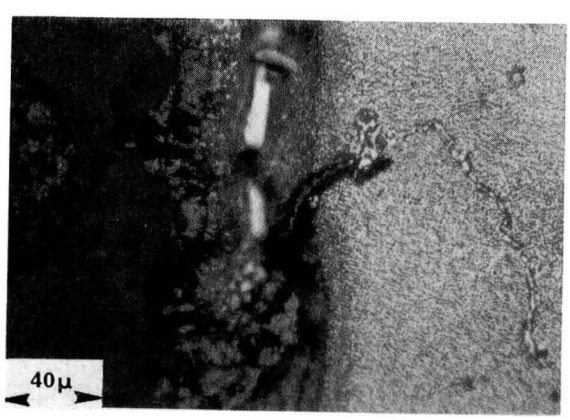

B4-DS

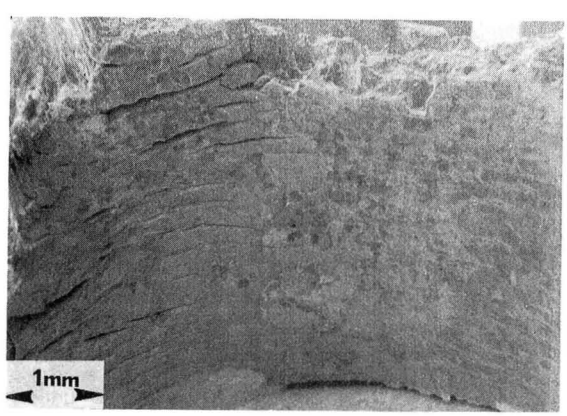

B3-IS

Figure 75. Uncoated René 80 (NASA); BCCR test in air at 1000C.
A. Ree 211: PP = 0.276%, CC = 1.557%, N_f = 10, t_f = 1.56 hr., Maximum Tensile stress = 244.1 MPa.
B. Ree 212: PP = 0.071%, CC = 0.232%, N_f = 191, t_f = 85.10 hr., Maximum Tensile Stress = 157.8 MPa.

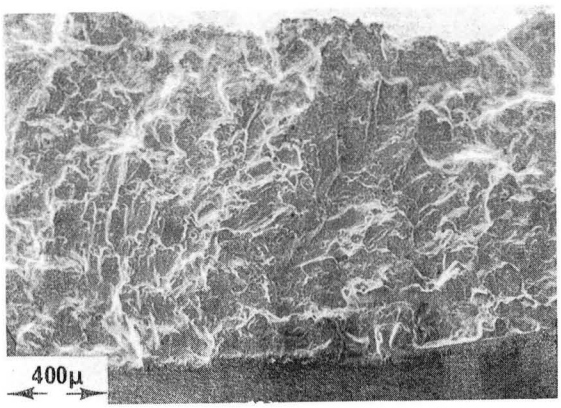

A1-FS

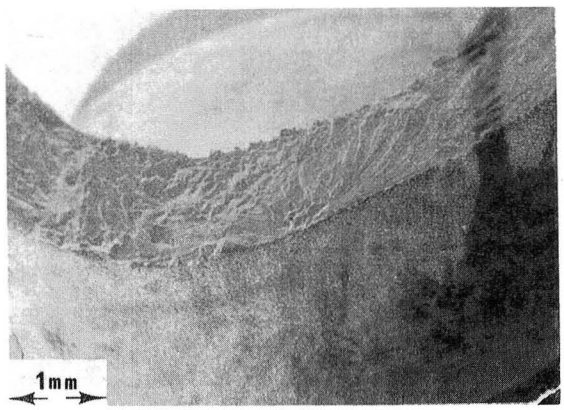

B1-FS

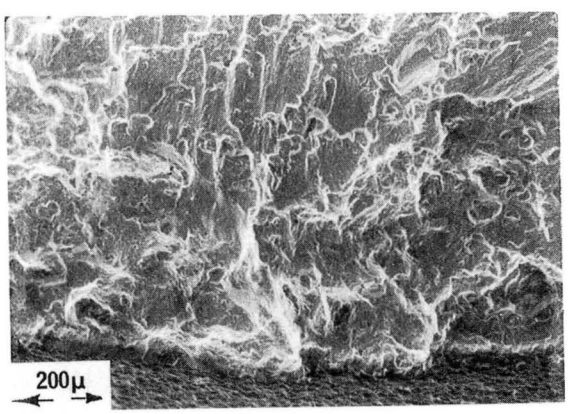

A2-FS

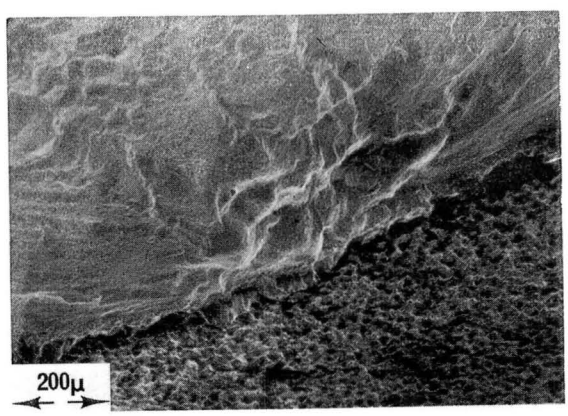

B2-FS

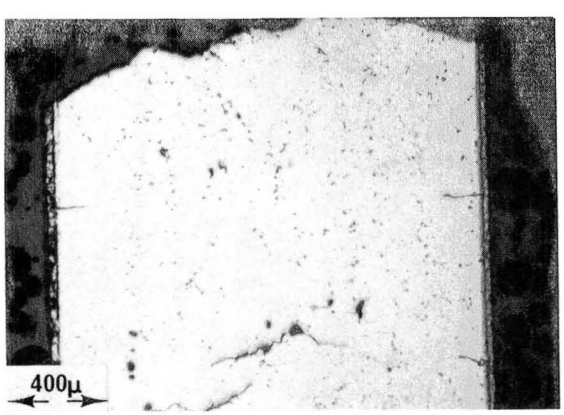

A3-DS

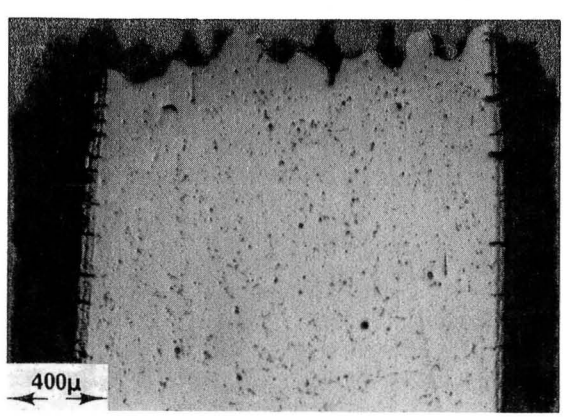

B3-DS

Figure 76 Coated René 80 (NASA); HRSC test in air at 1000C.
A. Ree 306: PP = 0.231%, N_f = 650, t_f = 0.18 hr., Maximum Tensile Stress = 298.6 MPa.
B. Ree 311: PP = 0.046%, N_f = 15,000, t_f = 4.28 hr., Maximum Tensile Stress = 178.2 MPa.

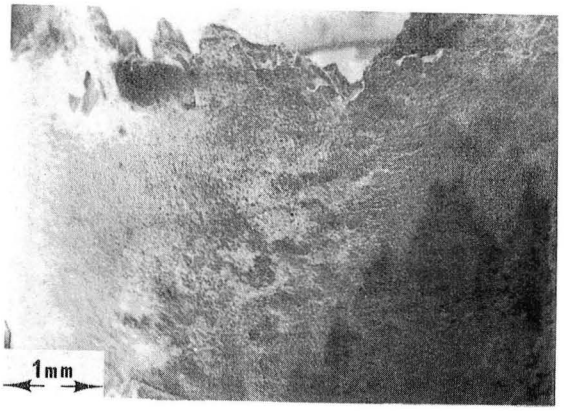

A1-OS

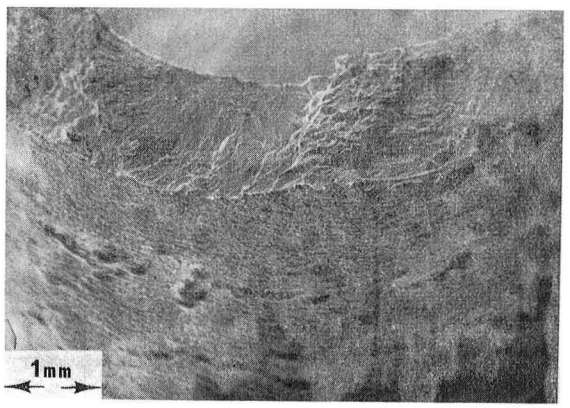

B1-OS

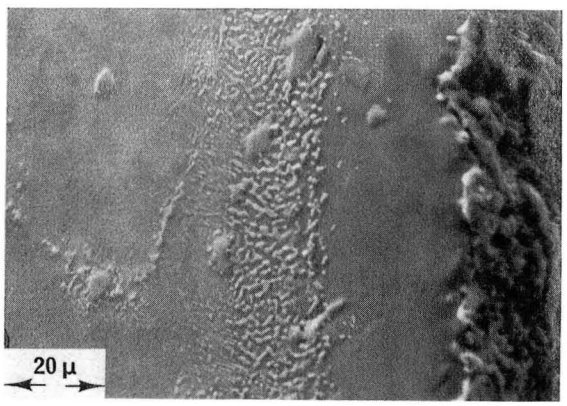

A2-DS

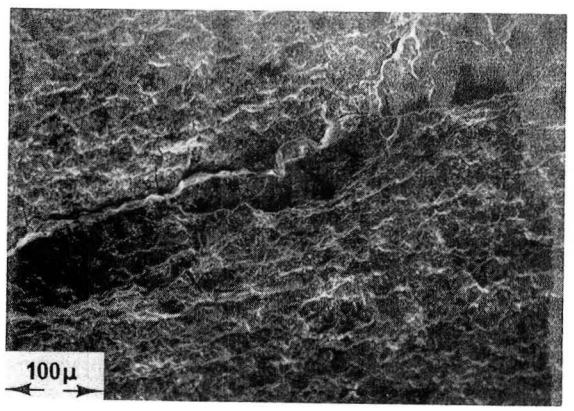

B2-OS

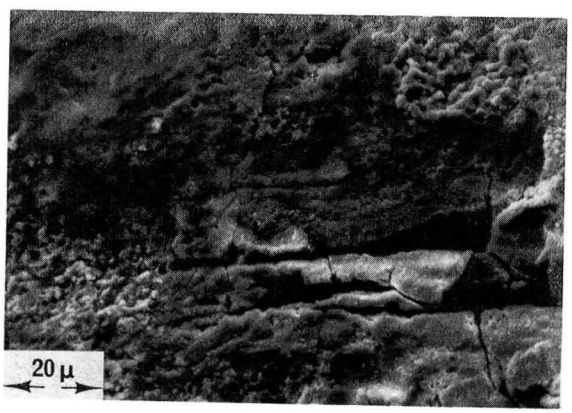

B4-IS

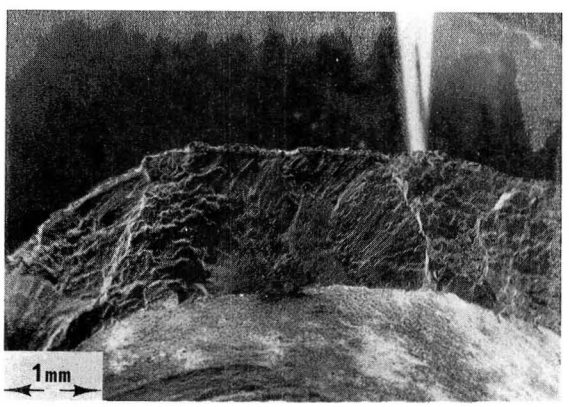

B3-FS

Figure 77. Coated René 80 (NASA); CCCR test in air at 1000C.
A. Ree 301: PP = 0.228%, PC = 0.392%, N_f = 159, t_f = 20.47 hr., Maximum Tensile Stress = 323.5 MPa.
B. Ree 328: PP = 0.044%, PC = 0.044%, N_f = 1900, t_f = 4.10 hr., Maximum Tensile Stress = 210.1 MPa.

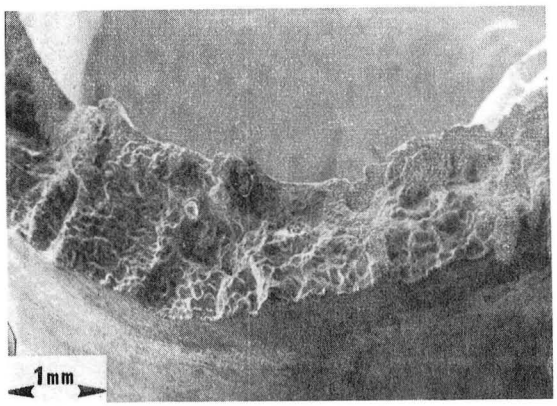

A1-FS

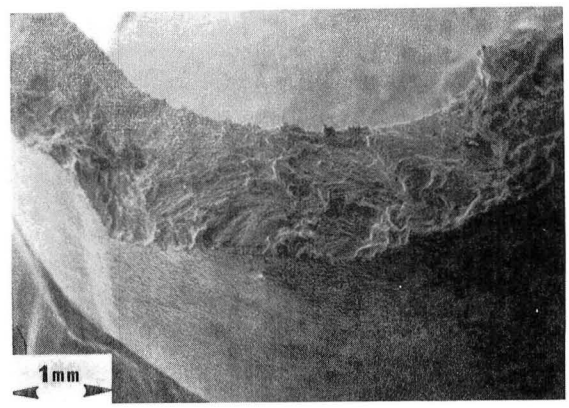

B1-FS

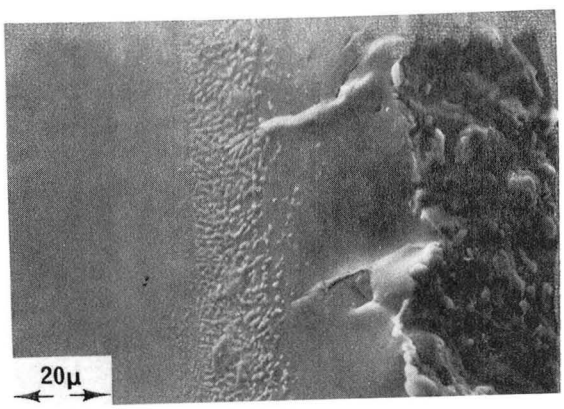

A2-DS

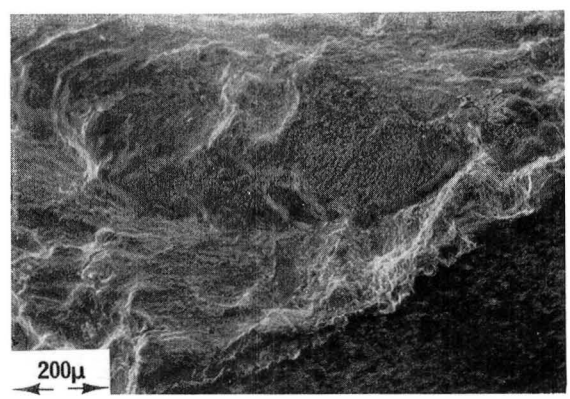

B2-FS

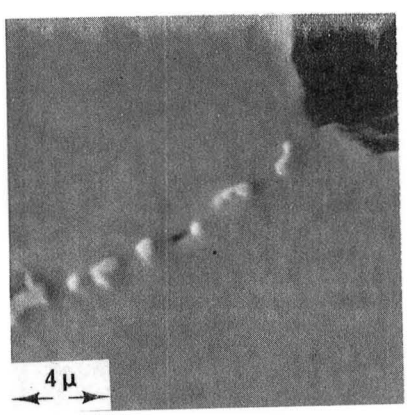

A3-DS

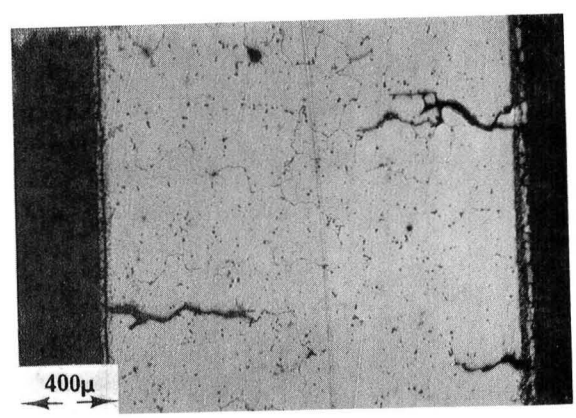

B3-DS

Figure 78. Coated René 80 (NASA); TCCR test in air at 1000C.
A. Ree 305: PP = 0.134%, CP = 0.496%, N_f = 48, t_f = 11.6 hr., Maximum Tensile Stress = 152.9 MPa.
B. Ree 302: PP = 0.058%, CP = 0.044%, N_f = 3928, t_f = 45.45 hr., Maximum Tensile Stress = 90.3 MPa.

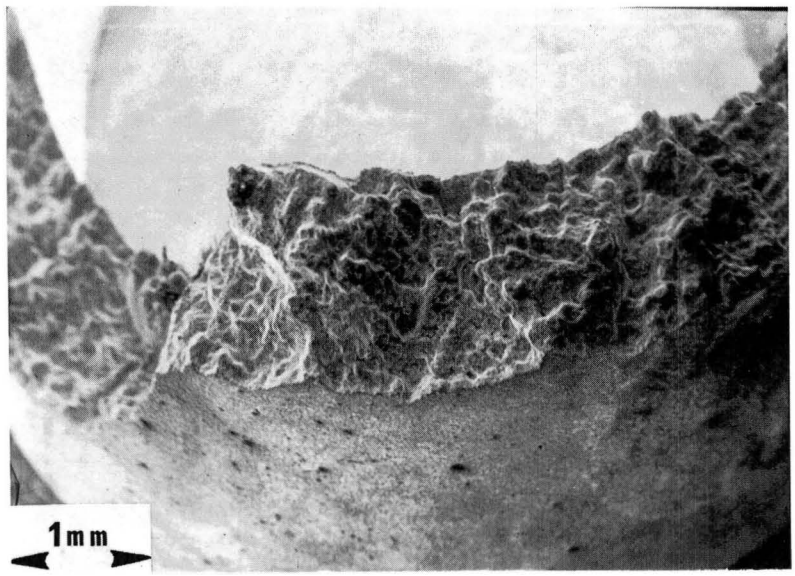

A-FS

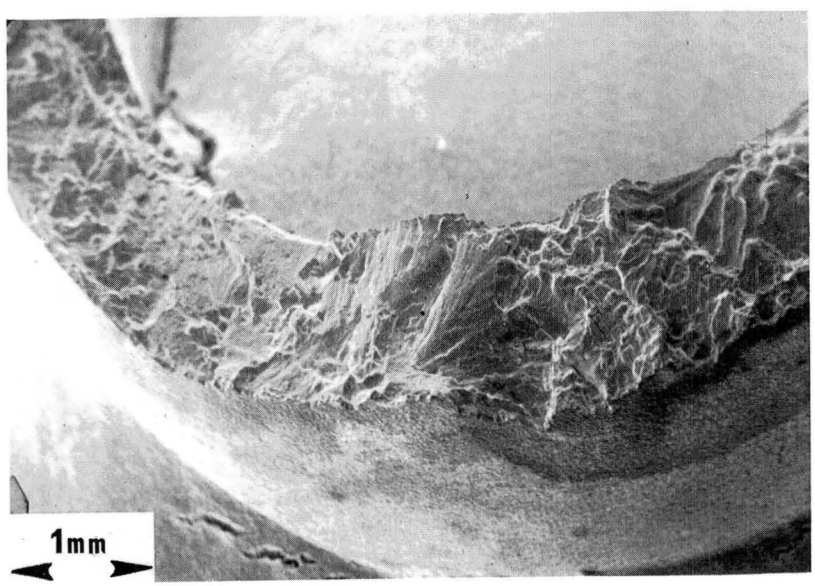

B-FS

Figure 79. Coated René 80 (NASA); BCCR test in air at 1000C.
A. Ree 316: PP = 0.141%, CP = 0.036%, CC = 0.546%, N_f = 36, t_f = 20.44 hr., Maximum Tensile Stress 169.1 MPa.
B. Ree 314: PP = 0.011%, CC = 0.082%, N_f 4457, t_f = 25.92 hr., Maximum Tensile Stress = 103.4 MPa.

1-OS|DS

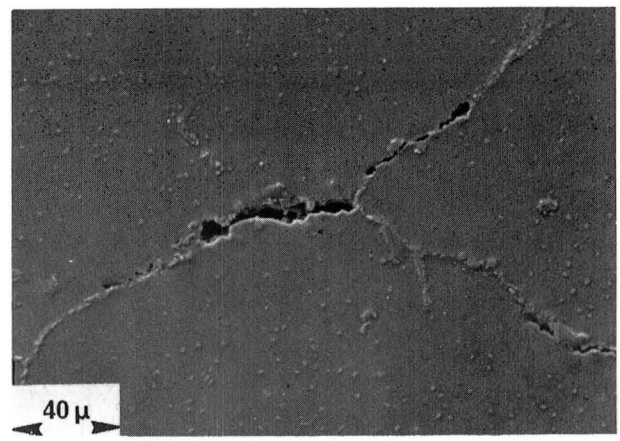

3-DS

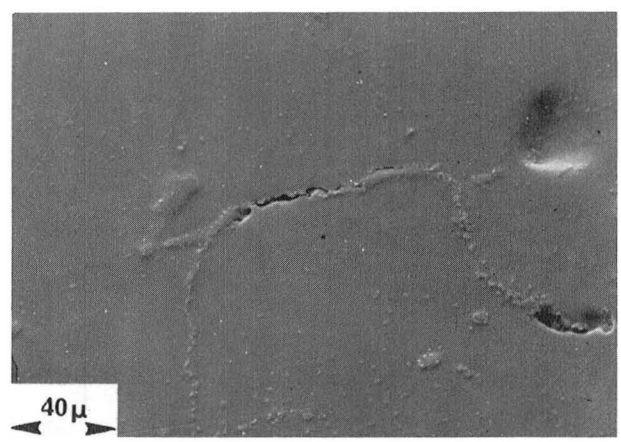

4-DS

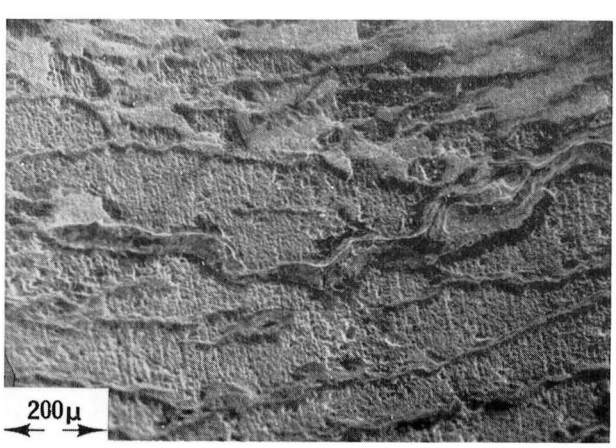

2-OS

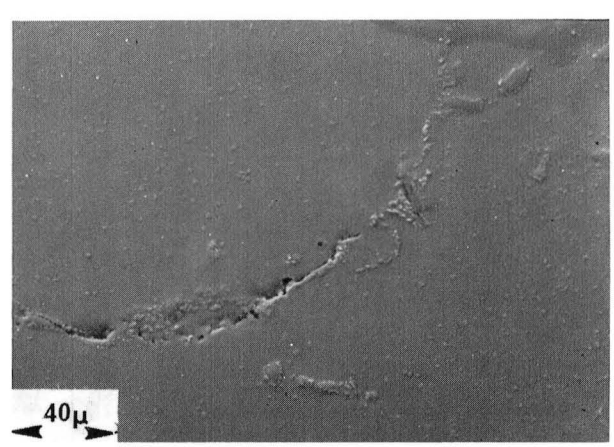

4-DS

Figure 80. Uncoated René 80 (U of C); TCCR test in air at 1000C. GR-1: PP = 0.272%, CP = 0.325%, N_f = 130, t_f = 16.56 hr., Maximum Tensile Stress = 172 MPa.

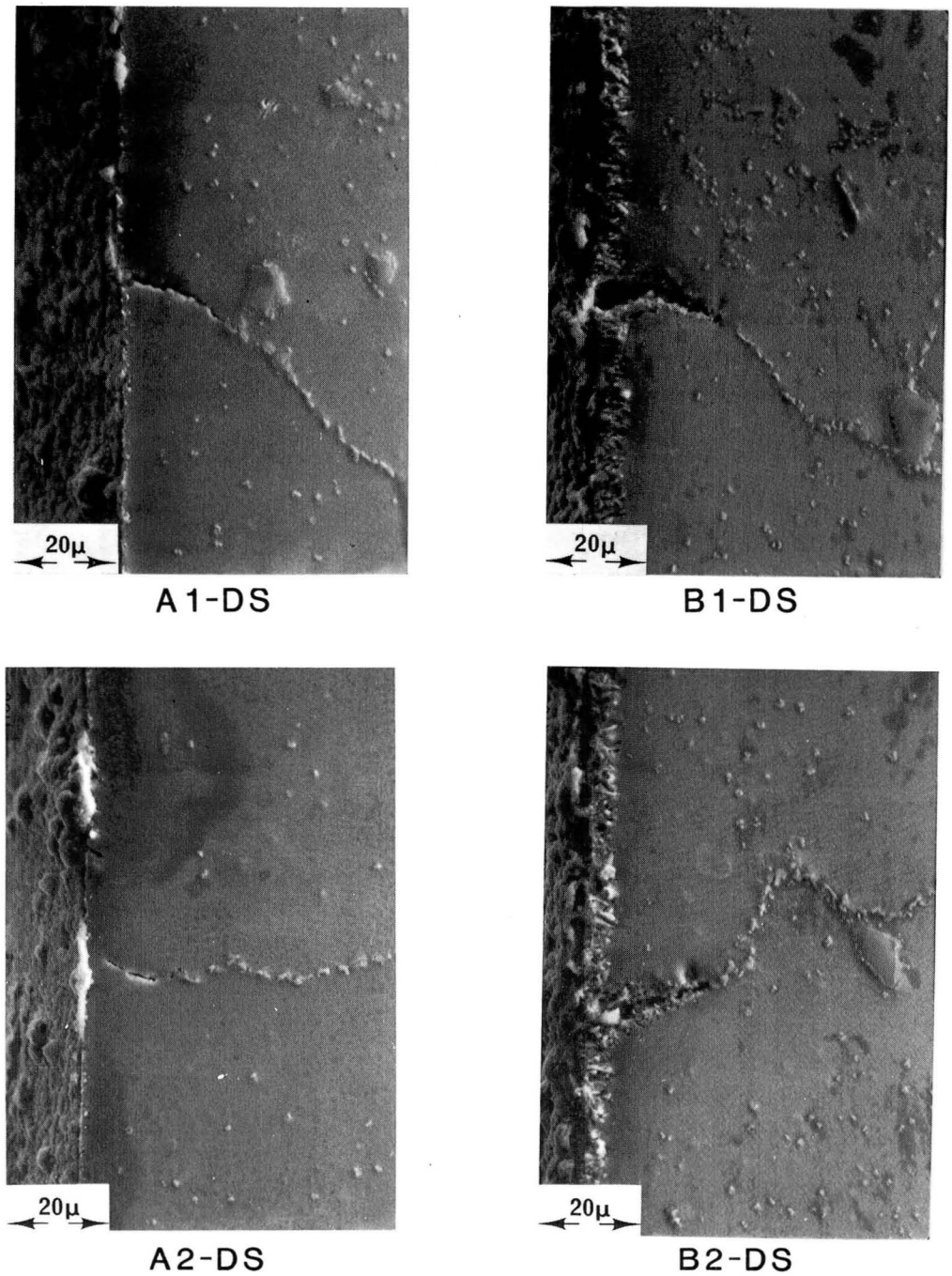

Figure 81. Uncoated René 80 (U of C); TCCR test in air at 1000C.
A. GR-2: PP = 0.272%, CP = 0.325%, Test stopped at t = 3.31 hr. and N = 7, Maximum Tensile Stress = 172 MPa.
B. GR-3: PP = 0.272%, CP = 0.325% Test stopped at t = 7.39 hr. and N = 27, Maximum Tensile Stress = 172 MPa.

1-DS

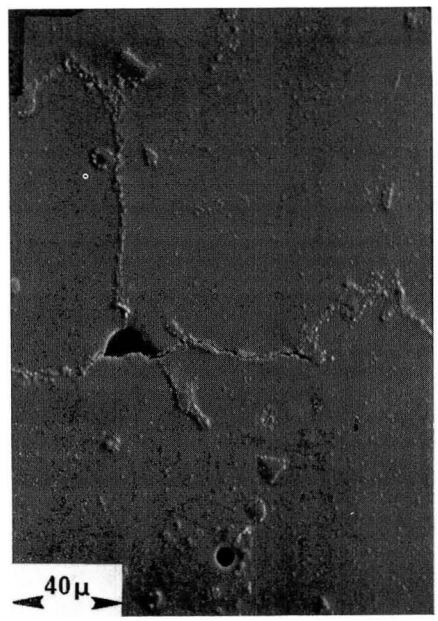

3-DS

2-DS

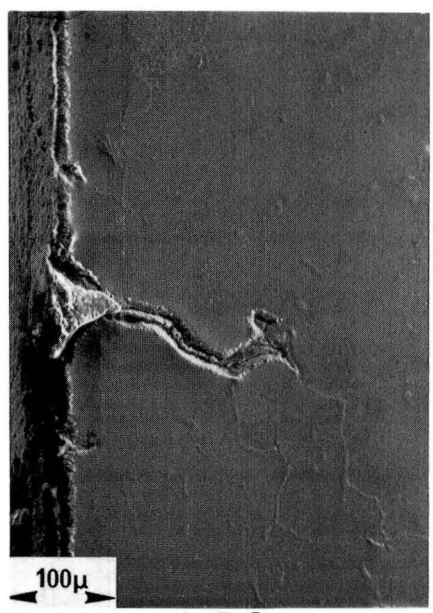

4-DS

Figure 82. Uncoated René 80 (U of C); strain hold test in air at 1000C.
GR-4: PP = 0.576%, CP = 0.095%, N_f = 160, t_f = 17.33 hr., Maximum Tensile Stress = 243.36 MPa.

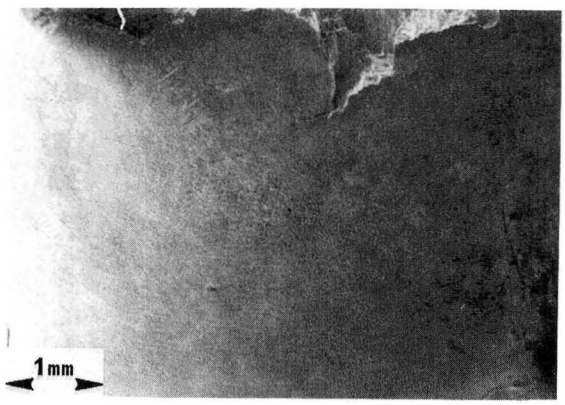

A1-OS

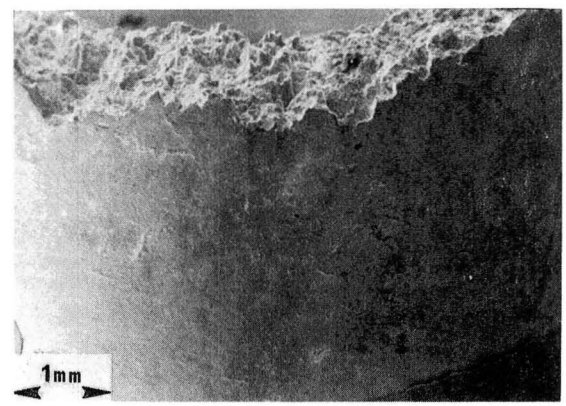

B1-OS

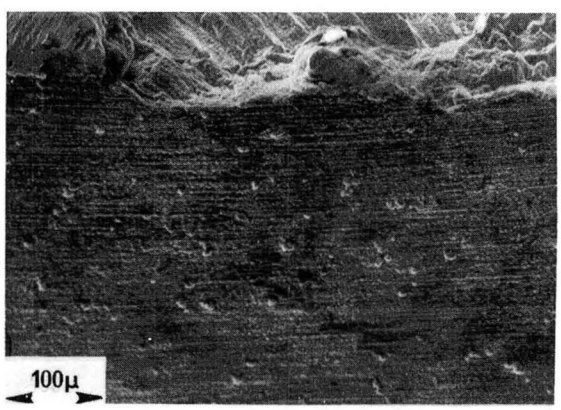

A2-OS

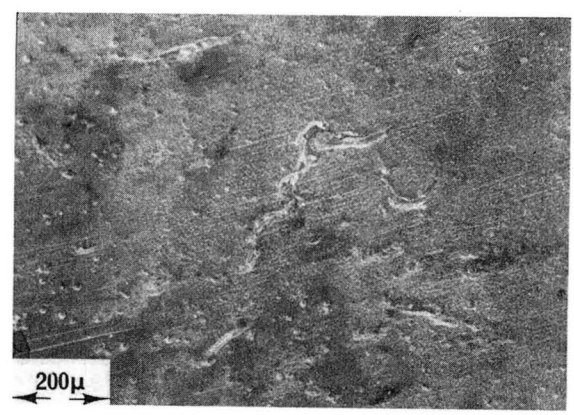

B2-OS

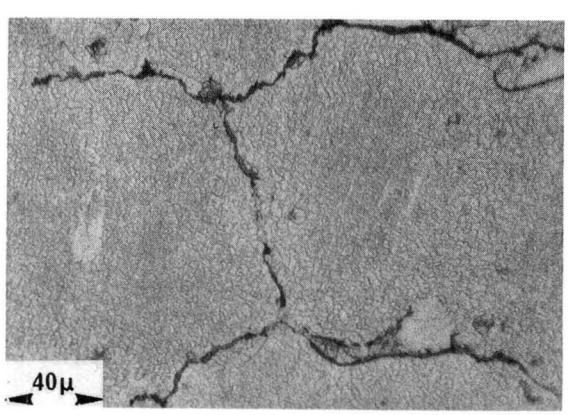

B4-DS

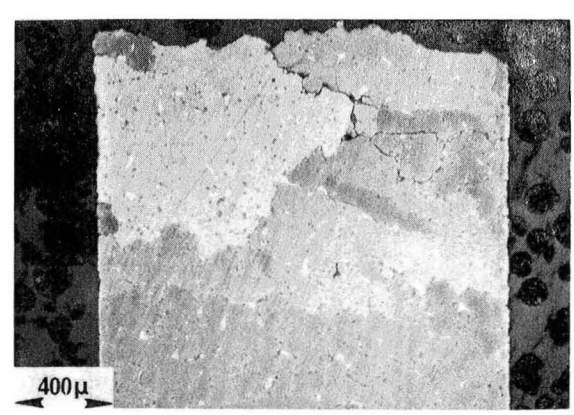

B3-DS

Figure 83. Uncoated IN 100 (NASA); HRSC test in air at 925C.
A. INN-17: PP = 0.417%, N_f = 160, t_f = 0.11 hr., Maximum Tensile Stress = 548.7 MPa.
B. INN-36: PP = 0.040, N_f = 4015, t_f = 2.23 hr., Maximum Tensile Stress = 224.1 MPa.

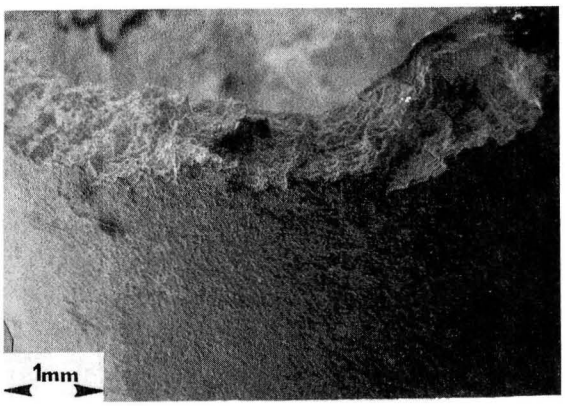

A1-OS

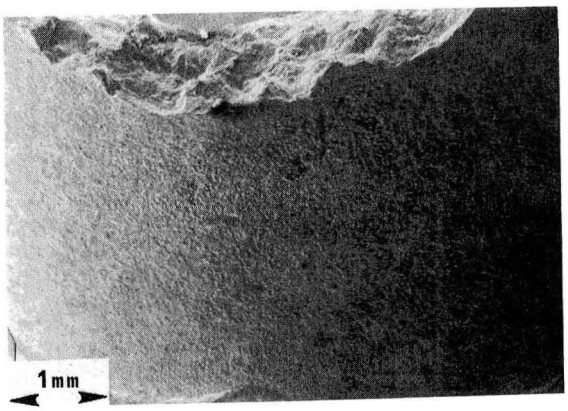

B1-OS

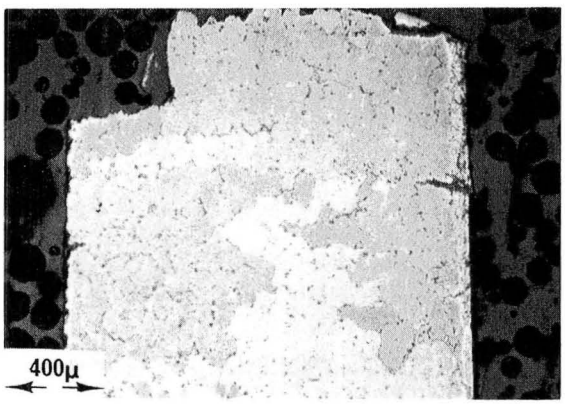

A2-DS

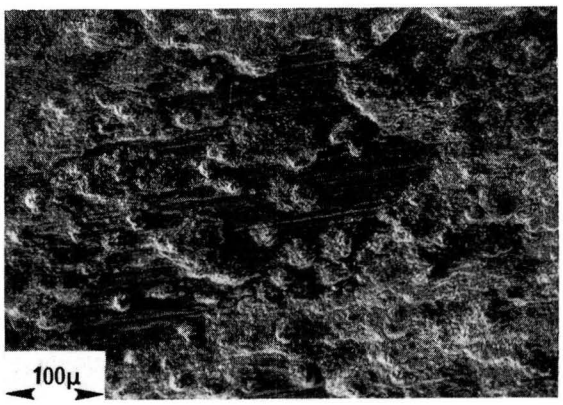

B2-OS

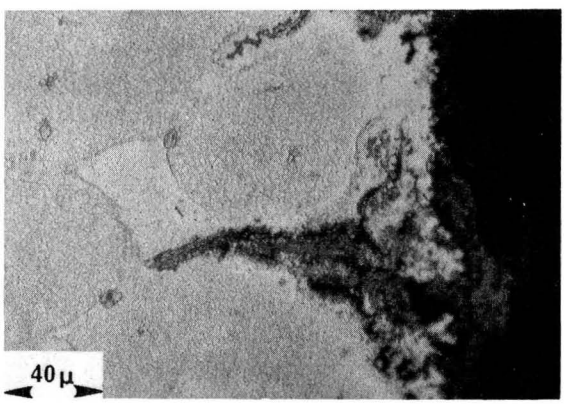

B4-DS

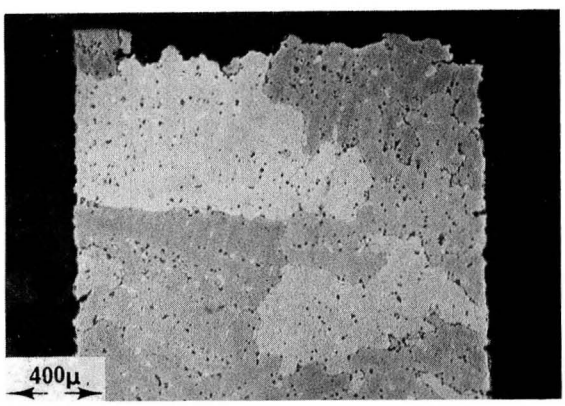

B3-DS

Figure 84. Uncoated IN 100 (NASA); CCCR test in air at 925C.
A. INN-13: PP = 0.076%, PC = 0.102%, N_f = 139, t_f = 87.31 hr., Maximum Tensile Stress = 486.8 MPa.
B. INN-15: PP = 0.034%, PC = 0.064%, N_f = 332, t_f = 129.11 hr., Maximum tensile Stress = 412.3 MPa.

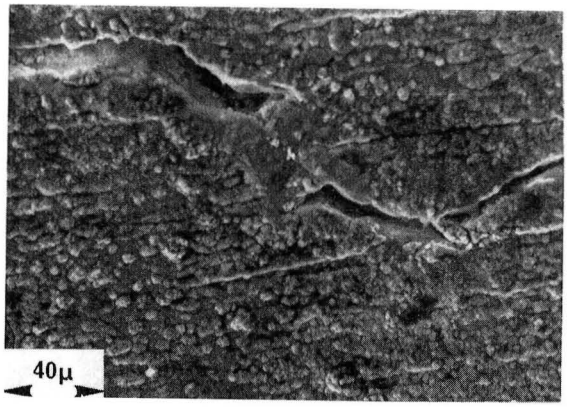

A1-OS

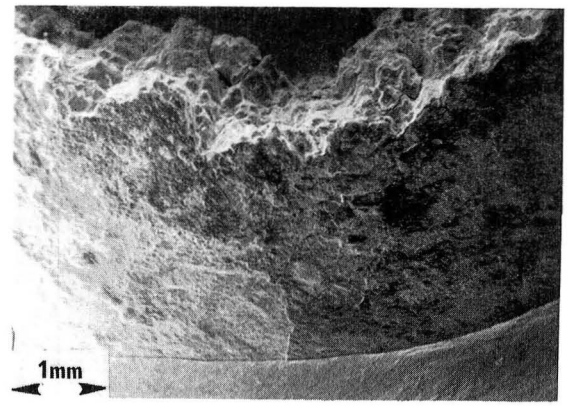

B1-OS

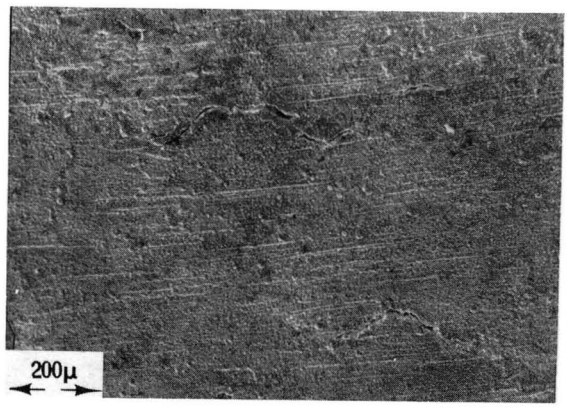

A2-OS

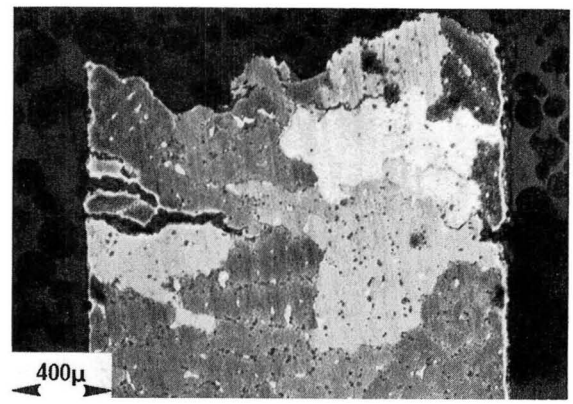

B2-DS

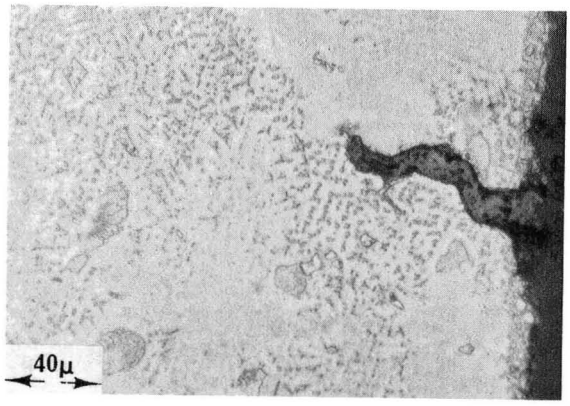

A3-DS

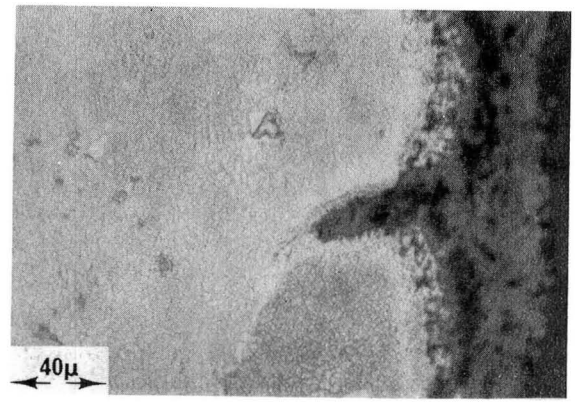

B3-DS

Figure 85. Uncoated IN 100 (NASA); TCCR test in air at 925C.
A. INN-99: PP = 0.369%, CP = 1.288%, N_f = 6, t_f = 6.99 hr., Maximum Tensile Stress = 322.7 MPa.
B. INN-9: PP = 0.047%, CP = 0.047%, N_f = 1100, t_f = 159.32 hr., Maximum Tensile Stress = 142.0 MPa.

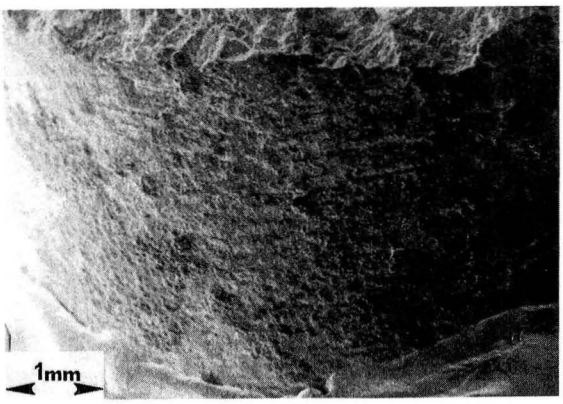

A1-OS

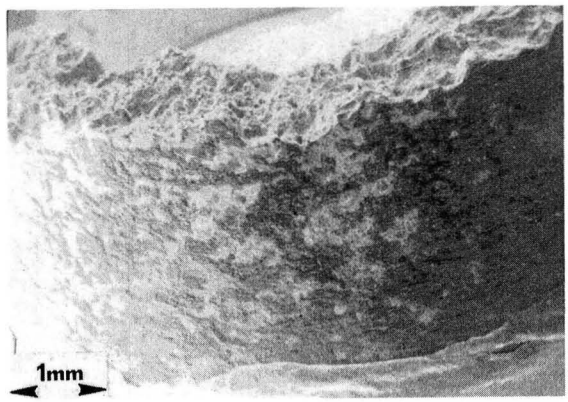

B1-OS

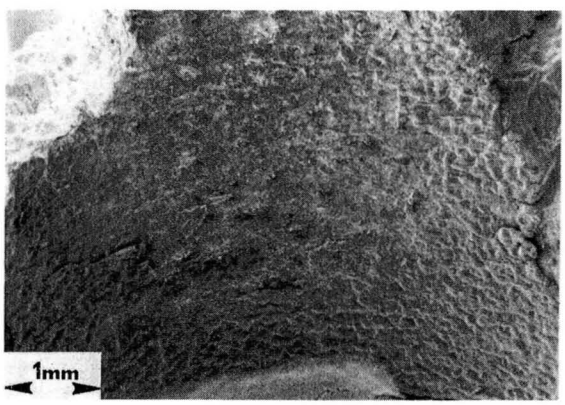

A2-IS

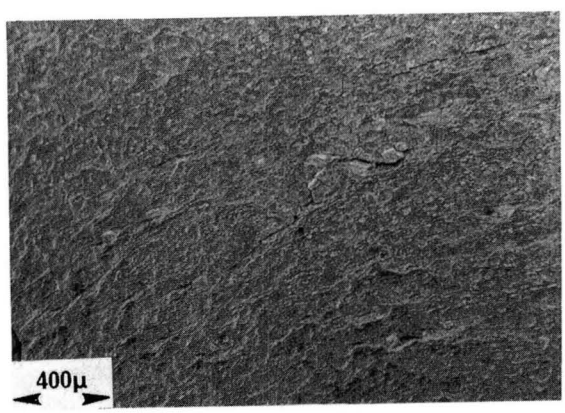

B2-IS

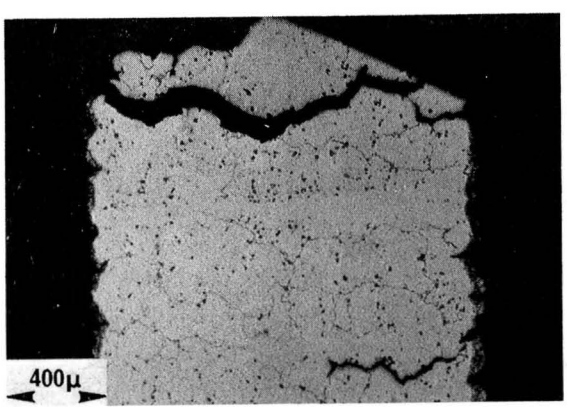

A3-DS

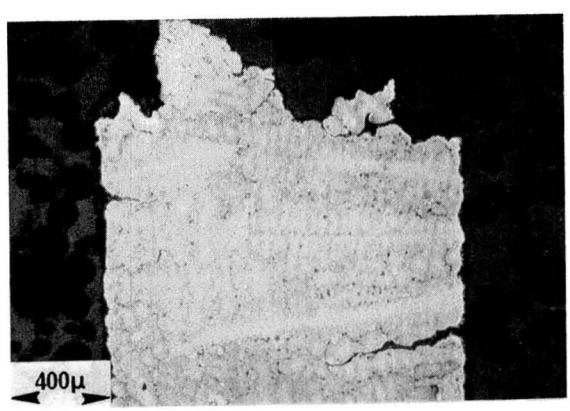

B3-DS

Figure 86. Uncoated IN 100 (NASA); BCCR test in air at 925C.
A. INN-16: PP = 0.039%, PC = 0.019%, CC = 0.374%, N_f = 102, t_f = 203.37 hr., Maximum Tensile Stress = 171.0 MPa.
B. INN-89: PP = 0.045%, CC = 0.099%, N_f = 840, t_f = 78.33 hr., Maximum Tensile Stress = 200.7 MPa.

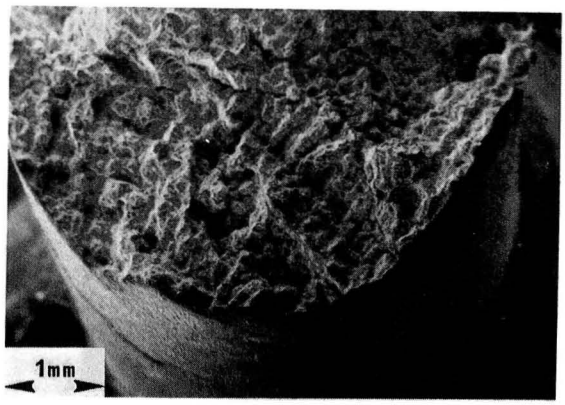

A1-FS

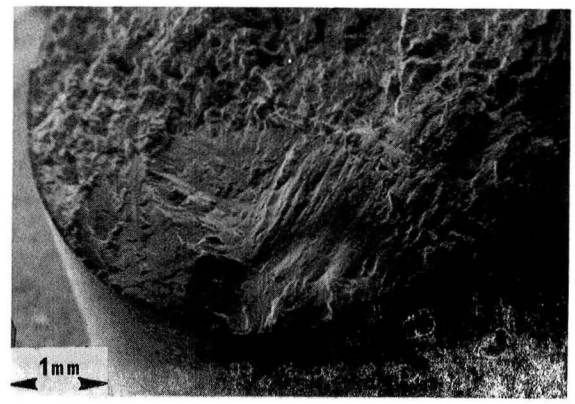

B1-FS

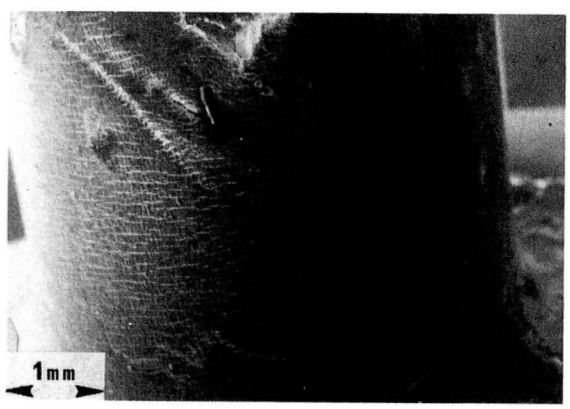

A2-OS

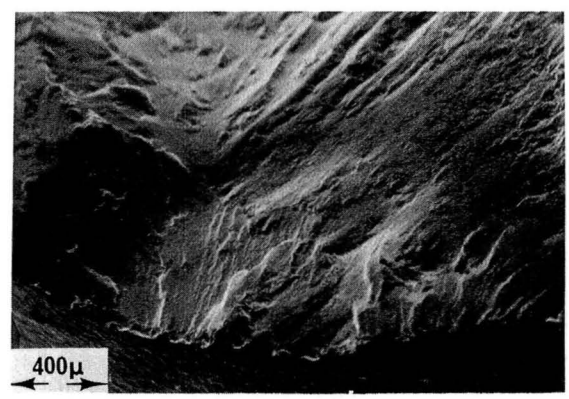

B2-FS

A3-OS

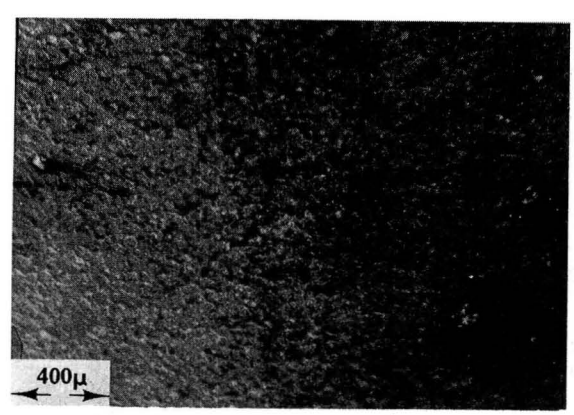

B3-OS

Figure 87. Coated IN 100 (ONERA); test in air at 1000C.
A. N-14: Creep Rupture Test, t_r = 10.54 hr., Maximum Tensile Stress = 205.5 MPa.
B. N-4: Pure Fatiuge Test, N_f = 24,278, Maximum Tensile Stress = 203 MPa.

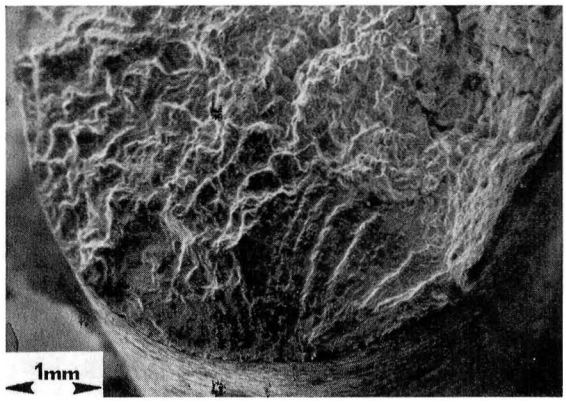

A1-FS

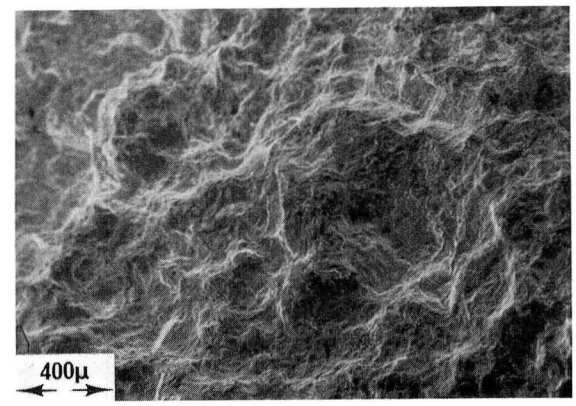

B1-FS

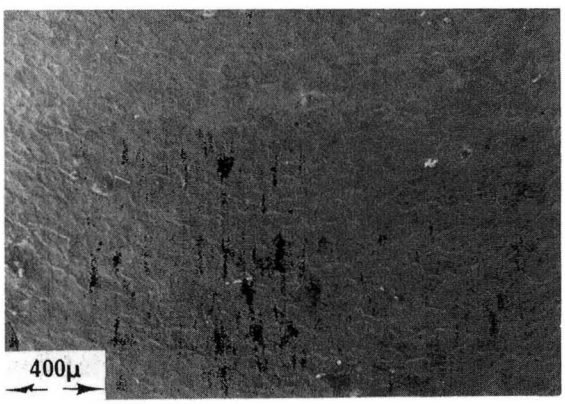

A2-OS

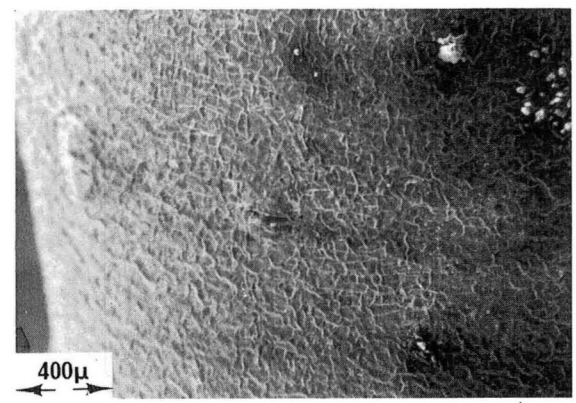

B2-OS

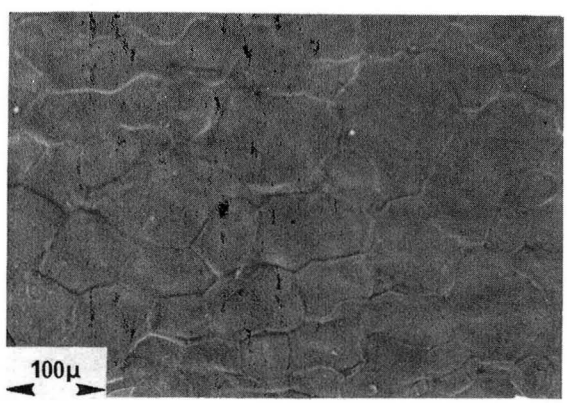

A3-OS

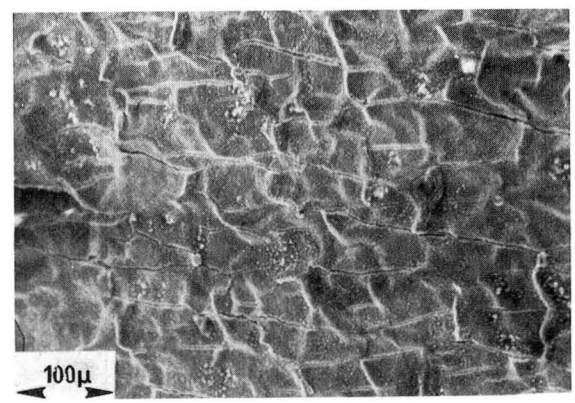

B3-OS

Figure 88. Coated IN 100 (ONERA): test in air at 1000C.
A. 34; PP = 0.013%, CC = 0.053%, N_f = 2520, t_f = 21.00 hr., Maximum Tensile Stress = 175 MPa.
B. N-32; PP = 0.036%, CC = 0.136%, N_f = 568, t_f = 61.50 hr., Maximum Tensile Stress = 171.0 MPa.

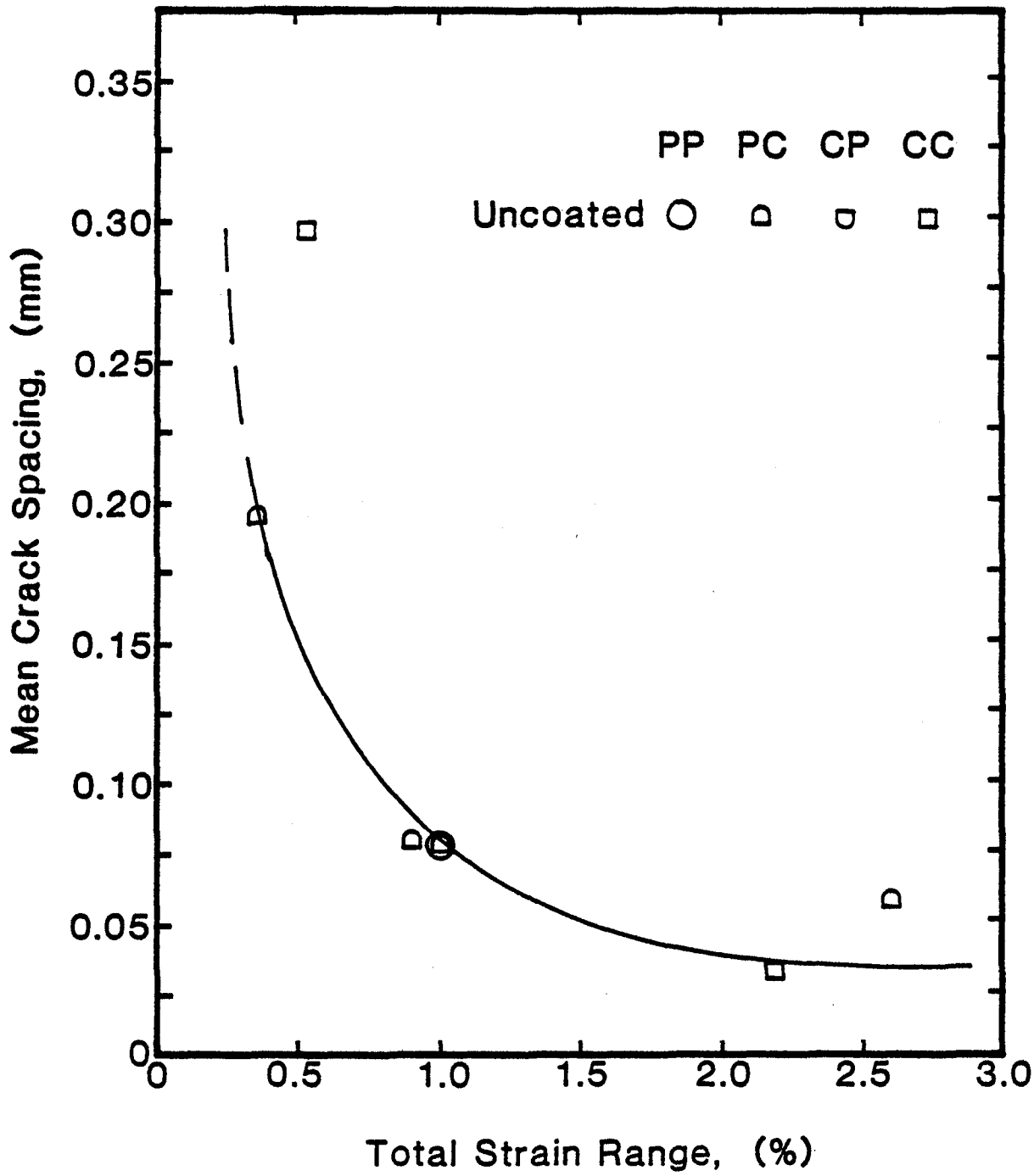

Figure 89. Mean Crack Spacing versus Total Strain Range for uncoated René 80 tested in air at 1000C (NASA)

A

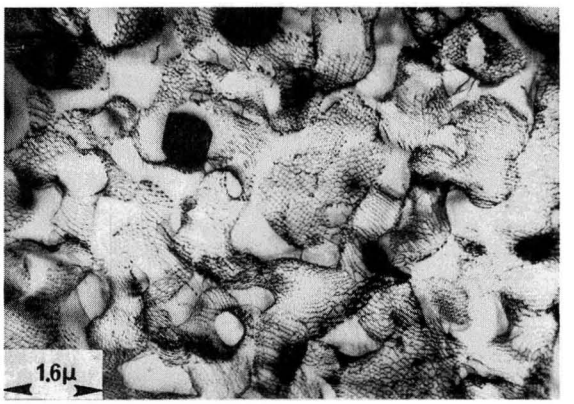

D

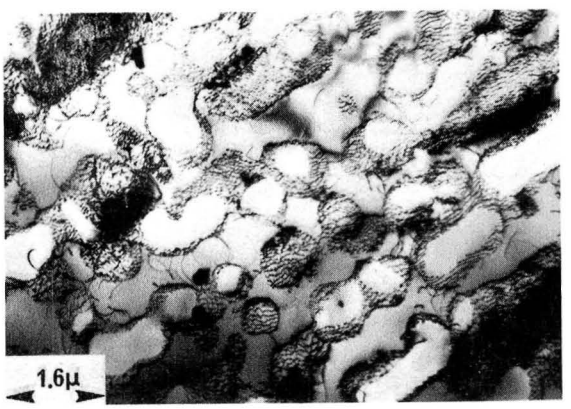

B

E

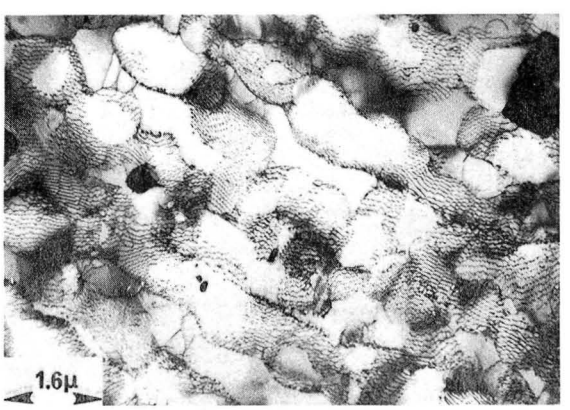

C

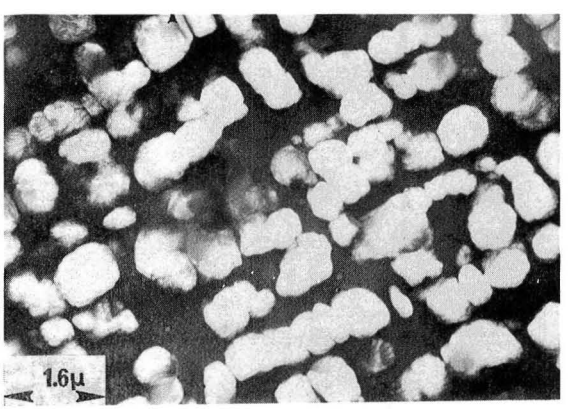

F

Figure 90. Uncoated René 80 (U of C); Transmission Electron Microscopy of a few selected specimens tested in air at 1000C.

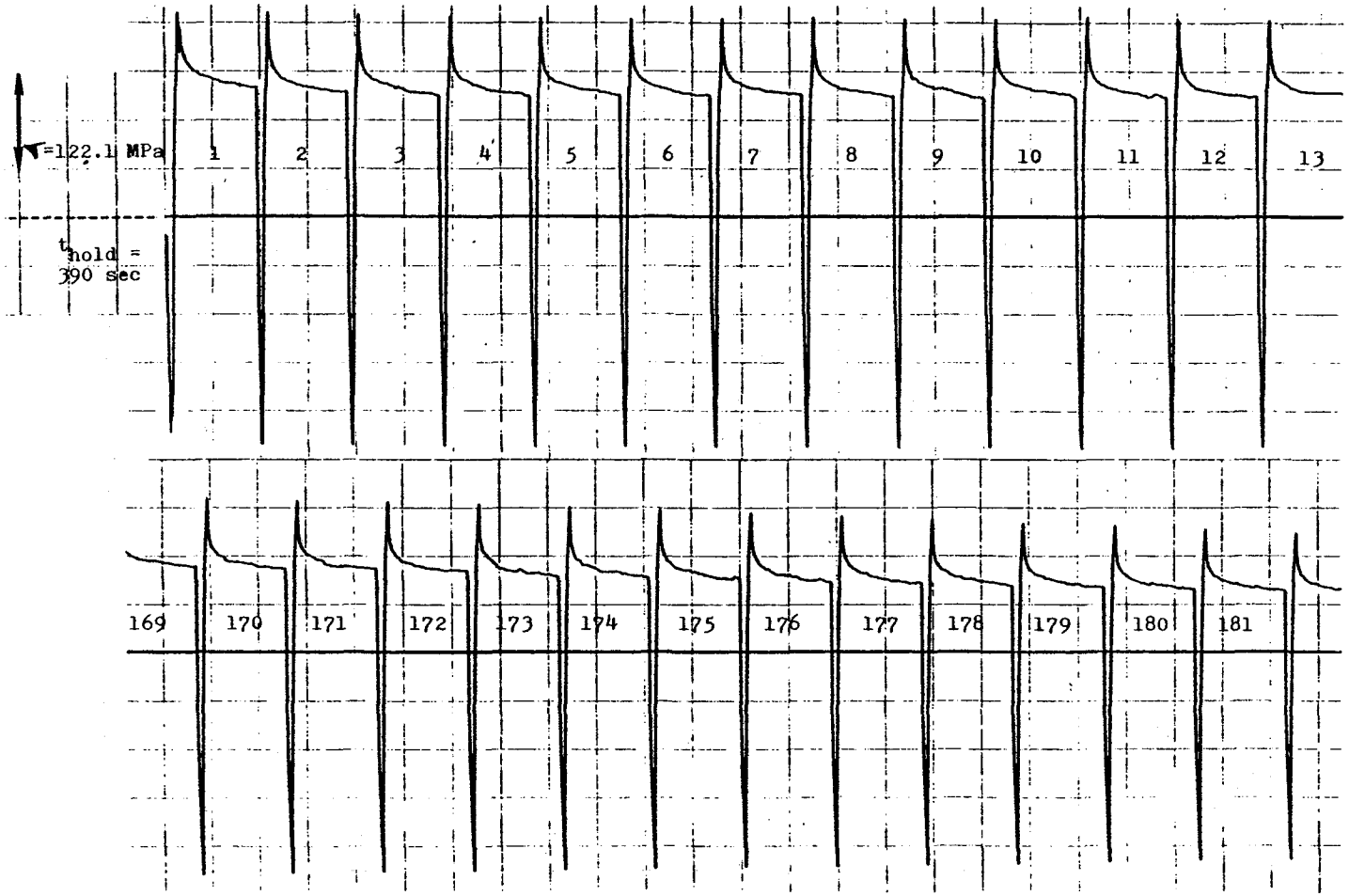

Figure 91. Uncoated René 80 (U of C); Stress-time record for strain hold test, GR-4 (Case I).

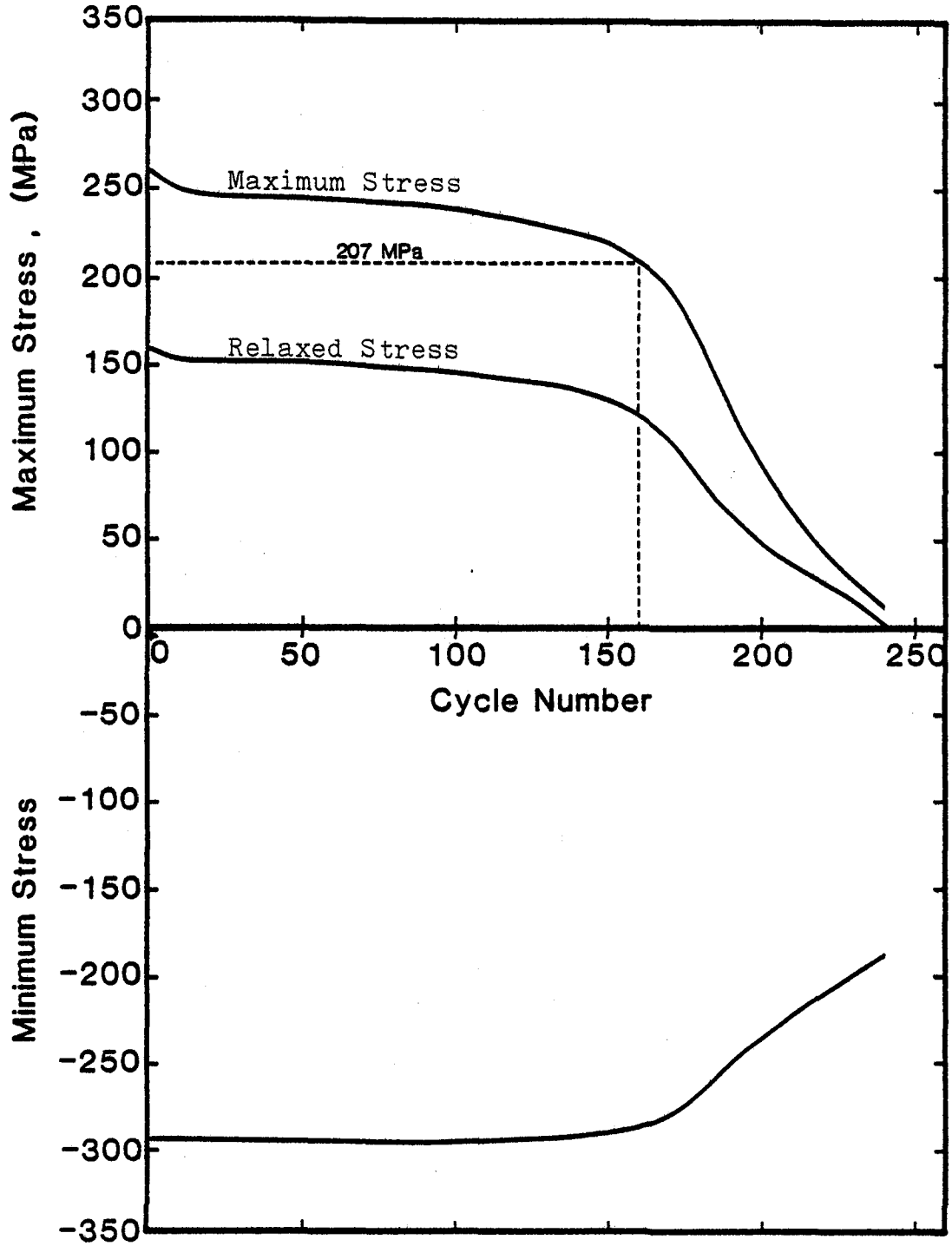

Figure 92. Uncoated René 80 (U of C); Stress versus Cycle Number for the strain hold test, GR-4 (Case I).

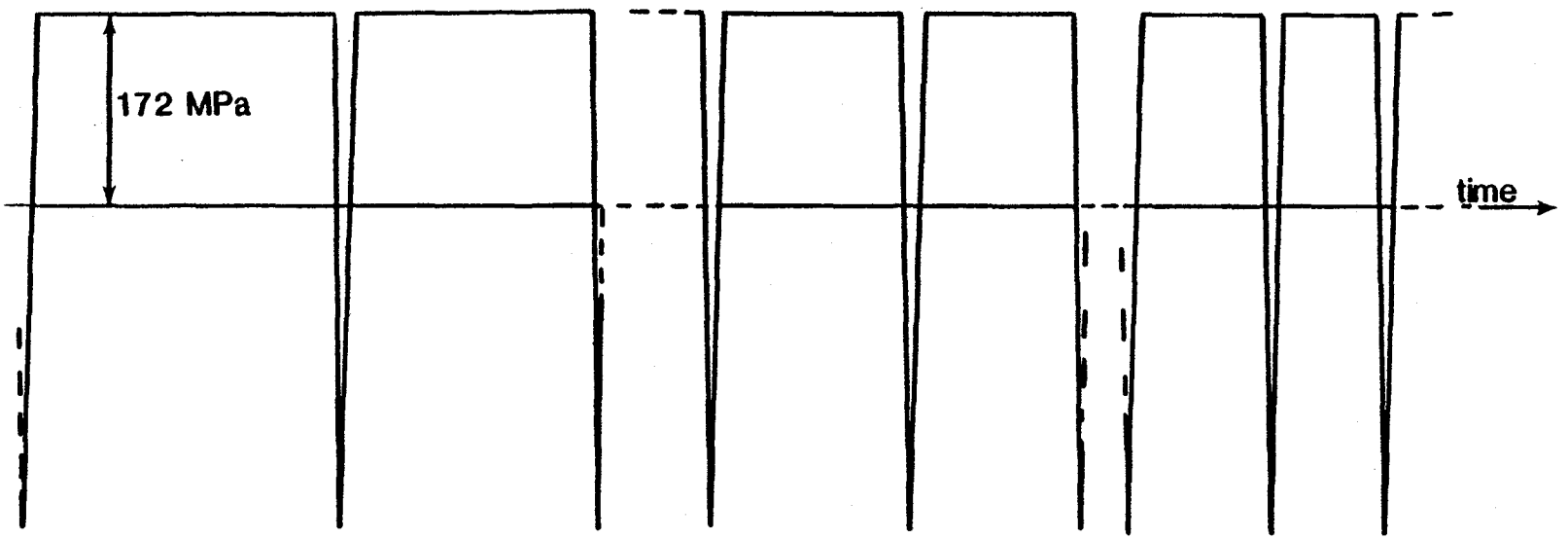

Figure 93. Uncoated René 80 (U of C) Schematic of the stress-time record for the tensile cyclic creep rupture test, GR-1 (Case II).

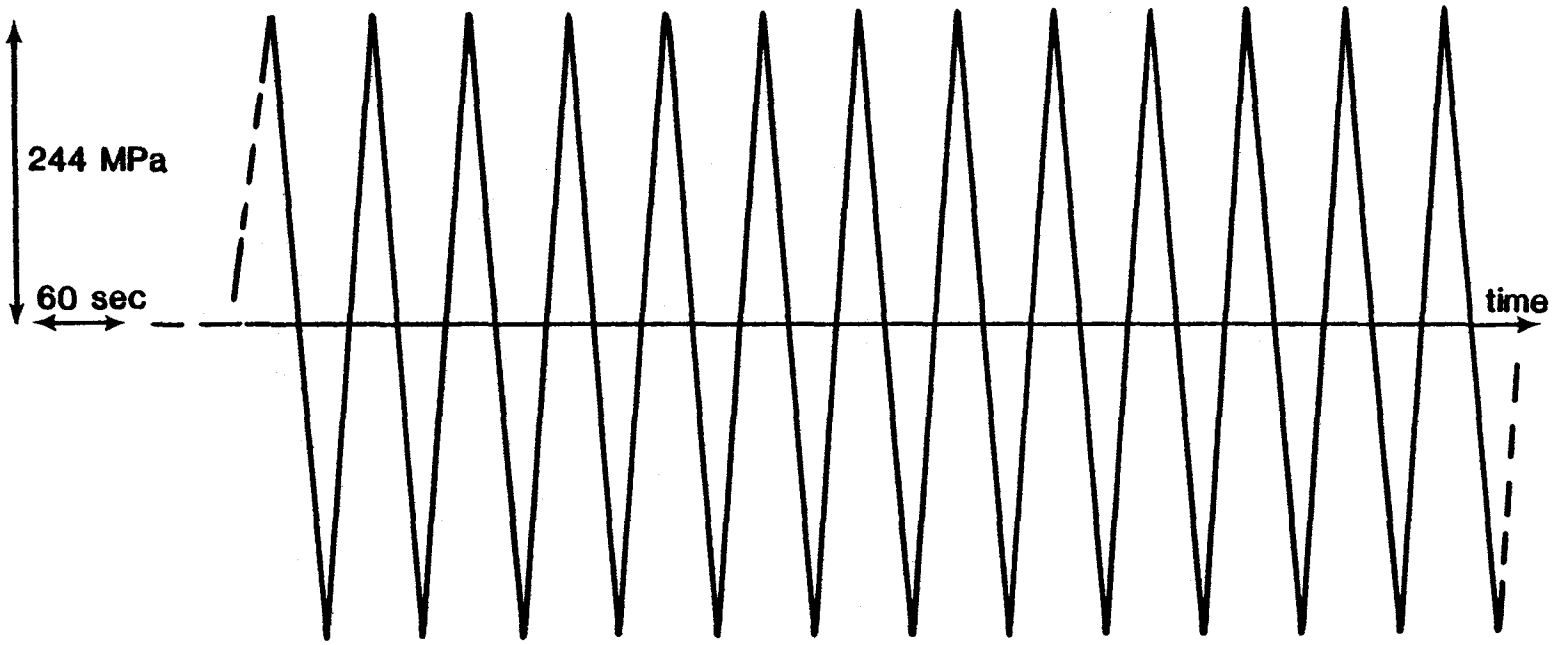

Figure 94. Uncoated René 80 (U of C); Schematic of the stress-time record for the continuous cycling test, GR-5 (Case III).

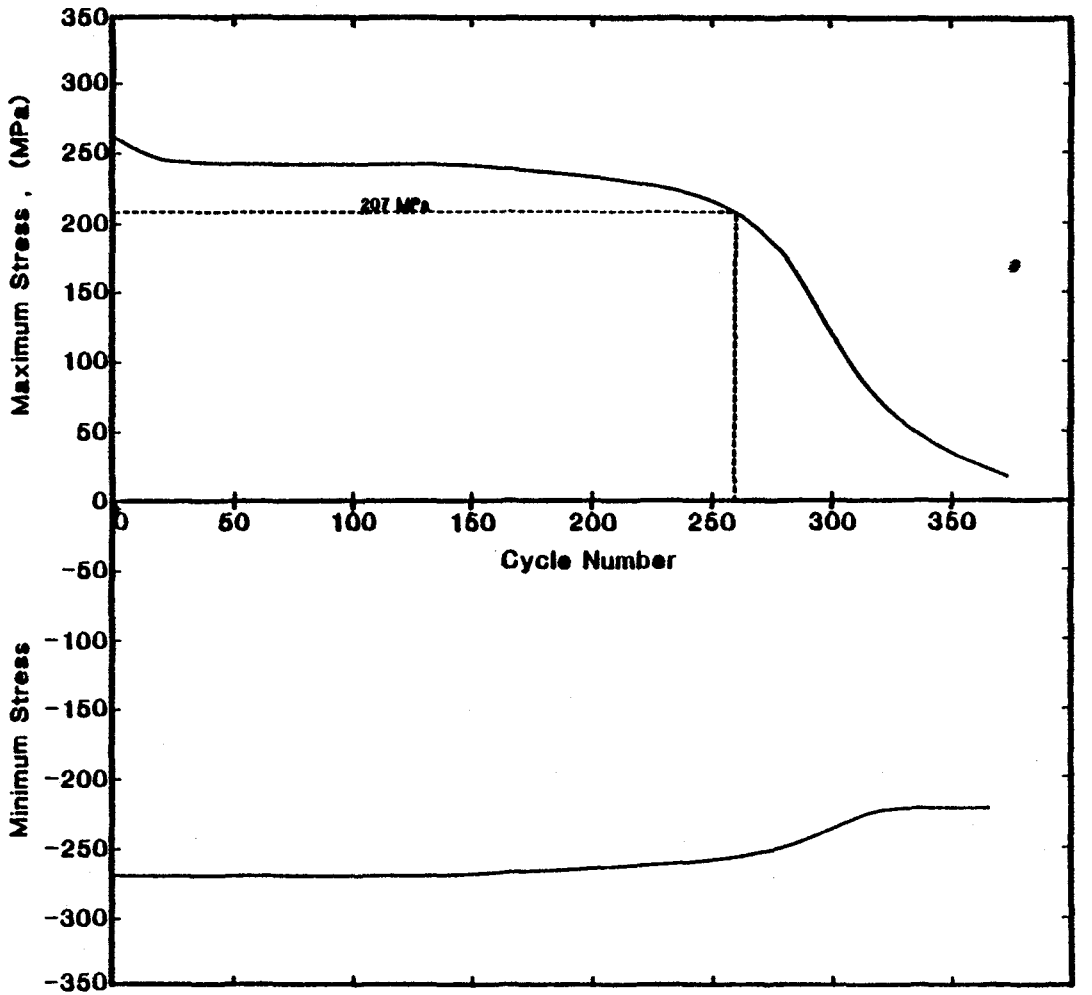

Figure 95. Uncoated René 80 (U of C); Stress versus Cycle Number for the continuous cycling test, GR-5 (Case III).

1. Report No.	2. Government Accession No.	3. Recipient's Catalog No.
NASA CR-165498		

4. Title and Subtitle	5. Report Date
MECHANISMS OF DEFORMATION AND FRACTURE IN HIGH-TEMPERATURE LOW-CYCLE FATIGUE OF RENÉ 80 AND IN 100	March 1982
	6. Performing Organization Code
7. Author(s)	8. Performing Organization Report No.
Glenn Roy Romanoski, Jr.	None
9. Performing Organization Name and Address	10. Work Unit No.
University of Cincinnati Department of Materials Science & Metallurgical Engineering Cincinnati, Ohio	11. Contract or Grant No. NSG-3-263
12. Sponsoring Agency Name and Address	13. Type of Report and Period Covered
National Aeronautics and Space Administration Washington. D.C. 20546	Contractor Report
	14. Sponsoring Agency Code 505-33-22

15. Supplementary Notes Final Report. Project Manager, Robert E. Oldrieve, Structures and Mechanical Technologies Division, NASA Lewis Research Center, Cleveland, Ohio 44135. Based on dissertation submitted by G.R. Romanoski, Jr. in partial fulfillment of the requirements for the degree Master of Science to the University of Cincinnati, Cincinnati, Ohio.

16. Abstract

An investigation of specimens tested for the AGARD strain range partitioning program has been performed. René 80 and IN 100 were tested in air and in vacuum; at 871°, 925°, and 1000° C; and in the coated and uncoated condition. The specimens exhibited a multiplicity of high-temperature low-cycle fatigue damage. Observations of the various forms of damage were consistent with material and testing conditions and were generally in agreement with previous studies. In every case observations support a contention that failure occurs at a particular combination of crack length and maximum stress. A failure criterion which is applicable in the regime of testing studied is presented. The predictive capabilities of this criterion are straight forward.

17. Key Words (Suggested by Author(s))	18. Distribution Statement
Fatigue Metallurgy Superalloys Microstructure	Unclassified - unlimited STAR Category 39

19. Security Classif. (of this report)	20. Security Classif. (of this page)	21. No. of Pages	22. Price*
Unclassified	Unclassified	226	

* For sale by the National Technical Information Service, Springfield, Virginia 22161

☆USGPO: 1982 — 559-091/3235

National Aeronautics and
Space Administration

Washington, D.C.
20546

Official Business
Penalty for Private Use, $300

SPECIAL FOURTH CLASS MAIL
BOOK

Postage and Fees Paid
National Aeronautics and
Space Administration
NASA-451

U.S. MAIL

NASA

POSTMASTER: If Undeliverable (Section 158 Postal Manual) Do Not Return